From carrier cooling to polaron formation: Ultrafast phonon dynamics across the Brillouin zone

Laurent P. René de Cotret

Department of Physics
Faculty of Science
McGill University, Montréal

December 15, 2021

A dissertation submitted to McGill University in partial fulfillment of the requirements of the degree of Doctor of Philosophy

Abstract

Ultrafast electron diffraction with bunch compression has reached a level of performance which allows for the accurate measurement of time-resolved diffuse scattering with a time-resolution of 150 femtoseconds. This information extends ultrafast electron diffraction to time- and momentum-resolved studies of phonon systems (lattice waves) in single-crystal materials. In this dissertation, time-resolved diffuse scattering is explored in two low-dimensional materials. First comes graphite, where anisotropic electron-phonon coupling and stiff phonon bands allow for maximum measurement contrast. The redundancy in ultrafast electron scattering patterns, as well as crystal symmetry, are used to robustly recover the occupancy of all in-plane phonon modes. The mode-, momentum- and time-dependent phonon populations reveal the nonequilibrium lattice states that follow photoexcitation and the complete breakdown of the two-temperature model often used to describe dynamics on the femtosecond time-scale. The measurements presented also provide a direct view of anharmonic decay pathways of phonons across the Brillouin zone, and a technique to extract electron-phonon coupling matrix elements from phonon population is developed. The lessons are then applied to further our understanding of the best intrinsic thermoelectric materials, tin selenide. There, combined ultrafast electron diffraction and diffuse scattering measurements elucidate the mystery of ultralow thermal conductivity and high carrier mobility that gives tin selenide its high thermoelectric efficiency. It is found that strong and anisotropic electron-phonon coupling to polar modes dominates the zone-center phonon dynamics. Light-induced lattice distortions are found to be attributable with fast-forming one-dimensional electron polarons and slow-forming hole polarons isotropic in the plane. These findings recontextualize what was thought about the determinants of thermoelectric performance, primarily the role of electron-phonon coupling to polar modes in preserving high carrier mobility in low-symmetry crystals.

Résumé

La diffraction ultrarapide par électron avec compression radio-fréquence a atteint un niveau de performance qui permet la mesure précise de diffusion diffuse par électron résolue dans le temps avec une résolution de 150 femtosecondes. Cette technique étend la diffraction ultrarapide par électron aux études du système phononique (ondes du réseau d'atomes) résolues dans le temps et l'espace réciproque. Cette thèse élabore l'exploration de la diffusion diffuse d'électron résolue dans le temps dans deux matériaux bidimensionels. Le premier matériau est le graphite, dans lequel l'anisotropie du couplage électron-phonon et le réseau d'atomes très tendu donne un contraste maximal aux mesures expérimentales. La redondance dans les patrons de diffusion, ainsi que la symmétrie du réseau d'atomes, sont exploitées pour déterminer l'occupation de tous les modes phononiques dans le plan atomique. L'occupation des modes phononiques résolue dans le temps et l'espace réciproque révèle l'effondrement du modèle à deux températures souvent utilisé pour expliquer les résultats d'expèriences ultrarapides. Ces mesures donnent aussi une vue directe des chemins de relaxation des phonons à travers la zone de Brillouin, et une méthode pour en extraire le couplage électron-phonon est aussi présentée. Ces leçons sont ensuite appliquées à l'étude d'un des meilleurs matériaux thermoélectriques, le séléniure d'étain. Dans ces expériences, la combinaison de diffraction et diffusion diffuse ultrarapide par électron élucide le mystère de la pauvre conduction thermique et bonne mobilité des porteurs de charges qui donnent au séléniure d'étain sa performance thermoélectrique remarquable. Les résultats démontrent un important couplage électron-phonon aux modes phononique polarisés qui dominent la dynamique au centre de la zone de Brillouin. La distortion du réseau d'atomes qui ensuit la photoexcitation est attribuable à deux types de polarons, l'un formé par des électrons et l'autre par des trous d'électrons, qui se forment à deux vitesses différentes. Ces résultats expliquent comment le séléniure d'étain peut à la fois être un mauvais conducteur thermique et un bon conducteur électrique dû au couplage électron-phonon particulier.

Contents

List of Figures

List of Tables

Acknowledgements

I would like to thank everyone who has made this work possible.

I am most grateful to my doctoral advisor Bradley Siwick for his continuing support. Following the trail marked by his questions has led me to be a better scientist. I am also indebted to my fellow research group members who have played a pivotal role in my research: Martin Otto, Mark Stern, Jan-Hendrick Pöhls, Tristan Britt, and Syed Ali Hassan. Other members of the Center of Physics of Materials have also positively influenced my research, most importantly Benjamin Dringoli and Dominique Matte.

I am also grateful to faculty members Mark Sutton and David Cooke for their advice and support throughout the years.

The research presented in this dissertation would not have been possible without the support of many McGill employees. I would like to thank Jeannie Mui and S. Kelly Sears from the McGill Facility for Electron Microscopy Research, Richard Rossi and Weihua Wang from the Chemistry department, and Jean-Philippe Guay and John Smeros from the Physics department.

I would like to thank the students in our shared office for their friendship and personal support: Dallas Strandell, Gabriela Romero Esquivel, Patrick Brosseau, Cameron Reid, Colin Sonnichsen, Harry Baker, Hélène Seiler, Samuel Palato, and many others. I also thank my significant other, Jessica, for her support throughout the years this work took to complete.

Finally, I am grateful for the love and support of my parents Martine and Pierre, who inspired me to reach my full potential.

Preface

The author declares that the work presented in this dissertation constitutes original scholarship and distinct contributions to the field of condensed matter physics.

The contributions of other members of the Siwick research group and collaborators to this dissertation are described.

The ultrafast electron diffractometer with which experiments were performed by the author was initially designed and built by Robert Chatelain and Vance Morrison, with significant advances in performance brought by Martin Otto. The data acquisition and reduction software that powers the instrument was designed and realized by the author. The ultrafast electron scattering experiments on graphite were performed by Robert Chatelain. The density-functional perturbation theory calculations of the phonon vibrational frequencies and polarization vectors were conducted by Jan-Hendrick Pöhls. The author was responsible for the graphite data analysis and conclusions (Chapter 3). The ultrafast electron scattering experiments on tin selenide were performed by the author, with help from Martin Otto, and the results were analyzed by the author. The bulk SnSe crystals were synthesized by Zhongzhen Luo from Northwestern University (Chapter 4). Ultramicrotomy on SnSe crystals was done by J. Mui from the Facility for Electron Microscopy Research at McGill University (Chapter 4). Smaller contributions are noted in the main text where appropriate.

1. Introduction

The basic physical principles of low-energy quantum mechanics, described by the Schrödinger equation, are understood reasonably-well. And yet, the emergence of new phenomena from the fundamental laws of physics continues to surprise.

The field of condensed matter physics tackles a variety of intertwined questions, from fundamental physics to concrete applications. Given that condensed matter systems are complex, many experimental dimensions are used to distinguish between phenomena.

The processes by which quantum systems equilibrate strongly influence their properties *at equilibrium*. Ultrafast science – which has now reached the ability to observe atomic-scale dynamics in real-time with ultrafast electron scattering – is poised to answer fundamental questions about condensed matter systems which could not be answered due to the stringent spatiotemporal resolution requirements.

1.1. Outrunning temperature to resolve atomic dynamics

In quantum systems, the time scales associated with fundamental actions are determined by the energy scale around experimental temperature. Phonons populated at room temperature (300 K) might have a period shorter than 1 ps (1×10^{-12} s), as $\omega = k_B T/\hbar = 25\,\text{meV}/\hbar = 6\,\text{THz}$. The canonical example of this is superconductivity,[1,2,3] where the lifetime of Cooper pairs can be as short as 40 fs.[4] Not only are the dynamics incredibly fast, but the energy exchange between lattice waves and electrons happens at the Angstrom length scale (1 Å = 1×10^{-10} m).[5]

The coupling phenomena in a condensed matter system may be manifested as a phase transition, some of which can be induced by light. Some of these phases are metastable,[6] hinting at complex networks of energy flow that gives rise to the systems traditionally studied at equilibrium. One such example is an insulator-to-metal phase transition in $Pr_{0.7}Ca_{0.3}MnO_3$, triggered by directly populating an IR-active phonon mode.[7] By photoexciting the sample with the right photons,

resistivity in the near-infrared range (0.5 eV to 1.9 eV) drops by 5 orders of magnitude. This state lives for quite a long time in microscopic terms (tens of nanoseconds). The coherent, large-amplitude lattice oscillations strongly modify the electron hopping probability. This is a stark example of strong lattice-electron interactions which are extremely difficult to measure at equilibrium.

Another exotic consequence of strong lattice-electron interactions are charge-density waves phases. These phases are characterized by a spatial distribution of electron density with a characteristic wavelength, which can be commensurate[8,9,10] or incommensurate[11,12] with the atomic lattice dimensions. There is no unifying principle behind the formation of charge-density waves. In the excitonic insulator titanium diselenide, for example, a transition from a commensurate charge-density wave phase below 190 K to a normal phase is accompanied by the freezing of a zone-boundary optical phonon, which results in a lattice distortion. The appearance of the charge-density wave state is inextricably linked to the order parameter of the phase transition,[13,14] indicating the importance of interactions between charge-carriers and lattice waves. The lattice response to a light-induced suppression of charge-density wave phase can be measured as early as 140 fs following photoexcitation, which shows the strength of the coupling between the lattice and charge-carriers.[15]

On the other hand, ultrafast methodologies are able to *rule out* apparent couplings based on time-scales. Consider vanadium dioxide, a Mott insulator which undergoes a phase transition between semiconducting below 340 K to metallic.[16] This change in conductivity is concomitant with a structural phase transition, from a low-temperature monoclinic lattice to a high-temperature rutile lattice.[17] It has been shown via a combination of structural (ultrafast electron diffraction) and spectroscopic probes (ultrafast infrared reflectivity and time-resolved terahertz spectroscopy) that the structural phase transition is distinct from the insulator-to-metal transition as a metastable metallic state with low-symmetry exists.[18,19] In this case, it is the ability to experimentally outrun thermalization that revealed how vanadium dioxide's electronic properties and lattice structures are not so coupled after all.

The power of ultrafast methodologies lies in their ability to deconvolve interactions in the time-domain.[20] By definition, measurements at equilibrium are unable to determine energy flow and resulting couplings, as equilibrium is defined by the balanced flow of energy throughout a system.

1.1.1. An analogy with Green's functions

Ultrafast methodologies are a way to lift the veil and peer at an aspect of the system's impulse response. In this sense, an analogy with Green's functions is appropriate.

Consider a one-dimensional harmonic oscillator, with its position represented by x. The behavior of the oscillator is determined by the following differential equation:

$$\frac{\partial^2 x}{\partial t^2} + \omega^2 x = F(t) \tag{1.1}$$

where ω is the natural oscillation frequency and is $F(t)$ is an arbitrary driving force. The response of the system $x(t)$ will depend on the driving force $F(t)$. Solving this particular system does not yield insights on similar problems with different driving forces.

Now consider the response of the system to a very specific driving force: the impulse $\delta(t - t_0)$. $\delta(t - t_0)$ is the Dirac delta distribution, the infinite impulse at t_0. The response of the system in Equation (1.1) to an impulse $F(t) = \delta(t - t_0)$ is special. Assume that the solution to

$$\frac{\partial^2 x}{\partial t^2} + \omega^2 x = \delta(t - t_0) \tag{1.2}$$

is known to be $G(t, t_0)$. Then, it can be shown that the solution to an arbitrary driving force $F(t)$, $x_F(t)$, is given by:

$$x_F(t) = \int_{-\infty}^{t} dt_0 \, G(t, t_0) F(t_0) \tag{1.3}$$

Note that the solution to an arbitrary driving force is completely determined by $G(t, t_0)$.

In the general case, consider a physical system whose state is represented by the phase-space vector $\mathbf{x}$, and its behavior is governed by the linear differential operator $\hat{L}$:

$$\hat{L}\mathbf{x}(t) = F(\mathbf{x}, t) \tag{1.4}$$

where the function $F(\mathbf{x}, t)$ is a driving force, or *source term*. Given the impulse response of the system, $G(\mathbf{x}, \mathbf{x}_0, t, t_0)$, which solves

$$\hat{L}\, G(\mathbf{x}, \mathbf{x}_0, t, t_0) = \delta(\mathbf{x} - \mathbf{x}_0, t - t_0), \tag{1.5}$$

the solution to Equation (1.4), $\mathbf{x}_F(t)$, can be expressed as a function of $G(\mathbf{x}, \mathbf{x}_0, t, t_0)$:

$$\mathbf{x}_F(t) = \int dt_0 d\mathbf{x}_0 \, G(\mathbf{x}, \mathbf{x}_0, t, t_0) F(\mathbf{x}_0, t_0) \tag{1.6}$$

The impulse response G is called the Green's function. The response to the system to any perturbation F is *completely determined* by the Green's function*.

Why is this relevant? Real physical systems in condensed matter physics are governed by a linear differential operator, the Schrödinger operator:

$$\hat{L} = i\hbar \frac{d}{dt} - \hat{H} \tag{1.7}$$

where $\hat{H}$ is the Hamiltonian of the (non-driven) system. The response of the total wavefunction Ψ under some external potential $\hat{V}_0$ becomes:

$$\hat{L}\Psi = \hat{V}_0 \Psi \tag{1.8}$$

which is equivalent to the usual Schrödinger equation $i\hbar \frac{d\Psi}{dt} = (\hat{H} + \hat{V}_0)\Psi$. The Green's function of the Schrödinger operator is sometimes called the propagator.[21] In practice, the total wavefunction Ψ is intractable, with more than 10^{23} degrees of freedom at the macroscopic scale. Nonetheless, this system is completely determined by the response to an energy impulse, i.e. the Green's function of $\hat{L}$. In fact, the Green's function formalism is at the heart of many-body theory.[20,22]

Ultrafast measurements allow us to measure an approximation of this impulse response. Distinct excitation conditions and probing techniques explore separate parts of the Hilbert space of possibilities. With the right probes, a shadow of the true impulse response may be assembled to understand important physics which – while not experimentally-accessible at equilibrium – still govern macroscopic phenomena. The knowledge of the impulse response of materials can then inform on the behavior of systems under a variety of external conditions $\hat{V}_0$ such as thermal gradients, external electric and magnetic fields, stoichiometric doping, and pressure.[23]

*In time-dependent situations, the Green's function can be separated into retarded and advanced components, but this distinction is overly technical in the context of this section.

1.1.2. The reversible pump-probe scheme

The time-resolution which gives experimentalists a glimpse of the impulse response of physical systems is derived from ultrafast laser pulses. The pump-probe scheme is used to achieve high time-resolution in experiments where detectors are slow. This scheme involves two pulses. One pulse, the *pump pulse*, is an ultrashort laser pulse which impulsively dumps energy in a sample. The sample is pumped at regular intervals with a period T, which is generally fixed by the laser source. The period T must be great enough to allow the sample to recover between pump pulses. A *probe pulse* is made to interact with the sample after some time-delay τ. Digital measurement devices are generally limited to nanosecond resolution, and are therefore too slow to observe dynamics in the femtosecond range. To circumvent this limiration, the probe pulse is also derived from an ultrafast laser. This probe pulse might be another ultrashort pulse of light, or electrons in the case of ultrafast electron scattering. The delay can usually be adjusted with great precision by changing the path length of the light used to generate the probe pulse. The probe pulse will encode the state of the sample at time-delay τ within the width of the probe pulse.

The process will be repeated n times, where nT is a long-enough delay that the detector of the probe pulse can resolve (e.g. 1 s). Then, the time-delay will be adjusted to a new value, and the process is repeated. By scanning over values of τ in this way, a complete view of the dynamics of the sample following the pump can be assembled. This process is represented in Figure 1.1.

1.1.3. Exploring the lattice impulse response with ultrafast electron scattering

The impulse response of a macroscopic system is an intractable quantity with more than 10^{23} dimensions. Even in the case of non-interacting systems of electrons and ions, the impulse responses of each subsystem is too large to characterize completely. The problem is greatly reduced by studying highly periodic crystalline systems, where instead the response in the spatial-frequency domain is studied. The spatial-frequency-domain impulse response is reduced in that the degrees-of-freedom which are related by symmetry are equivalent.

The description of the impulse response of ordered systems like crystals is fundamentally-different. The relevant physics of 10^{23} particles, 10^{22} of which are related by symmetry, is better described using *collective modes* such as lattice waves, also known as phonons. The instantaneous geometry of the crystal lattice determines the allowed phonon modes, and the energy

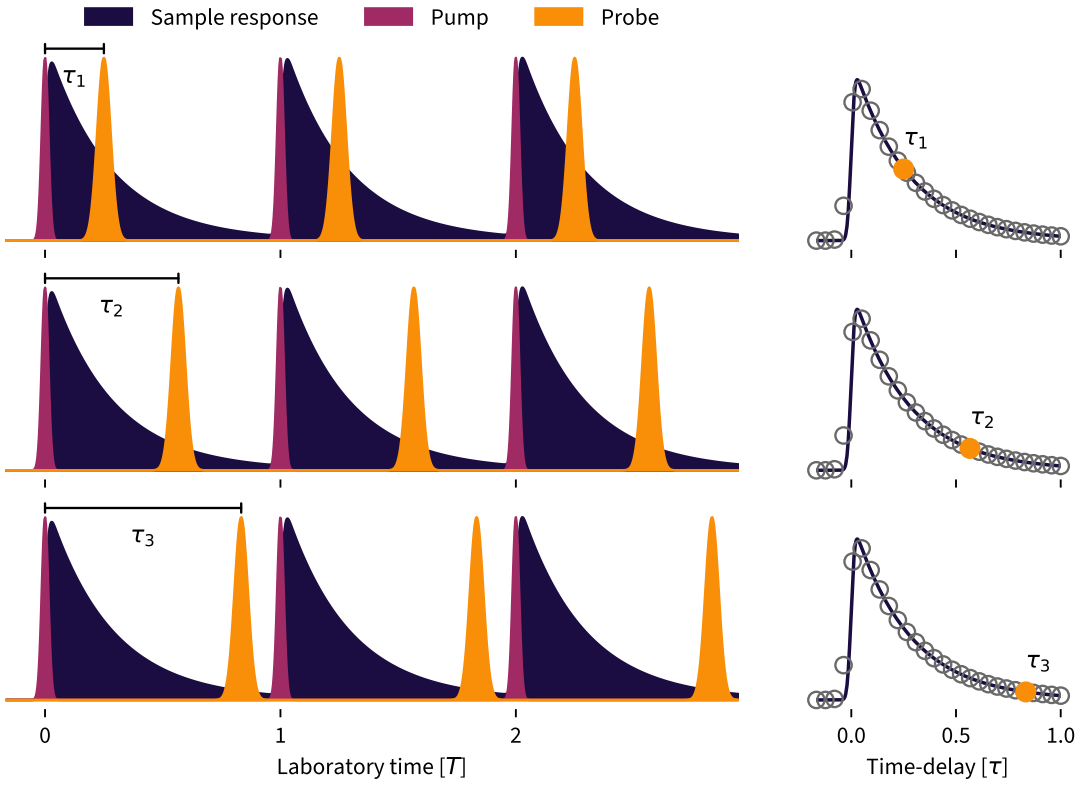

Figure 1.1.: Representation of the pump-probe scheme in laboratory time. On the left, dynamics are initiated with a period T, and the system is allowed to relax back to its initial state. After a time-delay, the system is probed with a separate probe pulse. The process is repeated multiple times while the detector is recording. On the right, the sampled dynamics are shown. The solid trace is the true response, while the grey circles show the measurements convolved with the instrument time resolution. By scanning the time-delay ($\tau_1, \tau_2, \tau_3, \ldots$), a complete picture of sample response can be assembled.

distribution among modes represent a generalization of the idea of temperature at equilibrium.

While the lattice impulse response in terms of lattice modes represent a large part of the total impulse response of a crystalline system, few techniques are capable of resolving such lattice waves. This is due to two main reasons. First, lattice waves are a mostly low-energy phenomena ($<$ 200 meV). This energy scale has historically been hard to access due to what is known as the *terahertz gap*.[24] Second, lattice waves may not induce a dipole moment, which makes some of the modes optically-dark. At equilibrium, multiple techniques are either sensitive to some modes (e.g. Raman[25] and Brillouin[26] spectroscopies) or all modes (x-ray[27,28] and neutron[29] thermal diffuse scattering). But at ultrafast time-scales, where modes can be effectively be populated at

any wavevector and phonon populations change rapidly over time, the choices are much more restrictive. Ultrafast x-ray scattering techniques[30,31] can be used, although the only bright source of ultrashoft x-ray pulses are located in user facilities such as the SLAC National Accelerator Laboratory and the European XFEL. The only available laboratory-scale technique is ultrafast electron scattering, which has reached a level precision sufficient to measure the effects of lattice waves following impulsive photoexcitation in the past decade.[15,32,33,34,35,36]

1.1.4. Electron-phonon interactions

As stated above, electron-phonon interactions play an important role in many interesting systems. It is therefore no surprise that electron-phonon interactions are central to the understanding of the lattice response to ultrafast photoexcitation, as most of the optical pump energy is absorbed by charge-carriers. The photoexcitation energy must dissipate as lattice waves, as acoustic phonons are some of the lowest energy excitations. Therefore, a complete understanding of systems away from equilibrium inherently involves electron-phonon interactions. In this section, a basic description of electron-phonon interactions is given, and more details are presented when needed in Chapter 3 and Chapter 4.

The Hamiltonian which describes a system of electrons and ions is given by:

$$\hat{H} = \hat{H}_{ph} + \hat{H}_e + \hat{H}_i \tag{1.9}$$

where $\hat{H}_{ph}$ is the Hamiltonian of the phonon subsystem, $\hat{H}_e$ is the Hamiltonian of the electronic subsystem, and $\hat{H}_i$ represents the interaction between ions and electrons.[37] The interaction Hamiltonian can be conceptually-expressed as:

$$\hat{H}_i = \sum_{j,j'} \hat{V}_i(\mathbf{r}_j^e - \mathbf{r}_{j'}^i) \tag{1.10}$$

where $\mathbf{r}_j^e$ and $\mathbf{r}_{j'}^i$ are the positions of electron j and ion j', respectively. The interaction potential $\hat{V}_i$ is kept general for this discussion. Now consider that the atomic positions $\mathbf{r}_{j'}^i$ are perturbed by thermal fluctuations, which results in a small displacement $\mathbf{u}_{j'}$ such that $\mathbf{r}_{j'}^i \rightarrow \mathbf{r}_{j'}^i + \mathbf{u}_{j'}$. In this scheme, $\mathbf{r}_{j'}^i$ is now the equilibrium position of ions. To first order, the change in interaction strength is given by the gradient of the interaction potential:

$$\hat{V}_i(\mathbf{r}_j^e - \mathbf{r}_{j'}^i - \mathbf{u}_{j'}) \approx \hat{V}_i(\mathbf{r}_j^e - \mathbf{r}_{j'}^i) - \mathbf{u}_{j'} \cdot \nabla \hat{V}_i(\mathbf{r}_j^e - \mathbf{r}_{j'}^i) \tag{1.11}$$

The first term is the interaction of electrons with ions at their ground-state positions. The second term may be intuitively named the *electron-phonon interaction*:

$$\hat{V}_{ep}(\mathbf{r}) \equiv \sum_{j'} \mathbf{u}_{j'} \cdot \nabla \hat{V}_i(\mathbf{r} - \mathbf{r}^i_{j'}) \tag{1.12}$$

The associated interaction Hamiltonian is given by:

$$\hat{H}_{ep} = \int d\mathbf{r} \hat{\rho}(\mathbf{r}) \hat{V}_{ep}(\mathbf{r}) \tag{1.13}$$

where $\hat{\rho}(\mathbf{r})$ is the electron density operator.

For highly-ordered crystalline systems like the ones studied in this dissertation, phonons are well-defined. In this case, the displacement vectors can be expressed as a sum of phonons in reciprocal space in the second quantization framework:

$$\mathbf{u}_j \propto \sum_{\lambda} \int \frac{d\mathbf{k}_p}{(2\pi)^3} \frac{1}{\sqrt{\omega_\lambda(\mathbf{k}_p)}} \left[\hat{a}_\lambda(\mathbf{k}_p) + \hat{a}^\dagger_\lambda(-\mathbf{k}_p)\right] \mathbf{e}_\lambda(\mathbf{k}_p) e^{i\mathbf{k}_p \cdot \mathbf{r}_j} \tag{1.14}$$

where λ labels phonon modes, $\mathbf{k}_p$ are the phonon wavevectors, $\hat{a}^\dagger_\lambda$ ($\hat{a}_\lambda$) is the creation (annihilation) operator for phonon mode λ, and $\mathbf{e}_\lambda(\mathbf{k}_p)$ ($\omega_\lambda(\mathbf{k}_p)$) is the polarization direction (vibrational frequency) of mode λ. This expansion will be discussed further in Section 2.4. Substituting the expanded form for $\mathbf{u}_j$ in Equation (1.12) yields the following expression for the interaction Hamiltonian $\hat{H}_{ep}$:[38]

$$\hat{H}_{ep} = \sum_{a,b,\lambda} \int \frac{d\mathbf{k}_e}{(2\pi)^3} \int \frac{d\mathbf{k}_p}{(2\pi)^3} g^\lambda_{ab}(\mathbf{k}_p, \mathbf{k}_e) \hat{c}^\dagger_a(\mathbf{k_e} + \mathbf{k}_p) \hat{c}_b(\mathbf{k}_e) \left(\hat{a}_\lambda(\mathbf{k}_p) + \hat{a}^\dagger_\lambda(-\mathbf{k}_p)\right) \tag{1.15}$$

where a and b label electron bands, $\hat{c}^\dagger_a$ ($\hat{c}_a$) is the creation (annihilation) operator for electrons in band a, $\mathbf{k}_e$ is the electronic wavevector, and g is the electron-phonon coupling tensor which describes the strength of the coupling (in units of energy) between the electronic and phonon subsystems. The tensor element $g^\lambda_{ab}(\mathbf{k}_p, \mathbf{k}_e)$ encodes the strength of the scattering of an electron from band a and wavevector $\mathbf{k}_e$ to band b and wavevector $\mathbf{k}_e + \mathbf{k}_p$ through the interaction (emission or absorption) of a phonon in branch λ with wavevector $\mathbf{k}_p$.

The electron-phonon coupling tensor is effectively impossible to measure at equilibrium. Until recently, the determination of this coupling tensor was the purview of calculations. Ultrafast measurements are able to get at g via the lifetime of excitations.[39,40,41] Ultrafast electron diffuse

scattering is currently the only laboratory-scale technique where electron-phonon coupling tensor elements are accessible with momentum-resolution across the entire Brillouin zone.[36]

1.2. A brief history of ultrafast electron scattering

The extension of electron microscopy into time-domain studies is not new. This section will be limited to ultrafast electron scattering in the form of diffraction; see the review by King *et al.*[42] for a historical perspective on ultrafast electron microscopy in general. As early as 1982, Gerard Mourou and Steve Williamson[43] followed the picosecond-scale transformation of an aluminum film following photoexcitation. In this work, the authors prepare 100 ps electron bunches using a streak camera. They note that the temporal resolution of the experiment is ultimately limited by the length of the electron bunch:[43]

> *The electron pulse width has been measured by using the camera in the normal streak mode and is found to be ∼100 ps. This value departs significantly from the 15 ps pulse width expected. The pulse broadening is due to the space-charge effect caused by the relatively high electron flux required to photograph the pattern with our present system.*

The challenges of ultrafast electron scattering on the 100 fs time-scale – which is the current state-of-the-art – were apparent in the first ultrafast electron scattering experiments. Measurements of atomic structure require high beam brightness to achieve a high signal-to-noise ratio, but dense electron bunches experience space-charge repulsion (i.e. worsening time-resolution). The trade-off between signal-to-noise and time-resolution is represented as the expansion of the bunch length l. Using a mean-field equation,[44] the bunch length l expands as follows:

$$\frac{d^2l}{dt^2} = \frac{Ne^2}{m_e\epsilon_0\pi r^2}\left[1 - \frac{l}{\sqrt{l^2+4r^2}}\right] \tag{1.16}$$

where N is the number of electrons in the bunch, e the quantum of charge, m_e the electron mass, ϵ_0 the vacuum permittivity, and r is the beam radius. The first demonstration of ultrafast electron scattering was done by the same authors[43] to study the ultrafast melting of aluminium[45] with a time-resolution a tens of picoseconds.

The modern form of pump-probe ultrafast electron scattering was brought by Ahmed Zewail and his team. At the time, Zewail was already known as the “Father of Femtochemistry” for the development of ultrafast spectroscopy.[46] Zewail and collaborators proposed to replace the

optical probe pulse used in pump-probe femtosecond spectroscopy with an electron pulse.[47,48] What followed was a series of experiments probing the transient molecular structures at the picosecond time-scale following photoexcitation in the gas phase.[49,50,51] The ability to track the nuclear coordinates directly represented the perfect complement to Zewail's Nobel prize-winning work on femtochemistry via ultrafast spectroscopy.

It was not until Siwick *et al.*,[52,53] however, that the ideas of Mourou and Williamson were applied with sub-picosecond sensitivity (600 fs) to the solid state. This work reached a time-resolution sufficient to address whether or not the ultrafast phase transition from solid to liquid-like was analogous to the thermal phase transition.[54]

By 2005, the prevalent sentiment was that the space-charge problem limited the applicability of ultrafast electron scattering to a time-resolution of 1 ps. King *et al.*[42] identify three paths to control space-charge effects:

1. Reducing the electron-emission – sample distance. By reducing this distance, the space-charge-driven expansion of the electron bunch remains limited.[44]

2. Using higher electron energies. The space-charge explosion is reduced significantly for electrons with relativistic energies ($>$1 MeV).[55]

3. Reducing space-charge pulse expansion by limiting the energy spread in the electron bunch.[56]

The solution to the space-charge probleme came from the insight of Siwick *et al.*,[44] who showed that the electrons in a bunch develop a strong correlation in phase space as it propagates. Space-charge effectively slows down the front electrons with respect to the center of charge, while it accelerates the electrons at the front of the bunch. After some propagation time, a linear correlation is established between the relative axial position within the bunch and the relative velocity within the bunch. It is precisely because the correlation is so strong that a solution can be devised. Siwick, Luiten, and collaborators[57] showed with advanced charged particles simulations how an electromagnetic cavity operating in the radio-frequency band could be used to reverse the correlation between the axial position and velocity of electrons within the bunch. The particular implementation in the Siwick research group is presented below in Section 1.3. The design of a radio-frequency compression cavity was validated by Chatelain *et al.*[58] in 2012.

1.2.1. The landscape today

At the time of writing, there are many research groups across the world using ultrafast electron scattering techniques with great success. This section is a non-exhaustive enumeration of the field as of the year 2021.

First, the most traditional approach of ultrafast electron diffraction in the compact geometry is still alive today. One of the most successful research groups using this tool is led by R. Ernstorfer at the Fritz-Haber Institute in Berlin which has been studying multiple solid-state systems.[34,59,60]

There are also multiple radio-frequency-compressed ultrafast electron diffraction instruments in use today. Such an instrument is used in the author's research group led by B. Siwick at McGill University.[15,18,35,36,61] Several instruments are located at the University of Toronto, in the group led by R. J. D. Miller.[62,63,64,65] Another instrument based on the design by van Oudheusden *et al.*[57] has been in use at the University of Nebraska, in the research group led by M. Centurion, with special emphasis on gas-phase electron diffraction.[66]

Finally, there are a few high-energy (MeV) accelerator-based ultrafast electron diffraction instruments in operation today. The most well-known is located at the Stanford Linear Accelerator Center (SLAC), part of a group led by X. Wang. Several research groups have been using this instrument as it has turned into a user-facility.[67,68,69] Another high-energy instrument is located at the University of California, Los Angeles, in a research group led by P. Musumeci[70] which focuses on instrument development.

1.3. Electron bunch compressor

The compression of electron bunches has been the key technological advancement that has allowed the work presented here. It has allowed for high time-resolution while preserving a high bunch charge, which is required to observe the small signals presented in Chapter 3 and Chapter 4. The electron bunch compression that was used for the experiments presented herein has been the subject of much work and refinement in the past decade. Its function is briefly described in this section, with a particular emphasis on recent developments regarding laser-compressor synchronization.

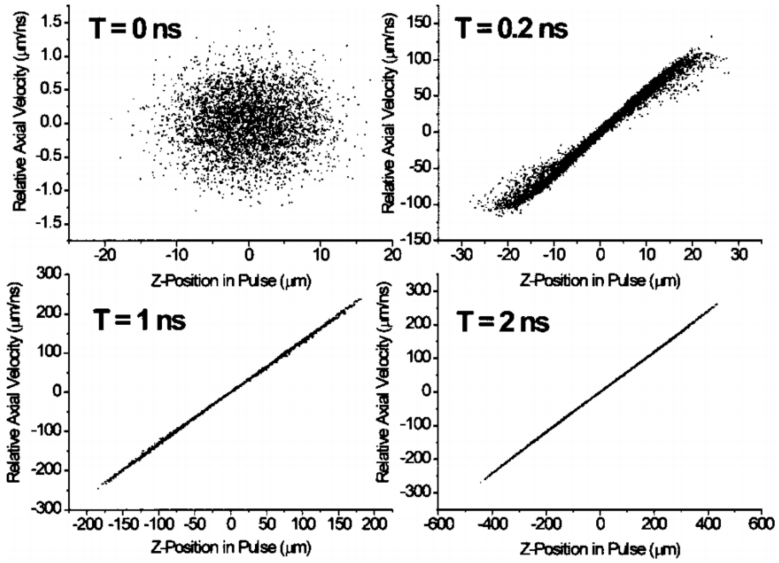

Figure 1.2.: Relative axial velocity vs axial position (Z) for all electrons in the pulse at four times (T) during its propagation. The pulse is composed of 10 000 electrons at 30 keV, with an initial bunch length equivalent to 150 fs, an initial radius ut 75 µm, and initial beam divergence of 1.5 mrad. The width of the velocity distribution becomes larger as the pulse lengthens. The spatial distribution of velocities also evolves. As electrons redistribute themselves inside the packet a linear velocity chirp develops on the electron pulse. For 30 keV electrons, a propagation time of 2 ns is equivalent to a propagation distance of roughly 20 cm. Reused with permission from Siwick *et al.*[44]

1.3.1. Bunch correlations

The idea of an electron bunch compressor is to control the electron bunch in phase space. As stated previously, a landmark paper by Siwick *et al.*[44] showed that as the electron bunch propagates, electrons in develop a linear correlation between their position within the bunch and their velocity with respect to the average bunch velocity. This is shown in Figure 1.2. The idea behind the radio-frequency compressor is to reverse this correlation using a standing radio-frequency wave to slow down the electrons at the front of the bunch, and accelerate the electrons at the back of the bunch, so that there is a single point downstream where the electron bunch is very short. This can be done by using an electromagnetic wave, oriented with the electric field along the propagation axis z (TM_{010} mode), and timed such that the amplitude of the electric field vanishes when the bunch center-of-charge is located in the center of the cavity. This procedure is effectively a rotation in phase-space. The procedure and its effect on the phase-space representation of electron bunches is shown in Figure 1.3.

The visualization in Figure 1.3 also shows the importance the timing of the compression field. If

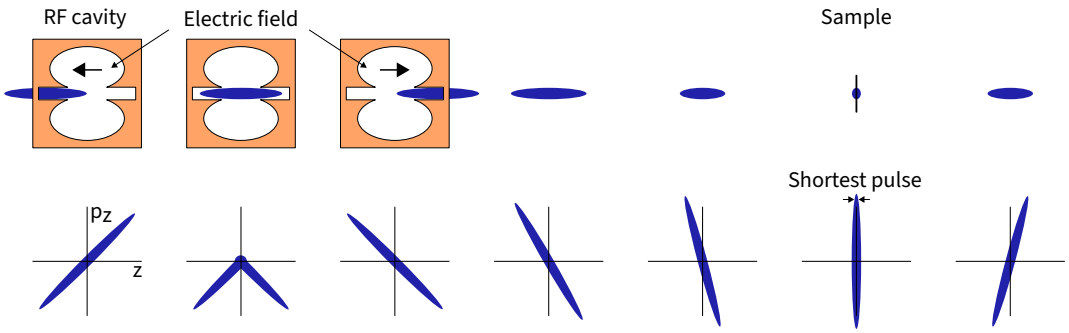

Figure 1.3.: Timeline of the compression of an electron pulse as it propagates to the sample. In the top row, the electron pulse is shown in real-space as it propagates through the compression cavity towards the sample. In the bottom row, the phase-space representation of the bunch is shown like in Figure 1.2.

the field is not timed properly, a net momentum kick will be imparted on the electron bunch, which will change the arrival time of the electrons at the sample. This is equivalent to a *translation* in phase space. This is discussed in Section 1.3.4.

1.3.2. Compressor design

The general idea of phase-space rotation may be realized in multiple ways. Some design considerations that explain the particularities of the radio-frequency cavity used in this work are addressed here.

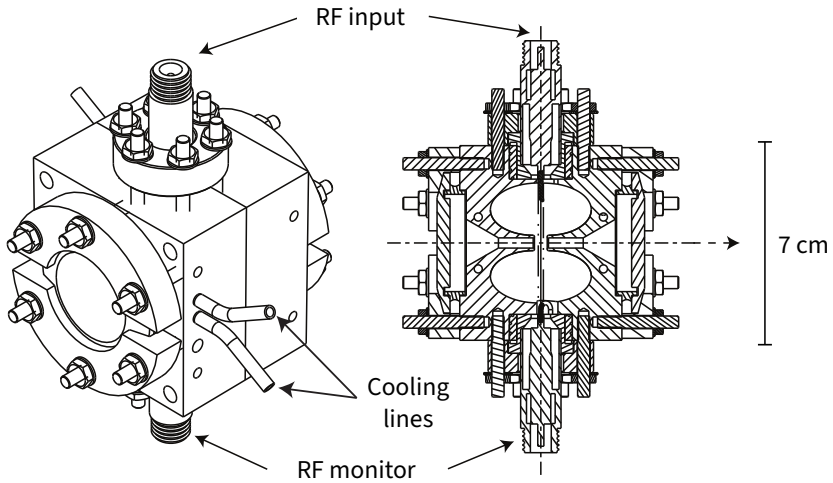

Figure 1.4.: Machining diagram of the radio-frequency compression cavity used in this work. Modified from Chatelain.[71]

Consider the choice of the wavelength of the compression electric field. The main requirement

here is that the electron bunch experiences a field that varies linearly as it travels through the cavity. Waves in the 0.5 GHz to 6 GHz range are required given that uncompressed electron bunch with 10^6 electrons may be $\sim$100 ps long. The choice of 3 GHz was ultimately chosen because of previous work in synchronizing 3 GHz radio-frequency cavities to 800 nm laser pulse trains.[72]

The shape of the cavity is also important. In its simplest form, a "pillbox" cavity (hollow cylinder) of appropriate dimensions would support the right radio-frequency compression wave.[73] However, pillbox cavities are rather inefficient in terms of field-strength per Watt of input power. The final lobe design reduced input power requirements by 90% compared to the pillbox geometry.[57] The design of the cavity as manufactured is shown in Figure 1.4.

1.3.3. Compressor characterization

Initial characterization of the electron compressor in 2012 was performed with a vector network analyzer up to 3 GHz only. The author characterized the cavity again in December 2019 across a much larger bandwidth of 50 GHz, using an Agilent Technologies N5247A vector network analyzer. The transmission spectrum is presented in Figure 1.5. The main resonance near 3 GHz is clearly visible. Simulations have revealed that some higher-frequency modes are also suitable for electron pulse compression[†]. Further work is planned to test whether using two or more cavity compression modes can enhance instrument performance.

The temperature-dependence of the resonant frequency was also investigated. By changing the temperature of the cavity via liquid cooling, its dimensions are modified slightly due to thermal expansion. The change in the transmission spectrum near 3 GHz is presented in Figure 1.6.

1.3.4. Driving field generation and timing considerations

The relative timing of the microwave compression field is of paramount importance. As stated previously, jitter or drift in the phase of the field will impart a net momentum kick to electron bunches, which will in turn deteriorate the time-resolution of experiments. The zero-crossing of the sinusoidal compression field needs to be synchronized to the moment the center-of-charge of the bunch passes through the center of the cavity. If the zero-crossing is too early, more of the bunch will be accelerated, resulting in a net momentum kick. If the zero-crossing is too late, more

[†]The cavity resonance simulation and modelling have been performed by Tristan Britt.

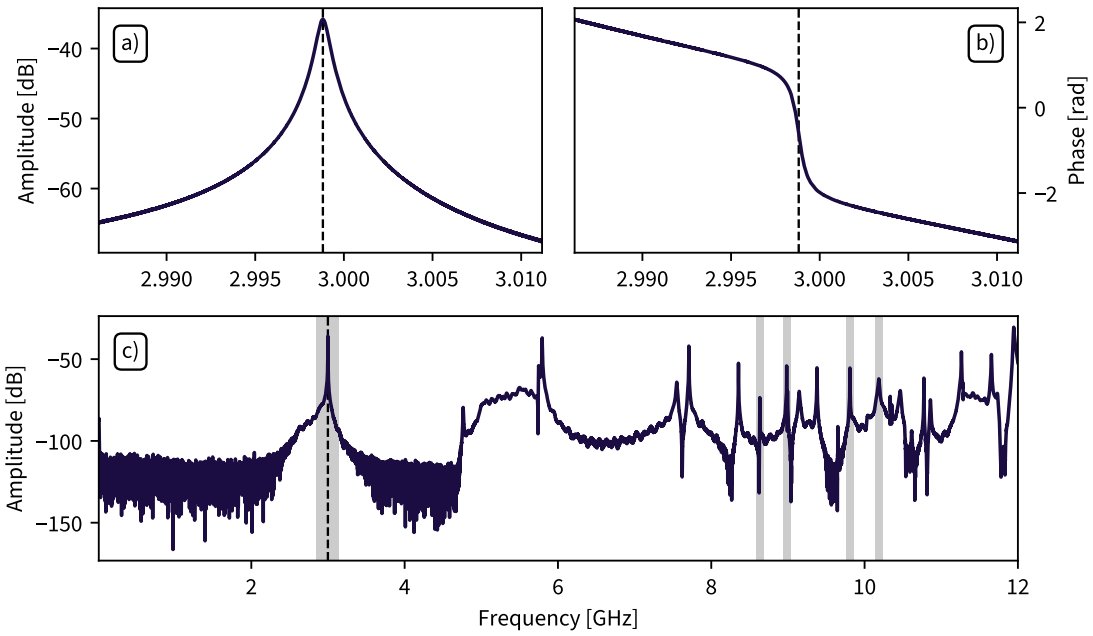

Figure 1.5.: Characterization of the cavity transmission spectrum at 13 °C. **a)** Transmitted amplitude near 3 GHz. **b)** Phase of the transmitted signal near 3 GHz. **c)** Amplitude spectrum in a wide band shows multiple resonances up to 12 GHz. Gray overlays mark compression modes of the cavity.

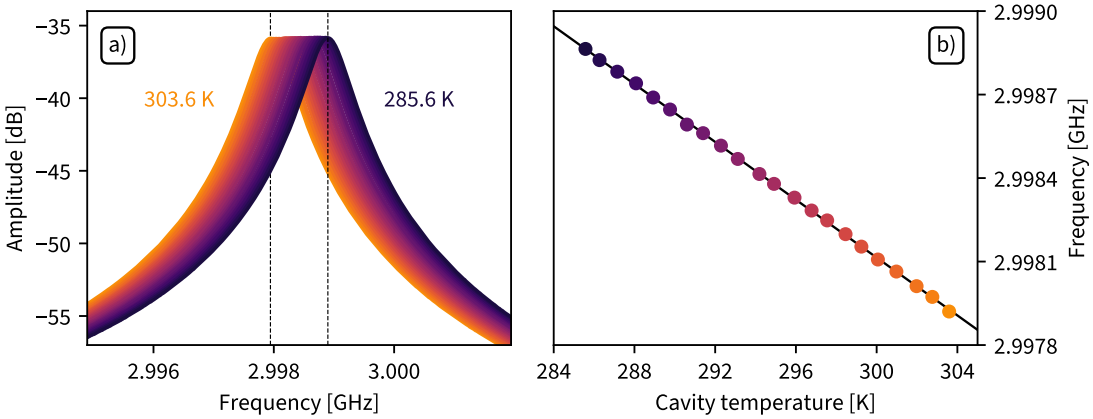

Figure 1.6.: Effect of cavity temperature on resonant frequency near 3 GHz. **a)** Transmission function from 285 K to 304 K in steps of 1 K. **b)** Temperature dependence of the resonant frequency shows a linear dependence with a slope of $-52.6 \pm 0.2\,\mathrm{kHz\,K^{-1}}$.

of the bunch will be decelerated, resulting in a net momentum loss. The main consequence is a drift in the arrival time of the electron bunch at the sample, relative to the laser photoexcitation, which degrades time-resolution. This is shown in Figure 1.7.

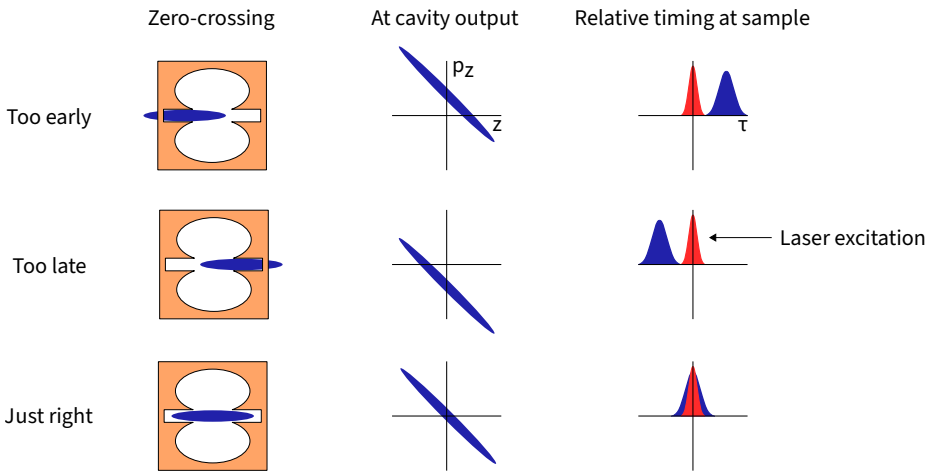

Figure 1.7.: Effect of mistiming of electron compression on the electron bunch. The zero-crossing ($\tau = 0$) determines the moment where the electric field vanishes in the cavity. If the compression zero-crossing happens too early ($\tau < 0$), electron bunches are effectively slowed down, and arrive late at the sample relative to the photoexcitation. On the other hand, if the compression zero-crossing happens too late $\tau > 0$, electron bunches are accelerated, and arrive early at the sample relative to the laser excitation.

Because the electron bunches are photogenerated from a laser pulse train, timing the microwave compression field is effectively a problem in synchronizing an electromagnetic wave to laser pulses. The initial synchronization system used until 2017 is described in Kiewiet *et al.*[72] In broad strokes, this initial synchronization system generated its own 3 GHz signal from an internal clock. The phase of this signal was adjusted based on the phase of laser pulse train as measured with a photodiode. This approach suffered from relatively large drift over the course of multiple hours.

Since 2017, a direct synchronization approach has been in use. This synchronization system is described in detail in Otto *et al.*,[74] and a brief summary is given here. There are two parts to this improved synchronization system. First, a 3 GHz signal is generated directly from the 75 MHz laser oscillator pulse train, which is then amplified to drive the electron compressor. Second, the phase of the input to the electron compressor is controlled to eliminate long-term phase drifts. These two aspects of the synchronization system are addressed in their own subsections below.

1.3.4.1. Direct generation of a driving field

High-bandwidth photodiodes (>10 GHz) are now available as commercial products. Their response time is good enough (∼25 ps) to capture the 100$^{\text{th}}$ harmonic from a typical 70 MHz to 80 MHz laser oscillator.

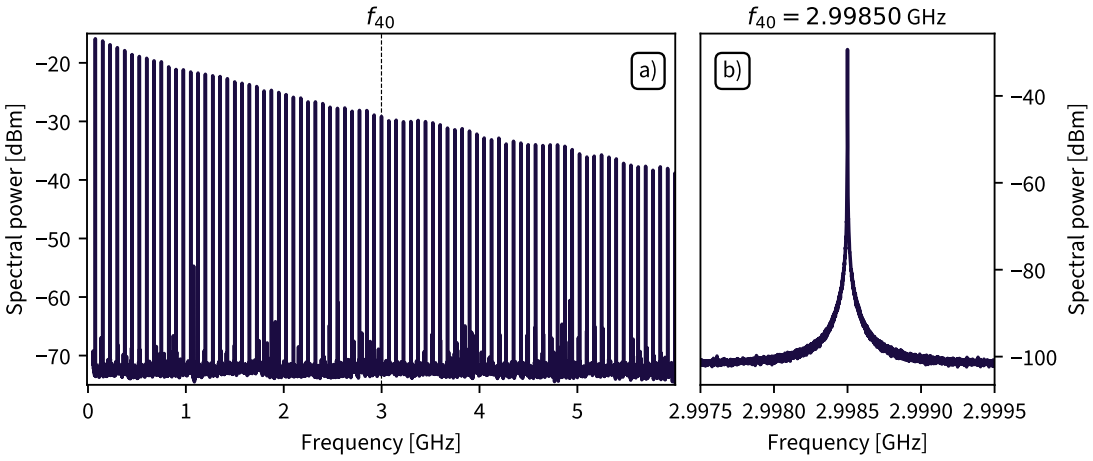

Figure 1.8.: Spectrum of a 75 MHz oscillator pulse train on a high-bandwidth (12.5 GHz) photodiode, with an input power of 20 mW. f_{40} marks the location of the 40$^{\text{th}}$ harmonic of the fundamental frequency. **a)** Full bandwidth measurement shows harmonics up to at least 6 GHz. **b)** Spectrum centered on the 40$^{\text{th}}$ harmonic of the oscillator repetition rate.

A master clock signal is generated by splitting 5% of the laser oscillator power (20 mW) and focusing it on a high-bandwidth photodiode. The harmonics of the 75 MHz pulse train are visible in the power spectrum, as shown in Figure 1.8; 3 GHz corresponds to the 40$^{\text{th}}$ harmonic. A combination of low-phase-noise amplifiers and a band-pass filter is used to isolate a master clock signal at a power of −2.5 dBm (0.5 mW). At this stage, a portion of the master clock signal is split off for use in a feedback loop, described in the next section.

The master clock signal is then amplified in a commercial continuous-wave solid-state amplifier, which can provide up to 60 dB of amplification (up to a maximum of 200 W of amplification). Typically, an output power in 47.5 dBm to 48.5 dBm (56 W to 71 W) range was used to drive the electron compressor. To ensure that the cavity is driven at resonance, either the temperature of the cavity (see Figure 1.6) or the oscillator pulse train repetition rate can be adjusted.

1.3.4.2. Feedback system to eliminate long-term drift

Ultrafast electron scattering experiments take multiple hours to complete; some of the experiments presented in Chapter 4 ran for 72 h. It is therefore important to ensure that the phase of the compressor driving field (i.e. the timing of the zero-crossing) be stable over this period. Drift in the phase of the driving field can occur due to many factors. One major source of drift is due to temperature changes of the electron compression, which induces thermal expansion/contraction of the radio-frequency cavity. The resonance of the cavity is therefore changed, and the driving field becomes detuned from the cavity resonance. Another source of drift is due to amplitude drift in the laser oscillator, which can cause a phase drift in a process called amplitude-phase conversion.[75,76]

A solution to the drift problem was implemented based on a feedback loop. The radio-frequency cavity was machined with an output port which can be used to measure the radio-frequency signal transmitted through the cavity. The phase of this transmitted signal is a measure of how detuned the driving field is compared to the cavity resonance. The phase difference is then measured by comparing the two signals, and a phase shift is applied to minimize the detuning of the driving field.

1.3.5. Alternative approaches

Electron bunch compression can be achieved in two orthogonal ways. The first method, one form of which was presented above, is to adjust the velocity of electrons with respect to the bunch. The other method is to change the electron path length based on their energy (velocity). The result is the same: the electron bunch is compressed in time at a specific point downstream.

Electron bunch compression via a modification of electron energies must be done with strong electric fields, but electromagnetic cavities are not necessary. Ehberger *et al.*[77] have demonstrated the compression of electron bunches with THz fields, although with very low bunch charge (1.6×10^{-7} pC, 3 electrons per bunch). This approach is fully-optical, meaning that there is no need to synchronize the laser pulses to electronics. In fact, THz fields can be used to generate, compress, and streak electron bunches.[77,78]

Electron bunch compression via path length modulation has been proposed and implemented to varying degrees of success. The advantage of many of these approaches based on electron beam geometry is that laser-electronics synchronization is not required. Geometries include 360°

magnet compressors,[79] spherical electrostatic capacitor compressors,[80] and reflectron-based mirror compressors.[81,82,83] More recently, a scheme that combines a magnetic beam separator and a reflectron – with better experimental alignment and spatial aberration correction – has been proposed by Mankos *et al.*[84] The most impressive experimental demonstration of a jitter-free electron bunch compressor remains the *achromatic bend* design, which uses a magnet to disperse the electrons spatially according to their energies, and then recombine them further downstream.[85,86]

1.4. Experimental apparatus

All ultrafast electron scattering experiments presented in this dissertation were performed with the same experimental apparatus, presented in Figure 1.9.

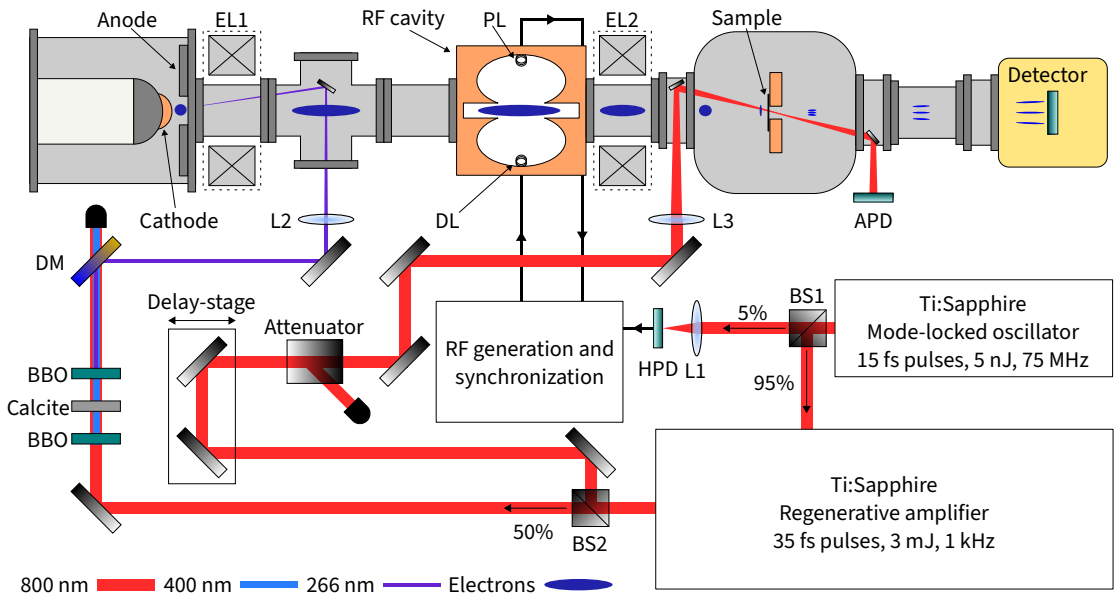

Figure 1.9.: Experimental setup diagram for the ultrafast electron scattering instrument. BS1/2: Beam splitter. HPD: high-bandwidth photodiode. BBO: β-Barium borate crystal. DM: Dichroic mirror. BS1/2: Beamsplitter. L1/2/3: Focusing lens. EL1/2: Electron lens. APD: alignment photodiode. DL: Driving loop. PL: Pickup loop.

The heart of the apparatus consists of the ultrafast laser system. A mode-locked oscillator (Spectra-Physics Tsunami) generates short (<20 fs) pulses of 800 nm light, at a pulse repetition rate of 75 MHz. Each oscillator pulse carries 5 nJ of energy, which is not enough to generate the bright electron pulses required by ultrafast electron scattering experiments. Five percent of the oscillator pulse train is focused down to a 35 µm spot on a photodiode with large bandwidth

(12.5 GHz), generating a master clock signal with non-negligible spectral power up to 3 GHz (Section 1.3.4). The remaining ninety-five percent of the oscillator power is used to seed a regenerative laser amplifier (Spectra-Physics Spitfire Pro). The oscillator pulses are amplified via chirped-pulse amplification,[87] outputting 35 fs pulses each carrying 3 mJ of energy, at a repetition rate of 1 kHz. The amplified pulse train is split between two branches: pump and probe.

1.4.1. Pump line

On the pump line, the laser pulses propagate to a delay stage (Newport ILS200CCHA) on which a retroreflector is installed. This delay stage provides a resolution of 300 nm, with total travel of 20 cm. These dimensions translate to a time-delay resolution of 2 fs and temporal range of 1.3 ns. The energy of the pump pulses is then attenuated by using an ultrafast attenuator assembly, composed of a waveplate and polarizing filter. A lens is used to focus the pump pulses onto the sample.

The attenuation and focus of the beam are adjusted to achieve the desired photoexcitation density (or *fluence*) on an area that is much larger than the sample, ensuring uniform illumination conditions. The attenuated and focused pump pulses are routed inside the vacuum chamber through a z-cut quartz (SiO_2) window, which is transparent over a large range of wavelengths. Inside the vacuum, two mirrors is positioned so that the pump pulses are transmitted through the sample and routed outside to a photodiode, for alignment purposes.

1.4.2. Probe line

On the probe line, two beta barium borate (BBO) crystals are used to generate the third harmonic of 800 nm: a first conversion to 400 nm, and then a second conversion to 266 nm. A calcite crystal is placed between the two BBO crystals to compensate for the wavelength-dependent dispersion in the BBO crystals, and keep the optical pulse short. This non-linear light conversion is possible because the pulses are extremely energy-dense, resulting in a conversion efficiency of 1% from 800 nm to 266 nm. The ultraviolet photons are then routed into the electron gun assembly, where they are focused on a copper hemispherical cathode. The work function of copper (4.5 eV[88]) is slightly lower than the ultraviolet photon energy (4.65 eV), resulting in electrons being freed from the copper cathode with little extra energy. These electrons are

accelerated via a static potential of 90 kV. The kinetic energy can be converted to a velocity v_e as follows:

$$\frac{v_e}{c} = \sqrt{1 - \frac{m_0 c^2}{m_0 c^2 + eV}} \tag{1.17}$$

where m_0 is the electron rest mass, V is the accelerating potential, and e is the quantum of charge.[89] For an accelerating potential $V = 90$ kV, $v_e \approx 0.526\ c$[‡].

After acceleration, a solenoid lens loosely focuses the electron bunches through the 3 mm aperture of the radio-frequency compression cavity described in Section 1.3, ensuring that electron bunches do not lose much charge before compression. After the radio-frequency compression cavity, another solenoid lens focuses the transverse profile of the electron bunches onto the detector, so that the diffraction pattern is imaged clearly. Electron bunches are transmitted through the sample at normal incidence. The scattering pattern is collected by an electron camera (Gatan Ultrascan 895), on a cooled charge-coupled detector. The transmitted, unscattered beam is collected by a Faraday cup. A Keithley 6514 electrometer measures the charge on the Faraday cup at a rate of 1 kHz, giving a rough estimation of the bunch-to-bunch charge fluctuations.

1.4.3. Interactive data exploration software

The experimental procedure employed in the Siwick research group acquires data in a repeating fashion, in order to increase the signal-to-noise ratio. The resulting experimental raw data can be hundreds of gigabytes in size. The author has created a software suite that performs data reduction and allows for the interactive exploration of the reduced data, in real-time. While this software suite has had a profound impact on the research presented in this work, the details are not necessary to appreciate the results presented in Chapter 3 and Chapter 4. Interested readers are encouraged to read more in Appendix A.

1.5. Overview of the dissertation

This dissertation has two goals: to push the understanding of nonequilibrium lattice dynamics as measured by ultrafast electron scattering, and to apply this understanding to elucidate the couplings in two-dimensional materials such as graphite and tin selenide.

[‡]Equation (1.17) takes into account the relativistic modification of the electron mass, without which the electron velocity is overestimated by roughly 10% for $V = 90$ kV.

To this end, the dissertation starts proper with a description of the theoretical framework of ultrafast electron diffraction and diffuse scattering in Chapter 2. This chapter holds a special place in the author's heart. At the time of writing, it is the only quantum-mechanical derivation of ultrafast diffuse scattering amplitude for either x-ray or electrons. The thorny subject of multiple electron scattering is also discussed.

Ultrafast electron diffuse scattering measurements in graphite are considered next in Chapter 3. Graphite is a wonderful benchmark system because of the stiffness of the lattice, which gives diffuse scattering measurements incredibly high contrast. In a way, diffuse scattering in graphite is the most definitive diffuse scattering experiment. The work in this chapter was peer-reviewed and published in René de Cotret *et al.*[36]

The study of the origin of tin selenide's high thermoelectric performance is the subject of Chapter 4. In this material, ultrafast electron diffraction and diffuse scattering are used in conjunction to observe polaron formation, which might explain how strong electron-phonon coupling can positively impact thermoelectric performance. The work in this chapter was peer-reviewed and published in René de Cotret *et al.*[90]

References

1 L. N. Cooper. *Bound electron pairs in a degenerate Fermi gas*. *Physical Review* **104** no. 4 (1956), p. 1189. DOI: 10.1103/physrev.104.1189.

2 J. Bardeen, L. N. Cooper, and J. R. Schrieffer. *Theory of superconductivity*. *Physical Review* **108** no. 5 (1957), p. 1175. DOI: 10.1103/physrev.108.1175.

3 J. R. Schrieffer, D. J. Scalapino, and J. W. Wilkins. *Effective tunneling density of states in superconductors*. *Physical Review Letters* **10** no. 8 (1963), p. 336. DOI: 10.1103/physrevlett.10.336.

4 F. Boschini, E. H. da Silva Neto, E. Razzoli, M. Zonno, S. Peli, R. P. Day, M. Michiardi, M. Schneider, B. Zwartsenberg, P. Nigge, R. D. Zhong, J. Schneeloch, G. D. Gu, S. Zhdanovich, A. K. Mills, G. Levy, D. J. Jones, C. Giannetti, and A. Damascelli. *Collapse of superconductivity in cuprates via ultrafast quenching of phase coherence*. *Nature Materials* **17** no. 5 (2018), pp. 416–420.

5 G. M. Eliashberg. *Interactions between electrons and lattice vibrations in a superconductor*. *Soviet Physics JETP* **11** no. 3 (1960), pp. 696–702.

[6] S. Koshihara, Y. Tokura, K. Takeda, T. Koda, and A. Kobayashi. *Reversible and irreversible thermochromic phase transitions in single crystals of polydiacetylenes substituted with alkylurethanes*. *The Journal of Chemical Physics* **92** no. 12 (1990), pp. 7581–7588. DOI: 10.1063/1.458195.

[7] M. Rini, N. Dean, J. Itatani, Y. Tomioka, Y. Tokura, R. W. Schoenlein, and A. Cavalleri. *Control of the electronic phase of a manganite by mode-selective vibrational excitation*. *Nature* **449** no. 7158 (2007), pp. 72–74. DOI: 10.1038/nature06119.

[8] T. M. Rice and G. K. Scott. *New mechanism for a charge-density-wave instability*. *Physical Review Letters* **35** no. 2 (1975), pp. 120–123. DOI: 10.1103/physrevlett.35.120.

[9] S. Hellmann, M. Beye, C. Sohrt, T. Rohwer, F. Sorgenfrei, H. Redlin, M. Kalläne, M. Marczynski-Bühlow, F. Hennies, M. Bauer, A. Föhlisch, L. Kipp, W. Wurth, and K. Rossnagel. *Ultrafast melting of a charge-density wave in the Mott insulator* $1T$*-TaS*$_2$. *Physical Review Letters* **105** no. 18 (2010), pp. 187401–187405. DOI: 10.1103/physrevlett.105.187401.

[10] N. Erasmus, M. Eichberger, K. Haupt, I. Boshoff, G. Kassier, R. Birmurske, H. Berger, J. Demsar, and H. Schwoerer. *Ultrafast dynamics of charge density waves in* $4H_b$ *–* $TaSe_2$ *probed by femtosecond electron diffraction*. *Physical Review Letters* **109** no. 16 (2012), p. 167402. DOI: 10.1103/physrevlett.109.167402.

[11] W. L. McMillan. *Theory of discommensurations and the commensurate-incommensurate charge-density-wave phase transition*. *Physical Review B* **14** no. 4 (1976), p. 1496. DOI: 10.1103/physrevb.14.1496.

[12] G. Storeck, J. G. Horstmann, T. Diekmann, S. Vogelgesang, G. von Witte, S. V. Yalunin, K. Rossnagel, and C. Ropers. *Structural dynamics of incommensurate charge-density waves tracked by ultrafast low-energy electron diffraction*. *Structural Dynamics* **7** no. 3 (2020), p. 034304. DOI: 10.1063/4.0000018.

[13] A. Kogar, M. S. Rak, S. Vig, A. A. Husain, F. Flicker, Y. I. Joe, L. Venema, G. J. MacDougall, T. C. Chiang, E. Fradkin, J. van Wezel, and P. Abbamonte. *Signatures of exciton condensation in a transition metal dichalcogenide*. *Science* **358** no. 6368 (2017), pp. 1314–1317. DOI: 10.1126/science.aam6432.

[14] T. Kaneko, Y. Ohta, and S. Yunoki. *Exciton-phonon cooperative mechanism of the triple-*q *charge-density-wave and antiferroelectric electron polarization in* $TiSe_2$. *Physical Review B* **97** no. 15 (2018), pp. 155131–155154. DOI: 10.1103/physrevb.97.155131.

[15] M. R. Otto, J.-H. Pöhls, L. P. René de Cotret, M. J. Stern, M. Sutton, and B. J. Siwick. *Mechanisms of electron-phonon coupling unraveled in momentum and time: the case of soft phonons in $TiSe_2$*. *Science Advances* **7** no. 20 (2021). DOI: 10.1126/sciadv.abf2810.

[16] F. J. Morin. *Oxides which show a metal-to-insulator transition at the Néel temperature*. *Physical Review Letters* **3** no. 1 (1959), pp. 34–36. DOI: 10.1103/physrevlett.3.34.

[17] J. B. Goodenough. *The two components of the crystallographic transition in VO2*. *Journal of Solid State Chemistry* **3** no. 4 (1971), pp. 490–500. DOI: 10.1016/0022-4596(71)90091-0.

[18] V. R. Morrison, R. P. Chatelain, K. L. Tiwari, A. Hendaoui, A. Bruhács, M. Chaker, and B. J. Siwick. *A photoinduced metal-like phase of monoclinic VO_2 revealed by ultrafast electron diffraction*. *Science* **346** no. 6208 (2014), pp. 445–448. DOI: 10.1126/science.1253779.

[19] M. R. Otto, L. P. René de Cotret, D. A. Valverde-Chavez, K. L. Tiwari, N. Émond, M. Chaker, D. G. Cooke, and B. J. Siwick. *How optical excitation controls the structure and properties of vanadium dioxide*. *Proceedings of the National Academy of Sciences* **116** no. 2 (2019), pp. 450–455. DOI: 10.1073/pnas.1808414115.

[20] M. Sentef, A. F. Kemper, B. Moritz, J. K. Freericks, Z.-X. Shen, and T. P. Devereaux. *Examining Electron-Boson Coupling Using Time-Resolved Spectroscopy*. *Physical Review X* **3** no. 4 (2013), pp. 041033–041044. DOI: 10.1103/physrevx.3.041033.

[21] J. J. Sakurai Sakurai and J. J. Napolitano. In: *Modern quantum mechanics*. Section 2.6. Pearson, 2014.

[22] A. L. Fetter and J. D. Walecka. In: *Quantum theory of many-particle systems*. McGraw-Hill, 1971. Chap. 3, pp. 64–65. DOI: 10.1063/1.3071096.

[23] Y. Tokura, M. Kawasaki, and N. Nagaosa. *Emergent functions of quantum materials*. *Nature Physics* **13** no. 11 (2017), pp. 1056–1068. DOI: 10.1038/nphys4274.

[24] R. Köhler, A. Tredicucci, F. Beltram, H. E. Beere, E. H. Linfield, A. G. Davies, D. A. Ritchie, R. C. Iotti, and F. Rossi. *Terahertz semiconductor-heterostructure laser*. *Nature* **417** no. 6885 (2002), pp. 156–159. DOI: 10.1038/417156a.

[25] R. Saito, A. Jorio, A. G. Souza Filho, G. Dresselhaus, M. S. Dresselhaus, and M. A. Pimenta. *Probing phonon dispersion relations of graphite by double resonance Raman scattering*. *Physical Review Letters* **88** no. 2 (2001), p. 027401. DOI: 10.1103/physrevlett.88.027401.

[26] Z. Bai, H. Yuan, Z. Liu, P. Xu, Q. Gao, R. J. Williams, O. Kitzler, R. P. Mildren, Y. Wang, and Z. Lu. *Stimulated Brillouin scattering materials, experimental design and applications: a review*. *Optical Materials* **75** (2018), pp. 626–645. DOI: 10.1016/j.optmat.2017.10.035.

[27] M. Holt, Z. Wu, H. Hong, P. Zschack, P. Jemian, J. Tischler, H. Chen, and T. C. Chiang. *Determination of phonon dispersions from x-ray transmission scattering: the example of silicon*. *Physical Review Letters* **83** no. 16 (1999), p. 3317. DOI: 10.1103/physrevlett.84.3733.

[28] R. Xu and T. C. Chiang. *Determination of phonon dispersion relations by x-ray thermal diffuse scattering*. *Zeitschrift für Kristallographie* **220** no. 12 (2005), pp. 1009–1016. DOI: 10.1524/zkri.2005.220.12_2005.1009.

[29] R. Hempelmann. *Coherent quasielastic neutron scattering*. In: *Quasielastic Neutron Scattering and Solid State Diffusion*. Oxford University Press, 2000, pp. 140–157. DOI: 10.1093/acprof:oso/9780198517436.003.0006.

[30] S. W. Teitelbaum, T. Henighan, Y. Huang, H. Liu, M. P. Jiang, D. Zhu, M. Chollet, T. Sato, É. D. Murray, S. Fahy, S. O'Mahony, T. P. Bailey, C. Uher, M. Trigo, and D. A. Reis. *Direct measurement of anharmonic decay channels of a coherent phonon*. *Physical Review Letters* **121** no. 12 (2018), p. 125901. DOI: 10.1103/physrevlett.121.125901.

[31] S. Wall, S. Yang, L. Vidas, M. Chollet, J. M. Glownia, M. Kozina, T. Katayama, T. Henighan, M. Jiang, T. A Miller, D. A. Reis, L. A. Boatnes, O. Delaire, and M. Trigo. *Ultrafast disordering of vanadium dimers in photoexcited VO_2*. *Science* **362** no. 6414 (2018), pp. 572–576. DOI: 10.1126/science.aau3873.

[32] M. Harb, H. Enquist, A. Jurgilaitis, F. T. Tuyakova, A. N. Obraztsov, and J. Larsson. *Phonon-phonon interactions in photoexcited graphite studied by ultrafast electron diffraction*. *Physical Review B* **93** no. 10 (2016), pp. 104104–104111. DOI: 10.1103/physrevb.93.104104.

[33] T. Chase, M. Trigo, A. H. Reid, R. K. Li, T. Vecchione, X. Shen, S. Weathersby, R. N. Coffee, N. Hartmann, D. A. Reis, X. J. Wang, and H. A. Dürr. *Ultrafast electron diffraction from non-equilibrium phonons in femtosecond laser heated Au films*. *Applied Physics Letters* **108** no. 4 (2016), p. 041909. DOI: 10.1063/1.4940981.

[34] L. Waldecker, R. Bertoni, H. Hübener, T. Brumme, T. Vasileiadis, D. Zahn, A. Rubio, and R. Ernstorfer. *Momentum-resolved view of electron-phonon coupling in multilayer WSe_2*. *Physical Review Letters* **119** no. 3 (2017), p. 036803. DOI: 10.1103/physrevlett.119.036803.

[35] M. J Stern, L. P. René de Cotret, M. R. Otto, R. P. Chatelain, J.-P. Boisvert, M. Sutton, and B. J. Siwick. *Mapping momentum-dependent electron-phonon coupling and nonequilibrium phonon dynamics with ultrafast electron diffuse scattering*. *Physical Review B* **97** no. 16 (2018), p. 165416. DOI: 10.1103/physrevb.97.165416.

[36] L. P. René de Cotret, J.-H. Pöhls, M. J. Stern, M. R. Otto, M. Sutton, and B. J. Siwick. *Time-and momentum-resolved phonon population dynamics with ultrafast electron diffuse scattering*. *Physical Review B* **100** no. 21 (2019), p. 214115. DOI: 10.1103/physrevb.100.214115.

[37] G. D. Mahan. In: *Many-particle physics*. Section 1.3.1. Springer Science & Business Media, 2000.

[38] F. Giustino. *Electron-phonon interactions from first principles*. *Reviews of Modern Physics* **89** no. 1 (2017), p. 015003. DOI: 10.1103/revmodphys.89.015003.

[39] S. D. Brorson, A. Kazeroonian, J. S. Moodera, D. W. Face, T. K. Cheng, E. P. Ippen, M. S. Dresselhaus, and G. Dresselhaus. *Femtosecond room-temperature measurement of the electron-phonon coupling constant γ in metallic superconductors*. *Physical Review Letters* **64** no. 18 (1990), p. 2172. DOI: 10.1103/physrevlett.64.2172.

[40] A. C. Ferrari. *Raman spectroscopy of graphene and graphite: disorder, electron–phonon coupling, doping and nonadiabatic effects*. *Solid State Communications* **143** no. 1-2 (2007), pp. 47–57. DOI: 10.1016/j.ssc.2007.03.052.

[41] M. Na, A. K. Mills, F. Boschini, M. Michiardi, B. Nosarzewski, R. P. Day, E. Razzoli, A. Sheyerman, M. Schneider, G. Levy, S. Zhdanovich, T. P. Devereaux, A. F. Kemper, D. J. Jones, and A. Damascelli. *Direct determination of mode-projected electron-phonon coupling in the time domain*. *Science* **366** no. 6470 (2019), pp. 1231–1236. DOI: 10.1126/science.aaw1662.

[42] W. E. King, G. H. Campbell, A. Frank, B. Reed, J. F. Schmerge, B. J. Siwick, B. C. Stuart, and P. M. Weber. *Ultrafast electron microscopy in materials science, biology, and chemistry*. *Journal of Applied Physics* **97** no. 11 (2005), p. 8. DOI: 10.1063/1.1927699.

[43] G. Mourou and S. Williamson. *Picosecond electron diffraction*. *Applied Physics Letters* **41** no. 1 (1982), pp. 44–45. DOI: 10.1063/1.93316.

[44] B. J. Siwick, J. R. Dwyer, R. E. Jordan, and R. J. D. Miller. *Ultrafast electron optics: propagation dynamics of femtosecond electron packets*. *Journal of Applied Physics* **92** no. 3 (2002), pp. 1643–1648. DOI: 10.1063/1.1487437.

[45] S. Williamson, G. Mourou, and J. C. M. Li. *Time-resolved laser-induced phase transformation in aluminum*. *Physical Review Letters* **52** no. 26 (1984), p. 2364. DOI: 10.1557/proc-35-87.

[46] A. H. Zewail. *Laser femtochemistry*. *Science* **242** no. 4886 (1988), pp. 1645–1653. DOI: 10.1126/science.242.4886.1645.

[47] J. C. Williamson and A. H. Zewail. *Structural femtochemistry: experimental methodology*. *Proceedings of the National Academy of Sciences* **88** no. 11 (1991), pp. 5021–5025. DOI: 10.1073/pnas.88.11.5021.

[48] J. C. Williamson, J. Cao, H. Ihee, H. Frey, and A. H. Zewail. *Clocking transient chemical changes by ultrafast electron diffraction*. *Nature* **386** no. 6621 (1997), pp. 159–162. DOI: 10.1038/386159a0.

[49] H. Ihee, V. A Lobastov, U. M. Gomez, B. M. Goodson, R. Srinivasan, C.-Y. Ruan, and A. H. Zewail. *Direct imaging of transient molecular structures with ultrafast diffraction*. *Science* **291** no. 5503 (2001), pp. 458–462. DOI: 10.1126/science.291.5503.458.

[50] C.-Y. Ruan, V. A Lobastov, R. Srinivasan, B. M. Goodson, H. Ihee, and A. H. Zewail. *Ultrafast diffraction and structural dynamics: the nature of complex molecules far from equilibrium*. *Proceedings of the National Academy of Sciences* **98** no. 13 (2001), pp. 7117–7122. DOI: 10.1073/pnas.131192898.

[51] V. A. Lobastov, R. Srinivasan, B. M. Goodson, C.-Y. Ruan, J. S. Feenstra, and A. H. Zewail. *Ultrafast diffraction of transient molecular structures in radiationless transitions*. *The Journal of Physical Chemistry A* **105** no. 50 (2001), pp. 11159–11164. DOI: 10.1021/jp013705b.

[52] B. J. Siwick, J. R. Dwyer, R. E Jordan, and R. J. D. Miller. *An atomic-level view of melting using femtosecond electron diffraction*. *Science* **302** no. 5649 (2003), pp. 1382–1385. DOI: 10.1126/science.1090052.

[53] B. J. Siwick, J. R. Dwyer, R. E. Jordan, and R. J. D. Miller. *Femtosecond electron diffraction studies of strongly driven structural phase transitions*. *Chemical Physics* **299** no. 2-3 (2004), pp. 285–305. DOI: 10.1016/j.chemphys.2003.11.040.

[54] C. Guo, G. Rodriguez, A. Lobad, and A. J. Taylor. *Structural phase transition of aluminum induced by electronic excitation*. *Physical Review Letters* **84** no. 19 (2000), p. 4493. DOI: 10.1103/physrevlett.84.4493.

[55] B.-L. Qian and H. E. Elsayed-Ali. *Electron pulse broadening due to space charge effects in a photoelectron gun for electron diffraction and streak camera systems*. *Journal of Applied Physics* **91** no. 1 (2002), pp. 462–468. DOI: 10.1063/1.1419209.

[56] P. Gallant, P. Forget, F. Dorchies, Z. Jiang, J. C. Kieffer, P. A. Jaanimagi, J. C. Rebuffie, C. Goulmy, J. F. Pelletier, and M. Sutton. *Characterization of a subpicosecond x-ray streak camera for ultrashort laser-produced plasmas experiments*. *Review of Scientific Instruments* **71** no. 10 (2000), pp. 3627–3633. DOI: 10.1063/1.1310347.

[57] T. Van Oudheusden, E. F. De Jong, S. B. Van der Geer, W. P. E. M. 't Root, O. J. Luiten, and B. J. Siwick. *Electron source concept for single-shot sub-100 fs electron diffraction in the 100 keV range*. *Journal of Applied Physics* **102** no. 9 (2007), p. 093501. DOI: 10.1063/1.2801027.

[58] R. P. Chatelain, V. R. Morrison, C. Godbout, and B. J. Siwick. *Ultrafast electron diffraction with radio-frequency compressed electron pulses*. *Applied Physics Letters* **101** no. 8 (2012), p. 081901. DOI: 10.1063/1.4747155.

[59] L. Waldecker, R. Bertoni, R. Ernstorfer, and J. Vorberger. *Electron-phonon coupling and energy flow in a simple metal beyond the two-temperature approximation*. *Physical Review X* **6** no. 2 (2016), p. 021003. DOI: 10.1103/physrevx.6.021003.

[60] D. Zahn, P.-N. Hildebrandt, T. Vasileiadis, Y. W. Windsor, Y. Qi, H. Seiler, and R. Ernstorfer. *Anisotropic nonequilibrium lattice dynamics of black phosphorus*. *Nano Letters* **20** no. 5 (2020), pp. 3728–3733. DOI: 10.1021/acs.nanolett.0c00734.

[61] R. P. Chatelain, V. R. Morrison, B. L. M. Klarenaar, and B. J. Siwick. *Coherent and incoherent electron-phonon coupling in graphite observed with radio-frequency compressed ultrafast electron diffraction*. *Physical Review Letters* **113** no. 23 (2014), p. 235502. DOI: 10.1103/physrevlett.113.235502.

[62] R. Ernstorfer, M. Harb, C. T. Hebeisen, G. Sciaini, T. Dartigalongue, and R. J. D. Miller. *The formation of warm dense matter: experimental evidence for electronic bond hardening in gold*. *Science* **323** no. 5917 (2009), pp. 1033–1037. DOI: 10.1126/science.1162697.

[63] M. Gao, C. Lu, H. Jean-Ruel, L. C. Liu, A. Marx, K. Onda, S. Koshihara, Y. Nakano, X. Shao, T. Hiramatsu, G. Saito, H. Yamochi, R. R. Cooney, G. Moriena, G. Sciaini, and R. J. D. Miller. *Mapping molecular motions leading to charge delocalization with ultrabright electrons*. *Nature* **496** no. 7445 (2013), pp. 343–346. DOI: 10.1038/nature12044.

[64] Y. Jiang, L. C. Liu, H. M. Müller-Werkmeister, C. Lu, D. Zhang, R. L. Field, A. Sarracini, G. Moriena, E. Collet, and R. J. D. Miller. *Structural dynamics upon photoexcitation in a spin crossover crystal probed with femtosecond electron diffraction*. *Angewandte Chemie International Edition* **56** no. 25 (2017), pp. 7130–7134. DOI: 10.1002/ange.201702497.

[65] Y. Jiang, L. C. Liu, A. Sarracini, K. M. Krawczyk, J. S. Wentzell, C. Lu, R. L. Field, S. F. Matar, W. Gawelda, H. M Müller-Werkmeister, and R. J. D. Miller. *Direct observation of nuclear reorganization driven by ultrafast spin transitions*. *Nature Communications* **11** no. 1 (2020), pp. 1–8. DOI: 10.1038/s41467-020-15187-y.

[66] J. Yang, J. Beck, C. J. Uiterwaal, and M. Centurion. *Imaging of alignment and structural changes of carbon disulfide molecules using ultrafast electron diffraction*. *Nature Communications* **6** no. 1 (2015), pp. 1–9. DOI: 10.1038/ncomms9172.

[67] M. Z. Mo, Z. Chen, R. K. Li, M. Dunning, B. B. L. Witte, J. K. Baldwin, L. B. Fletcher, J. B. Kim, A. Ng, R. Redmer, A. H. Reid, P. Shekhar, X. Y. Shen, M. Shen, K. Sokolowski-Tinten, Y. Y. Tsui, Y. Q. Wang, Q. Zheng, X. J. Wang, and S. H. Glenzer. *Heterogeneous to homogeneous melting transition visualized with ultrafast electron diffraction*. *Science* **360** no. 6396 (2018), pp. 1451–1455. DOI: 10.1126/science.aar2058.

[68] E. J. Sie, C. M. Nyby, C. D. Pemmaraju, S. J. Park, X. Shen, J. Yang, M. C. Hoffmann, B. K. Ofori-Okai, R. Li, A. H. Reid, S. Weathersby, E. Mannebach, N. Finney, D. Rhodes, D. Chenet, A. Abhinandan, L. Balicas, J. Hone, T. P. Devereaux, T. F. Heinz, X. Wang, and A. M. Lindenberg. *An ultrafast symmetry switch in a Weyl semimetal*. *Nature* **565** no. 7737 (2019), pp. 61–66. DOI: 10.1038/s41586-018-0809-4.

[69] A. Kogar, A. Zong, P. E. Dolgirev, X. Shen, J. Straquadine, Y.-Q. Bie, X. Wang, T. Rohwer, I.-C. Tung, Y. Yang, R. Li, J. Yang, S. Weathersby, S. Park, M. E. Kozina, E. J. Sie, H. Wen, P. Jarillo-Herrero, I. R. Fisher, X. Wang, and N. Gedik. *Light-induced charge density wave in $LaTe_3$*. *Nature Physics* **16** no. 2 (2020), pp. 159–163. DOI: 10.1038/s41567-019-0705-3.

[70] J. Maxson, D. Cesar, G. Calmasini, A. Ody, P. Musumeci, and D. Alesini. *Direct measurement of sub-10 fs relativistic electron beams with ultralow emittance*. *Physical Review Letters* **118** no. 15 (2017), p. 154802. DOI: 10.1103/physrevlett.118.154802.

[71] R. Chatelain. *Radio-frequency pulse compression for high-brightness ultrafast electron diffraction: design, characterization and application*. PhD thesis. McGill University, 2014.

[72] F. B. Kiewiet, A. H. Kemper, O. J. Luiten, G. J. H. Brussaard, and M. J. Van der Wiel. *Femtosecond synchronization of a RF oscillator to a mode-locked Ti:sapphire laser*. *Nuclear Instruments and Methods in Physics Research A* **484** no. 1-3 (2002), pp. 619–624. DOI: 10.1016/s0168-9002(01)01994-5.

[73] E. Fill, L. Veisz, A. Apolonski, and F. Krausz. *Sub-fs electron pulses for ultrafast electron diffraction*. *New Journal of Physics* **8** no. 11 (2006), pp. 272–272. DOI: 10.1088/1367-2630/8/11/272.

[74] M. R. Otto, L. P. René de Cotret, M. J. Stern, and B. J. Siwick. *Solving the jitter problem in microwave compressed ultrafast electron diffraction instruments: robust sub-50 fs cavity-laser phase stabilization*. *Structural Dynamics* **4** no. 5 (2017), p. 051101. DOI: 10.1063/1.4989960.

[75] J. Taylor, S. Datta, A. Hati, C. Nelson, F. Quinlan, A. Joshi, and S. Diddams. *Characterization of power-to-phase conversion in high-speed P-I-N photodiodes*. *IEEE Photonics Journal* **3** no. 1 (2011), pp. 140–151. DOI: 10.1109/jphot.2011.2109703.

[76] W. Zhang, T. Li, M. Lours, S. Seidelin, G. Santarelli, and Y. Le Coq. *Amplitude to phase conversion of InGaAs pin photo-diodes for femtosecond lasers microwave signal generation*. *Applied Physics B* **106** no. 2 (2012), pp. 301–308. DOI: 10.1007/s00340-011-4710-1.

[77] D. Ehberger, K. J. Mohler, T. Vasileiadis, R. Ernstorfer, L. Waldecker, and P. Baum. *Terahertz compression of electron pulses at a planar mirror membrane*. *Physical Review Applied* **11** no. 2 (2019), pp. 024034–024040. DOI: 10.1103/physrevapplied.11.024034.

[78] D. Matte, N. Chamanara, L. Gingras, L. P. René de Cotret, T. L. Britt, B. J. Siwick, and D. G. Cooke. *Extreme lightwave electron field emission from a nanotip*. *Physical Review Research* **3** no. 1 (2021), pp. 013137–013147. DOI: 10.1103/physrevresearch.3.013137.

[79] S. Tokita, M. Hashida, S. Inoue, T. Nishoji, K. Otani, and S. Sakabe. *Single-shot femtosecond electron diffraction with laser-accelerated electrons: experimental demonstration of electron pulse compression*. *Physical Review Letters* **105** no. 21 (2010), pp. 215004–215008. DOI: 10.1103/physrevlett.105.215004.

[80] K. P. Grzelakowski and R. M. Tromp. *Temporal and lateral electron pulse compression by a compact spherical electrostatic capacitor*. *Ultramicroscopy* **130** (2013), pp. 36–43. DOI: 10.1016/j.ultramic.2013.03.022.

[81] P. M. Weber, S. D. Carpenter, and T. Lucza. *Reflectron design for femtosecond electron guns*. *Time-resolved electron and X-ray diffraction*. Ed. by P. M. Rentzepis. Society of Photo-Optical Instrumentation Engineers, 1995. DOI: 10.1117/12.218364.

[82] G. H. Kassier, K. Haupt, N. Erasmus, E. G. Rohwer, and H. Schwoerer. *Achromatic reflectron compressor design for bright pulses in femtosecond electron diffraction*. *Journal of Applied Physics* **105** no. 11 (2009), p. 113111. DOI: 10.1063/1.3132834.

[83] Y. Wang and N. Gedik. *Electron pulse compression with a practical reflectron design for ultrafast electron diffraction*. *IEEE Journal of Selected Topics in Quantum Electronics* **18** no. 1 (2011), pp. 140–147. DOI: 10.1109/jstqe.2011.2112339.

[84] M. Mankos, K. Shadman, and B. J. Siwick. *A novel electron mirror pulse compressor*. *Ultramicroscopy* **183** (2017), pp. 77–83. DOI: 10.1016/j.ultramic.2017.05.004.

[85] H. W. Kim, N. A. Vinokurov, I. H. Baek, K. Y. Oang, M. H. Kim, Y. C. Kim, K.-H. Jang, K. Lee, S. H. Park, S. Park, J. Shin, J. Kim, F. Rotermund, and S. Cho. *Towards jitter-free ultrafast electron diffraction technology*. *Nature Photonics* **14** no. 4 (2020), pp. 245–249. DOI: 10.1038/s41566-019-0566-4.

[86] F. Qi, Z. Ma, L. Zhao, Y. Cheng, W. Jiang, C. Lu, T. Jiang, D. Qian, Z. Wang, W. Zhang, P. Zhu, X. Zou, W. Wan, D. Xiang, and J. Zhang. *Breaking 50 femtosecond resolution barrier in MeV ultrafast electron diffraction with a double bend achromat compressor*. *Physical Review Letters* **124** no. 13 (2020), pp. 134803–134809. DOI: 10.1103/physrevlett.124.134803.

[87] D. Strickland and G. Mourou. *Compression of amplified chirped optical pulses*. *Optics Communications* **55** no. 6 (1985), pp. 447–449. DOI: 10.1016/0030-4018(85)90151-8.

[88] P. A. Anderson. *The work function of copper*. *Physical Review* **76** no. 3 (1949), p. 388. DOI: 10.1103/physrev.76.388.

[89] E. J. Kirkland. In: *Advanced computing in electron microscopy*. Springer Science & Business Media, 2010. Chap. 2.3, p. 11. DOI: 10.1007/978-1-4419-6533-2.

[90] L. P. René de Cotret, M. R. Otto, J.-H. Pöhls, Z. Luo, M. G. Kanatzidis, and B. J. Siwick. *Direct visualization of polaron formation in the thermoelectric SnSe*. Accepted for publication in the Proceedings of the National Academy of Science on November 16, 2021. 2021. arXiv: 2111.10012 [cond-mat.mtrl-sci].

2. The theory of ultrafast electron scattering

The scattering of light or particles by a sample is used by a large class of experimental techniques, dating back a hundred years. Scattering can be broadly defined as the modification of an incoming wave by a potential into outgoing wave, a process which imprints the outgoing wave with some characteristic of the potential. The outgoing wave may lose or gain energy, and its momentum might be changed. When multiple incoming waves are simultaneously used – forming an incoming wavefront –, the outgoing waves may interfere constructively or destructively. This effect is particularly intense for periodic scattering potentials, for example in crystals.

This chapter will consider the special case of *electron scattering*. In crystals, electrons are scattered by the electrostatic potential of ions and the electronic charge-density. Thanks to improvements to instrument stability (Section 1.3), as well as advances in data acquisition and data analysis attributable to the author (Appendix A), the ultrafast electron scattering instrument used herein can reliably measure the effects of *diffuse scattering*.

In writing this chapter, the author has tried original derivations that emphasize concepts that are important for the remainder of this dissertation. The derivation of ultrafast diffuse scattering intensity is of particular interest, because it is the only full quantum-mechanical treatment relevant to ultrafast electron scattering specifically in the literature today.

2.1. Electron scattering and the Lippmann-Schwinger formalism

Consider an electron wavefunction $\Psi(\mathbf{x}, t)$. The scattering of $\Psi(\mathbf{x}, t)$ by an arbitrary potential $V(\mathbf{x}, t)$ is described by the Schrödinger equation:

$$i\hbar \frac{d}{dt}\Psi(\mathbf{x}, t) = \left[\frac{-\hbar^2}{2m_e}\nabla^2 + V(\mathbf{x}, t)\right]\Psi(\mathbf{x}, t). \tag{2.1}$$

The scattering electrons used in this work have an enormous amount of kinetic energy (90 keV).

The potential energy from the atomic Coulomb interaction, on the other hand, is much smaller:

$$V = \frac{Ze^2}{4\pi\epsilon_0|\mathbf{x}|} \tag{2.2}$$

where ϵ_0 is the vacuum dielectric constant, Z the atomic number, e is the unit of charge. For the simple example of graphite ($Z = 12$, $|\mathbf{x}| \approx 1$ Å), the potential energy associated with the Coulomb interaction is less than 10 eV. This is very small compared to the kinetic energy of scattering electrons (90 keV), and so the potential $V(\mathbf{x}, t)$ shall be treated as a perturbation.

2.1.1. Electrons propagating in free space

In the case of free space ($V(\mathbf{x}, t) = 0$), Equation (2.1) reduces to the following equation:

$$i\hbar\frac{d}{dt}\Psi(\mathbf{x}, t) = \frac{-\hbar^2}{2m_e}\nabla^2\Psi(\mathbf{x}, t). \tag{2.3}$$

It is instructive to consider the energy eigenfunction satisfying Equation (2.3). Let the solutions be labeled as $\{\,(\Psi_a(\mathbf{x}, t), \omega_a)\,\}$, where the associated energy eigenvalues are $\omega_a \equiv E_a/\hbar$. The energy eigenfunction can be factorized into spatial and temporal parts as:

$$\Psi_a(\mathbf{x}, t) = u_a(\mathbf{x})e^{-i\omega_a t} \tag{2.4}$$

where $u_a(\mathbf{x})$ solves the time-independent Schrödinger equation:[1]

$$\hbar\omega_a u_a(\mathbf{x}) = \frac{-\hbar^2}{2m_e}\nabla^2 u_a(\mathbf{x}). \tag{2.5}$$

Equation (2.5) is an instance of the Helmholtz equation, which can be re-written as:

$$\left[\nabla^2 + k_a^2\right] u_a(\mathbf{x}) = 0 \tag{2.6}$$

where $k_a^2 \equiv 2m_e E_a/\hbar^2$. Physical reasoning and the classical result of the Helmholtz equation reveal that k_a is the *wavevector*, related to the wave momentum as $k_a^2 \equiv \mathbf{k}_a \cdot \mathbf{k}_a \equiv \mathbf{p}_a^2/\hbar^2$. Equation (2.6) can be solved using separation of variables, where the solution along linearly-independent directions are considered independently:

$$u_a(\mathbf{x}) \equiv u_{a,x}(\mathbf{x}\cdot\hat{\mathbf{x}})u_{a,y}(\mathbf{x}\cdot\hat{\mathbf{y}})u_{a,z}(\mathbf{x}\cdot\hat{\mathbf{z}}). \tag{2.7}$$

Equation (2.6) then becomes:

$$\sum_{i\in\{x,y,z\}} \frac{1}{u_{a,i}(\mathbf{x}\cdot\hat{\mathbf{i}})}\frac{d^2u_{a,i}}{di^2}(\mathbf{x}\cdot\hat{\mathbf{i}}) + |\mathbf{k}\cdot\hat{\mathbf{i}}| = 0 \tag{2.8}$$

and the solution can be synthesized as a product of one-dimensional plane wave:

$$\begin{aligned} u_a(\mathbf{x}) &= \prod_{j\in\{x,y,z\}} A_j e^{i(\mathbf{k}_a\cdot\hat{\mathbf{j}})(\mathbf{x}\cdot\hat{\mathbf{j}})} \\ &= Ae^{i\mathbf{k}_a\cdot\mathbf{x}} \end{aligned} \tag{2.9}$$

for some scalars $\{A_x, A_y, A_z, A\}$. Combining Equation (2.4) Equation (2.9) leads to the energy eigenstate of a free electron propagating in vacuum:

$$\Psi_a(\mathbf{x},t) = Ae^{i(\mathbf{k}_a\cdot\mathbf{x}-\omega_a t)} \tag{2.10}$$

with associated energy eigenvalue $E_a = \hbar^2\mathbf{k}_a^2/2m_e = \hbar\omega_a$.

2.1.2. The Lippmann-Schwinger equation

The problem of scattering with a non-trivial potential $\hat{V}$will now be considered. This is a fundamental problem in quantum mechanics; approximations appropriate for the research presented in this dissertation will be made to simplify and clarify the presentation. In particular, the following derivations assume that the scattering potential $V(\mathbf{x})$ is *local*, that is:

$$\langle\mathbf{x}'|\,\hat{V}\,|\mathbf{x}''\rangle = V(\mathbf{x}')\delta(\mathbf{x}'-\mathbf{x}'') \tag{2.11}$$

This is a reasonable assumption as the electrostatic potential has a $1/|\mathbf{x}|$ dependence (Equation (2.2)). Further simplifications can be made if allowed momentum states are assumed to be defined in a (large) cube of size-length L, such that

$$\langle\mathbf{x}|\mathbf{k}\rangle = \frac{1}{L^{3/2}}e^{i\mathbf{k}\cdot\mathbf{x}} \tag{2.12}$$

and $\mathbf{k}$ takes discrete values. The calculations will become physical after taking the limit $L\to\infty$. In this approximation, the scattered wave $\langle\mathbf{x}|\Psi\rangle$ is given by the *Lippmann-Schwinger* equa-

tion:[2]

$$\langle \mathbf{x}|\Psi\rangle = \langle \mathbf{x}|\mathbf{k}_i\rangle - \frac{2m_e}{\hbar^2}\int d^3x' \frac{e^{i|\mathbf{k}_i||\mathbf{x}-\mathbf{x}'|}}{4\pi|\mathbf{x}-\mathbf{x}'|}V(\mathbf{x}')\langle \mathbf{x}'|\Psi\rangle \tag{2.13}$$

where $|\mathbf{k}_i\rangle$ represents the initial plane-wave of incoming scattering electrons, and $|\Psi\rangle$ is the final scattered state. Provided that the scattered wavefunction $\langle \mathbf{x}|\Psi\rangle$ is measured far from where the scattering potential is localized:

$$e^{i|\mathbf{k}||\mathbf{x}-\mathbf{x}'|} \approx e^{ikr}e^{-i\mathbf{k}_i\cdot\mathbf{x}'} \tag{2.14}$$

where $r \equiv |\mathbf{x}-\mathbf{x}'|$ and $k \equiv |\mathbf{k}|$. Equation (2.13) can then be simplified as:

$$\langle \mathbf{x}|\Psi\rangle = \langle \mathbf{x}|\mathbf{k}_i\rangle - \frac{m_e}{2\pi\hbar^2}\frac{e^{ik_fr}}{r}\int d^3x' e^{-i\mathbf{k}_f\cdot\mathbf{x}'}V(\mathbf{x}')\langle \mathbf{x}'|\Psi\rangle \tag{2.15}$$

The canonical description of the Lippmann-Schwinger equation is usually reduced to:

$$\langle \mathbf{x}|\Psi\rangle = \frac{1}{L^{3/2}}\left[e^{i\mathbf{k}_i\cdot\mathbf{x}} + \frac{e^{ik_fr}}{r}f(\mathbf{k}_f,\mathbf{k}_i)\right] \tag{2.16}$$

where

$$\begin{aligned} f(\mathbf{k}_f,\mathbf{k}_i) &\equiv -\frac{m_eL^3}{2\pi\hbar^2}\int d\mathbf{x}' \frac{e^{-i\mathbf{k}_f\cdot\mathbf{x}'}}{L^{3/2}}V(\mathbf{x}')\langle \mathbf{x}'|\Psi\rangle \\ &= -\frac{m_eL^3}{2\pi\hbar^2}\langle \mathbf{k}_f|\,\hat{V}\,|\Psi\rangle \end{aligned} \tag{2.17}$$

$f(\mathbf{k}_f,\mathbf{k})$ is called the *scattering amplitude*. In this notation, the vector $\mathbf{k}_f$ is a formal variable, and not a known state like $\mathbf{k}_i$. The form of Equation (2.16) complies with intuition: the final scattered wavefunction is composed of an unscattered part ($\langle \mathbf{x}|\mathbf{k}_i\rangle \propto e^{i\mathbf{k}_i\cdot\mathbf{x}}$) as well as an outgoing spherical wave with amplitude $f(\mathbf{k}_f,\mathbf{k}_i)$ in the $\mathbf{k}_f$ direction.

The calculation of the scattered wavefunction $\langle \mathbf{x}|\Psi\rangle$ has been reduced to the calculation of $\langle \mathbf{k}_f|\,\hat{V}\,|\Psi\rangle$ for arbitrary values of $\mathbf{k}_f$. The derivation of an expression for this is beyond the scope of this work, and the final result is stated*:

$$\langle \mathbf{k}_f|\,\hat{V}\,|\Psi\rangle = \langle \mathbf{k}_f|\left[\sum_{n=1}^{\infty}\hat{V}\left(\frac{1}{E_i-\hat{H}_0+i\epsilon}\hat{V}\right)^{n-1}\right]|\mathbf{k}_i\rangle \tag{2.18}$$

where $\hat{H}_0$ is the free-space Hamiltonian with eigenvalue $E_i = \hbar^2|\mathbf{k}_i|^2/2m_e$, and ϵ is a vanishingly

*Interested readers are encouraged to peruse Chapter 6 of Sakurai and Napolitano.[3]

small real number. In particular, each term with index n in the sum of Equation (2.18) corresponds to the electron scattering n times.[4]

2.1.3. Measuring the scattered wavefunction

Electron cameras measure the intensity of the wavefunction. In the case of electron microscopy in the transmission geometry, where the wavefunction is imaged directly, the intensity on the detector is given by:

$$I(\mathbf{x}) \equiv |\langle \mathbf{x}|\Psi\rangle|^2 \tag{2.19}$$

where $\mathbf{x}$ represents the possible spatial positions of the detector. In order to sample the scattered wavefunction in reciprocal space, an electron lens can be used to focus the scattered electrons onto the detector. Given that electrons are prepared with definite momentum $\mathbf{k}_i$, it is trivial to ignore the unscattered part of the wavefunction – the first term in Equation (2.16) – which is found only at $\mathbf{k}_f = \mathbf{k}_i$. Therefore, the intensity away from $\mathbf{k}_i$ is related only to the scattered wavefunction, Ψ:

$$\begin{aligned} I(\mathbf{k}_f - \mathbf{k}_i) &= |\langle \mathbf{x}|\Psi\rangle|^2 \\ &= \left|\frac{e^{ikr}}{r} f(\mathbf{k}_f, \mathbf{k}_i)\right|^2 \\ &= \frac{1}{r^2}|f(\mathbf{k}_f, \mathbf{k}_i)|^2 \end{aligned} \tag{2.20}$$

Therefore, the diffracted intensity $I(\mathbf{k}_f - \mathbf{k}_i)$ is proportional to the square of the scattering amplitude.

Note that the factor of $1/r^2$ is generally ignored.[5] For the instrument configuration presented in Section 1.4, $1/r^2$ varies from 15.92 m^{-2} to 16 m^{-2}, from the corner to the center of the detector respectively. While not an insignificant variation, the experiments presented herein generally measure the relative change in intensity, in which case factors are not important.

2.2. Elastic scattering in a crystal

In this section, the consequences of an electron scattering *once* in crystalline solid will be explored. In this approximation, historically called the *first Born approximation*,[6] only the first term

in Equation (2.18) ($n = 1$) is considered:

$$\begin{aligned} f^{(1)}(\mathbf{k}_f, \mathbf{k}_i) &= -\frac{m_e L^3}{2\pi\hbar^2} \langle \mathbf{k}_f | \hat{V} | \mathbf{k}_i \rangle \\ &= -\frac{m_e L^3}{2\pi\hbar^2} \int d\mathbf{x}' \langle \mathbf{k}_f | V(\mathbf{x}') | \mathbf{x}' \rangle \langle \mathbf{x}' | \mathbf{k}_i \rangle \\ &= -\frac{m_e L^3}{2\pi\hbar^2} \int d\mathbf{x}' \frac{e^{i(\mathbf{k}_i - \mathbf{k}_f)\cdot\mathbf{x}'}}{L^3} V(\mathbf{x}') \\ &= -\frac{m_e}{2\pi\hbar^2} \int d\mathbf{x}' e^{i(\mathbf{k}_i - \mathbf{k}_f)\cdot\mathbf{x}'} V(\mathbf{x}') \end{aligned} \tag{2.21}$$

where the normalization of Equation (2.12) was used. The reader may recognize that the scattering amplitude $f^{(1)}(\mathbf{k}_f, \mathbf{k}_i)$ is proportional to the Fourier transform of the scattering potential with respect to $\mathbf{k}_f - \mathbf{k}_i \equiv \mathbf{q}$, the *scattering vector*. If the Fourier transform functional operator is defined as:

$$\mathcal{F}\left[f(\mathbf{x})\right] \equiv \tilde{f}(\mathbf{q}) = \frac{1}{2\pi} \int d\mathbf{x}' e^{-i\mathbf{q}\cdot\mathbf{x}'} f(\mathbf{x}'). \tag{2.22}$$

then Equation (2.21) can be simplified to:

$$f^{(1)}(\mathbf{q} = \mathbf{k}_f - \mathbf{k}_i) = -\frac{m_e}{\hbar^2} \tilde{V}(\mathbf{q}) \tag{2.23}$$

2.2.1. Scattering potential of a single atom

The scattering potential of a single atom is given by:

$$V_a(\mathbf{x}) = -\frac{Ze^2}{|\mathbf{x}|} + \sum_{i=1}^{Z} \frac{e^2}{|\mathbf{x} - \mathbf{x}_i|} \tag{2.24}$$

where Z is the atomic weight, $\mathbf{x}$ is a position with respect to the ionic core, and $\mathbf{x}_i$ is the position of the i^{th} electron. The potential in Equation (2.24) can be calculated from first principles, using relativistic Hartree-Fock calculations[7,8] to get the real-space electron density (i.e. determining the possible set $\{\, \mathbf{x}_i \,\}$). This is beyond the scope of the present work, and the final result is used here. When discussing electron scattering, the scattering amplitude for a single atom is usually called the *atomic form factors for electron scattering*. To a reasonable degree of accuracy, the atomic form factors for electrons for light atoms are spherically symmetric.[9] They can be parametrized as:

$$f_e(\mathbf{q}) = \sum_{i=1}^{3} \frac{a_i}{|\mathbf{q}|^2 + b_i} + c_i e^{-d_i |\mathbf{q}|^2} \tag{2.25}$$

where the constants $\{ a_i, b_i, c_i, d_i \}$ are element-specific fitting parameters which are tabulated in Kirkland.[8] The associated real-space potential can be calculated via the reciprocal of Equation (2.23). Examples of $f_e(\mathbf{q})$ and associated $V_a(\mathbf{x})$ are shown in Figure 2.1 for a few elements.

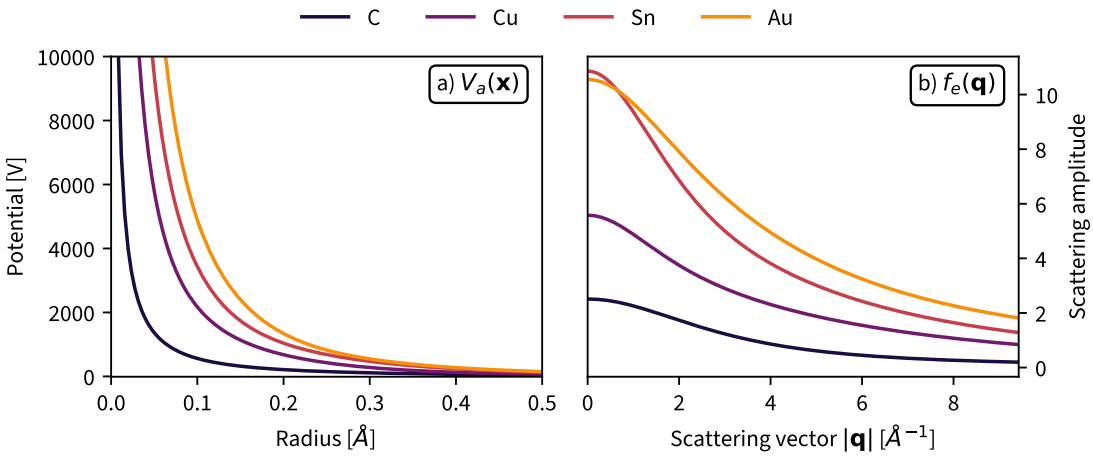

Figure 2.1.: Demonstration of the electrostatic potential of atoms, which scatters electrons. **a)** Radial view of the electrostatic potential in real-space **b)** Radial view of the electrostatic potential in reciprocal space, also known as the *atomic form factor*.

The contribution of individual electronic orbitals to the atomic form factor for electrons is discussed in Zheng *et al.*[9]

2.2.2. Scattering potential of a crystal

The scattering potential of a crystalline lattice can be expressed as:

$$V_c(\mathbf{x}) = \sum_i V_{a,i}(\mathbf{x} - \mathbf{r}_i) \tag{2.26}$$

where the sum index i runs over atoms in the crystal with positions $\mathbf{r}_i$. The potential for each atom $V_{a,i}$ is taken to be more general than the single-atom potential of Equation (2.24), in order to model ion-ion interactions (e.g. bonding). Note that for any function $h(\mathbf{x})$:

$$\begin{aligned} \mathcal{F}\left[h(\mathbf{x}+\mathbf{y})\right] &= \frac{1}{2\pi}\int d\mathbf{x}' e^{-i\mathbf{q}\cdot(\mathbf{x}'+\mathbf{y})} h(\mathbf{x}') \\ &= \frac{e^{-i\mathbf{q}\cdot\mathbf{y}}}{2\pi}\int d\mathbf{x}' e^{i\mathbf{q}\mathbf{x}'} h(\mathbf{x}') \\ &= e^{-i\mathbf{q}\cdot\mathbf{y}}\mathcal{F}\left[h(\mathbf{x})\right] \end{aligned} \tag{2.27}$$

where $\mathbf{y}$ is some arbitrary translation vector. Therefore, the Fourier transform of the scattering potential of the entire crystal is related to the Fourier transform the potential its constituent atoms (Equation (2.24)) as:

$$\begin{aligned}\tilde{V}_c(\mathbf{q}) &= \mathcal{F}\left[\sum_i V_{a,i}(\mathbf{x}+\mathbf{r}_i)\right] \\ &= \sum_i \mathcal{F}\left[V_{a,i}(\mathbf{x}+\mathbf{r}_i)\right] \\ &= \sum_i \mathcal{F}\left[V_{a,i}(\mathbf{x})\right] e^{-i\mathbf{q}\cdot\mathbf{r}_i} \\ &= \sum_i f_{e,i}(\mathbf{q}) e^{-i\mathbf{q}\cdot\mathbf{r}_i} \end{aligned} \tag{2.28}$$

The scattering form factor for each atom $\{ f_{e,i} \}$ are not in general equal to the single-atom scattering form factors of Equation (2.25). This difference may explain, for example, why the diffraction intensity for the (222) reflection is visible in diamond[10] and silicon.[11]

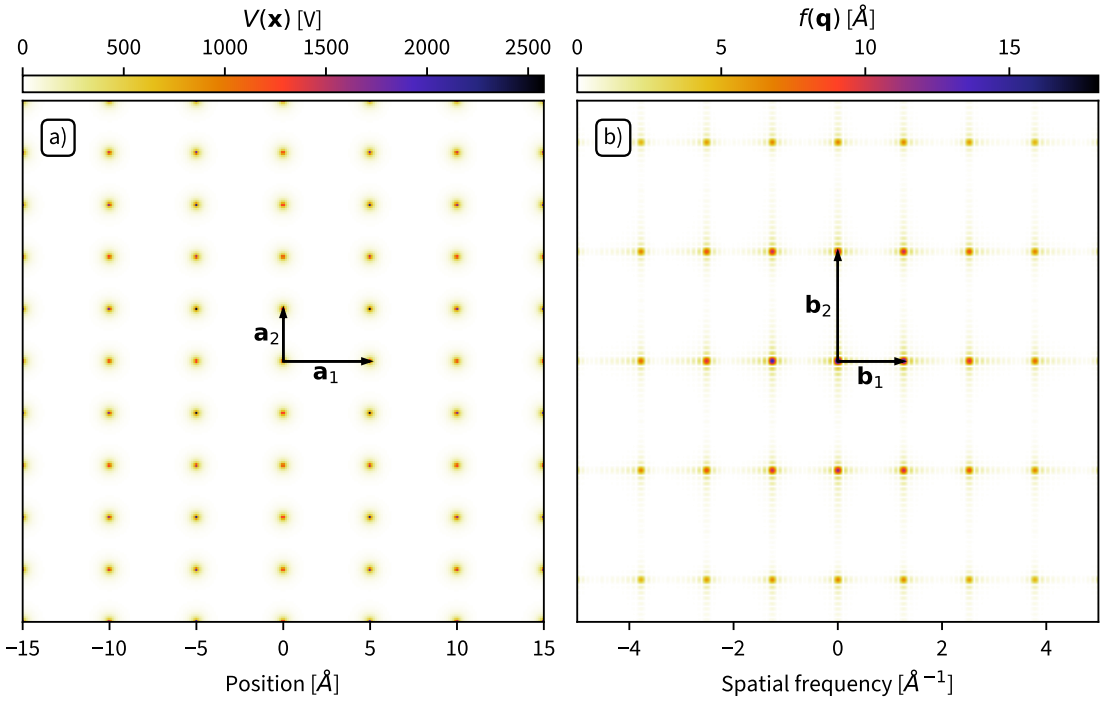

Figure 2.2.: Calculated scattering potential and associated scattering amplitude for an abstract crystal. **a)** Electrostatic potential $V(\mathbf{x})$ in the $z = 0$ plane. The two in-plane lattice vectors $\mathbf{a}_1$ and $\mathbf{a}_2$ are shown; lattice vector $\mathbf{a}_3$ points out of the page. **b)** Scattering amplitude $f(\mathbf{q})$ associated with the electrostatic potential shown in a). The periodic nature of the potential in real-space creates a structure in reciprocal space called the *reciprocal lattice*.

Equation (2.28) has historically been called the *static structure factor*, named thus because the atomic positions are assumed to be fixed. This stands in contrast to the *dynamic structure factor* discussed below in Section 2.4.3. A visual representation of the scattering potential of a crystal is helpful. Consider the example of an abstract crystal, consisting in an atom at the every vertex of a rectangular prism of dimensions 5 Å $\times$ 3 Å $\times$ 3 Å. The calculated electrostatic potential of this arrangement along the unit cell base is shown in Figure 2.2 a). The lattice vectors $\mathbf{a}_1$ and $\mathbf{a}_2$ are indicated, with $\mathbf{a}_3$ being aligned out of the page. The periodic nature of this scattering potential is demonstrated by calculating the resulting scattering amplitude $f_e(\mathbf{q})$ from Equation (2.23), which is shown in Figure 2.2 b). The periodicity in spatial-frequency-space, also called *reciprocal space*, is evident, and forms a *reciprocal lattice*, formally defined in the next section.

From Equation (2.20) and Equation (2.23), the measured diffracted intensity is:

$$I(\mathbf{q}) = \frac{m_e^2}{4\pi^2\hbar^4 r^2}\left|\sum_i f_{e,i}(\mathbf{q})e^{-i\mathbf{q}\cdot\mathbf{r}_i}\right|^2 \tag{2.29}$$

This is the standard result for the diffracted intensity being proportional to the square of the static structure factor.[12,13,14,15]

2.2.3. The reciprocal lattice

The geometry of reciprocal space and the reciprocal lattice are foundational concepts that drive the understanding of ultrafast electron diffraction.

A perfectly periodic structure in real-space that extends to infinity, with associated lattice vectors $\{\,\mathbf{a}_i\,\}$, possesses a *dual* lattice in reciprocal space. The lattice vectors $\{\,\mathbf{b}_i\,\}$ for this reciprocal lattice are defined by the relation

$$\mathbf{a}_i \cdot \mathbf{b}_j = 2\pi\delta_{ij} \tag{2.30}$$

which leads to the following reciprocal lattice vectors:

$$\left\{\mathbf{b}_i = 2\pi\frac{\mathbf{a}_j \times \mathbf{a}_k}{\mathbf{a}_i \cdot (\mathbf{a}_j \times \mathbf{a}_k)}\,\middle|\,(i,j,k) \in C\right\} \tag{2.31}$$

where C is the set of cyclic permutations. For the example of α-Pu, where

$$\mathbf{a}_1 = 3.63\,\hat{\mathbf{x}},\ \mathbf{a}_2 = 3.63\,\hat{\mathbf{y}},\ \mathbf{a}_3 = 3.63\,\hat{\mathbf{z}} \tag{2.32}$$

the associated reciprocal lattice vectors are

$$\mathbf{b}_1 = \frac{2\pi}{3.63}\,\hat{\mathbf{x}},\ \mathbf{b}_2 = \frac{2\pi}{3.63}\,\hat{\mathbf{y}},\ \mathbf{b}_3 = \frac{2\pi}{3.63}\,\hat{\mathbf{z}}. \tag{2.33}$$

The geometry of vectors in Equation (2.32) and Equation (2.33) are shown in Figure 2.2. The position of *reciprocal points* $\mathbf{H}$ – the location of the fundamental frequencies of the Fourier transform of Equation (2.23) – is a linear combination of vectors reciprocal basis vectors $\{\,\mathbf{b}_i\,\}$:

$$\mathbf{H} = h\,\mathbf{b}_1 + k\,\mathbf{b}_2 + l\,\mathbf{b}_3 \tag{2.34}$$

where h, k, and l are all integers. Expressed in the reciprocal basis, reciprocal points are traditionally denoted as $\mathbf{H} = (hkl)$. The indices h, k, and l are called *Miller indices*, named for W. H. Miller.[16]

2.2.3.1. Diffraction for large crystals

Now that the reciprocal points $\{\,\mathbf{H}\,\}$ have been introduced, an alternative form of Equation (2.29) for large crystals can be written down. Consider the counting of atoms to change from label i to labels (m, s), where m labels unit cells and s labels unit cell atoms. In this case, the atomic positions can be written as:

$$\mathbf{r}_i \equiv \mathbf{r}_{m,s} = \mathbf{R}_m + \mathbf{x}_s \tag{2.35}$$

where $\mathbf{R}_m$ is the position of unit cell m, and $\mathbf{x}_s$ is the position of atom s with respect to the unit cell origin. Then, Equation (2.29) becomes:

$$\begin{aligned} I(\mathbf{q}) &= \frac{m_e^2}{4\pi^2\hbar^4 r^2}\left|\sum_i f_{e,i}(\mathbf{q})e^{-i\mathbf{q}\cdot\mathbf{r}_i}\right|^2 \\ &= \frac{m_e^2}{4\pi^2\hbar^4 r^2}\left|\sum_{m,s} f_{e,s}(\mathbf{q})e^{-i\mathbf{q}\cdot(\mathbf{R}_m+\mathbf{x}_s)}\right|^2 \end{aligned} \tag{2.36}$$

Finally, note that because the vectors $\{\,\mathbf{R}_m\,\}$ are integer multiples of lattice vectors:

$$\sum_{m=1}^{N_c} e^{-i\mathbf{q}\cdot\mathbf{R}_m} \xrightarrow{N_c\to\infty} N_c \sum_{\{\,\mathbf{H}\,\}} \delta(\mathbf{q}-\mathbf{H}) \tag{2.37}$$

which follows from the definition of the Fourier transform.[17] Therefore, for large N_c (large crys-

tals):

$$I(\mathbf{q}) = \frac{N_c^2 m_e^2}{4\pi^2 \hbar^4 r^2} \left| \sum_{\{\mathbf{H}\}} \sum_s f_{e,s}(\mathbf{q}) e^{-i\mathbf{q}\cdot\mathbf{x}_s} \delta(\mathbf{q} - \mathbf{H}) \right|^2 \tag{2.38}$$

This form of Equation (2.29) makes it more obvious why, for large periodic structures, the scattering pattern is composed of Bragg peaks at reciprocal points (Figure 2.2).

2.2.4. Bragg's law

It is possible to *deduce* Bragg's law from Equation (2.23) and our definition of the reciprocal lattice.

By definition, the reciprocal points of the crystal scattering potential, located at the spatial frequencies where the crystal potential is strong, form a lattice with basis vectors $\{\, \mathbf{b}_i \,\}$. Consider an electron with initial wavevector $\mathbf{k}_i$ that scatters elastically to a final wavevector $\mathbf{k}_f$. The scattering amplitude for this event, $f(\mathbf{k}_f, \mathbf{k}_i)$ is most intense where $\hat{V}(\mathbf{k}_f - \mathbf{k}_i)$ is strong; that is, the condition for strong scattering is:

$$\mathbf{k}_f - \mathbf{k}_i = h\,\mathbf{b}_1 + k\,\mathbf{b}_2 + l\,\mathbf{b}_3 \quad \forall\, h, k, l \in \mathbb{Z} \tag{2.39}$$

This is precisely the *vector* form of Bragg's law.[18] To recover the canonical form of Bragg's law, consider that an electron state with wavevector $\mathbf{k}$ can be associated with a *de Broglie* wavelength of $\lambda = \frac{2\pi}{|\mathbf{k}|}$. Since for elastic scattering, $|\mathbf{k}_i| = |\mathbf{k}_f| = \frac{2\pi}{\lambda}$, Equation (2.39) becomes:

$$\frac{2\pi}{\lambda}\left(\hat{\mathbf{k}}_f - \hat{\mathbf{k}}_i\right) = \mathbf{H} \tag{2.40}$$

where $\hat{\mathbf{k}}$ denotes a unit-length vector in the direction of $\mathbf{k}$. Given that the vectors on both sides of the equation have the same magnitude and direction, the direction of $\mathbf{H}$ must bisect the angle between $\mathbf{k}_f$ and $\mathbf{k}_i$, historically defined as 2θ. Taking the amplitude of Equation (2.40):

$$\frac{2\pi}{\lambda}\left|\hat{\mathbf{k}}_f - \hat{\mathbf{k}}_i\right| = \frac{2\pi \sin\theta}{\lambda} \tag{2.41}$$

and

$$|\mathbf{H}| = \frac{1}{d_{hkl}}, \tag{2.42}$$

which can be combined as

$$\frac{4\pi \sin\theta}{\lambda} = \frac{1}{d_{hkl}}. \tag{2.43}$$

Equation (2.43) is the historical form of Bragg's law as it relates to polycrystalline diffraction patterns.[19] Note that the vector form of Equation (2.39) is richer than the original form of Bragg's law as it places constraint on the full three-dimensional direction of the scattering vector $\mathbf{q} = \mathbf{k}_f - \mathbf{k}_i$.

2.2.5. The Ewald sphere

Elastic electron scattering, or *electron diffraction*, can be discussed more concretely. Consider an electron initially propagating in the $\hat{\mathbf{z}}$ direction with wavevector $\mathbf{k}_i$ that interacts with a scattering potential $\tilde{V}(\mathbf{q})$, and scatters to a final wavevector $\mathbf{k}_f$. The elastic scattering condition $|\mathbf{k}_i| = |\mathbf{k}_f|$ constrains the observation of $\tilde{V}(\mathbf{q})$ to scattering vectors $\mathbf{q}$ that lie on a sphere of radius $|\mathbf{q}| = \frac{2\pi}{\lambda}$. This sphere is called the *Ewald sphere*.[20]

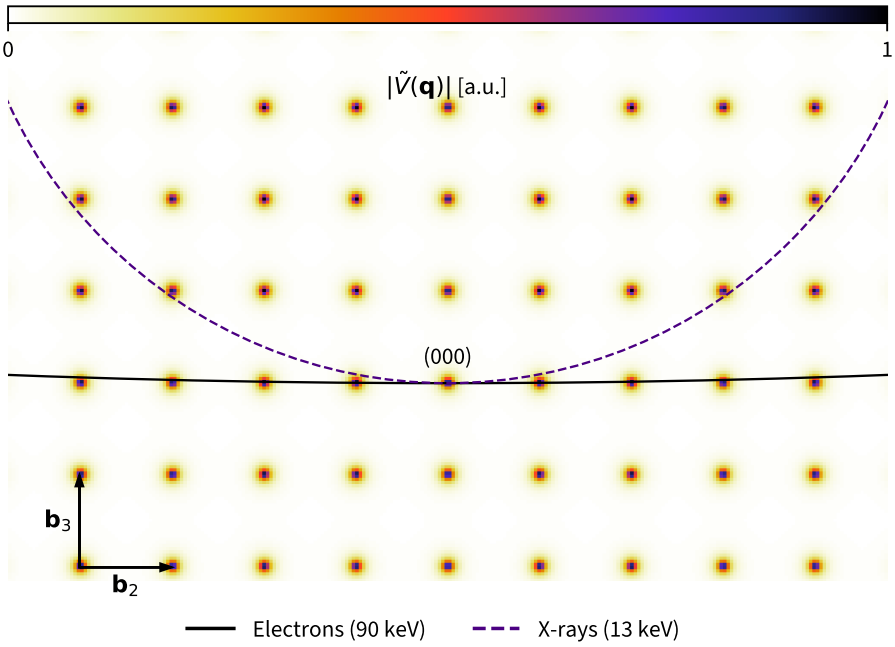

Figure 2.3.: Demonstration of the Ewald sphere, a visual representation of the conservation of energy in diffraction. The Fourier transform of the scattering potential from an abstract cubic lattice of side length 5 Å, $\tilde{V}(\mathbf{q})$, is shown in the background, with the associated reciprocal lattice vectors $\{\mathbf{b}_i\}$. The Ewald sphere of radius $\mathbf{q}$ is shown for two scatterers: electrons (solid) and hard x-ray (dashed).

The Ewald sphere is a great mental model of the information contained in diffraction patterns. Because diffracting electrons can only sample scattering vectors on the Ewald sphere, any

particular measurement of a scattering potential $V(\mathbf{x})$ is effectively a two-dimensional *slice* of the three-dimensional Fourier transform of $V(\mathbf{x})$, $\tilde{V}(\mathbf{q})$. This is represented in Figure 2.3. In this figure, the potential $\tilde{V}(\mathbf{q})$ for an idealized simple cubic crystal with side-length 5 Å is shown in the plane spanned by $\mathbf{b}_2$ and $\mathbf{b}_3$. The Ewald spheres associated with 90 keV electrons (large $|\mathbf{q}|$) and 13 keV x-rays (smaller $|\mathbf{q}|$) are also shown. This electron energy is typical of the work presented in this dissertation, while the x-ray energy is an upper bound on the available energies at the Linac Coherent Light Source, an x-ray free-electron laser,[21] as of 2021.[22] The reciprocal points that intersect the Ewald sphere appear in measurements as diffraction peaks, or Bragg peaks. Figure 2.3 shows the advantage of electron scattering to study two-dimensional materials: given the proper orientation of the electron beam, a large range of wavevectors can be studied in the plane of interest in a single experiment.

2.3. Multiple scattering of electrons

Electrons interact quite strongly with matter through the Coulomb interaction. For scattering targets which are thick enough, an electron may scatter more than once before exiting the scattering potential volume. In this section, the scattering of an electron *twice* will be considered. In this case, the second term in Equation (2.18) ($n = 2$) is considered:

$$f^{(2)}(\mathbf{k}_f, \mathbf{k}_i) = -\frac{m_e L^3}{2\pi\hbar^2} \langle \mathbf{k}_f | \, \hat{V} \frac{1}{E_i - \hat{H}_0 + i\epsilon} \hat{V} \, | \mathbf{k}_i \rangle \tag{2.44}$$

The calculation of $f^{(2)}(\mathbf{k}_f, \mathbf{k}_i)$ involves the insertion of two complete sets of basis states:

$$\langle \mathbf{k}_f | \, \hat{V} \frac{1}{E_i - \hat{H}_0 + i\epsilon} \hat{V} \, | \mathbf{k}_i \rangle = \int d\mathbf{x}' \int d\mathbf{x}'' \, \langle \mathbf{k}_f | \mathbf{x}' \rangle \, V(\mathbf{x}') \, \langle \mathbf{x}' | \, \frac{1}{E_i - \hat{H}_0 + i\epsilon} \, | \mathbf{x}'' \rangle \, V(\mathbf{x}'') \, \langle \mathbf{x}'' | \mathbf{k}_i \rangle \tag{2.45}$$

The evaluation of the term $\langle \mathbf{x}' | \, \frac{1}{E_i - \hat{H}_0 + i\epsilon} \, | \mathbf{x}'' \rangle$ naturally happens in the derivation of Equation (2.13), and so the result is simply stated here:

$$\langle \mathbf{x}' | \, \frac{1}{E_i - \hat{H}_0 + i\epsilon} \, | \mathbf{x}'' \rangle = -\frac{m_e}{2\pi\hbar^2} \frac{e^{i|\mathbf{k}_i||\mathbf{x}' - \mathbf{x}''|}}{|\mathbf{x}' - \mathbf{x}''|} \tag{2.46}$$

It follows that the scattering amplitude for the double-scattering of an electron is given by:

$$f^{(2)}(\mathbf{k}_f, \mathbf{k}_i) = \left(\frac{m_e}{2\pi\hbar^2}\right)^2 \int d\mathbf{x}' \int d\mathbf{x}'' e^{-i\mathbf{k}_f\cdot\mathbf{x}'} V(\mathbf{x}') \left(\frac{e^{i|\mathbf{k}_i||\mathbf{x}'-\mathbf{x}''|}}{|\mathbf{x}'-\mathbf{x}''|}\right) e^{i\mathbf{k}_i\cdot\mathbf{x}''} V(\mathbf{x}'') \quad (2.47)$$

The structure of Equation (2.47) informs on the following physical interpretation. Double scattering involves a first scattering at $\mathbf{x}''$ ($V(\mathbf{x}'')$), which "radiates" as a spherical wave moving from $\mathbf{x}''$ to $\mathbf{x}'$ ($e^{i|\mathbf{k}_i||\mathbf{x}'-\mathbf{x}''|}/|\mathbf{x}'-\mathbf{x}''|$), followed by a second scattering at $\mathbf{x}'$ ($V(\mathbf{x}')$).

2.3.1. Comparing cross-sections

The computation of the differential scattering cross section for two elastic scattering events is given by:

$$\begin{aligned}\frac{d\sigma_2}{d\Omega} &= |f^{(2)}(\mathbf{k}_f, \mathbf{k}_i)|^2 \\ &= \left|\left(\frac{m_e}{2\pi\hbar^2}\right)^2 \int d\mathbf{x}' \int d\mathbf{x}'' e^{-i\mathbf{k}_f\cdot\mathbf{x}'} V(\mathbf{x}') \left(\frac{e^{i|\mathbf{k}_i||\mathbf{x}'-\mathbf{x}''|}}{|\mathbf{x}'-\mathbf{x}''|}\right) e^{i\mathbf{k}_i\cdot\mathbf{x}''} V(\mathbf{x}'')\right|^2 \end{aligned} \quad (2.48)$$

The evaluation of Equation (2.48) for a realistic potential $V(\mathbf{x})$ is arduous. However, given that this type of scattering is *undesirable*, getting an upper bound on its scattering cross-section is a worthwhile exercise.

In electron scattering experiment with thin specimens, the elastic scattering cross section is small enough that an electron is unlikely to scatter twice from the *same atom*. This means that the integral is 0 when $|\mathbf{x}'-\mathbf{x}''|$ is small. The inner integral over $\mathbf{x}''$ in Equation (2.48) can be split:

$$\int d\mathbf{x}' \int d\mathbf{x}'' \to \int d\mathbf{x}' \left[\int_{|\mathbf{x}'-\mathbf{x}''|\leq a} d\mathbf{x}'' + \int_{|\mathbf{x}'-\mathbf{x}''|>a} d\mathbf{x}''\right] \quad (2.49)$$

where a is the inter-atomic distance of the crystal. In the approximation described above, where double-scattering is only possible for $|\mathbf{x}'-\mathbf{x}''| > a$ the first integral over $\mathbf{x}''$ vanishes. Moreover,

$|e^{i|\mathbf{k}_i||\mathbf{x}'-\mathbf{x}''|}|/|\mathbf{x}'-\mathbf{x}''| < 1/a$ for $|\mathbf{x}'-\mathbf{x}''| > a$. Then:

$$\begin{aligned}\frac{d\sigma_2}{d\Omega} &< \frac{1}{a}\left|\left(\frac{m_e}{2\pi\hbar^2}\right)^2 \int d\mathbf{x}' \int d\mathbf{x}'' e^{-i\mathbf{k}_f\cdot\mathbf{x}'} V(\mathbf{x}') e^{i\mathbf{k}_i\cdot\mathbf{x}''} V(\mathbf{x}'')\right|^2 \\ &< \frac{1}{a}\left|\left(\frac{m_e}{2\pi\hbar^2}\right)^2 \int d\mathbf{x}' e^{-i\mathbf{k}_f\cdot\mathbf{x}'} V(\mathbf{x}') \int d\mathbf{x}'' e^{i\mathbf{k}_i\cdot\mathbf{x}''} V(\mathbf{x}'')\right|^2 \\ &< \frac{1}{a}\left|\frac{m_e}{2\pi\hbar^2} \int d\mathbf{x}' e^{-i\mathbf{k}_f\cdot\mathbf{x}'} V(\mathbf{x}')\right|^2 \left|\frac{m_e}{2\pi\hbar^2} \int d\mathbf{x}'' e^{i\mathbf{k}_i\cdot\mathbf{x}''} V(\mathbf{x}'')\right|^2 \\ &< \frac{1}{a}\left(\frac{d\sigma_1}{d\Omega}\right)^2 \end{aligned} \tag{2.50}$$

where $d\sigma_1/d\Omega$ is the differential cross-section for a single elastic scattering event[†]. Importantly, the cross-section for multiple scattering integrated over the sample thickness scales quadratically with sample thickness, given that the scattering cross-section for a single scattering event is linear in the sample thickness. Measurements of multiple scattering effects will be discussed further in Chapter 4.

2.4. The effect of lattice waves on ultrafast electron scattering

In this section, the effect of lattice waves on ultrafast electron diffraction measurements will be considered, ending in the derivation of what is known as *diffuse scattering*.

This section will only consider single-scattering events. A discussion of dynamical diffuse scattering is not necessary to understand the experiments presented in this dissertation, as the samples are not thick enough to display a key signature of multiple diffuse scattering events known as *Kikuchi lines*.[23] A complete discussion of all orders of *thermal* diffuse scattering is presented in Wang.[24] Time-resolved multi-phonon diffuse scattering has also been discussed elsewhere.[25,26]

Consider the vector $\mathbf{r}_{m,s}$ to be the position of atom s in the unit cell m. In this scheme, the indices s run over the size of the unit cell, while the indices m run over the number of unit cells: $1 \leq m \leq N_c$. Due to the presence of lattice waves, the atoms are displaced from their equilibrium positions $\{\,\mathbf{r}_{m,s}\,\}$. Let $\{\,\mathbf{u}_{m,s}\,\}$ be the *displacement vectors* due to lattice waves. Then, the atomic positions can be expressed as $\{\,\mathbf{r}_{m,s} \rightarrow \mathbf{r}_{m,s} + \mathbf{u}_{m,s}\,\}$. The scattering potential

[†]Note that because $V(\mathbf{x})$ is real, the complex conjugate of $\tilde{V}(\mathbf{k})$ is $\tilde{V}(-\mathbf{k})$.

of the crystal (Equation (2.28)) becomes:

$$\begin{aligned}\tilde{V}_c(\mathbf{q}) &= \mathcal{F}\left[\sum_m \sum_s V_{a,s}(\mathbf{x}+\mathbf{r}_{m,s}+\mathbf{u}_{m,s})\right] \\ &= \sum_m \sum_s f_{e,s}(\mathbf{q}) e^{-i\mathbf{q}\cdot\mathbf{r}_{m,s}} e^{-i\mathbf{q}\cdot\mathbf{u}_{m,s}}\end{aligned} \tag{2.51}$$

Recall from Equation (2.20) that the measurable quantity $|f^{(1)}(\mathbf{q})|^2$ is proportional to $|\tilde{V}(\mathbf{q})|$:

$$\begin{aligned}|f^{(1)}(\mathbf{q})|^2 &= \left|-\frac{m_e}{\hbar^2}\tilde{V}(\mathbf{q})\right|^2 \\ &= \frac{m_e^2}{\hbar^4}\tilde{V}(\mathbf{q})\tilde{V}^\star(\mathbf{q}) \\ &= \frac{m_e^2}{\hbar^4}\left(\sum_m\sum_s f_{e,s}(\mathbf{q}) e^{-i\mathbf{q}\cdot\mathbf{r}_{m,s}} e^{-i\mathbf{q}\cdot\mathbf{u}_{m,s}}\right)\left(\sum_{m'}\sum_{s'} f_{e,s'}(\mathbf{q}) e^{i\mathbf{q}\cdot\mathbf{r}_{m',s'}} e^{i\mathbf{q}\cdot\mathbf{u}_{m',s'}}\right) \\ &= \frac{m_e^2}{\hbar^4}\sum_{m,m'}\sum_{s,s'} f_{e,s}(\mathbf{q}) f_{e,s'}(\mathbf{q}) e^{-i\mathbf{q}\cdot(\mathbf{r}_{m,s}-\mathbf{r}_{m',s'})} e^{-i\mathbf{q}\cdot\mathbf{u}_{m,s}} e^{i\mathbf{q}\cdot\mathbf{u}_{m',s'}}\end{aligned} \tag{2.52}$$

The evaluation of the sum in Equation (2.52) requires some thought. The displacement vectors $\mathbf{u}_{m,s}$ and $\mathbf{u}_{m',s'}$ are essentially uncorrelated (for $m \neq m'$) for a large enough crystal. Then, the sum over m and m' is equivalent to a thermal average over time. To this end, let us define the average $\langle\cdots\rangle \equiv \frac{1}{N_c}\sum_m \cdots$. Equation (2.52) can then be expressed as:

$$|f^{(1)}(\mathbf{q})|^2 = \frac{m_e^2}{N_c^2\hbar^4}\sum_{m,m'}\sum_{s,s'} f_{e,s}(\mathbf{q}) f_{e,s'}(\mathbf{q}) e^{-i\mathbf{q}\cdot(\mathbf{r}_{m,s}-\mathbf{r}_{m',s'})}\langle e^{-i\mathbf{q}\cdot\mathbf{u}_s} e^{i\mathbf{q}\cdot\mathbf{u}_{s'}}\rangle \tag{2.53}$$

where the problem has been reduced to the evaluation of $\langle e^{-i\mathbf{q}\cdot\mathbf{u}_s} e^{i\mathbf{q}\cdot\mathbf{u}_{s'}}\rangle$. The indices m have been dropped from the displacement vectors as the average is over all values of m.

2.4.1. Quantizing lattice waves

Consider now the description of the displacement vectors as a superposition of lattice waves, or phonons. This is most easily done in the second quantization framework,[27,28] which states that atomic displacement can be expressed as the quantum-mechanical operator:

$$\hat{\mathbf{u}}_{m,s} = \sum_\lambda \sum_{\{\mathbf{k}\}} \sqrt{\frac{\hbar}{2\mu_s N\omega_\lambda(\mathbf{k})}}\left(\hat{a}_\lambda(\mathbf{k}) e^{-i\phi_{s,m,\lambda}(\mathbf{k})} + \hat{a}_\lambda^\dagger(\mathbf{k}) e^{i\phi_{s,m,\lambda}(\mathbf{k})}\right) e^{i\mathbf{k}\cdot\mathbf{r}_{m,s}} \mathbf{e}_{s,\lambda}(\mathbf{k}) \tag{2.54}$$

where $\{\lambda\}$ label phonon branches, μ_s is the mass of atom s, N is the number of atoms in the crystal, $\omega_\lambda(\mathbf{k})$ is the vibrational frequency of mode λ at wavevector $\mathbf{k}$, $\hat{a}_\lambda(\mathbf{k})$ and $\hat{a}_\lambda^\dagger(\mathbf{k})$ are

the creation and annihilation operators for the phonon mode λ, $\phi_{s,m,\lambda}(\mathbf{k})$ is the phase of a lattice wave, and $\mathbf{e}_{s,\lambda}(\mathbf{k})$ is the polarization vector of mode λ.[29] The expression for $\hat{\mathbf{u}}_{m,s}$ is the combined effect of all possible phonon modes at the $\mathbf{r}_{m,s}$ lattice site. The sum $\sum_{\{\mathbf{k}\}}$ assumes the normalization of Equation (2.12).

The Baker-Campbell-Hausdorff lemma can be used to compute the average $\langle e^{-i\mathbf{q}\cdot\hat{\mathbf{u}}_s} e^{i\mathbf{q}\cdot\hat{\mathbf{u}}_{s'}}\rangle$.[30] It states that for two operators $\hat{A}$ and $\hat{B}$:

$$e^{\hat{A}}e^{\hat{B}} = \exp\left(\hat{A}+\hat{B}+\frac{1}{2}[\hat{A},\hat{B}]+\frac{1}{12}\left(\left[\hat{A},[\hat{A},\hat{B}]\right]+\left[\hat{B},[\hat{B},\hat{A}]\right]\right)+...\right) \tag{2.55}$$

where the omitted terms involve higher commutators of $\hat{A}$ and $\hat{B}$.[31] Since $[\hat{a}_\lambda(\mathbf{k}),\hat{a}^\dagger_{\lambda'}(\mathbf{k}')] = \delta_{\mathbf{k}\mathbf{k}'}\delta_{\lambda\lambda'}$, the higher order commutators for operators $\hat{A}$ and $\hat{B}$ that are linear in $\hat{a}_\lambda(\mathbf{k})$ and $\hat{a}^\dagger_\lambda(\mathbf{k})$ vanish, and the following relation holds:

$$e^{\hat{A}}e^{\hat{B}} = e^{\hat{A}+\hat{B}+\frac{1}{2}[\hat{A},\hat{B}]} \tag{2.56}$$

This special case of the Baker-Campbell-Hausdorff allows to simplify the average of Equation (2.53) as:

$$\begin{aligned}\langle e^{-i\mathbf{q}\cdot\hat{\mathbf{u}}_s} e^{i\mathbf{q}\cdot\hat{\mathbf{u}}_{s'}}\rangle &= \langle e^{-i\mathbf{q}\cdot(\hat{\mathbf{u}}_s-\hat{\mathbf{u}}_{s'})+\frac{1}{2}[\mathbf{q}\cdot\hat{\mathbf{u}}_s,\mathbf{q}\cdot\hat{\mathbf{u}}_{s'}]}\rangle \\ &= \langle e^{-i\mathbf{q}\cdot(\hat{\mathbf{u}}_s-\hat{\mathbf{u}}_{s'})}\rangle\langle e^{\frac{1}{2}[\mathbf{q}\cdot\hat{\mathbf{u}}_s,\mathbf{q}\cdot\hat{\mathbf{u}}_{s'}]}\rangle\end{aligned} \tag{2.57}$$

where the second line follows from the commutation relation of $\hat{a}_\lambda(\mathbf{k})$ and $\hat{a}^\dagger_\lambda(\mathbf{k})$. Finally, for operators $\hat{A}$ which are a linear combination of position and momentum operators of a harmonic system, $\langle e^{\hat{A}}\rangle = e^{\frac{1}{2}\langle\hat{A}^2\rangle}$,[32] sometimes known as the Bloch identity. This leads to:

$$\langle e^{-i\mathbf{q}\cdot\hat{\mathbf{u}}_s} e^{i\mathbf{q}\cdot\hat{\mathbf{u}}_{s'}}\rangle = e^{-\frac{1}{2}\langle(\mathbf{q}\cdot\hat{\mathbf{u}}_s)^2\rangle} e^{-\frac{1}{2}\langle(\mathbf{q}\cdot\hat{\mathbf{u}}_{s'})^2\rangle} e^{\langle(\mathbf{q}\cdot\hat{\mathbf{u}}_s)\,(\mathbf{q}\cdot\hat{\mathbf{u}}_{s'})\rangle} \tag{2.58}$$

The terms $e^{-\frac{1}{2}\langle(\mathbf{q}\cdot\hat{\mathbf{u}}_s)^2\rangle}$ and $e^{-\frac{1}{2}\langle(\mathbf{q}\cdot\hat{\mathbf{u}}_{s'})^2\rangle}$ are known as the Debye-Waller factors,[33,34] historically defined as:

$$e^{-\frac{1}{2}\langle(\mathbf{q}\cdot\hat{\mathbf{u}}_s)^2\rangle} \equiv e^{-W_s} \tag{2.59}$$

which means that

$$\langle e^{-i\mathbf{q}\cdot\hat{\mathbf{u}}_s} e^{i\mathbf{q}\cdot\hat{\mathbf{u}}_{s'}}\rangle = e^{-W_s} e^{-W_{s'}} e^{\langle(\mathbf{q}\cdot\hat{\mathbf{u}}_s)\,(\mathbf{q}\cdot\hat{\mathbf{u}}_{s'})\rangle} \tag{2.60}$$

For small displacement vectors $\hat{\mathbf{u}}$, $\mathbf{q}\cdot\hat{\mathbf{u}} \leq |\mathbf{q}||\hat{\mathbf{u}}|$ is also small, and so:

$$\begin{aligned} e^{\langle(\mathbf{q}\cdot\hat{\mathbf{u}}_s)\,(\mathbf{q}\cdot\hat{\mathbf{u}}_{s'})\rangle} &= 1 + \langle(\mathbf{q}\cdot\hat{\mathbf{u}}_s)\,(\mathbf{q}\cdot\hat{\mathbf{u}}_{s'})\rangle + \mathcal{O}\left(|\hat{\mathbf{u}}_s|^2|\hat{\mathbf{u}}_{s'}|^2\right) \\ &\approx 1 + \langle(\mathbf{q}\cdot\hat{\mathbf{u}}_s)\,(\mathbf{q}\cdot\hat{\mathbf{u}}_{s'})\rangle \end{aligned} \tag{2.61}$$

This approximation limits the final expression to the effects of *one-phonon* scattering. This is a good first approximation for simple crystal structures like graphite and MoS_2,[26] but there are reports that compounds with intrinsically-low thermal conductivity – specifically black Phosphorus – display a measureable degree of multi-phonon diffuse scattering.[26,35] Using Equation (2.54):

$$\begin{aligned} &(\mathbf{q}\cdot\hat{\mathbf{u}}_s)\,(\mathbf{q}\cdot\hat{\mathbf{u}}_{s'}) = \\ &\quad\frac{\hbar}{2N}\left(\sum_{\lambda}\sum_{\{\mathbf{k}\}}\frac{\mathbf{q}\cdot\mathbf{e}_{\lambda,s}(\mathbf{k})}{\sqrt{\mu_s\omega_\lambda(\mathbf{k})}}\left[\hat{a}_\lambda(\mathbf{k})e^{-i\phi_{s,m,\lambda}(\mathbf{k})} + \hat{a}^\dagger_\lambda(\mathbf{k})e^{i\phi_{s,m,\lambda}(\mathbf{k})}\right]e^{i\mathbf{k}\cdot\mathbf{r}_{m,s}}\right) \\ &\left(\sum_{\lambda'}\sum_{\{\mathbf{k}'\}}\frac{\mathbf{q}\cdot\mathbf{e}_{\lambda',s'}(\mathbf{k}')}{\sqrt{\mu_{s'}\omega_{\lambda'}(\mathbf{k}')}}\left[\hat{a}_{\lambda'}(\mathbf{k}')e^{-i\phi_{s',m',\lambda'}(\mathbf{k}')} + \hat{a}^\dagger_{\lambda'}(\mathbf{k}')e^{i\phi_{s',m',\lambda'}(\mathbf{k}')}\right]e^{i\mathbf{k}'\cdot\mathbf{r}_{m',s'}}\right) \end{aligned} \tag{2.62}$$

Equivalently:

$$\begin{aligned} &\langle(\mathbf{q}\cdot\hat{\mathbf{u}}_s)\,(\mathbf{q}\cdot\hat{\mathbf{u}}_{s'})\rangle = \\ &\quad\frac{\hbar}{2N}\sum_{\lambda,\lambda'}\sum_{\{\mathbf{k}\},\{\mathbf{k}'\}}\frac{\left(\mathbf{q}\cdot\mathbf{e}_{\lambda,s}(\mathbf{k})\right)\left(\mathbf{q}\cdot\mathbf{e}_{\lambda,s'}(\mathbf{k})\right)}{\sqrt{\mu_s\mu_{s'}\omega_\lambda(\mathbf{k})\omega_{\lambda'}(\mathbf{k}')}}e^{i\mathbf{k}\cdot\mathbf{r}_{m,s}}e^{i\mathbf{k}'\cdot\mathbf{r}_{m',s'}} \\ &\left\langle\left[\hat{a}_\lambda(\mathbf{k})e^{-i\phi_{s,m,\lambda}(\mathbf{k})} + \hat{a}^\dagger_\lambda(\mathbf{k})e^{i\phi_{s,m,\lambda}(\mathbf{k})}\right]\left[\hat{a}_{\lambda'}(\mathbf{k}')e^{-i\phi_{s',m',\lambda'}(\mathbf{k}')} + \hat{a}^\dagger_{\lambda'}(\mathbf{k}')e^{i\phi_{s',m',\lambda'}(\mathbf{k}')}\right]\right\rangle \end{aligned} \tag{2.63}$$

Since the phases $\phi_{s,m,\lambda}(\mathbf{k})$ are not correlated across unit cells, the cross terms vanish:

$$\begin{aligned} \langle(\mathbf{q}\cdot\hat{\mathbf{u}}_s)\,(\mathbf{q}\cdot\hat{\mathbf{u}}_{s'})\rangle =& \frac{\hbar}{2N}\sum_{\lambda}\sum_{\{\mathbf{k}\}}\frac{\left(\mathbf{q}\cdot\mathbf{e}_{\lambda,s}(\mathbf{k})\right)\left(\mathbf{q}\cdot\mathbf{e}_{\lambda,s'}(\mathbf{k})\right)}{\omega_\lambda(\mathbf{k})\sqrt{\mu_s\mu_{s'}}}e^{i\mathbf{k}\cdot\mathbf{r}_{m,s}}e^{i\mathbf{k}\cdot\mathbf{r}_{m,s'}} \\ &\left[\hat{a}_\lambda(\mathbf{k})\hat{a}_\lambda(\mathbf{k}) + \hat{a}_\lambda(\mathbf{k})\hat{a}^\dagger_\lambda(\mathbf{k}) + \hat{a}^\dagger_\lambda(\mathbf{k})\hat{a}_\lambda(\mathbf{k}) + \hat{a}^\dagger_\lambda(\mathbf{k})\hat{a}^\dagger_\lambda(\mathbf{k})\right] \\ =& \frac{\hbar}{2N}\sum_{\lambda}\sum_{\{\mathbf{k}\}}\frac{\left(\mathbf{q}\cdot\mathbf{e}_{\lambda,s}(\mathbf{k})\right)\left(\mathbf{q}\cdot\mathbf{e}_{\lambda,s'}(\mathbf{k})\right)}{\omega_\lambda(\mathbf{k})\sqrt{\mu_s\mu_{s'}}}e^{i\mathbf{k}\cdot\mathbf{r}_{m,s}}e^{i\mathbf{k}\cdot\mathbf{r}_{m,s'}}\left[2\hat{n}_\lambda(\mathbf{k})+1\right] \end{aligned} \tag{2.64}$$

where $\hat{n}_\lambda(\mathbf{k}) \equiv \hat{a}_\lambda(\mathbf{k})\hat{a}^\dagger_\lambda(\mathbf{k}) = \hat{a}^\dagger_\lambda(\mathbf{k})\hat{a}_\lambda(\mathbf{k}) - 1$ is the excitation number operator. Simplifying

further:

$$\langle(\mathbf{q}\cdot\hat{\mathbf{u}}_s)\,(\mathbf{q}\cdot\hat{\mathbf{u}}_{s'})\rangle = \frac{\hbar}{N}\sum_{\lambda}\sum_{\{\mathbf{k}\}}\left(\frac{\hat{n}_\lambda(\mathbf{k})+1/2}{\omega_\lambda(\mathbf{k})}\right)\left(\frac{\left(\mathbf{q}\cdot\mathbf{e}_{\lambda,s}(\mathbf{k})\right)\left(\mathbf{q}\cdot\mathbf{e}_{\lambda,s'}(\mathbf{k})\right)}{\sqrt{\mu_s\mu_{s'}}}\right)e^{i\mathbf{k}\cdot\mathbf{r}_{m,s}}e^{i\mathbf{k}\cdot\mathbf{r}_{m,s'}} \tag{2.65}$$

2.4.2. Scattering amplitude

Using the calculation of the previous section, the scattering amplitude can be computed. Since this calculation holds for a prepared initial state $|\mathbf{k}_i\rangle$ and arbitrary final state $|\mathbf{k}_f\rangle$ (where $\mathbf{q}=\mathbf{k}_f-\mathbf{k}_i$), the quantities $\hat{\mathbf{u}}$ and $\hat{n}$ are no longer operators, but observables $\mathbf{u}$ and n respectively. Equation (2.53) can then be expressed as:

$$\begin{aligned}|f^{(1)}(\mathbf{q})|^2 =& \frac{m_e^2}{N_c^2\hbar^4}\sum_{m,m'}\sum_{s,s'}f_{e,s}(\mathbf{q})f_{e,s'}(\mathbf{q})e^{-i\mathbf{q}\cdot(\mathbf{r}_{m,s}-\mathbf{r}_{m',s'})}e^{-W_s}e^{-W_{s'}}\left[1+\langle(\mathbf{q}\cdot\mathbf{u}_s)\,(\mathbf{q}\cdot\mathbf{u}_{s'})\rangle\right]\\ =&\frac{m_e^2}{N_c^2\hbar^4}\left|\sum_m\sum_s f_{e,s}(\mathbf{q})e^{-W_s}e^{-i\mathbf{q}\cdot\mathbf{r}_{m,s}}\right|^2\\ &+\frac{m_e^2}{NN_c^2\hbar^3}\sum_\lambda\sum_{\{\mathbf{k}\}}\frac{n_\lambda(\mathbf{k})+1/2}{\omega_\lambda(\mathbf{k})}\left|\sum_m\sum_s\frac{f_{e,s}(\mathbf{q})e^{-W_s}}{\sqrt{\mu_s}}\left(\mathbf{q}\cdot\mathbf{e}_{\lambda,s}(\mathbf{k})\right)e^{-i(\mathbf{q}-\mathbf{k})\cdot\mathbf{r}_{m,s}}\right|^2\end{aligned} \tag{2.66}$$

It is now convenient to express the atomic positions $\mathbf{r}_{m,s}=\mathbf{R}_m+\mathbf{x}_s$, where $\mathbf{R}_m$ is the absolute position of unit cell m, and $\mathbf{x}_s$ is the position of atom s with respect to the unit cell origin. The above equation becomes:

$$\begin{aligned}|f^{(1)}(\mathbf{q})|^2 =&\frac{m_e^2}{N_c^2\hbar^4}\left|\sum_m\sum_s f_{e,s}(\mathbf{q})e^{-W_s}e^{-i\mathbf{q}\cdot\mathbf{R}_m}e^{-i\mathbf{q}\cdot\mathbf{x}_s}\right|^2\\ &+\frac{m_e^2}{NN_c^2\hbar^3}\sum_\lambda\sum_{\{\mathbf{k}\}}\frac{n_\lambda(\mathbf{k})+1/2}{\omega_\lambda(\mathbf{k})}\left|\sum_m\sum_s\frac{f_{e,s}(\mathbf{q})e^{-W_s}}{\sqrt{\mu_s}}\left(\mathbf{q}\cdot\mathbf{e}_{\lambda,s}(\mathbf{k})\right)e^{-i(\mathbf{q}-\mathbf{k})\cdot\mathbf{R}_m}e^{-i(\mathbf{q}-\mathbf{k})\cdot\mathbf{x}_s}\right|^2\end{aligned} \tag{2.67}$$

The Fourier transform identity can be used (Equation (2.37)):

$$\sum_{m=1}^{N_c}e^{-i\mathbf{q}\cdot\mathbf{R}_m}\xrightarrow{N_c\to\infty}N_c\sum_{\{\mathbf{H}\}}\delta(\mathbf{q}-\mathbf{H}) \tag{2.68}$$

The equation for the scattering amplitude becomes:

$$|f^{(1)}(\mathbf{q})|^2 = \frac{m_e^2}{\hbar^4}\left|\sum_{\{\mathbf{H}\}}\sum_s f_{e,s}(\mathbf{q})e^{-W_s}e^{-i\mathbf{q}\cdot\mathbf{x}_s}\delta(\mathbf{q}-\mathbf{H})\right|^2 + \frac{m_e^2}{NN_c^2\hbar^3}\sum_\lambda\sum_{\{\mathbf{k}\}}\frac{n_\lambda(\mathbf{k})+1/2}{\omega_\lambda(\mathbf{k})}\left|\sum_m\sum_s\frac{f_{e,s}(\mathbf{q})e^{-W_s}}{\sqrt{\mu_s}}\left(\mathbf{q}\cdot\mathbf{e}_{\lambda,s}(\mathbf{k})\right)e^{-i(\mathbf{q}-\mathbf{k})\cdot\mathbf{R}_m}e^{-i(\mathbf{q}-\mathbf{k})\cdot\mathbf{x}_s}\right|^2 \tag{2.69}$$

The sum over $\mathbf{k}$ in the second term can be simplified in a similar way. For any $\mathbf{q}$, there is one reciprocal point which is closest, $\mathbf{H}_\mathbf{q}$. Define $\mathbf{k}_0$ to be such that $\mathbf{q} = \mathbf{H}_\mathbf{q}+\mathbf{k}_0$, i.e. $\mathbf{k}_0$ is constrained to lie in the first Brillouin zone. Then:

$$\sum_m e^{-i(\mathbf{q}-\mathbf{k})\cdot\mathbf{r}_{m,s}} = N_c\delta(\mathbf{k}-\mathbf{k}_0) \tag{2.70}$$

The sum $\sum_{\{\mathbf{H}\}}$ is implicitly contained in the constraints on the values of $\mathbf{k}_0$. It follows that:

$$|f^{(1)}(\mathbf{q})|^2 = \frac{m_e^2}{\hbar^4}\left|\sum_{\{\mathbf{H}\}}\sum_s f_{e,s}(\mathbf{q})e^{-W_s}e^{-i\mathbf{q}\cdot\mathbf{x}_s}\delta(\mathbf{q}-\mathbf{H})\right|^2 + \frac{m_e^2}{N\hbar^3}\sum_\lambda\frac{n_\lambda(\mathbf{k}_0)+1/2}{\omega_\lambda(\mathbf{k}_0)}\left|\sum_s\frac{f_{e,s}(\mathbf{q})e^{-W_s}}{\sqrt{\mu_s}}\left(\mathbf{q}\cdot\mathbf{e}_{\lambda,s}(\mathbf{k}_0)\right)e^{-i\mathbf{H}_\mathbf{q}\cdot\mathbf{x}_s}\right|^2 \tag{2.71}$$

The phase factor $e^{-i\mathbf{H}_\mathbf{q}\cdot\mathbf{x}_s}$ is a matter of convention.[36] In the expression for the displacement vectors in Equation (2.54), it was assumed that the phonon eigenvectors were not periodic in general, that is:

$$\mathbf{e}_{\lambda,s}(\mathbf{k}+\mathbf{k}') = \mathbf{e}_{\lambda,s}(\mathbf{k})e^{-i\mathbf{k}'\cdot\mathbf{x_s}} \tag{2.72}$$

Henceforth, the phonon eigenvectors are assumed to be periodic, that is, $\mathbf{e}_{\lambda,s}(\mathbf{k}+\mathbf{H}) \equiv \mathbf{e}_{\lambda,s}(\mathbf{k})$ for a reciprocal point $\mathbf{H}$. Then $\mathbf{e}_{\lambda,s}(\mathbf{k}_0)e^{-i\mathbf{H}_\mathbf{q}\cdot\mathbf{x}_s} = \mathbf{e}_{\lambda,s}(\mathbf{k}_0-\mathbf{H}_\mathbf{q}) = \mathbf{e}_{\lambda,s}(\mathbf{k}_0)$. It follows that:

$$|f^{(1)}(\mathbf{q})|^2 = \frac{m_e^2}{\hbar^4}\left|\sum_{\{\mathbf{H}\}}\sum_s f_{e,s}(\mathbf{q})e^{-W_s}e^{-i\mathbf{q}\cdot\mathbf{x}_s}\delta(\mathbf{q}-\mathbf{H})\right|^2 + \frac{m_e^2}{N\hbar^3}\sum_\lambda\frac{n_\lambda(\mathbf{k}_0)+1/2}{\omega_\lambda(\mathbf{k}_0)}\left|\sum_s\frac{f_{e,s}(\mathbf{q})e^{-W_s}}{\sqrt{\mu_s}}\left(\mathbf{q}\cdot\mathbf{e}_{\lambda,s}(\mathbf{k}_0)\right)\right|^2 \tag{2.73}$$

A visual representation of the relationship between vectors $\mathbf{H}_\mathbf{q}$, $\mathbf{q}$, and $\mathbf{k_0}$ is shown in Figure 2.4.

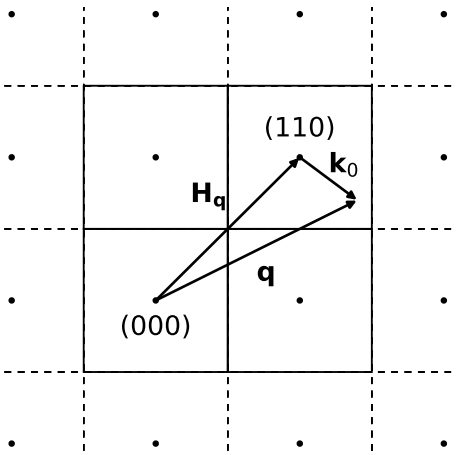

Figure 2.4.: Geometrical relationship between the scattering vector $\mathbf{q}$, the reciprocal point closest to $\mathbf{q}$, $\mathbf{H}_\mathbf{q}$, and wavevector $\mathbf{k}_0$ for a hypothetical cubic crystal. The in-plane section of the Brillouin, where $\mathbf{k}_0$ is confined, is shown as well.

Combining Equation (2.73) and Equation (2.20), the measured intensity is therefore:

$$I(\mathbf{q}) = I_0(\mathbf{q}) + I_1(\mathbf{q}) \tag{2.74}$$

where

$$I_0(\mathbf{q}) = \frac{m_e^2}{r^2\hbar^4}\left|\sum_{\{\mathbf{H}\}}\sum_s f_{e,s}(\mathbf{q})e^{-W_s}e^{-i\mathbf{q}\cdot\mathbf{x}_s}\delta(\mathbf{q}-\mathbf{H})\right|^2 \tag{2.75}$$

is the diffracted intensity. The diffracted intensity at finite temperature is equivalent to Equation (2.29), with the substitution $f_{e,s}(\mathbf{q}) \rightarrow f_{e,s}(\mathbf{q})e^{-W_s}$. The physical meaning of this substitution is that atomic vibrations due to temperature decrease the periodicity of the lattice, which results in a suppression of the atomic form factor in reciprocal space. The other term, $I_1(\mathbf{q})$, is known as *first order diffuse scattering*:

$$I_1(\mathbf{q}) = \frac{m_e^2}{r^2 N\hbar^3}\sum_\lambda \frac{n_\lambda(\mathbf{k})+1/2}{\omega_\lambda(\mathbf{k})}\left|\sum_s \frac{f_{e,s}(\mathbf{q})e^{-W_s}}{\sqrt{\mu_s}}\left(\mathbf{q}\cdot\mathbf{e}_{\lambda,s}(\mathbf{k})\right)\right|^2 \tag{2.76}$$

2.4.3. Diffuse scattering

The diffuse intensity can be expressed as:

$$I_1(\mathbf{q}) = I_e \sum_{\lambda} \frac{n_\lambda(\mathbf{k}) + 1/2}{\omega_\lambda(\mathbf{k})} |F_{1\lambda}(\mathbf{q})|^2 \tag{2.77}$$

where $F_{1\lambda}(\mathbf{q})$ is known as the *one-phonon structure factor*:

$$|F_{1\lambda}(\mathbf{q})|^2 = \left| \sum_s \frac{f_{e,s}(\mathbf{q}) e^{-W_s}}{\sqrt{\mu_s}} \left(\mathbf{q} \cdot \mathbf{e}_{\lambda,s}(\mathbf{k}) \right) \right|^2 \tag{2.78}$$

named thus in contrast to the static structure factor of Equation (2.28).

A few clarifications can be made about diffuse intensity. The diffuse intensity at any scattering vector $\mathbf{q}$ involves the contribution of all phonon modes λ. The contribution of each mode can be conceptually separated into two parts.

The first part of each term in the sum of Equation (2.77), proportional to $(n_\lambda(\mathbf{k}) + 1/2)/\omega_\lambda(\mathbf{k})$, represents the vibrational amplitude of each mode by analogy with the expression of Equation (2.54). A higher population ($\uparrow n_\lambda$) results in a larger vibrational amplitude because the displacement of atoms is linear in the number of phonons that participate. A lower vibrational frequency ($\downarrow \omega_\lambda$) implies a smaller restoring force (in the harmonic oscillator sense), which also intuitively results in a wider vibrational amplitude.

The second part of the summation terms are the one-phonon structure factors. These factors are a geometrical weight ($|F_{1\lambda}(\mathbf{q})|^2$) which determines if the atomic motion associated with a phonon mode can be captured on the detector. The most important terms to consider are terms of the form $\{ \mathbf{q} \cdot \mathbf{e}_{\lambda,s}(\mathbf{k}) \}$. For a phonon polarization which is parallel to the propagation of the scattering electrons, the projection of the polarization onto the detector plane is 0, and hence the associated diffuse intensity will not contribute. An example of one-phonon structure factor for the in-plane longitudinal acoustic mode of graphite is shown in Figure 2.5. Being a longitudinal mode, the polarization of this mode is in the direction of propagation, which means that terms $\mathbf{q} \cdot \mathbf{e}_{\lambda,s}(\mathbf{k})$ should have a radial character in reciprocal space.

Diffuse scattering and the effect of one-phonon structure factors is further explored in Chapter 3. The key takeaway from this section is that the Debye-Waller effect and diffuse scattering are two faces of the same coin. Both arise from the same physical phenomenon: atomic vibrations expressed as a superposition of lattice waves.

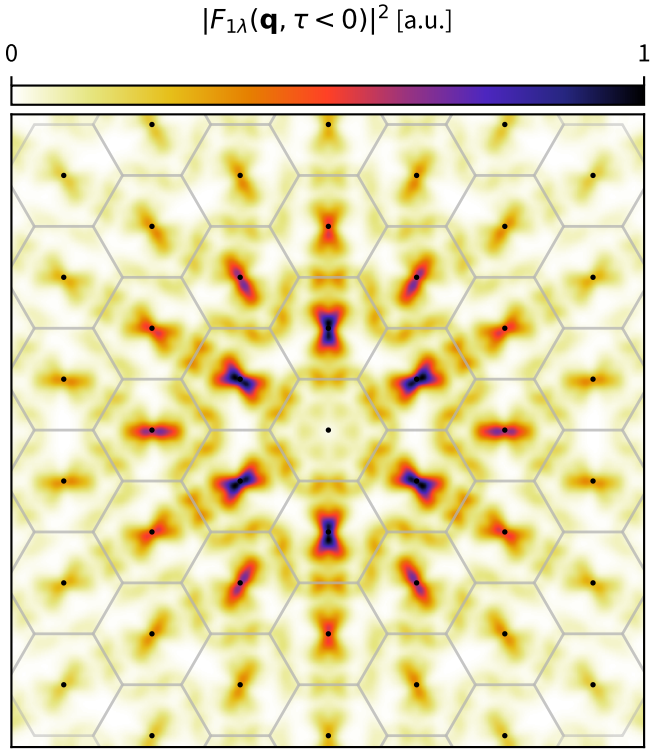

Figure 2.5.: One-phonon structure factor $|F_{1\lambda}(\mathbf{q})|^2$ for the in-plane longitudinal acoustic mode of graphite. The range of scattering vectors $\mathbf{q}$ corresponds to the geometry of the instrument described in Section 1.4.

2.5. Conclusion

In this chapter, the theory of ultrafast electron scattering measurements were presented. First, the scattering of electrons by any potential was considered. This was then applied to the case of elastic scattering of electrons by atoms, and then periodic arrangements of atoms at zero temperature. Finally, the full quantum derivation of ultrafast electron diffuse scattering was presented.

In Chapter 3, ultrafast measurements in a prototypical benchmark system will show the full power of diffuse scattering measurements, while the link between the Debye-Waller effect and diffuse scattering will play a large role in Chapter 4.

References

[1] E. Schrödinger. *An undulatory theory of the mechanics of atoms and molecules*. *Physical Review* **28** no. 6 (1926), pp. 1049–1070. DOI: 10.1103/physrev.28.1049.

[2] B. A. Lippmann and J. Schwinger. *Variational principles for scattering processes I*. *Physical Review* **79** no. 3 (1950), p. 469. DOI: 10.1103/physrev.79.469.

[3] J. J. Sakurai and J. J Napolitano. *Modern quantum mechanics*. Pearson, 2014.

[4] R. P. Feynman and A. R. Hibbs. In: *Quantum mechanics and path integrals*. McGraw-Hill, 1965. Chap. 6, pp. 122–129.

[5] B. Fultz and J. M. Howe. In: *Transmission electron microscopy and diffractometry of materials*. Section 5.1.2. Springer, 2002, pp. 228–229.

[6] M. Born. *Quantenmechanik der Stoßvorgänge*. *Zeitschrift für Physik* **38** (1926), pp. 803–840. DOI: 10.1007/bf01397184.

[7] C. F. Fischer. *Hartree–Fock method for atoms. A numerical approach*. John Wiley and Sons, 1977.

[8] E. J. Kirkland. In: *Advanced computing in electron microscopy*. Appendix C. Springer Science & Business Media, 2010. DOI: 10.1007/978-1-4419-6533-2.

[9] J.-C. Zheng, L. Wu, and Y. Zhu. *Aspherical electron scattering factors and their parameterizations for elements from H to Xe*. *Journal of Applied Crystallography* **42** no. 6 (2009), pp. 1043–1053. DOI: 10.1107/s0021889809033147.

[10] W. H. Bragg. *The intensity of x-ray reflection by diamond*. *Proceedings of the Physical Society of London* **33** no. 1 (1920), pp. 304–311. DOI: 10.1088/1478-7814/33/1/331.

[11] D. Keating, A. Nunes, B. Batterman, and J. Hastings. *Forbidden (222) neutron reflection in silicon: anharmonicity and the bonding electrons*. *Physical Review B* **4** no. 8 (1971), pp. 2472–2478. DOI: 10.1103/physrevb.4.2472.

[12] B. E. Warren. In: *X-ray diffraction*. Dover Publications, 1990. Chap. 3, p. 28.

[13] C. Kittel and P. McEuen. In: *Introduction to solid state physics*. Wiley, 2005. Chap. 2, pp. 30–31.

[14] B. Fultz and J. M. Howe. In: *Transmission electron microscopy and diffractometry of materials*. Springer, 2002. Chap. 3, pp. 123–124.

[15] E. J. Kirkland. In: *Advanced computing in electron microscopy*. Springer Science & Business Media, 2010. Chap. 5.3, p. 90. DOI: 10.1007/978-1-4419-6533-2.

[16] W. H. Miller. *A treatise on crystallography*. J. & J. J. Deighton, 1839.

[17] E. L. Robinson. In: *Data analysis for scientists and engineers*. Table 8.1. Princeton University Press, 2016. Chap. 8.

[18] B. E. Warren. In: *X-ray diffraction*. Dover Publications, 1990. Chap. 2, p. 18.

[19] W. H. Bragg and W. L. Bragg. *The reflection of X-rays by crystals*. *Proceedings of the Royal Society of London A* **88** no. 605 (1913), pp. 428–438. DOI: 10.1038/091477b0.

[20] P. P. Ewald. *Die Berechnung optischer und elektrostatischer Gitterpotentiale*. *Annalen der Physik* **369** no. 3 (1921), pp. 253–287. DOI: 10.1002/andp.19213690304.

[21] Z. Huang and K.-J. Kim. *Review of x-ray free-electron laser theory*. *Physical Review Special Topics - Accelerators and Beams* **10** no. 3 (2007). DOI: 10.1103/physrevstab.10.034801.

[22] C. Bostedt, J. D. Bozek, P. H. Bucksbaum, R. N. Coffee, J. B. Hastings, Z. Huang, R. W. Lee, S. Schorb, J. N. Corlett, P. Denes, P. Emma, R. W. Falcone, R. W. Schoenlein, G. Doumy, E. P. Kanter, B. Kraessig, S. Southworth, L. Young, L. Fang, M. Hoener, N. Berrah, C. Roedig, and L. F. DiMauro. *Ultra-fast and ultra-intense x-ray sciences: first results from the Linac Coherent Light Source free-electron laser*. *Journal of Physics B: Atomic, Molecular and Optical Physics* **46** no. 16 (2013), p. 164003. DOI: 10.1088/0953-4075/46/16/164003.

[23] B. Fultz and J. Howe. In: *Transmission electron microscopy and diffractometry of materials*. Section 7.3. Springer, 2013.

[24] Z.-L. Wang. *Elastic and inelastic scattering in electron diffraction and imaging*. Springer, 1995.

[25] M. Zacharias, H Seiler, F. Caruso, D. Zahn, F. Giustino, P. C. Kelires, and R. Ernstorfer. *Efficient first-principles methodology for the calculation of the all-phonon inelastic scattering in solids*. *Physical Review Letters* **127** no. 20 (2021), p. 207401.

[26] M. Zacharias, H. Seiler, F. Caruso, D. Zahn, F. Giustino, P. C. Kelires, and R. Ernstorfer. *Multi-phonon diffuse scattering in solids from first principles: Application to layered crystals and two-dimensional materials*. *Physical Review B* **104** no. 20 (2021), p. 205109.

[27] A. Altland and B. D. Simons. In: *Condensed matter field theory*. Cambridge University Press, 2010. Chap. 2.

[28] F. Giustino. *Electron-phonon interactions from first principles*. *Reviews of Modern Physics* **89** no. 1 (2017), p. 015003. DOI: 10.1103/revmodphys.89.015003.

[29] S. K. Sinha. *Theory of inelastic X-ray scattering from condensed matter*. *Journal of Physics: Condensed Matter* **13** no. 34 (2001), p. 7511. DOI: 10.1088/0953-8984/13/34/304.

[30] J. E. Campbell. *On a law of combination of operators (second paper)*. *Proceedings of the London Mathematical Society* **29** no. 1 (1897), pp. 14–32. DOI: 10.1112/plms/s1-29.1.14.

[31] E. B Dynkin. *Calculation of the coefficients in the Campbell-Hausdorff formula*. **57**. Doklady Akademii Nauk SSSR, 1947, pp. 323–326.

[32] M. Born and K. Sarginson. *The effect of thermal vibrations on the scattering of X-rays*. *Proceedings of the Royal Society of London A* **179** no. 976 (1941), pp. 69–93. DOI: 10.1098/rspa.1941.0080.

[33] I. Waller. *Zur frage der einwirkung der wärmebewegung auf die interferenz von röntgenstrahlen*. *Zeitschrift für Physik* **17** no. 1 (1923), pp. 398–408. DOI: 10.1007/bf01328696.

[34] I. Waller. *Über eine verallgemeinerte Streuungsformel*. *Zeitschrift für Physik* **51** no. 3-4 (1928), pp. 213–231. DOI: 10.1007/bf01343197.

[35] H. Seiler, D. Zahn, M. Zacharias, P.-N. Hildebrandt, T. Vasileiadis, Y. W. Windsor, Y. Qi, C. Carbogno, C. Draxl, R. Ernstorfer, and F. Caruso. *Accessing the anisotropic nonthermal phonon populations in black phosphorus*. *Nano Letters* (2021). DOI: 10.1021/acs.nanolett.1c01786.

[36] R. Xu and T. C. Chiang. *Determination of phonon dispersion relations by x-ray thermal diffuse scattering*. *Zeitschrift für Kristallographie* **220** no. 12 (2005), pp. 1009–1016. DOI: 10.1524/zkri.2005.220.12_2005.1009.

3. Momentum-resolved excitation couplings in graphite

This chapter is an exploration of ultrafast electron diffuse scattering measurements applied to systems with strong couplings. To this end, graphite is the perfect benchmark system for ultrafast electron diffuse scattering measurements for two major reasons. On the one hand, it has a very stiff lattice in the plane due to inherently strong carbon-carbon bonds and a hexagonal structure.[1] The spectrum of lattice waves in graphite gives ultrafast electron diffuse scattering measurements incredible contrast, as the thermally-occupied phonon modes are localized to the Brillouin zone center.[2] On the other hand, much ultrafast work has been done on graphite and graphene. This presents an opportunity to compare and contrast results between spectroscopic probes such as terahertz spectroscopy or time- and angle-resolved photoemission spectroscopy, and ultrafast electron diffuse scattering.

The work in this chapter follows earlier work by the author in Stern *et al.*[3] which demonstrated that ultrafast electron diffuse scattering measurements were feasible in graphite. A picture of anharmonic decay from strongly-coupled optical phonon modes was assembled, which meshed very well with the existing literature. However, due to the energy-integrative nature of ultrafast electron diffuse scattering measurements, the analysis remained qualitative. This chapter is focused on the quantitative side of things. It will be demonstrated that the geometry of experiments, combined with the crystal symmetry, can be used to endow ultrafast electron diffuse scattering measurement with energy-resolution. The chapter culminates in the presentation of the time-resolved mode-dependent phonon population *across the Brillouin zone*, describing the energy flow within the graphite lattice.

This chapter is organized as follows. The properties of single-crystal graphite are first described, as well as a brief review of the ultrafast experiments on graphene and graphite. The experimental details are then given, as well as the computational parameters that were used to calculate the in-plane phonon dispersion. The ultrafast electron diffuse scattering measurements are then

presented. Next comes the calculation of the geometrical weights known as the one-phonon structure factors (Section 2.4.3). The high point of this chapter follows, with the presentation of time-resolved mode-dependent phonon populations across the Brillouin zone. Finally, the phenomenological electron-phonon coupling tensor element to the A_1' phonon mode is extracted and compared to other measurements and calculations.

3.1. Single-crystal graphite

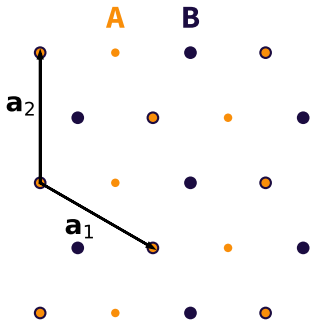

Figure 3.1.: In-plane crystal structure of graphite, which is composed of two offset sublattices **A** and **B**. In this geometry, the stacking axis $\mathbf{a}_3$ points through the page.

Single-crystal graphite is a two-dimensional material made of a repeating layers of carbon atoms arranged in a hexagonal lattice. Its lattice vectors $\{\,\mathbf{a}_i\,\}$ are:

$$\begin{pmatrix}\mathbf{a}_1\\ \mathbf{a}_2\\ \mathbf{a}_3\end{pmatrix} = \begin{pmatrix}\sqrt{3}a & -a & 0\\ 0 & 2a & 0\\ 0 & 0 & c\end{pmatrix}\begin{pmatrix}\mathbf{e}_1\\ \mathbf{e}_2\\ \mathbf{e}_3\end{pmatrix} \tag{3.1}$$

where $a = 1.232\,\text{Å}$, $c = 6.711\,\text{Å}$, and $\{\,\mathbf{e}_i\,\}$ are understood to be the usual Euclidean vectors. Carbon atoms $\{\,\mathbf{c}_i\,\}$ are positioned as follows:

$$\begin{pmatrix}\mathbf{c}_1\\ \mathbf{c}_2\\ \mathbf{c}_3\\ \mathbf{c}_4\end{pmatrix} = \begin{pmatrix}0 & 0 & 0\\ 1/3 & 2/3 & 0\\ 0 & 0 & 1/2\\ 2/3 & 1/3 & 1/2\end{pmatrix}\begin{pmatrix}\mathbf{a}_1\\ \mathbf{a}_2\\ \mathbf{a}_3\end{pmatrix} \tag{3.2}$$

Note that carbon atoms $\mathbf{c}_1$ and $\mathbf{c}_2$ form a sheet of graphene, while $\mathbf{c}_3$ and $\mathbf{c}_4$ form a separate

separate sheet of graphene rotated by $\frac{\pi}{3}$ (60°). The stacking of both sublattices along the $\mathbf{a}_3$ axis confers graphite increased discrete rotational symmetry (six-fold) about the stacking axis, compared to the 3-fold rotational symmetry of graphene. More specifically, the point group for graphite is $6/mmm$, while the Hermann-Mauguin symbol for the space group is $P6_3/mmc$. The crystal structure is presented in Figure 3.1.

The real-space six-fold rotational symmetry is mirrored in reciprocal space. The in-plane geometry of the Brillouin zone is shown in Figure 3.2, including the high-symmetry points $\mathbf{\Gamma}$ (zone-center), $\mathbf{M}$, and $\mathbf{K}$.

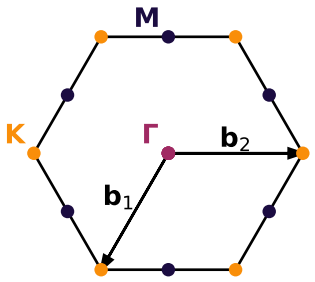

Figure 3.2.: In-plane section of the Brillouin zone of graphite, spanned by reciprocal lattice vectors $\mathbf{b}_1$ and $\mathbf{b}_2$. The three classes of high-symmetry points are shown. $\mathbf{M}$ and $\mathbf{K}$ have symmetry equivalents on every edge and vertex respectively.

3.1.1. Electronic structure

The electronic structure of graphite has been the subject of much study. Graphite is a very close relative of the Dirac semi-metal graphene; its electronic dispersion is very similar from the point of view of experiments presented in this chapter. The electronic dispersion of the π and $\pi^\star$ bands of graphite can be calculated in the tight-binding framework.[4,5] Taking into account nearest-neighbor interactions only, the dispersion for both bonding and antibonding bands are given by:

$$E(\mathbf{k})_{\pi^\star} = t\sqrt{3 + f(\mathbf{k})} \tag{3.3}$$

$$E(\mathbf{k})_{\pi} = -t\sqrt{3 + f(\mathbf{k})} \tag{3.4}$$

with

$$f(\mathbf{k}) = 2\cos\left[\sqrt{3}a\,(\mathbf{k}\cdot\mathbf{b}_2)\right] + 4\cos\left[\tfrac{\sqrt{3}a}{2}\,(\mathbf{k}\cdot\mathbf{b}_2)\right]\cos\left[\tfrac{3a}{2}\,(\mathbf{k}\cdot\mathbf{b}_1)\right] \tag{3.5}$$

where t is the tight-binding constant and a is the carbon-carbon distance. The in-plane dispersion for a tight-binding energy of $t = 2.7$ eV is shown on Figure 3.3. More complete expressions that are not limited to nearest neighbor interactions are given elsewhere,[6,7] but the essential details are captured by Equation (3.3) and Equation (3.4).

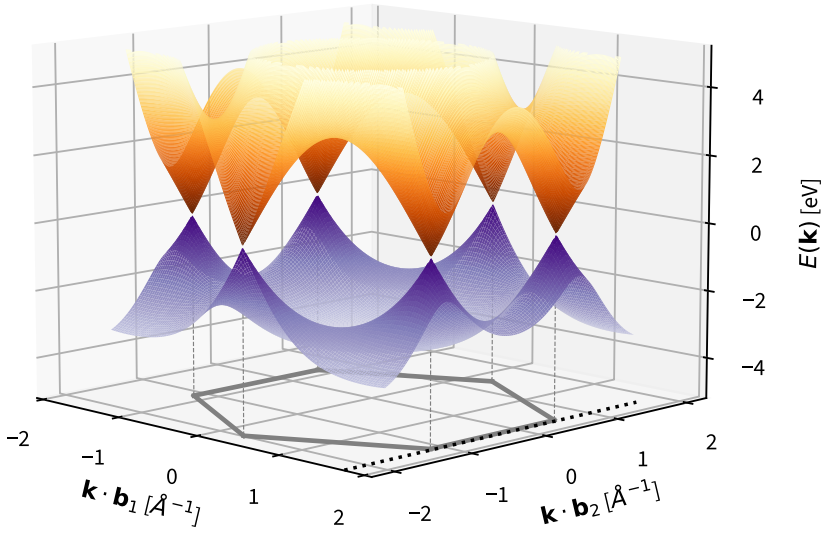

Figure 3.3.: In-plane electronic dispersion $E(\mathbf{k})$ for graphite. The in-plane section of the Brillouin zone is shown below. The dotted black line represents the line-cut used for Figure 3.6.

The nonequilibrium behavior of photoexcited graphite is dominated by the structure of the electronic dispersion near the $\mathbf{K}$ points, at the corner of the Brillouin zone. These points, where the dispersion of each band meet, are called Dirac points. In analogy to graphene,[8] the dispersion in graphite adopts a conical shape, called Dirac cones, near the Dirac points.[9]

3.1.2. Phonon landscape

With four atoms per unit cell, the structure of graphite supports twelve distinct phonon modes. The layered nature of graphite results in a clear distinction between in-plane and out-of-plane phonon modes. These modes are longitudinal modes LA, LO1 - LO3, in-plane transverse modes TA, TO1 - TO3, and out-of-plane traverse modes ZA, ZO1 - ZO3. The phonon dispersion relation for in-plane modes was calculated as described further below in Section 3.2.3, and is shown in Figure 3.4. The out-of-plane transverse modes are not taken into account as the experiments presented in this chapter are not sensitive to them.

Figure 3.4 reveals why graphite is the *perfect* benchmark material for ultrafast electron diffuse scattering. All of the lattice modes are so stiff (high-energy) that, at room temperature, thermally-occupied modes are concentrated at $\mathbf{\Gamma}$. The energy equivalent to room-temperature is shown on Figure 3.4 by a horizontal dashed line at 25 meV. Therefore, the contrast between static diffuse intensity and diffuse intensity after photoexcitation is bound to be maximal.

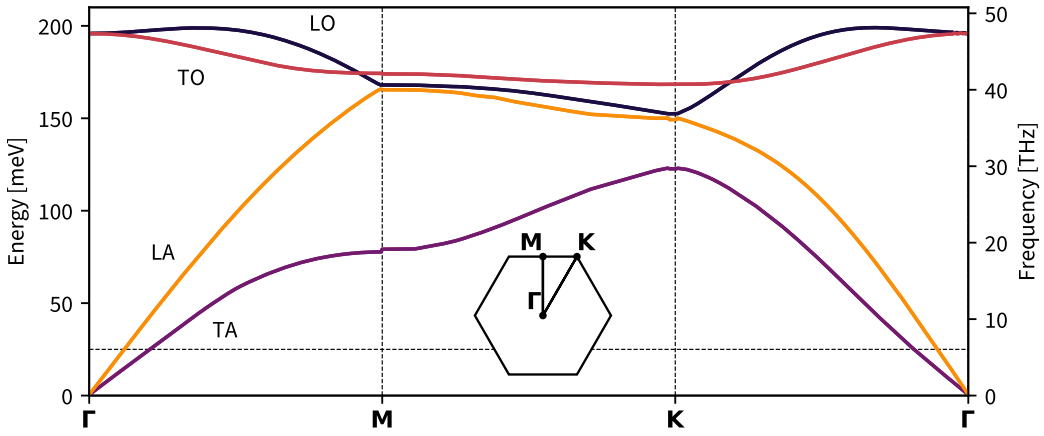

Figure 3.4.: Phonon dispersion relation of graphite for in-plane modes LA, TA, and two-fold degenerate modes LO and TO. The path in reciprocal space is shown in the center. A horizontal dashed line at 25 meV indicates the average energy stored in the phonon modes at room temperature (300 K).

3.1.3. Kohn anomalies

An important feature of the phonon dispersion of graphite that is not replicated by the simple calculation of Figure 3.4 are *Kohn anomalies*.[10] Kohn anomalies are pronounced dips with a $|E - E_0|$ character in the phonon dispersion of metals. In other words, the derivative of the

phononic dispersion curve is discontinuous. In extreme cases, the softening of the phonon dispersion to zero creates a lattice distortion, which is one of the causes of charge-density wave phases.[11,12,13]

Kohn anomalies have been shown to appear in graphite for transverse optical modes at $\mathbf{\Gamma}$ (mode E_{2g}) and $\mathbf{K}$ (mode A_1') by inelastic x-ray scattering measurements performed by Maultzsch *et al.*[14] Theoretical work by Piscanec *et al.*[15] has linked the slope of these kinks to the strength of the coupling between the electronic system and these specific modes. The calculated band structure including the two Kohn anomalies in graphite is presented in Figure 3.5.

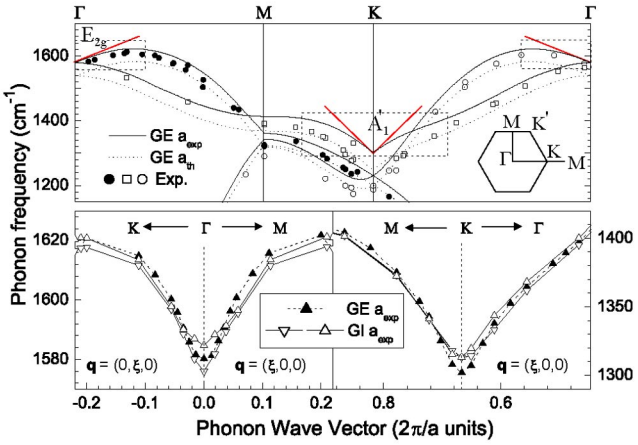

Figure 3.5.: Phonon dispersion of graphene (GE) and graphite (GI), calculated at the experimental and equilibrium lattice spacings (a_{exp} and a_{th}). The red straight lines at $\mathbf{\Gamma}$ and $\mathbf{K}$ show the slope of the Kohn anomalies. The two lower panels correspond to the dotted windows in the upper panel. The points are theoretical frequencies obtained by direct calculation. Reused with permission from Piscanec *et al.*[15]

3.1.4. Previous studies of nonequilibrium dynamics in graphite

Ultrafast studies of graphite conceptually start with the work by Kampfrath *et al.*[16] The strong coupling between charge carriers and optical phonons A_1' and E_{2g} was demonstrated using time-resolved terahertz spectroscopy by tracking the transient in-plane dielectric function after pumping with short pulses of 1.5 eV photons. The authors reveal that by 500 fs after photoexcitation, more than 90% of the absorbed pump energy has been transferred to the lattice. The authors subsequently determine the lifetime of the strongly-coupled optical modes.

The understanding of hot carrier dynamics in allotropes of carbon lept forward significantly following the development of time- and angle-resolved photoemission spectroscopy (trARPES).

Early work by Johannsen *et al.*[17] probed graphene photoexcited with 1.5 eV photons. This experiment showed that for all time-delay after photoexcitation, the energy distribution for electrons near the Dirac cones can be described by Fermi-Dirac statistics. This implies that by 60 fs after photoexcitation – the effective time-resolution of the experiment –, the electrons have thermalized. This estimate has been confirmed by optical pump-probe spectroscopy.[18] Johannsen *et al.*[17] also determined the process by which energy is transferred to acoustic phonons. According to their modelling, the restricted set of momentum-conserving energy-transfer pathways between the hot electron gas and acoustic phonon can be substantially expanded thanks to defect-mediated interactions, via a process called *supercollision*.[19,20]

The experiment by Stange *et al.*[21] on graphite showcases some important differences between ultrafast work on graphite and graphene. With a time-resolution of 32 fs, it was found that the electronic energy distribution is not well-described by Fermi-Dirac statistics until about 100 fs, after which an effective electronic temperature can be defined. The authors also weighed in on the subsequent phonon thermalization mechanism. Contrary to the work by Johannsen *et al.*,[17] Stange *et al.*[21] showed that the supercollision model *does not explain* ultrafast thermalization in graphite. Instead, anharmonic coupling between optical and acoustic modes, initially proposed by Yan *et al.*,[22] was found to be the most important thermalization mechanism. The difference in thermalization process is attributed to the much longer electron mean-free path in graphite (0.2 µm to 10 µm)[23] vs. substrate-supported graphene ($<$ 150 nm).[20]

Ultrafast studies of graphite with structural probes have also been performed. Carbone *et al.*[24] studied the ablation of whole graphene layers from graphite samples photoexcited with an optical density of up to 44.5 mJ cm^{-2} via ultrafast electron diffraction. Their results support the existence of strongly-coupled optical phonon modes, as demonstrated by Kampfrath *et al.*[16] Ultrafast electron diffraction measurements by Chatelain *et al.*[25] also confirm the existence of two strongly-coupled optical modes by observing their coherent generation, indicating that the characteristic energy-transfer time from the hot electron gas is shorter that the phonon period. The dynamics of strongly-coupled optical phonons measured with ultrafast diffraction (electron and X-ray) has been the subject of multiple other studies.[3,26,27,28,29,30,31]

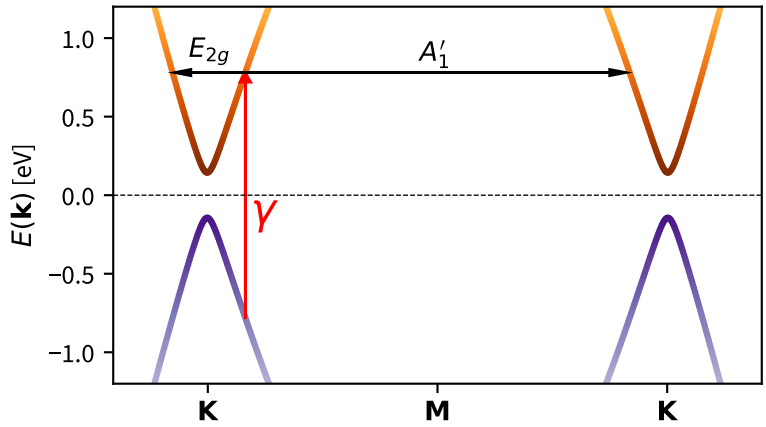

Figure 3.6.: Cut of the electronic dispersion $E(\mathbf{k})$ along the $\mathbf{K}-\mathbf{M}-\mathbf{K}$ line (see Figure 3.3) shows the effects of photoexcitation with 1.55 eV photons (γ). The momentum-conserving decay path are highlighted and explained in the text.

3.1.5. Geometrical interpretation of electron-phonon coupling in photoexcited graphite

Following the findings presented in the previous section, the effects of electron-phonon coupling in graphite after photoexcitation has been explained intuitively by Kampfrath *et al.*[16] The geometric relationship between the electronic structure and the strongly-coupled modes is shown in Figure 3.6. Specifically, it is the Dirac cones that tell us the consequences of photoexcitation with 800 nm light. Photons can only drive vertical (zero-momentum) transitions near the Dirac cones. As the electron cloud thermalizes, two classes of momentum-conserving decay pathways involving phonons emerge. One such pathway allows for an electron to move across the Dirac cone, emitting an E_{2g} phonon with small wavevector $\mathbf{k} \sim \mathbf{0}$. Another pathway allows for an electron to hop onto a neighboring Dirac cone, emitting an A_1' phonon with large wavevector $\mathbf{k} \sim \mathbf{K}$.

3.2. Experimental and computational methods

3.2.1. Sample preparation

Single-crystal flakes of natural graphite 10 nm to 90 nm thick were prepared using a mechanical exfoliation procedure analogous to the work by Novoselov *et al.*,[32] briefly described here. Thick flakes were embedded in Crystalbond glue on a 3 mm copper TEM grid (200 lines per inch). The

embedded flakes are then exfoliated using ordinary adhesive tape. The procedure was repeated until the embedded flakes were translucent when observed under an optical microscope. The glue is then delicately washed away with a solvent. The choice of the solvent is dependent on the glue used; in the present case, acetone was used. Sample thickness has been measured directly using atomic force microscopy characterization. Once a suitable sample has been identified, an aperture was made using aluminum foil to isolate a sample region with uniform thickness. The resulting sample used in this work covered 500 × 500 μm^2, with a thickness of 88 nm measured using an atomic force microscope.

3.2.2. Data acquisition

The ultrafast electron diffuse scattering experiments presented in this chapter made use of the experimental setup presented in Section 1.4. Ultrashort laser pulses of light were shone at $t = t_0$ on an 88 nm-thick single-crystal specimen of graphite, oriented in the $[001]$ direction, at a repetition rate of 1 kHz. Compressed electron bunches with 10^7 electrons per bunch were transmitted through the sample at $t = t_0 + \tau$. The time-delay τ was scanned from −40 ps to 680 ps.

The interrogated film were pumped with a pump spot of 1 × 1 mm^2 full-width at half-maximum, ensuring nearly uniform illumination of the probed volume. The film was pumped at a fluence of 12 mJ cm^{-2}, resulting in an absorbed energy density of 8 J m^{-3}. The scattering patterns are collected with a Gatan Ultrascan 895 camera: a 2.54 × 2.54 cm^2 scintillator fiber-coupled to a 2048 px × 2048 px charge-coupled detector (CCD) placed 25 cm away from the sample. Per-pixel scattering intensity fluctuations over laboratory time reveals a transient dynamic range of 1 : 10^8, allowing the acquisition of diffraction patterns and diffuse scattering patterns simultaneously. A static diffraction pattern is shown in Figure 3.7 a).

Due to the flatness of the Ewald sphere for 90 keV electrons (Section 2.2.5), many symmetry-related reflections are visible within each pattern. The information contained in a set of symmetry-equivalent reflections is redundant due to the point-group symmetry of the scattering crystal. As long as the point-group symmetry is not broken by photoexcitation, it is possible to harness the redundancy to enhance the signal-to-noise ratio of a ultrafast electron diffuse scattering dataset. In the case of graphite, no observable symmetry-breaking phenomena is brought on by photoexcitation at 1.55 eV when looking at the raw data. Moreover, trARPES experiments[21] do not show the opening of a gap in the electronic band structure, albeit at much

lower photoexcitation densities, which would be indicative of point-group symmetry breaking. The point-group of graphite is $6/mmm$, which encompasses six-fold discrete rotational symmetry in the $\mathbf{a}$ – $\mathbf{b}$ plane. Therefore, specifically in the case of graphite oriented in the $[001]$ direction, the diffuse signals can be safely enhanced by a factor of $\sqrt{6}$ by the use of a six-fold discrete azimuthal average:

$$I(\mathbf{q},\tau) \rightarrow \frac{1}{6}\sum_{n=1}^{6} I(\mathbf{R}(\tfrac{\pi n}{3})\cdot\mathbf{q},\tau) \tag{3.6}$$

where $\mathbf{R}(\theta)$ is the in-plane rotation matrix:

$$\mathbf{R}(\theta) = \begin{pmatrix} \cos\theta & -\sin\theta & 0 \\ \sin\theta & \cos\theta & 0 \\ 0 & 0 & 1 \end{pmatrix} \tag{3.7}$$

Throughout the rest of this chapter, "scattering intensity" will imply discrete azimuthal average unless otherwise noted. An example of six-fold averaged diffraction pattern is shown in Figure 3.7 b).

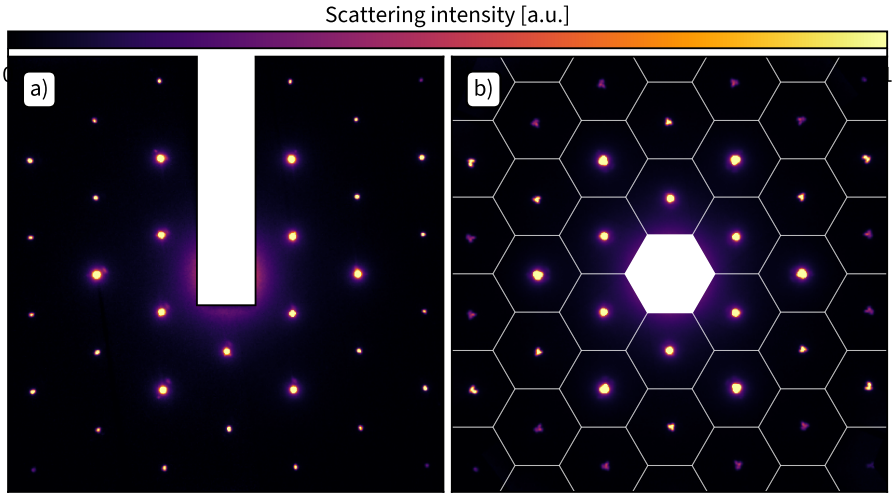

Figure 3.7.: Static diffraction pattern of graphite. **a)** static, unprocessed diffraction pattern. The white bar is used to hide the beam-block which prevents undiffracted electrons from saturating the detector. **b)** Six-fold discrete azimuthal average of the diffraction pattern in a) results in $\sqrt{6}$ increase in signal-to-noise ratio. Brillouin zones are shown around each reflection to guide the eye.

3.2.3. Computational details

This section contains the details of the calculations used throughout this chapter, including what is shown in Figure 3.4. The aim of the computations was to extract the phonon mode frequencies $\{\,\omega_\lambda(\mathbf{k})\,\}$ and polarization vectors $\{\,\mathbf{e}_{\lambda,s}(\mathbf{k})\,\}$ that appear in Equation (2.78).

3.2.3.1. Structure-determination

In order to calculate the force between atoms, the structure of graphite was computed via *structure relaxation*, performed using the plane-wave self-consistent field program PWSCF from the QUANTUM ESPRESSO software suite.[33] The structure was relaxed using a 18 × 18 × 10 $\mathbf{k}$ mesh centered at $\mathbf{\Gamma}$ – selected using the Monkhorst-Pack method[34] – and force and energy thresholds of 1×10^{-8} Ry ${a_0}^{-1}$ and 1×10^{-15} Ry respectively, where a_0 is the Bohr radius. Based on the force constants determined from the relaxed structure, the dynamical matrices were computed on a 5 × 5 × 3 $\mathbf{q}$ mesh using a self-consistency threshold of 1×10^{-18} Ry. The resulting graphite structure is equivalent to Equation (3.1), with $a = 1.231$ Å and $c = 6.837$ Å.

3.2.3.2. Phonon properties

From a structure with zero-temperature atomic positions $\{\,\mathbf{r}_s\,\}$ and instantaneous displacements $\{\,\mathbf{u}_s\,\}$, the potential energy U due to ions repulsion is given by:

$$U = \frac{1}{2}\sum_{s,s'} \mathbf{u}_s \cdot [\mathbf{D}(\mathbf{r}_s - \mathbf{r}_{s'})\,\mathbf{u}_{s'}] \tag{3.8}$$

where the *dynamical matrix* $\mathbf{D}$ encodes the change in potential energy associated with a small change in distance between ions.[35] Given that the displacement vectors $\{\,\mathbf{u}_s\,\}$ can be expressed as a sum of lattice waves (Equation (2.54)), the eigenvalues and eigenvectors of the dynamical matrix are related to vibrational frequencies and polarizations respectively*.

The phonon frequencies $\{\,\omega_\lambda(\mathbf{k})\,\}$ and polarization vectors $\{\,\mathbf{e}_{\lambda,s}(\mathbf{k})\,\}$ associated with the structure calculated in Section 3.2.3.1 were computed using the PHONON program, again within the QUANTUM ESPRESSO software suite. This calculation made use of the B86b exchange-coupled Perdew-Burke-Ernzerhof generalized-gradient approximation[37,38] and the projector augmented-wave method.[39] The cutoff energy of the wave function was set to 100 Ry, while the cutoff energy

*This is an intuitive picture of the dynamical matrix. In practice, diagonalization is usually performed in reciprocal space. For an example, see Al-Jishi and Dresselhaus.[36]

for the charge density was set to 1.2 $\times$ 10^3 Ry. A Fermi-Dirac smearing of 0.06 Ry was also applied. To include the dispersion of energy along the stacking axis $\mathbf{a}_3$, the exchange-hole dipole moment method was used.[40]

3.2.3.3. Clustering of phonon properties into physically-relevant branches

As with most diagonalization procedures, the eigenvalues and eigenvectors of the dynamical matrix are returned in an order that is not physically-relevant. Therefore, in order to determine what are the phonon properties of a phonon mode λ, the phonon properties calculated by PHONON need to be assigned a mode, or *clustered*.

As of writing this, there is no component within the QUANTUM ESPRESSO software suite that can do this. The scheme described in this section was used instead. The general idea behind the procedure is that phonon properties are continuous. Let $P_{\lambda,\mathbf{k}_i}$ be the abstract vector representing phonon properties of mode λ at one of the irreducible $\mathbf{k}$ points $\{\,\mathbf{k}_i\,\}$:

$$P_{\lambda,\mathbf{k}_i} \equiv \begin{bmatrix} \omega_{\lambda,\mathbf{k}_i} & \mathbf{e}_{s=1,\lambda,\mathbf{k}_i} & \cdots & \mathbf{e}_{s=M,\lambda,\mathbf{k}_i} \end{bmatrix}^T \tag{3.9}$$

where the index s runs over all M atoms of the unit cell. Define the metric between two such abstract vectors $\mathbf{P}_{\lambda',\mathbf{k}}$ and $\mathbf{P}_{\lambda,\mathbf{k}'}$ as:

$$\left\|\mathbf{P}_{\lambda',\mathbf{k}} - \mathbf{P}_{\lambda,\mathbf{k}'}\right\| = |\omega_{\lambda',\mathbf{k}} - \omega_{\lambda,\mathbf{k}'}|^2 + \sum_s \left\|\mathbf{e}_{\lambda',s,\mathbf{k}} - \mathbf{e}_{\lambda,s,\mathbf{k}'}\right\| \tag{3.10}$$

A one-dimensional path γ connecting all irreducible points $\{\,\mathbf{k}_i\,\}$ was defined, starting at $\mathbf{\Gamma}$. At $\mathbf{\Gamma}$, polarization vectors are associated with a mode based on geometry. For example, a mode with negligible frequency and polarization vectors that all point in the same direction physically corresponds to a longitudinal acoustic mode. The manual assignment for high-frequency optical modes is a bit more arbitrary. Then, following the path γ, the assignment of phonon branches λ' at $\gamma(\mathbf{k} + \mathbf{\Delta})$ minimizes the quantity $\left\|\mathbf{P}_{\lambda',\mathbf{k}} - \mathbf{P}_{\lambda,\mathbf{k}+\mathbf{\Delta}}\right\|$.

The procedure described above has been adapted for numerical evaluation and is now part of the `scikit-ued` software package,[41] which is described in more details in Appendix A. For the rest of this chapter, it will be assumed that the phonon properties are clustered such that the usual physical phonon branch labels (e.g. TA, LO) are meaningful.

3.3. Diffuse intensity dynamics

The change in scattering intensity $\Delta I(\mathbf{q}, t = \tau) \equiv I(\mathbf{q}, \tau) - I(\mathbf{q}, -\infty)$ for representative time-delays is shown in Figure 3.8.

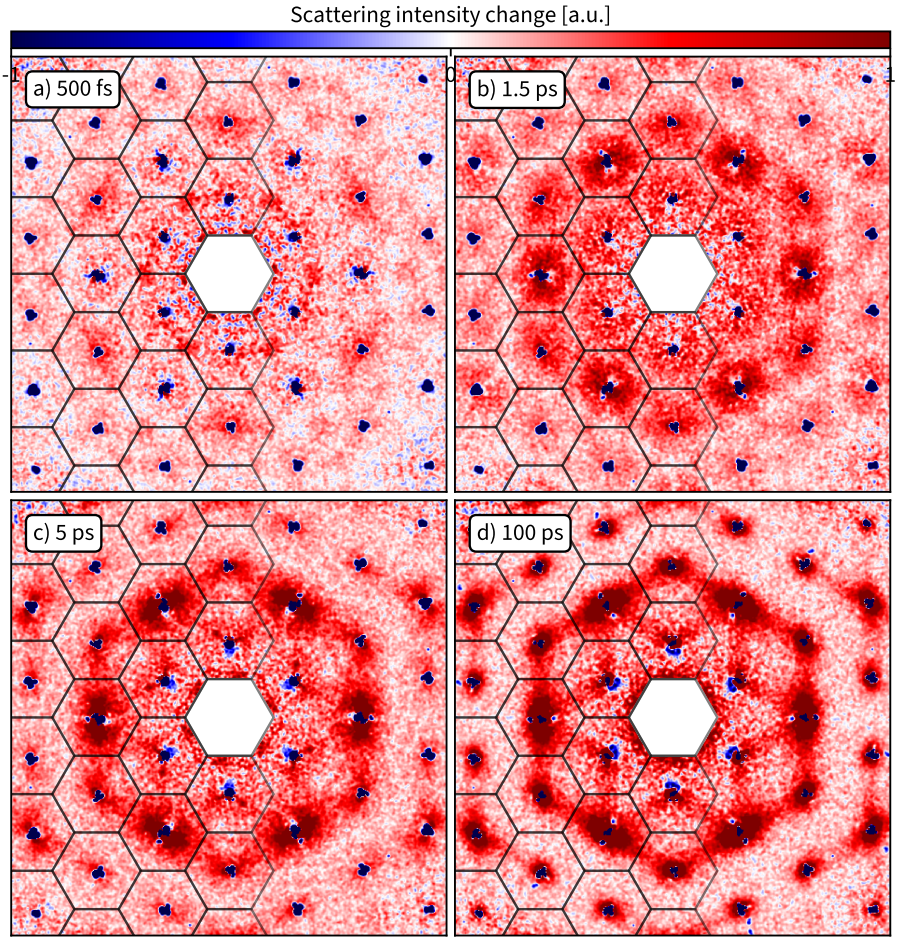

Figure 3.8.: Change in scattering intensity $\Delta I(\mathbf{q}, t = \tau) \equiv I(\mathbf{q}, \tau) - I(\mathbf{q}, \tau < 0)$ of photoexcited graphite for a few representative time-delays τ. Hexagonal Brillouin zones are shown on half of the reflections to guide the eye. Scattering patterns show diffuse scattering in the range of $|\mathbf{q}| < 12\,\text{Å}^{-1}$. Negative going features (blue) are exclusively due to the transient Debye-Waller effect on the Bragg peaks. All positive changes (red) are diffuse scattering intensity.

First and foremost, note that negative-going features are only visible in the vicinity of Bragg peaks. This is due exclusively to the transient Debye-Waller effect.[42] As photodeposited energy

transfers from the electrons to the lattice, average real-space disorder due to phonons lowers the overall periodicity of the lattice, which in turn results in smaller Bragg peaks (Section 2.4). This is analogous to the (static) thermal Debye-Waller effect.[43,44] An example curve for the (200) reflection is shown in Figure 3.9. The dynamics associated with the Bragg peaks in photoexcited graphite are discussed in detail elsewhere.[25,45] This leaves only positive-going features everywhere away from Bragg peaks, which are diffuse in nature.

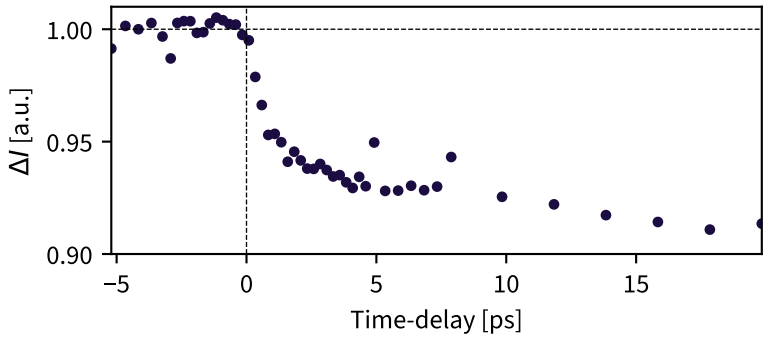

Figure 3.9.: Relative intensity change of the (200) reflection after photoexcitation examplifies the transient Debye-Waller effect.

Second, the structure visible across the Brillouin zone is different for reflections that ought to represent the same physical lattice waves. For example, consider the (010) and (020) reflections, 100 ps after photoexcitation, shown in Figure 3.10. Around (010), diffuse intensity increases near two of the $\mathbf{M}$ points, while diffuse intensity is increasing at two other $\mathbf{M}$ points near (020).

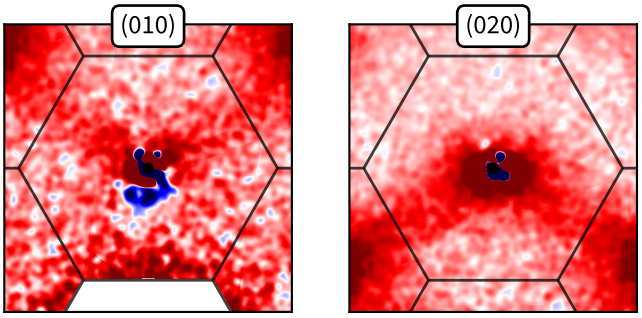

Figure 3.10.: Comparison of the diffuse intensity change after 100 ps for two Brillouin zones, (010) and (020). The colormap scaling is identical to Figure 3.8. The difference between those two images can be explained by the difference in one-phonon structure factors $|F_{1\lambda}(\mathbf{q},\tau)^2|$.

The drastic difference between physically-equivalent reflections can be explained by the difference in the one-phonon structure factors $|F_{1\lambda}(\mathbf{q},\tau)|^2$. Therefore, in order to understand

the scattering patterns presented in Figure 3.8, the one-phonon structure factors need to be computed. This is done in the next section.

3.4. The one-phonon structure factors

Recall the definition of diffuse intensity from Equation (2.78):

$$I_1(\mathbf{q},\tau) = N_c I_e \sum_{\lambda} \frac{n_\lambda(\mathbf{k},\tau) + \frac{1}{2}}{\omega_\lambda(\mathbf{k},\tau)} \left|F_{1\lambda}(\mathbf{q},\tau)\right|^2 \tag{3.11}$$

and

$$F_{1\lambda}(\mathbf{q},\tau) = \sum_{s} e^{-W_s} \frac{f_s(\mathbf{q})}{\sqrt{\mu_s}} \left(\mathbf{q}\cdot\mathbf{e}_{\lambda,s}(\mathbf{k})\right) \tag{3.12}$$

where N_c is the number of scattering unit cells, I_e is the intensity of a single scattering event, s are indices that label atoms in the unit cell, W_s is the Debye-Waller factor associated with atom s, $f_s(\mathbf{q})$ are the atomic form factors, $j \in \{\,1,2,...,12\,\}$ runs over the phonon modes, $\{\,n_\lambda(\mathbf{k},\tau)\,\}$ are the phonon populations, $\{\,\mathbf{e}_{\lambda,s}(\mathbf{k})\,\}$ are the phonon polarization vectors, and $\{\,\omega_\lambda(\mathbf{k},\tau)\,\}$ are the phonon frequencies.

As shown in Figure 3.10, observed diffuse intensity is the combination of quantities that can be separated in two categories. Some quantities, like phonon frequencies, are *local* in reciprocal space (i.e. defined on $\mathbf{k}$). On the other hand, the one-phonon structure factors are *nonlocal* in reciprocal space (defined on $\mathbf{q}$). This results in measurable differences when comparing diffuse intensity at various reflections, which will be used to overcome the energy-integrative nature of ultrafast electron diffuse scattering experiments.

In order to recover mode-dependent phonon populations, one-phonon structure factors need to be calculated for every relevant phonon mode. Most importantly, the phonon polarization vectors $\{\,\mathbf{e}_{\lambda,s}(\mathbf{k})\,\}$ need to be determined. These vectors describe the direction of movement for each atom due to a particular lattice wave. Fortunately, polarization vectors are a byproduct of the calculation of the phonon dispersion relation, shown in Figure 3.4.

3.4.1. Transient Debye-Waller factors

One more quantity needs to be discussed before one-phonon structure factors can be computed: the Debye-Waller factors $W_s(\mathbf{q},\tau)$. The Debye-Waller factors describe the reduction of scattering

intensity at $\mathbf{q}$ due to the effective deformation of the scattering potential of atom s by *all* phonon branches. The general expression for the *anisotropic* Debye-Waller factor for atom s is given by:[46]

$$W_s(\mathbf{q},\tau) = \frac{1}{4\mu_s}\sum_{s,\lambda}|a_\lambda(\mathbf{k},\tau)|^2|\mathbf{q}\cdot\mathbf{e}_{\lambda,s}(\mathbf{k})|^2 \tag{3.13}$$

where a_λ is vibrational amplitude for the phonon mode λ:

$$|a_\lambda(\mathbf{k},\tau)|^2 = \frac{2\hbar}{N_c}\left(\frac{n_\lambda(\mathbf{k},\tau)+\frac{1}{2}}{\omega_\lambda(\mathbf{k},\tau)}\right) \tag{3.14}$$

Based on Equation (3.13), the Debye-Waller factor is not a sensitive measure of the wavevector-dependent nonequilibrium dynamics of lattice waves because it involves the contribution from *all* lattice waves, integrated over $\mathbf{k}$. Therefore, phonon population dynamics can only affect the magnitude of Debye-Waller factors.

The potential time-dependence of the Debye-Waller factors was investigated, via the time-dependence of mode populations. Profoundly non-equilibrium distribution of phonon mode populations were simulated, with all modes populated according to room-temperature average energy except for one mode at high temperature. To account for differences in heat capacities, the maximum temperature for optical modes was 5000 K, while the maximum temperature for acoustic modes was capped at 1500 K. These extreme non-equilibrium scenarios increase the value of $\sum_s W_s(\mathbf{q})$ by at most 1.5% for optical modes, and 8% for acoustic modes. Since those fractional changes are constant across $\mathbf{q}$, wavevector-dependent changes in ultrafast electron diffuse scattering signals are not significantly impacted by changes in the Debye-Waller factors. Any time-dependence of the one-phonon structure factors can be ignored as a first approximation.

3.4.2. One-phonon structure factor calculations

The calculation for the one-phonon structure factors $|F_{1\lambda}(\mathbf{q},\tau)|^2$ was carried out from Equation (2.78). As discussed in the previous section, the dynamics in one-phonon structure factors due to photoexcitation via the change in Debye-Waller factors can be neglected in this work. Therefore, the calculations of this section assume room-temperature thermal distribution of lattice waves; this is implied by time-delay $\tau < 0$ (pre-photoexcitation). The one-phonon structure factors for longitudinal modes LA, LO1 - LO3 are shown Figure 3.11. The one-phonon structure factors for transverse modes TA, TO1 - TO3 are shown Figure 3.12. Out-of-plane modes yield trivial

one-phonon structure factors for all scattering vectors $\mathbf{q}$ probed by the experiments presented herein because $\mathbf{q} \cdot \mathbf{e}_{\lambda,s}(\mathbf{k}) = 0$.

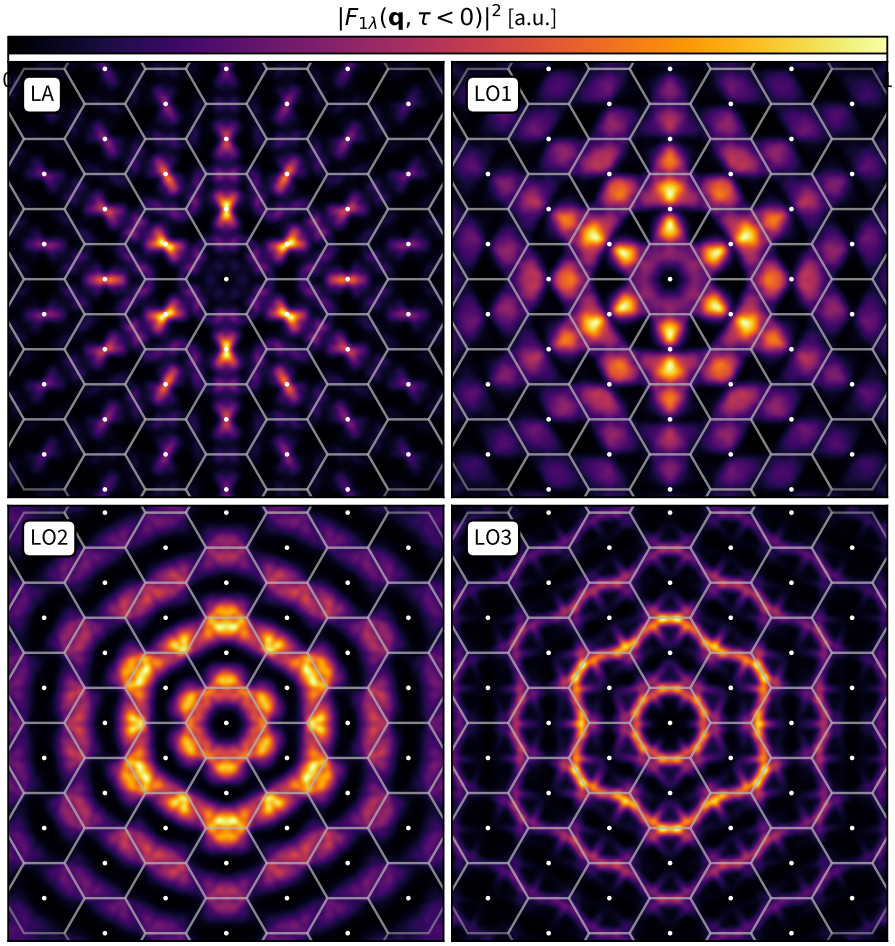

Figure 3.11.: Calculated one-phonon structure factors $|F_{1\lambda}(\mathbf{q}, \tau < 0)|^2$ of in-plane longitudinal modes at 300 K, for scattering vectors $\mathbf{q}$ equivalents to the detector area shown in Figure 3.8. See Figure 3.12 for the transverse modes equivalent.

The one-phonon structure factors display complex structure in reciprocal space. The structure for a particular mode can be thought of as continuous selection rule: regions in $\mathbf{q}$ space where the one-phonon structure factor for mode λ is large are regions where phonon mode λ contributes importantly atomic vibrations in reciprocal space. The structure of $|F_{1\lambda}|^2$ is most determined

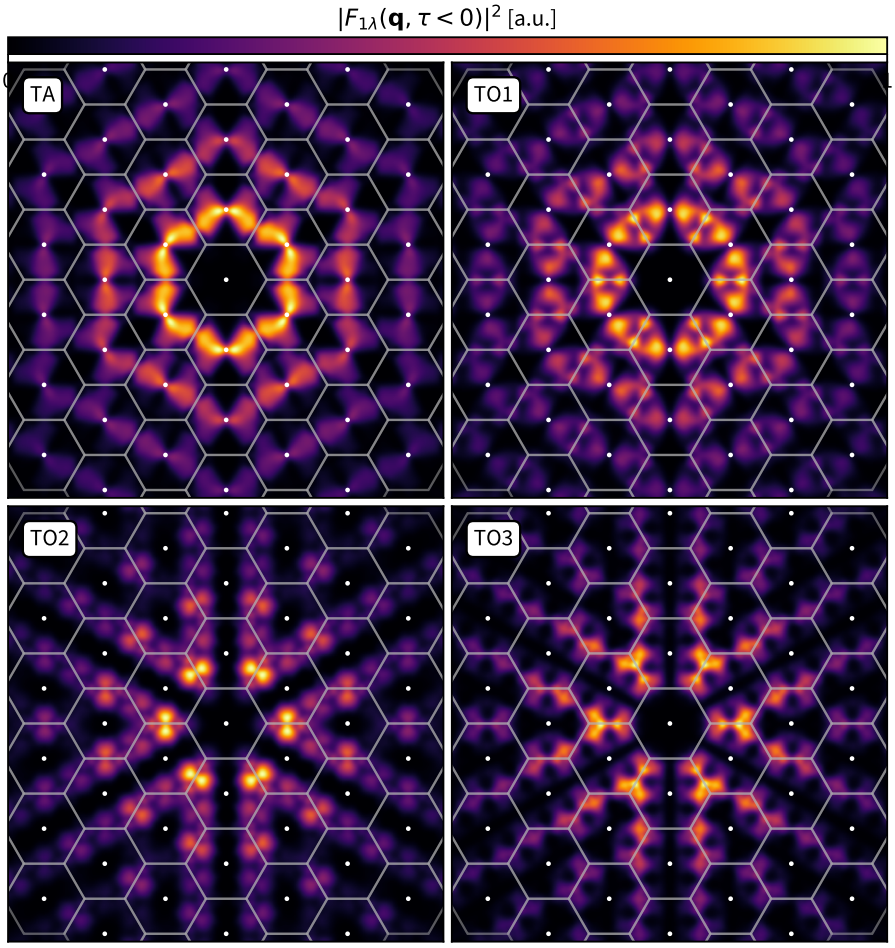

Figure 3.12.: Calculated one-phonon structure factors $|F_{1\lambda}(\mathbf{q}, \tau < 0)|^2$ of in-plane transverse modes at 300 K, for scattering vectors $\mathbf{q}$ equivalents to the detector area shown in Figure 3.8. See Figure 3.11 for the longitudinal modes equivalent.

by the values of terms like $\{\, \mathbf{q} \cdot \mathbf{e}_{\lambda,s}(\mathbf{k}) \,\}$. For acoustic modes LA and TA, the structure of the one-phonon structure factor is easier to understand near $\mathbf{\Gamma}$. For example, $|F_{1\lambda}|^2$ is highest for the LA mode in the radial $\mathbf{q}$ direction because the polarization vectors of those modes are parallel to $\mathbf{q}$; this fact defines longitudinal waves. For transverse waves, where atomic motion is perpendicular to the lattice wave propagation direction, $|F_{1\lambda}|^2$ is higher in the azimuthal direction.

3.4.3. Weighted phonon dispersion

An alternative visualization of one-phonon structure factors are weighted dispersion curves, as shown in Figure 3.13. This way of looking at $|F_{1\lambda}|^2$ clearly highlights the difference across Brillouin zones. For example, the difference $|F_{1\lambda=\mathrm{TA}}|^2 - |F_{1\lambda=\mathrm{LA}}|^2$ is either negative for $\mathbf{q} \approx \mathbf{\Gamma}_{(010)}$ or positive for $\mathbf{q} \approx \mathbf{\Gamma}_{(\bar{1}10)}$, even though the two reflections are adjacent. The variation of $|F_{1\lambda}|^2$ explains the diffuse intensity difference shown in Figure 3.10.

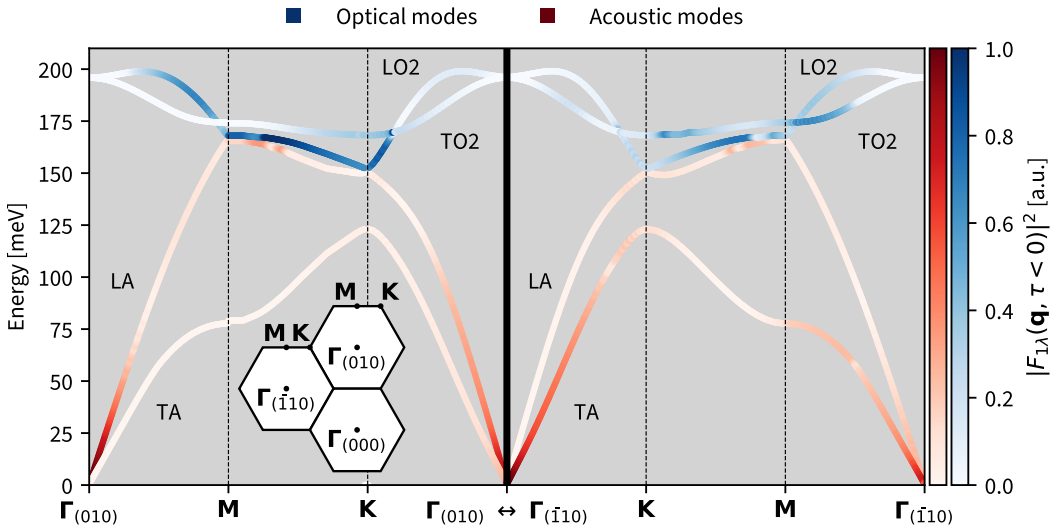

Figure 3.13.: Calculated one-phonon structure factors visualized as weighted dispersion curves for selected in-plane modes. The color saturation of dispersion curves is proportional to $|F_{1\lambda}|^2$ of the associated mode. Equivalent paths in the Brillouin zone around two reflections are shown to highlight the high degree of reciprocal space structure: (010) on the left and $(\bar{1}10)$ on the right. The geometry of the paths with respect to (000) are shown in the inset on the lower left.

By examining Figure 3.13, it appears that at certain locations, the one-phonon structure factor for one phonon mode dominates; for example, $|F_{1\lambda=\mathrm{LA}}|^2$ near $\mathbf{q} \approx \mathbf{\Gamma}_{(010)}$. It might be tempting to attribute the diffuse intensity dynamics at that location exclusively to one mode. If enough

such locations in reciprocal space existed, it would be possible to bypass the energy-insensitivity of ultrafast electron diffuse scattering and extract mode-dependent phonon dynamics at special points in the Brillouin zone; this idea forms the basis of previous work by the author in Stern *et al.*[3] The next section describes how crude this intuition really is.

3.4.4. Relative mode contributions

Are there locations in reciprocal space where the contribution of a particular lattice wave dominates the diffuse intensity? In order to compare the contribution of a particular phonon mode λ on ultrafast electron diffuse scattering data, the following weight can be defined:

$$W_\lambda(\mathbf{q},\tau) \equiv \frac{|F_{1\lambda}(\mathbf{q},\tau)|^2}{\omega_\lambda(\mathbf{k},\tau)} \tag{3.15}$$

With the weight definition of Equation (3.15), the change in diffuse intensity (Equation (2.77)) can be re-written as:

$$\begin{aligned}\Delta I_1(\mathbf{q},\tau) &\equiv I_1(\mathbf{q},\tau) - I_1(\mathbf{q},\tau<0) \\ &= (n_\lambda(\mathbf{q},\tau) + {}^1\!/_2)\, W_\lambda(\mathbf{q},\tau) - (n_\lambda(\mathbf{q},\tau<0) + {}^1\!/_2)\, W_\lambda(\mathbf{q},\tau<0) \\ &\approx [n_\lambda(\mathbf{q},\tau) - n_\lambda(\mathbf{q},\tau<0)]\, W_\lambda(\mathbf{q},\tau<0)\end{aligned} \tag{3.16}$$

In the last line, the quasi-static nature of the one-phonon structure factors $|F_{1\lambda}(\mathbf{q},\tau)|^2 \approx |F_{1\lambda}(\mathbf{q},\tau<0)|^2$ was used, as discussed in Section 3.4.1. The approximation $\omega_\lambda(\mathbf{k},\tau) \approx \omega_\lambda(\mathbf{k},\tau<0)$, valid for $\mathbf{k}$ away from $\mathbf{\Gamma}$, was also used; see Section 3.1.2 for a discussion.

Figure 3.14 shows where, across the reciprocal space area equivalent to Figure 3.8, a single new phonon from a particular branch contributes more than 50% or more than 75% of the diffuse intensity increase. In other words, Figure 3.14 shows where *any* branch λ, with associated weight $W_\lambda(\mathbf{q},\tau<0)$, contributes more than 50% or 75% of the total weight $\sum_\lambda W_\lambda(\mathbf{q},\tau<0)$. The calculation presented in Figure 3.14 is categorical: dynamics in the transient diffuse intensity **cannot** be associated with the dynamics of a single phonon branch. Furthermore, Figure 3.14 shows that at in-plane high symmetry points $\mathbf{K}$ and $\mathbf{M}$, no phonon branch contributes to more than 50% of the associated dynamics in the diffuse intensity.

In order to access the quantitative ultrafast phonon dynamics in a material with ultrafast electron diffuse scattering, a more comprehensive analysis of ultrafast electron diffuse scattering must

be devised – making good use of one-phonon structure factors.

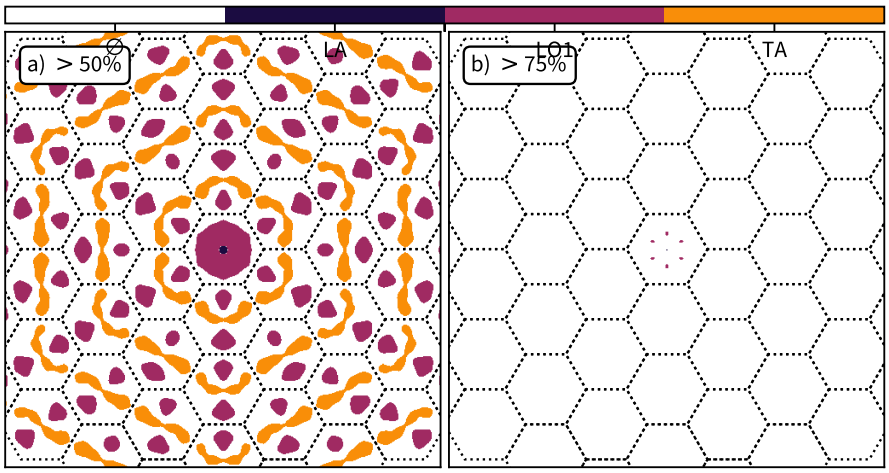

Figure 3.14.: Locations in reciprocal space where a single new phonon from a particular branch contributes to more than **a)** 50% and **b)** 75% of the associated increase in diffuse intensity. $\emptyset$ is used to denote that no phonon mode contributes higher than the threshold.

3.5. Phonon spectroscopy across the Brillouin zone

In this section, the calculation of the one-phonon structure factors will be used to endow ultrafast electron diffuse scattering with energy resolution. An important advantage of ultrafast electron diffuse scattering is that a large number of reflections are simultaneously visible due to the relative flatness of the Ewald sphere (Section 2.2.5). Compared to ultrafast diffuse x-ray scattering,[47,48] which is limited to the study of at most a few reflections, the shortcoming of ultrafast electron scattering – lack of energy-resolution – can be overcome by the redundancy present in the measurements.

Recall that the ultrafast change in diffuse intensity can be expressed as follows:

$$\frac{\Delta I(\mathbf{q},\tau)}{N_c I_e} = \sum_{\lambda} \frac{\Delta n_{\lambda}(\mathbf{k},\tau)}{\omega_{\lambda}(\mathbf{k},\tau<0)} \left|F_{1\lambda}(\mathbf{q},\tau<0)\right|^2 \tag{3.17}$$

Equation (3.17) is approximately valid for $\mathbf{k}$ away from $\mathbf{\Gamma}$ (see Section 3.1.2). Effectively, this restriction is trivial as diffraction peaks drown out the ultrafast electron diffuse scattering signals near $\mathbf{\Gamma}$.

The sum over all phonon branches λ encodes the lack of energy resolution in ultrafast electron diffuse scattering experiments. However, with enough data redundancy, the contribution of every mode λ to Equation (3.17) can be extracted. Let $\{ \mathbf{H}_1, ..., \mathbf{H}_M \}$ be in-plane reflections that are visible in the experiments. Then, the transient phonon population of mode λ, $\Delta n_\lambda(\mathbf{k}, \tau)$, solves the following linear system:

$$\mathbf{I}_\mathbf{k}(\tau) = \mathbf{F}_\mathbf{k}\mathbf{D}_\mathbf{k}(\tau) \tag{3.18}$$

with

$$\mathbf{I}_\mathbf{k}(\tau) = \frac{1}{N_c I_e}\begin{bmatrix}\Delta I(\mathbf{k}+\mathbf{H}_1, t) & ... & \Delta I(\mathbf{k}+\mathbf{H}_M, t)\end{bmatrix}^T \tag{3.19}$$

$$\mathbf{F}_\mathbf{k} = \begin{bmatrix}|F_{11}(\mathbf{k}+\mathbf{H}_1, \tau<0)|^2 & ... & |F_{1N}(\mathbf{k}+\mathbf{H}_1, \tau<0)|^2 \\ \vdots & \ddots & \vdots \\ |F_{11}(\mathbf{k}+\mathbf{H}_M, \tau<0)|^2 & ... & |F_{1N}(\mathbf{k}+\mathbf{H}_M, \tau<0)|^2\end{bmatrix} \tag{3.20}$$

$$\mathbf{D}_\mathbf{k}(\tau) = \begin{bmatrix}\Delta n_1(\mathbf{k}, \tau)/\omega_1(\mathbf{k}, \tau<0) & ... & \Delta n_N(\mathbf{k}, \tau)/\omega_N(\mathbf{k}, \tau<0)\end{bmatrix}^T \tag{3.21}$$

where N runs over the eight in-plane modes. This linear system of equations can be solved numerically provided enough experimental data, i.e. diffuse intensity for at least $M \geq N$ distinct Brillouin zones. Again, this constraint highlights the advantage that ultrafast electron diffuse scattering has over other techniques: the diffuse intensity measured with ultrafast electron diffuse scattering spans a large portion of reciprocal space.

The choice to solve for $\mathbf{D}_\mathbf{k}(\tau)$ rather than $\Delta n_\lambda(\mathbf{k}, \tau)$ directly, comes down to the degree of confidence that should be placed in the approximations that were made to get to Equation (3.17). Phonon polarization vectors are mostly determined by the symmetries of the crystal, which are fixed throughout the experiments. On the other hand, phonon vibrational frequencies in general might be influenced by non-equilibrium carrier and phonon distributions as would be the case with strongly anharmonic crystals (see Chapter 4). Solving for the ratio of phonon population to vibrational frequency is more robust against the weaknesses of this modeling because the one-phonon structure factors only take into account the polarization vectors.

3.5.1. Numerical procedure

The procedure used to numerically solve for $\mathbf{D}_\mathbf{k}(\tau)$ is described henceforth.

All visible Brillouin zones in the measurement were used to generate $\mathbf{I}_{\mathbf{k}}(\tau)$. Since the scattering patterns have been symmetrized (Figure 3.7), one would expect that using the intensity data for reflections related by symmetry would be redundant; however, the following procedure worked better when using the entire area of the detector. This is no doubt due to minute misalignment of the scattering patterns and uncertainty in detector position, which are averaged out when using all available data. The Brillouin zones associated with all in-plane reflections $\{\, \mathbf{H} \mid |\mathbf{H}| \leq 12\,\text{Å}^{-1} \,\}$ were used, for a total of 44 Brillouin zones. Therefore, at every $\mathbf{k}$ point, $\mathbf{I}_{\mathbf{k}}(\tau)$ and $\mathbf{F}_{\mathbf{k}}$ have matrix dimensions of $(44, 1)$ and $(44, 8)$, respectively.

The possible values for elements of $\mathbf{D}_{\mathbf{k}}(\tau)$ were constrained to be non-negative, implying that $\Delta n_{\lambda}(\mathbf{k}, \tau) \geq 0 \; \forall \tau$. In other words, it is assumed that the population of a phonon branch cannot drop below its equilibrium level. While not strictly necessary, it was found to lead to a more stable solution. This constraint allowed for the use of the non-negative approximate matrix inversion algorithm[49] to solve Equation (3.18). This procedure was repeated for every reduced wavevector $\mathbf{k}$ and time-delay $\boldsymbol{\tau}$. Stable solutions were found for $|\mathbf{k}| \geq 0.45\,\text{Å}^{-1}$, away from $\boldsymbol{\Gamma}$ and elastic scattering signals.

It must be emphasized that the numerical solution to $\mathbf{D}_{\mathbf{k}}(\tau)$ is not the result of fitting (iterative least-squares method), but rather a non-iterative approximate matrix inversion based on linear least-squares. The method described in this section admits no free parameter, other than the phonon vibrational frequencies and polarization vectors.

3.5.2. Population dynamics

The numerical solution for Equation (3.18) is shown in Figure 3.15. The transient phonon populations $\{\, \Delta n_{\lambda}(\mathbf{k}, \tau) \,\}$ across the Brillouin zone are shown for three important modes: TO2, TA, and LA.

While previous work by the author discussed the nonthermal phonon dynamics qualitatively,[3] Figure 3.15 allows to quantitatively determine how the energy deposited in the electronic system flows and thermalizes. A discussion of the observed physical processes is presented below.

As discussed in Section 3.1.4, two optical phonons modes are strongly-coupled to the electronic system: A_1' located near the $\mathbf{K}$ point, and E_{2g}, near $\boldsymbol{\Gamma}$. E_{2g} is obscured by the elastic signals near $\boldsymbol{\Gamma}$; however, its dynamics are accessible via ultrafast spectroscopy.[16] On the other hand, A_1' is clearly visible in Figure 3.15. It behaves as expected: a fast early increase in population is seen

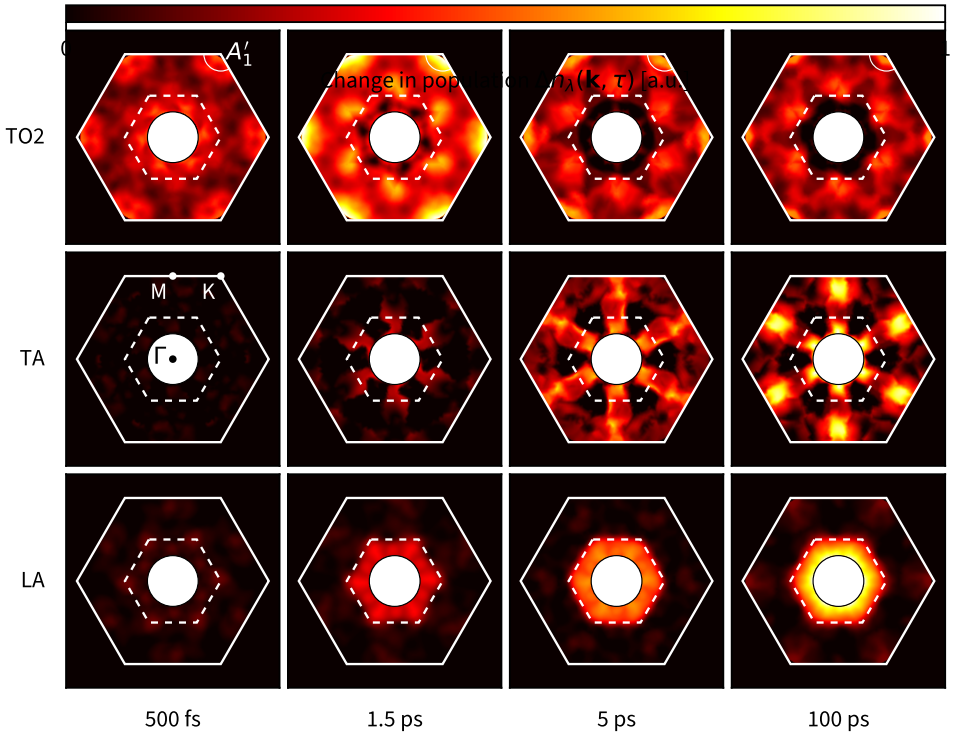

Figure 3.15.: Measurement of the change in transient phonon population $\Delta n_\lambda(\mathbf{k}, \tau)$ following photoexcitation for relevant in-plane modes of graphite across the Brillouin zone. The solution domain is bound by white circle at $|\mathbf{k}| \leq 0.45\,\text{Å}^{-1}$, and by a solid white hexagon at the Brillouin zone edge. The Brillouin zone midpoint is highlighted with a dashed white hexagon. The location of the A_1' mode is shown in the top row.

due to the transfer of energy from the electronic subsystem. By 5 ps, energy has already been transferred away through phonon-phonon coupling.

After a few picoseconds, the strongly-coupled optical modes decay into lower-energy lattice waves. Since one of the primary causes of phonon-phonon scattering is anharmonicity, the decay probabilities are usually computed via density functional perturbation theory calculations.[50] Ultrafast electron diffuse scattering shows an experimental determination of those decay pathways. The transfer of energy from high-energy optical phonons to lower-energy lattice waves must satisfy the conservation of momentum and energy. This restricts the number of possible decay pathways to mid-Brillouin zone phonons, either directly (from E_{2g}) or via Umklapp scattering[51] (from A_1'). Specifically, from 1.5 ps to 100 ps, acoustic phonon population increase is observed

along the $\mathbf{\Gamma} - \mathbf{M}$ line. This measurement is in accordance with predicted anharmonic decay probabilities from the E_{2g} mode.[50] The small increase of population of the LA mode around 500 fs at $\frac{1}{2}\mathbf{K}$ is also a confirmation of predictions by Bonini *et al.*[50]

Over longer time-scales (25 ps), the nonthermal TA population has significantly pooled at $\frac{1}{3}\mathbf{M}$ and $\mathbf{M}$. There are no three-phonon anharmonic decay processes that start in a transverse mode like TA. Allowed *in-plane* interband transitions are of the types L $\rightarrow$ T + T or L $\rightarrow$ L + T, where L and T represent longitudinal and transverse modes respectively.[52,53] It is therefore expected *a priori* that a nonthermal TA population remains until decay to out-of-plane phonon modes occur. Predicted decay probabilities also support this observation; both LA and TA modes will favor decay to out-of-plane modes[54] which are not visible to ultrafast electron diffuse scattering measurements. A special case is visible at $\frac{1}{2}\mathbf{M}$ and $\frac{1}{2}\mathbf{K}$, where predicted anharmonic lifetimes of TA and LA drop significantly due to the activation of Umklapp scattering to out-of-plane acoustic phonons.[54] The measurements of Figure 3.15 corroborate the predictions: energy flow away from TA and LA at the mid-Brillouin zone is fast enough that population never builds up.

The energy flow that follows photoexcitation described in this section is exactly what one would expect from the *hot phonon model*.[22,55] The measured phonon population dynamics are perfectly in line with the simple three-temperature modelling from Stange *et al.*[21] There is no indication in Figure 3.15 that defects allow the scattering of electrons and acoustic phonons, contrary to experiments on substrate-supported graphene described in Section 3.1.4, which would appear as a violation of momentum-conserving decay pathways.

3.5.3. Long-term decay

It is possible to quantify how long the non-equilibrium distribution of lattice waves lasts in graphite. The energy transferred to the sample from photoexcitation, stored in plane in a mode λ, can be expressed as follows:

$$\Delta E_\lambda(\tau) = \int_{\text{BZ}} d\mathbf{k}\, \Delta n_\lambda(\mathbf{k},\tau)\hbar\omega_\lambda(\mathbf{k},\tau) \tag{3.22}$$

where $\int_{\text{BZ}} d\mathbf{k}$ is understood to be the integral over the in-plane section of the Brillouin zone. Using the population measurements $\{\, n_\lambda(\mathbf{k},\tau)\,\}$ presented in Figure 3.15, the mode-dependent relative change in stored energy (in-plane) can be calculated. The results are shown in Figure 3.16.

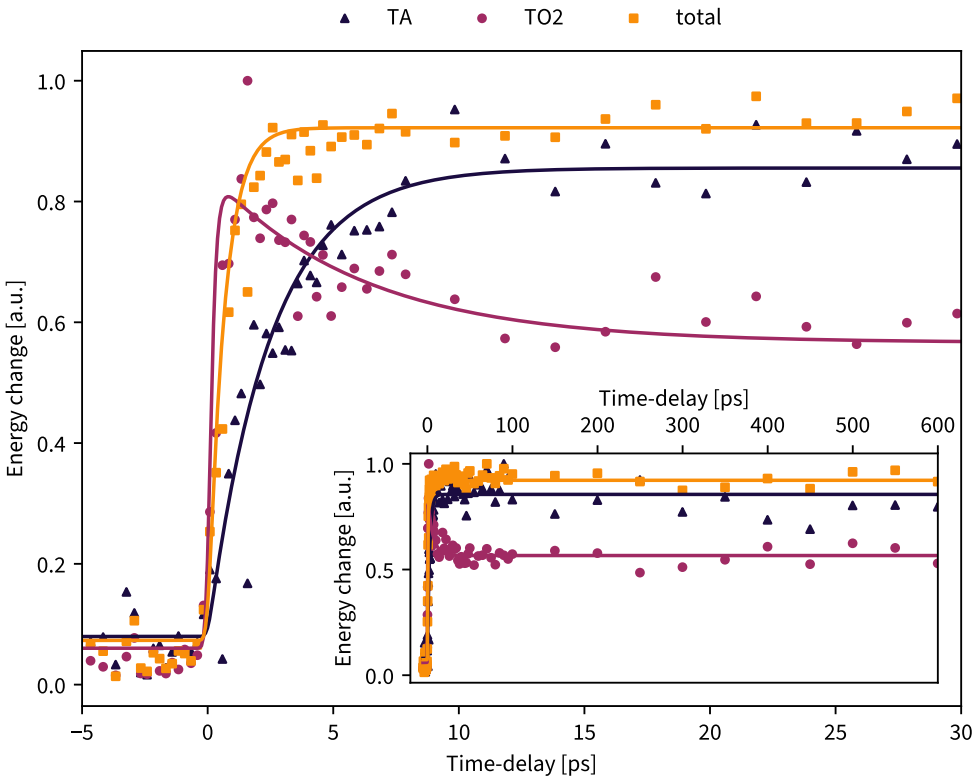

Figure 3.16.: Change in the energy stored in-plane as phonons after photoexcitation. **Inset** long-term trend shows that thermalization with the environment has not yet occurred by 600 ps, which would appear as the total energy change (yellow curve) going back to zero.

The energy trends for modes TA and TO2 are commensurate with the description of Section 3.5.2. The fascinating aspect of this analysis is revealed by looking at the total energy stored in-plane. Even by 600 ps, thermalization of the energy dumped into the sample by photoexcitation with the experimental environment (300 K) has not occurred at all. Note that this figure is not a representation of the thermalization of these modes with each other; there is no expectation of these trends to be equal due to their differing isobaric heat capacities.

3.6. Mode-projected excitation couplings

In this section, the phonon population dynamics will be used to extract the electron-phonon coupling matrix element to the A_1' mode, and compare the value to other measurements and calculations.

The nonequilibrium flow of energy between excitations, both electronic and lattice in nature,

has historically been crudely modelled using the *two-temperature model*.[56] In summary, this model states that while the concept of temperature does not apply to nonequilibrium situations, the energy distribution of the electrons and lattice waves may be treated separately. In other words, the separate thermalization of the electronic and lattice subsystems is much faster than the energy transfer between them. It is evident that such a description does not adequately model experimental results from Section 3.5 for two main reasons. First, the decay of optical phonons to acoustic ones overlaps significantly in time with the transfer of energy from the photoexcited electrons to strongly-coupled optical modes. Second, the energy distribution of lattice waves is far from thermal, even at 100 ps.

Some authors have extended the two-temperature model based on the details of the system being studied.[21] Ultrafast electron diffuse scattering measurements allow to move beyond the two-temperature approximation as the energy distribution of phonons is known across the Brillouin zone. And yet, theory has not caught up with this opportunity. The best way to extract electron-phonon and phonon-phonon couplings is still based on rate-equations. In this section, the extraction of electron-phonon and phonon-phonon couplings from ultrafast electron diffuse scattering measurements will be performed at the $\mathbf{K}$ point, using an extension of the two-temperature model called the *non-thermal lattice model*.[57]

The reader should keep in mind that the procedure presented in this section is a retrofit of the results presented in Section 3.5 into a more conventional framework. This is the best that can be done until theorist seize the opportunity provided by ultrafast electron diffuse scattering measurements.

3.6.1. The non-thermal lattice model

The non-thermal lattice model is an extension of the two-temperature model, with the added flexibility that lattice waves need not be thermalized.[57] It assumes that the energy distribution of each phonon mode admits a thermal description; that is, the energy transfer between phonons of different branches is slower than the scattering of phonons from the same branch. Within this framework, each phonon branch λ can be assigned its own molar heat capacity, $C_{ph,\lambda}$, and

temperature, $T_{ph,\lambda}$:

$$\left\{ \begin{array}{rcl} C_e(T_e)\frac{\partial T_e}{\partial \tau} & = & \sum_\lambda G_{ep,\lambda}\left[T_e(\tau) - T_{ph,\lambda}(\tau)\right] + f(\tau) \\ \\ C_{ph,\lambda}(T_{ph,\lambda})\frac{\partial T_{ph,\lambda}}{\partial \tau} & = & \sum_{\lambda' \neq \lambda} G_{ep,\lambda'}\left[T_e(\tau) - T_{ph,\lambda'}(\tau)\right] \\ & + & G_{pp,\lambda\lambda'}\left[T_{ph,\lambda}(\tau) - T_{ph,\lambda'}(\tau)\right] \end{array} \right\}_{\lambda=1}^{N} \tag{3.23}$$

where $f(\tau)$ is the laser pulse profile, and C_e and T_e are the electronic heat capacity and electron temperature, respectively. As discussed in Section 3.1.4, the use of an electronic temperature is acceptable for $\tau > 100$ fs, in the case of photoexcited graphite specifically. The constants $G_{ep,\lambda}$ describe the rate of energy flow between the electrons and phonon mode λ, while constants $G_{pp,\lambda\lambda'}$ encode the rate of energy flow between phonon modes λ and λ'.

A small clarification is needed. A coupling constant G describes the rate of energy transfer from one excitation type to another, if the temperature of one unit of volume was increase by 1 K. This is *not* directly equivalent to the electron-phonon coupling tensor g introduced in Section 1.1.4, but it is a helpful intermediate experimental quantity. The relationship between G and g is developed further below in Section 3.6.4.

Observations of transient phonon populations are more general than mode temperatures. However, in order to make use of the non-thermal lattice model, the mode temperature can be related to transient phonon mode populations via the Bose-Einstein distribution:[58]

$$n_\lambda(\mathbf{k},\tau) \propto \left[\exp\left(\frac{\hbar\omega_\lambda(\mathbf{k},\tau<0)}{k_B T_{ph,\lambda}(\tau)}\right) - 1\right]^{-1} \tag{3.24}$$

The expression for $n_\lambda(\mathbf{k},\tau)$ makes use of the approximation that phonon vibrational frequencies remain constant through the experiments ($\omega_\lambda(\mathbf{k},\tau) \approx \omega_\lambda(\mathbf{k},\tau<0)\ \forall\tau$), as discussed in Section 3.4.1, which is approximately true in the case of graphite away from $\mathbf{\Gamma}$. Equation (3.24) can be decomposed with a Laurent series[59] to extract the quasi-linear relationship between mode population and temperature:

$$n_\lambda(\mathbf{k},\tau) \propto \frac{k_B T_{ph,\lambda}(\tau)}{\hbar\omega_\lambda(\mathbf{k},\tau<0)} - 1/2 + \mathcal{O}\left(T_{ph,\lambda}^{-1}(\tau)\right) \tag{3.25}$$

The above holds for appropriately-high mode temperatures. It follows that $\Delta n_\lambda \propto \Delta T_{ph,\lambda}$:

$$\Delta n_\lambda(\mathbf{k},\tau) \propto \frac{k_B \Delta T_{ph,\lambda}(\tau)}{\hbar\omega_\lambda(\mathbf{k},\tau<0)} \tag{3.26}$$

3.6.2. The non-thermal lattice model at the K point

Based on the formalism presented in the Section 3.6.1, the couplings to the A_1' phonon mode will be extracted from the TO2 population measurements as an example. Let the differential population be $\Delta n_{\lambda=\text{TO2}}(\mathbf{k}=\mathbf{K},\tau) \equiv \Delta n_{A_1'}(\tau)$. $\Delta n_{A_1'}(\tau)$ is obtained by integrating the population of the TO2 mode in a circular arc of radius 0.3 Å^{-1} centered at $\mathbf{k}=\mathbf{K}$, as shown in Figure 3.15.

The number of coupled equations in Equation (3.23) can be reduced by aggregating lattice heat capacities into two categories: the heat capacity of A_1', $C_{A_1'}$, and the total effective heat capacity of all other relevant modes, defined as C_l. The calculation of C_l boils down to adding the contribution of mode that can scatter into A_1' or from it, based on conservation of energy and momentum, weighted by the decay probabilities reported by Bonini *et al.*[50] With this information:

$$\begin{aligned} C_l = &\frac{9}{100}\left[C_{ph,\lambda=\text{TA}} + C_{ph,\lambda=\text{TA}}\right] \\ &+ \frac{36}{100}\left[C_{ph,\lambda=\text{TA}} + C_{ph,\lambda=\text{LA}}\right] \\ &+ \frac{55}{100}\left[C_{ph,\lambda=\text{TA}} + C_{ph,\lambda=\text{LA}} + C_{ph,\lambda=\text{LO}} + C_{ph,\lambda=\text{LA}}\right] \end{aligned} \tag{3.27}$$

The system of equations from Section 3.6.1 can then be expressed as three equations: the flow of energy in and out of the electronic system, the A_1' mode, and all other modes coupled to the A_1' mode:

$$\left\{\begin{array}{rcl} C_e(T_e)\frac{\partial T_e}{\partial \tau} &=& f(\tau) \\ &-& G_{e,A_1'}\left[T_e(\tau) - T_{A_1'}(\tau)\right] \\ &-& G_{e,l}\left[T_e(\tau) - T_l(\tau)\right] \\ \\ C_{A_1'}(T_{A_1'})\frac{\partial T_{A_1'}}{\partial \tau} &=& G_{e,A_1'}\left[T_e(\tau) - T_{A_1'}(\tau)\right] \\ &-& G_{A_1',l}\left[T_{A_1'}(\tau) - T_l(\tau)\right] \\ \\ C_l(T_l)\frac{\partial T_l}{\partial \tau} &=& G_{e,l}\left[T_e(\tau) - T_l(\tau)\right] \\ &+& G_{A_1',l}\left[T_{A_1'}(\tau) - T_l(\tau)\right] \end{array}\right\} \tag{3.28}$$

3.6.2.1. Heat capacities

Before Equation (3.28) can be solved, the heat capacities of the electronic system and every relevant phonon mode must be parametrized. The electronic heat capacity is extracted from

Table 3.1.: Coupling strength between electronic system, the A_1' phonon, and the lattice system. Uncertainty is derived from fit covariances.

	Coupling strength [W m^{-3} K^{-1}]
$G_{e,A_1'}$	$(6.8 \pm 0.3) \times 10^{17}$
$G_{A_1',l}$	$(8.0 \pm 0.5) \times 10^{17}$
$G_{e,l}$	$(0.0 \pm 6.0) \times 10^{15}$

measurements by Nihira and Iwata:[60]

$$C_e(T_e) = 13.8\, T_e(\tau) + 1.16 \times 10^{-3}\, T_e^2(\tau) + 2.6 \times 10^{-7}\, T_e^3(\tau) \tag{3.29}$$

Extracting the lattice specific heat is simplified by the observation that thermal expansion has not occurred on the time-scale of the measurements ($\tau < 680$ ps). Bragg peak positions remain static throughout the measurement, as was also reported by Chatelain *et al.*[25] The specific heat capacity of each mode can therefore be taken as the heat capacity at constant volume:

$$C_{ph,\lambda}(T_{ph,\lambda}) = k_B \int_0^{\omega_D} d\omega\, D_\lambda(\omega) \left(\frac{\hbar\omega}{k_B T_{ph,\lambda}}\right)^2 \frac{e^{\hbar\omega/k_B T_{ph,\lambda}}}{\left(e^{\hbar\omega/k_B T_{ph,\lambda}} - 1\right)^2} \tag{3.30}$$

where ω_D is the Debye frequency, and $D_\lambda(\omega)$ is the density of states for phonon mode λ.[61] The momentum-resolution of ultrafast electron diffuse scattering allows for a simplification: a single frequency contributes to the density of states, so that $D_\lambda(\omega) \equiv \delta(\omega)$.

3.6.3. Heat rates

The solution to Equation (3.28) using the measurements of the A_1' population was computed using an iterative least-squares method.[62] The resulting temperature traces $\{\, T_e(\tau), T_{A_1'}(\tau), T_l(\tau) \,\}$ are shown in Figure 3.17. The coupling constants $\{\, G_{e,l}, G_{e,A_1'}, G_{A_1',l} \,\}$ are listed in Table 3.1

3.6.4. Mode-projected electron-phonon coupling tensor elements

In order to compare to theory and other experiments, the value of electron-phonon coupling g is calculated from the coupling constants G determined from solving Equation (3.28). Refer to Section 1.1.4 for an introduction to the electron-phonon coupling tensor.

Photoexcitation with 1.55 eV photons will drive vertical electronic transitions, many of which

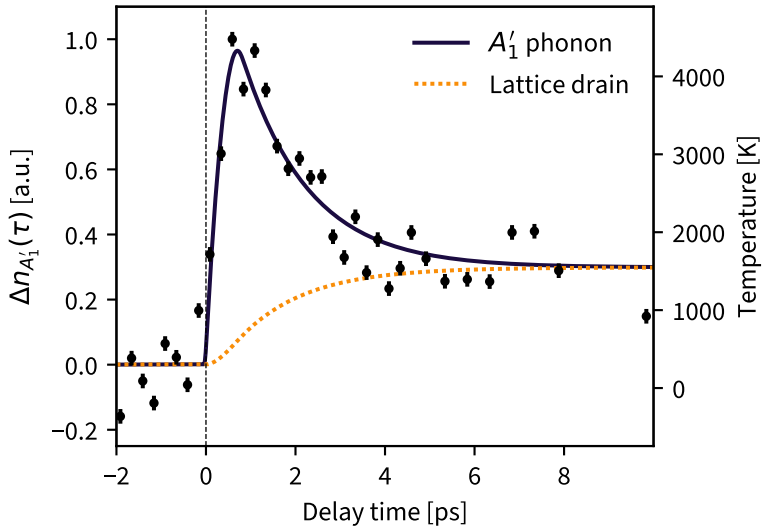

Figure 3.17.: Evolution of the A_1' mode population in graphite after ultrafast photoexcitation. Transient population $\Delta n_{A_1'}(\tau)$ is shown in black (circles). Error bars represent the standard error in the population mean before photoexcitation $\tau < 0$. The biexponential fit to the transient population is shown in blue (solid). The effective temperature of the modes that A_1' can decay into is shown in orange (dotted).

might couple to a particular phonon mode. Let $\langle\cdots\rangle_\gamma$ be the average over all photoexcited electron states. The average electron-phonon coupling $\langle g^2_{e,\lambda}(\mathbf{k})\rangle_\gamma$ is most simply related to the relaxation time $\tau_{e,\lambda}(\mathbf{k})$ between the two subsystems:[63,64]

$$\frac{1}{\tau_{e,\lambda}(\mathbf{k})} = \frac{2\pi}{\hbar}\langle g^2_{e,\lambda}(\mathbf{k})\rangle_\gamma D_e(\hbar\omega_\gamma - \hbar\omega_\lambda(\mathbf{k})) \tag{3.31}$$

where $D_e(\epsilon)$ is the electronic density-of-states, $\hbar\omega_\gamma$ is the optical excitation energy (1.55 eV in the case of 800 nm light), and $\omega_\lambda(\mathbf{k})$ is the vibrational frequency of phonon mode λ at wavevector $\mathbf{k}$, as defined previously.

The scattering rate in terms of heat rate constant G is simply given by the conversion factor between energy and particle number, the heat capacity:[60]

$$\tau_{e,A_1'} = \frac{G_{e,A_1'}}{C_e} \tag{3.32}$$

with associated error σ_τ related to the error in the heat rate σ_G:[65]

$$\sigma_\tau = \left|\frac{\partial\tau}{\partial G}\right|\sigma_G = \frac{C_e}{G^2_{e,A_1'}}\sigma_G \tag{3.33}$$

Table 3.2.: Comparison of measured and calculated values for the electron-phonon coupling matrix element $\langle g^2_{e,A'_1} \rangle_\gamma$

Source	$\langle g^2_{e,A'_1} \rangle_\gamma$ [eV^2]	Notes
This work,	0.032 ± 0.001	Experiment
Piscanec *et al.*[15]	< 0.0994	Theory (graphene, upper bound)
Johannsen *et al.*[17]	0.033 ± 0.007	Experiment (trARPES, graphene)
Na *et al.*[64]	0.050 ± 0.011	Experiment (trARPES)
	0.040	Theory

Using the coupling constant G_{e,A'_1} and electronic heat capacity from Section 3.6.3, $\tau_{e,A'_1} = 99 \pm 1$ fs. Since the electronic heat capacity is highly dependent on temperature, the maximum value of the electronic temperature after photoexcitation was used (8500 K according to the solution to Equation (3.28)).

In order to calculate the average electron-phonon coupling matrix element from the scattering rate, the electronic density-of-states needs to be approximated. Given the nature of the experiments presented here, as shown on Figure 3.6, an approximation to the electronic density of states for graphite close to the Dirac point can be used:[6,7]

$$D_e(\epsilon) = \frac{2A}{\pi} \frac{|\epsilon|}{(\hbar v_F)^2} \tag{3.34}$$

where A is the in-plane unit cell area and $v_F = 9.06 \times 10^5$ m s^{-1} is the Fermi velocity[†]. Combining this form the the density-of-states with the measurement of the scattering rate in Equation (3.31) gives $\langle g^2_{e,A'_1} \rangle_\gamma = 0.032 \pm 0.001$ eV^2. This value compares favourably to calculations and experiments from other works, summarized in Table 3.2.

3.7. Conclusion

In this chapter, a clear demonstration of the power of ultrafast electron diffuse scattering was presented. Harnessing the inherent redundancy of electron scattering patterns and prior knowledge of the crystal symmetry, ultrafast electron diffuse scattering measurements were endowed with energy resolution, resulting in a time-, energy-, and momentum-resolved view of phonon dynamics. The measurements were used to understand nonthermal phonon population dynamics. Finally, the phonon population dynamics at the $\mathbf{K}$ point was retrofitted into the non-thermal lat-

[†]Note that the factor of $\hbar$ has been erroneously ignored by Castro Neto *et al.*[7]

tice model in order to extract mode-dependent electron-phonon and phonon-phonon coupling matrix elements, which were in good agreement with other experiments and calculations.

3.7.1. Outlook

The procedure to extract phonon populations in Section 3.5 can be easily extended to other situations. One such situation is the case of thermal diffuse scattering measurements. At constant temperature, the phonon populations are directly related to their vibrational frequency; hence, the phonon band structure could be extracted. Phonon dispersion relations has been extracted before from x-ray diffuse scattering experiments,[46,66] but these schemes are based on iterative (and unstable) fitting procedures. Using electron diffuse scattering instead presents some advantages, namely the inherently stronger scattering cross-section of electrons – which might be the only way to observe diffuse scattering in monoyalers[67] – and the relative commodity of electron microscopes, and the ability to directly invert the measurements matrix without fitting. Another situation where the method presented here can be extended is for the case of non-thermal phonon renormalization. For very early time-delays (say, $\tau < 300$ fs), the phonon populations may be considered somewhat constant. The dynamics effect on ultrafast electron diffuse scattering signals may be attributed to phonon renormalization, i.e. a change in vibrational frequency. In this case, the change $\Delta\omega_\lambda(\mathbf{k}, \tau)$ can be extracted while keeping the phonon populations fixed. This has been used by the author in the case of photoexcited titanium diselenide, where a change in electronic correlations can change the dielectric screening, thereby hardening a particular phonon mode.[13]

References

1 J. D. Bernal and W. L. Bragg. *The structure of graphite*. *Proceedings of the Royal Society of London A* **106** no. 740 (1924), pp. 749–773. DOI: 10.1098/rspa.1924.0101.

2 F. Tuinstra and J. L. Koenig. *Raman spectrum of graphite*. *The Journal of Chemical Physics* **53** no. 3 (1970), pp. 1126–1130. DOI: 10.1063/1.1674108.

3 M. J Stern, L. P. René de Cotret, M. R. Otto, R. P. Chatelain, J.-P. Boisvert, M. Sutton, and B. J. Siwick. *Mapping momentum-dependent electron-phonon coupling and nonequilibrium phonon dynamics with ultrafast electron diffuse scattering*. *Physical Review B* **97** no. 16 (2018), p. 165416. DOI: 10.1103/physrevb.97.165416.

[4] P. R. Wallace. *The band theory of graphite*. *Physical Review* **71** no. 9 (1947), p. 622. DOI: 10.1103/physrev.71.622.

[5] J. C. Slonczewski and P. R. Weiss. *Band structure of graphite*. *Physical Review* **109** no. 2 (1958), pp. 272–279. DOI: 10.1103/physrev.109.272.

[6] B. Partoens and F. M. Peeters. *From graphene to graphite: electronic structure around the K point*. *Physical Review B* **74** no. 7 (2006). DOI: 10.1103/physrevb.74.075404.

[7] A. H. Castro-Neto, F. Guinea, N. M. R. Peres, K. S. Novoselov, and A. K. Geim. *The electronic properties of graphene*. *Reviews of Modern Physics* **81** no. 1 (2009), p. 109. DOI: 10.1103/revmodphys.81.109.

[8] K. S. Novoselov, A. K. Geim, S. V. Morozov, D. Jiang, M. I. Katsnelson, I. Grigorieva, S. V. Dubonos, Firsov, and A. A. Firsov. *Two-dimensional gas of massless Dirac fermions in graphene*. *Nature* **438** no. 7065 (2005), pp. 197–200. DOI: 10.1038/nature04233.

[9] S. Y. Zhou, G.-H. Gweon, J. Graf, A. V. Fedorov, C. D. Spataru, R. D. Diehl, Y. Kopelevich, D.-H. Lee, S. G. Louie, and A. Lanzara. *First direct observation of Dirac fermions in graphite*. *Nature Physics* **2** no. 9 (2006), pp. 595–599. DOI: 10.1038/nphys393.

[10] W. Kohn. *Image of the Fermi surface in the vibration spectrum of a metal*. *Physical Review Letters* **2** no. 9 (1959), p. 393. DOI: 10.1103/physrevlett.2.393.

[11] P. M. Williams, G. S. Parry, and C. B. Scrub. *Diffraction evidence for the Kohn anomaly in 1T-TaS_2*. *The Philosophical Magazine: A Journal of Theoretical Experimental and Applied Physics* **29** no. 3 (1974), pp. 695–699. DOI: 10.1080/14786437408213248.

[12] M. D. Johannes and I. I. Mazin. *Fermi surface nesting and the origin of charge density waves in metals*. *Physical Review B* **77** no. 16 (2008), pp. 165135–165143. DOI: 10.1103/physrevb.77.165135.

[13] M. R. Otto, J.-H. Pöhls, L. P. René de Cotret, M. J. Stern, M. Sutton, and B. J. Siwick. *Mechanisms of electron-phonon coupling unraveled in momentum and time: the case of soft phonons in $TiSe_2$*. *Science Advances* **7** no. 20 (2021). DOI: 10.1126/sciadv.abf2810.

[14] J. Maultzsch, S. Reich, C. Thomsen, H. Requardt, and P. Ordejón. *Phonon dispersion in graphite*. *Physical Review Letters* **92** no. 7 (2004), pp. 075501–075505. DOI: 10.1103/physrevlett.92.075501.

[15] S. Piscanec, M. Lazzeri, F. Mauri, A. C. Ferrari, and J. Robertson. *Kohn anomalies and electron-phonon interactions in graphite*. *Physical Review Letters* **93** no. 18 (2004), pp. 185503–185507. DOI: 10.1103/physrevlett.93.185503.

[16] T. Kampfrath, L. Perfetti, F. Schapper, C. Frischkorn, and M. Wolf. *Strongly coupled optical phonons in the ultrafast dynamics of the electronic energy and current relaxation in graphite*. *Physical Review Letters* **95** no. 18 (2005), p. 187403. DOI: 10.1103/physrevlett.95.187403.

[17] J. C. Johannsen, S. Ulstrup, F. Cilento, A. Crepaldi, M. Zacchigna, C. Cacho, I. C. E. Turcu, E. Springate, F. Fromm, C. Raidel, T. Seyller, F. Parmigiani, M. Grioni, and P. Hofmann. *Direct view of hot carrier dynamics in graphene*. *Physical Review Letters* **111** no. 2 (2013), p. 027403. DOI: 10.1103/physrevlett.111.027403.

[18] M. Breusing, C. Ropers, and T. Elsaesser. *Ultrafast Carrier Dynamics in Graphite*. *Physical Review Letters* **102** no. 8 (2009). DOI: 10.1103/physrevlett.102.086809.

[19] J. C. W. Song, M. Y. Reizer, and L. S. Levitov. *Disorder-assisted electron-phonon scattering and cooling pathways in graphene*. *Physical Review Letters* **109** no. 10 (2012), p. 106602. DOI: 10.1103/physrevlett.109.106602.

[20] A. C. Betz, S. H. Jhang, E. Pallecchi, R. Ferreira, G. Fève, J.-M. Berroir, and B. Plaçais. *Supercollision cooling in undoped graphene*. *Nature Physics* **9** no. 2 (2013), pp. 109–112. DOI: 10.1038/nphys2494.

[21] A. Stange, C. Sohrt, L. X. Yang, G. Rohde, K. Janssen, P. Hein, L.-P. Oloff, K. Hanff, K. Rossnagel, and M. Bauer. *Hot electron cooling in graphite: supercollision versus hot phonon decay*. *Physical Review B* **92** no. 18 (2015), p. 184303. DOI: 10.1103/physrevb.92.184303.

[22] H. Yan, D. Song, K. F. Mak, I. Chatzakis, J. Maultzsch, and T. F. Heinz. *Time-resolved Raman spectroscopy of optical phonons in graphite: phonon anharmonic coupling and anomalous stiffening*. *Physical Review B* **80** no. 12 (2009), p. 121403. DOI: 10.1103/physrevb.80.121403.

[23] N. García, P. Esquinazi, J. Barzola-Quiquia, B. Ming, and D. Spoddig. *Transition from Ohmic to ballistic transport in oriented graphite: measurements and numerical simulations*. *Physical Review B* **78** no. 3 (2008), p. 035413. DOI: 10.1103/physrevb.78.035413.

[24] F. Carbone, P. Baum, P. Rudolf, and A. H. Zewail. *Structural preablation dynamics of graphite observed by ultrafast electron crystallography*. *Physical Review Letters* **100** no. 3 (2008), p. 035501. DOI: 10.1103/physrevlett.100.035501.

[25] R. P. Chatelain, V. R. Morrison, B. L. M. Klarenaar, and B. J. Siwick. *Coherent and incoherent electron-phonon coupling in graphite observed with radio-frequency compressed ultrafast electron diffraction*. *Physical Review Letters* **113** no. 23 (2014), p. 235502. DOI: 10.1103/physrevlett.113.235502.

[26] R. K. Raman, Y. Murooka, C.-Y. Ruan, T. Yang, S. Berber, and D. Tománek. *Direct observation of optically induced transient structures in graphite using ultrafast electron crystallography*. *Physical Review Letters* **101** no. 7 (2008), p. 077401. DOI: 10.1103/physrevlett.101.077401.

[27] S. Schäfer, W. Liang, and A. H. Zewail. *Primary structural dynamics in graphite*. *New Journal of Physics* **13** no. 6 (2011), p. 063030. DOI: 10.1088/1367-2630/13/6/063030.

[28] M. W. Van Mourik, W. J. Engelen, E. J. D. Vredenbregt, and O. J. Luiten. *Ultrafast electron diffraction using an ultracold source*. *Structural Dynamics* **1** no. 3 (2014), p. 034302. DOI: 10.1063/1.4882074.

[29] W. Liang, G. M. Vanacore, and A. H. Zewail. *Observing (non)linear lattice dynamics in graphite by ultrafast Kikuchi diffraction*. *Proceedings of the National Academy of Sciences* **111** no. 15 (2014), pp. 5491–5496. DOI: 10.1073/pnas.1404101111.

[30] T. G. White, N. J. Hartley, B. Borm, B. J. B. Crowley, J. W. O Harris, D. C. Hochhaus, T. Kaempfer, K. Li, P. Neumayer, L. K. Pattison, F. Pfeifer, S. Richardson, A. P. L. Robinson, I. Uschmann, and G. Gregori. *Electron-Ion Equilibration in Ultrafast Heated Graphite*. *Physical Review Letters* **112** no. 14 (2014). DOI: 10.1103/physrevlett.112.145005.

[31] M. Harb, H. Enquist, A. Jurgilaitis, F. T. Tuyakova, A. N. Obraztsov, and J. Larsson. *Phonon-phonon interactions in photoexcited graphite studied by ultrafast electron diffraction*. *Physical Review B* **93** no. 10 (2016), pp. 104104–104111. DOI: 10.1103/physrevb.93.104104.

[32] K. S. Novoselov, A. K. Geim, S. V. Morozov, D. Jiang, Y. Zhang, S. V. Dubonos, I. V. Grigorieva, and A. A. Firsov. *Electric field effect in atomically thin carbon films*. *Science* **306** no. 5696 (2004), pp. 666–669. DOI: 10.1126/science.1102896.

[33] P. Giannozzi, O. Andreussi, T. Brumme, O. Bunau, M. B. Nardelli, M. Calandra, R. Car, C. Cavazzoni, D. Ceresoli, M. Cococcioni, N. Colonna, I. Carnimeo, A. Dal Corso, S. de Gironcoli, P. Delugas, R. A. DiStasio, A. Ferretti, A. Floris, G. Fratesi, G. Fugallo, R. Gebauer, U. Gerstmann, F. Giustino, T. Gorni, J. Jia, M. Kawamura, H.-Y. Ko, A. Kokalj, E. Küçükbenli, M. Lazzeri, M. Marsili, N. Marzari, F. Mauri, N. L. Nguyen, H.-V. Nguyen, A. Otero-de-la-Roza, L. Paulatto, S. Poncé, D. Rocca, R. Sabatini, B. Santra, M. Schlipf, A. P. Seitsonen, A. Smogunov, I. Timrov, T. Thonhauser, P. Umari, N. Vast, X. Wu, and S. Baroni. *Advanced capabilities for materials*

modelling with Quantum ESPRESSO. *Journal of Physics: Condensed Matter* **29** no. 46 (2017), p. 465901. DOI: 10.1088/1361-648x/aa8f79.

[34] H. J. Monkhorst and J. D. Pack. *Special points for Brillouin-zone integrations*. *Physical Review B* **13** no. 12 (1976), p. 5188. DOI: 10.1103/physrevb.13.5188.

[35] N. W. Ashcroft and N. D. Mermin. In: *Solid state physics*. Holt, Rinehart and Winston, 1976. Chap. 22. ISBN: 0030839939.

[36] R. Al-Jishi and G. Dresselhaus. *Lattice-dynamical model for graphite*. *Physical Review B* **26** no. 8 (1982), pp. 4514–4522. DOI: 10.1103/physrevb.26.4514.

[37] A. D. Becke. *On the large-gradient behavior of the density functional exchange energy*. *The Journal of Chemical Physics* **85** no. 12 (1986), pp. 7184–7187. DOI: 10.1063/1.451353.

[38] J. P. Perdew, K. Burke, and M. Ernzerhof. *Generalized gradient approximation made simple*. *Physical Review Letters* **77** no. 18 (1996), p. 3865. DOI: 10.1103/physrevlett.77.3865.

[39] P. E. Blöchl. *Projector augmented-wave method*. *Physical Review B* **50** no. 24 (1994), p. 17953. DOI: 10.1103/physrevb.50.17953.

[40] A. D. Becke and E. R. Johnson. *Exchange-hole dipole moment and the dispersion interaction revisited*. *The Journal of Chemical Physics* **127** no. 15 (2007), p. 154108. DOI: 10.1063/1.2139668.

[41] L. P. René de Cotret, M. R. Otto, M. J. Stern, and B. J. Siwick. *An open-source software ecosystem for the interactive exploration of ultrafast electron scattering data*. *Advanced Structural and Chemical Imaging* **4** no. 1 (2018), p. 11. DOI: 10.1186/s40679-018-0060-y.

[42] M. Ligges, I. Rajkovic, P. Zhou, O. Posth, C. Hassel, G. Dumpich, and D. Von Der Linde. *Observation of ultrafast lattice heating using time resolved electron diffraction*. *Applied Physics Letters* **94** no. 10 (2009), p. 101910. DOI: 10.1557/proc-1230-mm03-08.

[43] P. Debye. *Interferenz von röntgenstrahlen und wärmebewegung*. *Annalen der Physik* **348** no. 1 (1913), pp. 49–92. DOI: 10.1002/andp.19133480105.

[44] I. Waller. *Zur frage der einwirkung der wärmebewegung auf die interferenz von röntgenstrahlen*. *Zeitschrift für Physik* **17** no. 1 (1923), pp. 398–408. DOI: 10.1007/bf01328696.

[45] R. Chatelain. *Radio-frequency pulse compression for high-brightness ultrafast electron diffraction: design, characterization and application*. PhD thesis. McGill University, 2014.

[46] R. Xu and T. C. Chiang. *Determination of phonon dispersion relations by x-ray thermal diffuse scattering*. *Zeitschrift für Kristallographie* **220** no. 12 (2005), pp. 1009–1016. DOI: 10.1524/zkri.2005.220.12_2005.1009.

[47] S. Wall, S. Yang, L. Vidas, M. Chollet, J. M. Glownia, M. Kozina, T. Katayama, T. Henighan, M. Jiang, T. A Miller, D. A. Reis, L. A. Boatnes, O. Delaire, and M. Trigo. *Ultrafast disordering of vanadium dimers in photoexcited VO_2*. *Science* **362** no. 6414 (2018), pp. 572–576. DOI: 10.1126/science.aau3873.

[48] S. W. Teitelbaum, T. Henighan, Y. Huang, H. Liu, M. P. Jiang, D. Zhu, M. Chollet, T. Sato, É. D. Murray, S. Fahy, S. O'Mahony, T. P. Bailey, C. Uher, M. Trigo, and D. A. Reis. *Direct measurement of anharmonic decay channels of a coherent phonon*. *Physical Review Letters* **121** no. 12 (2018), p. 125901. DOI: 10.1103/physrevlett.121.125901.

[49] C. L. Lawson and R. J. Hanson. In: *Solving least squares problems*. Society for Industrial and Applied Mathematics, 1995. Chap. 23.

[50] N. Bonini, M. Lazzeri, N. Marzari, and F. Mauri. *Phonon anharmonicities in graphite and graphene*. *Physical Review Letters* **99** no. 17 (2007), p. 176802. DOI: 10.1103/physrevlett.99.176802.

[51] R. Peierls. *Zur kinetischen Theorie der Wärmeleitung in Kristallen*. *Annalen der Physik* **395** no. 8 (1929), pp. 1055–1101. DOI: 10.1002/andp.19293950803.

[52] M. Lax, P. Hu, and V. Narayanamurti. *Spontaneous phonon decay selection rule: N and U processes*. *Physical Review B* **23** no. 6 (1981), p. 3095. DOI: 10.1103/physrevb.23.3095.

[53] A. Khitun and K. L. Wang. *Modification of the three-phonon Umklapp process in a quantum wire*. *Applied Physics Letters* **79** no. 6 (2001), pp. 851–853. DOI: 10.1063/1.1391230.

[54] L. Paulatto, F. Mauri, and M. Lazzeri. *Anharmonic properties from a generalized third-order* ab initio *approach: theory and applications to graphite and graphene*. *Physical Review B* **87** no. 21 (2013), p. 214303. DOI: 10.1103/physrevb.87.214303.

[55] M. Scheuch, T. Kampfrath, M. Wolf, K. Von Volkmann, C. Frischkorn, and L. Perfetti. *Temperature dependence of ultrafast phonon dynamics in graphite*. *Applied Physics Letters* **99** no. 21 (2011), p. 211908. DOI: 10.1063/1.3663867.

[56] P. B. Allen. *Theory of thermal relaxation of electrons in metals*. *Physical Review Letters* **59** no. 13 (1987), p. 1460. DOI: 10.1103/physrevlett.59.1460.

[57] L. Waldecker, R. Bertoni, R. Ernstorfer, and J. Vorberger. *Electron-phonon coupling and energy flow in a simple metal beyond the two-temperature approximation*. *Physical Review X* **6** no. 2 (2016), p. 021003. DOI: 10.1103/physrevx.6.021003.

[58] S. N. Bose. *Plancks gesetz und lichtquantenhypothese*. *Zeitschrift für Physik* **26** (1924), pp. 178–181. DOI: 10.1007/bf01327326.

[59] A. D. Wunsch. In: *Complex variables with applications*. Addison-Wesley, 2005. Chap. 5.

[60] T. Nihira and T. Iwata. *Temperature dependence of lattice vibrations and analysis of the specific heat of graphite*. *Physical Review B* **68** no. 13 (2003), p. 134305. DOI: 10.1103/physrevb.68.134305.

[61] J. M. Ziman. In: *Principles of the theory of solids*. Cambridge University Press, 1979. Chap. 2.

[62] M. A. Branch, T. F. Coleman, and Y. Li. *A subspace, interior, and conjugate gradient method for large-scale bound-constrained minimization problems*. *SIAM Journal on Scientific Computing* **21** no. 1 (1999), pp. 1–23. DOI: 10.1137/s1064827595289108.

[63] M. Sentef, A. F. Kemper, B. Moritz, J. K. Freericks, Z.-X. Shen, and T. P. Devereaux. *Examining Electron-Boson Coupling Using Time-Resolved Spectroscopy*. *Physical Review X* **3** no. 4 (2013), pp. 041033–041044. DOI: 10.1103/physrevx.3.041033.

[64] M. Na, A. K. Mills, F. Boschini, M. Michiardi, B. Nosarzewski, R. P. Day, E. Razzoli, A. Sheyerman, M. Schneider, G. Levy, S. Zhdanovich, T. P. Devereaux, A. F. Kemper, D. J. Jones, and A. Damascelli. *Direct determination of mode-projected electron-phonon coupling in the time domain*. *Science* **366** no. 6470 (2019), pp. 1231–1236. DOI: 10.1126/science.aaw1662.

[65] P. R. Bevington and D. K. Robinson. *Error analysis*. In: *Data reduction and error analysis*. McGraw-Hill, New York, 2003. Chap. 3.

[66] M. Holt, Z. Wu, H. Hong, P. Zschack, P. Jemian, J. Tischler, H. Chen, and T. C. Chiang. *Determination of phonon dispersions from x-ray transmission scattering: the example of silicon*. *Physical Review Letters* **83** no. 16 (1999), p. 3317. DOI: 10.1103/physrevlett.84.3733.

[67] F. Caruso. *Nonequilibrium lattice dynamics in monolayer MoS_2*. *The Journal of Physical Chemistry Letters* **12** no. 6 (2021), pp. 1734–1740. DOI: 10.1021/acs.jpclett.0c03616.

4. Dynamic polaron formation in the thermoelectric tin selenide

Ultrafast electron scattering is an ideal tool in the study of materials and systems in which charge carrier-lattice interations are complex. Examples of such systems are charge-density wave materials like 1T-$TaSe_2$[1,2] and 1T-$TiSe_2$,[3,4] where the electron density can morph into a periodic structure which might or might not be commensurate with the lattice periodicity. Thermoelectric materials are another class of systems where the charge carriers and the lattice are out-of-sync in some ways.[5] In such materials, a thermal gradient also generates an electrical current due to discrepancy between the electrical and thermal conductivities.

Thermoelectric materials are of broad interest because can be used to harvest waste heat and transform this energy into useable electrical power.[6,7,8] The Perseverance rover, which has just landed at this time of writing, uses thermoelectrics as the main power source by converting the heat generated by the natural radioactive decay of plutonium dioxide.[9] The combination of thermal and electrical properties that make a good thermoelectric material is not found in nature; efficient thermoelectrics must be engineered. It will be described later that the relevant parameters that can be controlled by materials scientist are all interdependent, which makes the optimization of thermoelectrics an arduous task.

Ultrafast methodologies in general have the ability to disentangle couplings between excitations by distinguishing relaxation time-scales. What may appear intrinsic at equilibrium might be revealed as a complex interplay in ultrafast measurements. And yet, ultrafast methodologies have rarely been applied to thermoelectric materials. For example, no one has been able to challenge experimentally the notion that thermoelectric materials cannot display strong electron-phonon coupling.[10] This presents an opportunity to revolutionize the understanding of thermoelectrics which has only seen incremental progress in the past fifteen years.

In this chapter, the author seeks to understand one of the most performant thermoelectric

materials, SnSe. The fundamental determinants of thermoelectricity are first discussed, followed by a description of the electronic and lattice properties of SnSe. After, the experimental ultrafast electron diffraction and diffuse scattering results are presented. Finally, the experimental results are modelled as bimodal polaron formation, which help to explain the special properties of SnSe as a thermoelectric material.

4.1. The determinants of thermoelectric performance

The performance of a thermoelectric material is measured via the figure-of-merit ZT:

$$ZT = S^2 \frac{\sigma}{\kappa_e + \kappa_l} T \tag{4.1}$$

where S is the Seebeck coefficient, σ is the electrical conductivity, κ_e and κ_l are the thermal conductivities for the charge carriers and the lattice respectively, and $\mathbf{T}$ is the absolute temperature.[11] ZT is an important figure of merit because it is used to describe the efficiency of a thermoelectric module. Consider a device with a cold side at temperature T_C, and a hot side at temperature T_H. The heat harvesting efficiency is given by:

$$\eta = \frac{T_H - T_C}{T_H} \left(\frac{\sqrt{1 + ZT_{avg}} - 1}{\sqrt{1 + ZT_{avg}} + \frac{T_C}{T_H}} \right) \tag{4.2}$$

where $T_{avg} = {}^{(T_C + T_H)}/_2$ is the average device temperature, and ${}^{(T_H - T_C)}/_{T_H}$ is understood to be the Carnot efficiency.[7,12] The value of η for an abstract device with a given ZT is shown in Figure 4.1, which illustrates that good efficiency ($> 20\%$) at reasonable temperatures (< 600 K) requires a high ZT (> 4).

4.1.1. The Seebeck coefficient

The Seebeck coefficient is a measure of how much voltage can be induced by a temperature gradient, usually expressed in units of μV K^{-1}. It is negative (positive) for n-type (p-type) semiconductors. The Seebeck coefficient for a few elements are listed in Table 4.1. The Seebeck coefficient is highest for Selenium and Tellurium, while being vanishingly small for good conductors such as Gold and Platinum.

For a solid that is well-described by parabolic electronic bands, the Seebeck coefficient can be

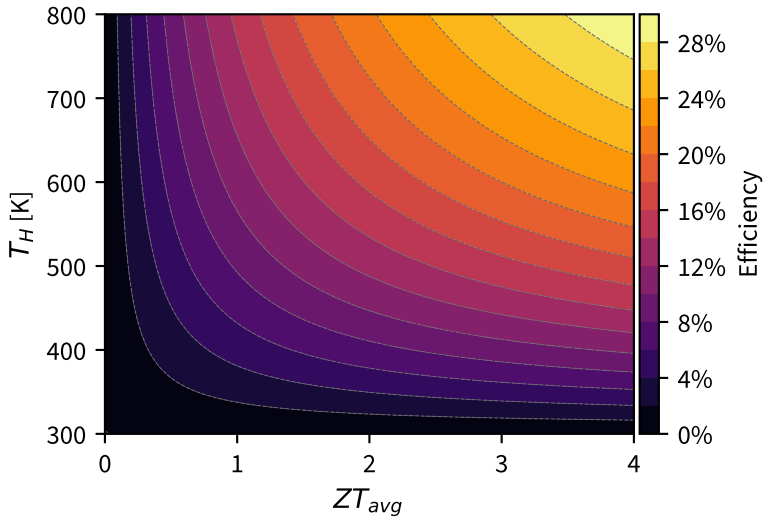

Figure 4.1.: Efficiency of an abstract thermoelectric device harvesting energy from an interface at temperature T_H and attached to a cold size at $T_C = 300$ K. ZT_{avg} is the thermoelectric figure-of-merit at the average device temperature.

Table 4.1.: Seebeck coefficients for a few selected elements.[13]

Element	Seebeck Coefficient [μV K^{-1}]
Selenium	895
Tellurium	495
Silicon	435
Gold	1.5
Platinum	-5
Bismuth	-67

expressed as:[14]

$$S = -\frac{k_B}{e}\left(\frac{5F_{3/2}(\bar{\mu})}{3F_{1/2}(\bar{\mu})} - \bar{\mu}\right) \tag{4.3}$$

where k_B is Boltzmann's constant, e is the quantum of charge, $\bar{\mu} = \mu/k_BT$ is the reduced chemical potential (relative to the edge of the conduction band), and F_i is the Fermi-Dirac function defined as:

$$F_i(\bar{\mu}) = \int_0^\infty dx \frac{x^i}{e^{x-\bar{\mu}}+1} \tag{4.4}$$

The above equation makes it clear that the Seebeck coefficient is largely determined by the value of the reduced chemical potential, and thus is mostly sensitive to doping.[15]

4.1.2. Electronic transport

The thermoelectric figure-of-merit (Equation (4.1)) is directly proportional to the DC electrical conductivity σ. For a given material, the conductivity can be improved via charge-carrier doping,[13,16] which is also known to negatively affect the Seebeck coefficient.[7,17,18] Therefore, the improvement of the term $S^2\sigma$ via charge-carrier doping reaches a maximum at some optimum carrier concentration,[16] which limits the overall potential for thermoelectric performance gains.

There is another complication related to targeted improvements in DC conductivity. Increasing the electrical conductivity of any material also necessarily increases the electronic contribution of the thermal conductivity. In fact, the electronic contribution to the thermal conductivity is directly proportional to the DC electrical conductivity, a phenomenon known as the *Wiedemann-Franz* law.[19]

4.1.3. Dimensionality-reduction

On the more practical, device-driven side of things, the thermoelectric figure-of-merit can be dramatically improved via nanostructuring. In two seminal papers, Hicks and Dresselhaus[15,20] described the desireable effects of dimensionality reduction (nanosheets and quantum wires) on the both $S^2\sigma$ and κ_l. With respect to electronic transport, quantum confinement pseudo-discretizes the electronic density-of-states;[21] with the appropriate doping, the power factor* $S^2\sigma$ can be dramatically improved.[22] Nanostructuring also reduces the lattice thermal conductivity. The reduction in phonon mean-free-path at interfaces is appreciable,[23,24] and this is no different in nanostructured devices.[25]

However, the maximum performance of nanostructured thermoelectrics – while enhanced – is still limited by the intrinsic thermoelectric performance of the underlying bulk material. There are also concerns regarding the longevity of nanostructured devices.[26]

4.1.4. Lattice thermal conductivity

The last major thermoelectric tuning parameter is the lattice thermal conductivity, which has been historically considered essentially independent from electronic structure changes in most of

*The term power factor is an unfortunate misnomer, as it does not relate to energy flow over time. It is used here for historical coherence.

the litterature on thermoelectrics. The canonical way to alter the lattice heat transport properties from a given compound is to introduce defects via solid solutions.[27]

Which bulk compounds should be used as a starting point for further performance improvements? From the point-of-view of low lattice thermal conductivity, the ideal material has been called a *phonon glass–electron crystal*.[28] The prototypical phonon glass–electron crystal is a low-symmetry material with heavy atoms that are somewhat free to vibrate, resulting in an intrisically-low thermal conductivity (phonon glass), but with high-enough electron mobility (electron crystal). Well-known phonon glass–electron crystals include Bi_2Se_3 Hicks and Dresselhaus [15], PbTe,[29] and more recently SnSe.[30] The phonon glass-electron crystal concept also applies to the light-harvesting lead-halide perovskites.[31]

4.2. Tin selenide

Tin selenide (SnSe) is a layered mono-chalcogen which has attracted attention in the past few years because of its very high thermoelectric figure of merit ZT, especially at high temperature, as reported by Zhao *et al.*[30] and others.[32,33] While the exact value of this figure of merit is debated,[34] SnSe remains one of the most promising bulk thermoelectric materials[†]. The axis-projected ZT based on the work by Zhao *et al.*[30] is shown in Figure 4.2, along with the Seebeck coefficient and lattice thermal conductivity. SnSe is interesting not only from a scientific standpoint but also from a practical one, because it is lead-free and composed of earth-abundant elements. SnSe has also been suggested as an air-stable alternative to black phosphorus in real-world applications.[36,37,38,39]

SnSe's high thermoelectric efficiency is thought to be primarily due to an anomalously-low lattice thermal conductivity, especially in-plane. At room temperature, $\kappa_l \sim 1\,\mathrm{W\,m^{-1}\,K^{-1}}$ and it decreases further at higher temperatures.[30] The quasi-two-dimensional nature of SnSe is also a natural confinement of the charge carriers and provides a mechanism through which phonons are scattered, in line with the proposals by Hicks and Dresselhaus.[15] Single-crystal tin selenide at ambient pressure is found in two related phases, both of which are layered:[40] the low-temperature $Pnma$ phase (space group number 62) and the high-temperature $Cmcm$ phase (space group number 63). The in-plane thermoelectric figure-of-merit increases dramatically

[†]Work by Wei *et al.*[35] has shown that in fully-dense SnSe single crystals, the maximum value for ZT is reduced to < 1 at 800 K.

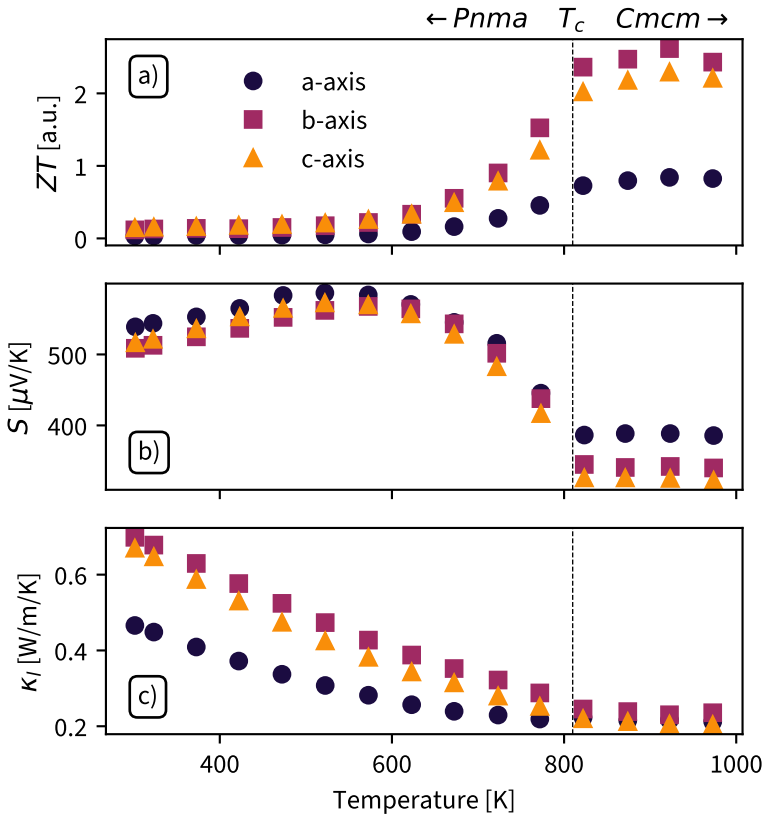

Figure 4.2.: Thermoelectric performance characteristic of SnSe along all three crystallographic axes. **a)** Thermoelectric figure-of-merit ZT. **b)** Seebeck coefficient S. **c)** Lattice thermal conductivity κ_l.

near the transition temperature between the two phases, T_c, and is maximized in the high-temperature $Cmcm$ phase.

The $Cmcm$ phase is a better thermoelectric for three reasons. First, it has a smaller band gap (0.4 eV) compared to the $Pnma$ phase (0.6 eV) which results in an increased carrier concentration. Second, $Cmcm$ exhibits higher carrier mobilities than the $Pnma$ phase.[30] Finally, the lattice thermal conductivity is also low in the $Cmcm$ phase. Together, these properties make $Cmcm$ the better thermoelectric form of SnSe.

4.2.1. Lattice instability and zone-center soft modes

In the high-temperature $Cmcm$ phase, the lattice is stabilized by two soft, anharmonically-coupled phonon modes: an optical mode at $\mathbf{\Gamma}$ polarized along the stacking axis $\mathbf{a}$ and an acoustic mode polarized in the $\mathbf{b}$–$\mathbf{c}$ plane at $\mathbf{Y}$.[41,42] The in-plane section of the Brillouin zone is shown in

Figure 4.3 for context. When cooling towards the phase transition temperature T_c, both modes freeze, which reduces the Brillouin zone volume as every $\mathbf{Y}$ point in the $Cmcm$ phase becomes zone-center in the $Pnma$ phase. Below T_c, the two anharmonically-coupled modes of the $Cmcm$ phase combine into a single soft mode called A_g, which is polarized mostly along the $\mathbf{c}$ axis with a small component along the stacking axis $\mathbf{a}$. This A_g soft mode in the $Pnma$ phase hardens when cooling away from T_c.[40,43]

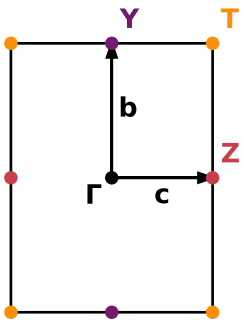

Figure 4.3.: In-plane section of the Brillouin zone of SnSe.

There are actually many soft-modes with characteristics similar to the lowest energy A_g mode that soften towards the phase transition; A_g simply happens to be the lowest-energy one, and therefore freezes at the phase transition. Work by Gong *et al.*[44] and others[45] has shown the temperature-dependence of multiple modes. Of interest is the B_g mode (14 meV at 300 K), which is also polarized along the $Pnma$ lattice distortion just like the A_g mode, but displays one of the most pronounced temperature-dependence across multiple two-dimensional systems such as black phosphorus, monolayer and few-layers MoS_2, and graphene.

4.2.2. Electronic structure

The electronic structure of SnSe is also of interest. The in-plane electronic dispersion at room temperature based on calculations[35,46,47] is shown in Figure 4.4. The valence band of SnSe is primarily composed of Se-$4p$ orbitals, while the conduction band is primarily composed of Sn-$5p$ orbitals.[42,46,48,49] Moreover, different valence and conduction pockets in momentum space correspond to particular p-orbital polarizations.[46] SnSe is a p-type semiconductor with an indirect band gap in the $Pnma$ phase, and a direct band gap in the $Cmcm$ phase. In the $Pnma$ phase in particular, the valence band maximum and conduction band minimum are located near the $\mathbf{Z}$ and $\mathbf{Y}$ points, respectively.[47] The shape of the valence band maximum near $\mathbf{Z}$ – known as

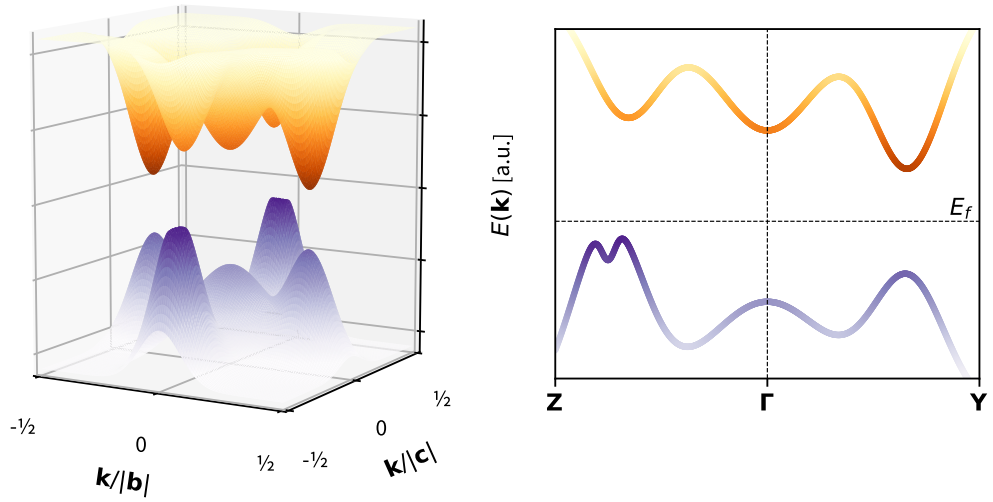

Figure 4.4.: Qualitative diagram of the in-plane electronic dispersion $E(\mathbf{k})$ for tin selenide at room temperature.

"pudding mold" shape – is thought to strongly improve the power factor $S^2\sigma$.[50]

Interestingly, the *nature* of the band gap is strongly-dependent on the in-plane lattice parameters. Towards T_c, the $\mathbf{a}$ and $\mathbf{b}$ axes expand, while the $\mathbf{c}$ axis contracts towards the length of the $\mathbf{b}$ axis.[40] At 300 K, the conduction band minimum is located at $\frac{2}{3}Y$ and is composed of Sn-$5p_y$ orbitals. At 600 K, the conduction band minimum switches to a pocket of Sn-$5p_x$ at $\mathbf{\Gamma}$.[35] The valence band maximum for the $Pnma$ phase remains near $\mathbf{Z}$ across the temperature range and is composed of Se-$4p_z$ orbitals[‡]. Above the phase transition temperature T_c, the valence band minimum moves to the $\mathbf{\Gamma}$ point, and thus the band gap becomes direct.

4.2.3. Structural parameters

The low-temperature $Pnma$ phase is defined by the lattice vectors $\mathbf{a} = a\,\mathbf{e}_1$, $\mathbf{b} = b\,\mathbf{e}_2$, and $\mathbf{c} = c\,\mathbf{e}_3$ where $a = 11.42$ Å, $b = 4.19$ Å, and $c = 4.46$ Å. The vectors $\{\,\mathbf{e}_i\,\}$ are understood to be

[‡]The orbital make-up of the electronic bands is known thanks to work by Cuong *et al.*,[46] but note that their lattice parameters swap the $\mathbf{b}$ and $\mathbf{c}$ axes compared to work by all other papers referenced in this chapter.

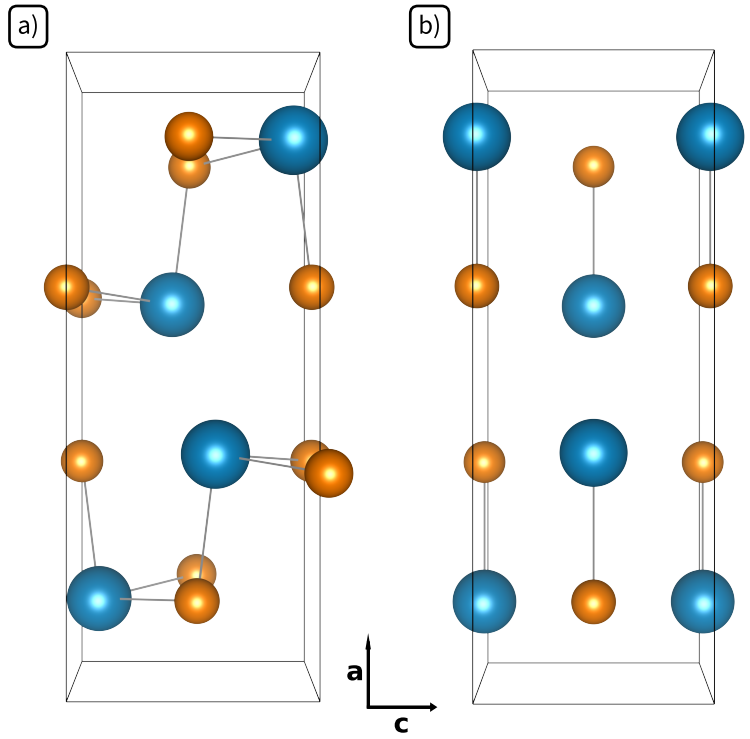

Figure 4.5.: Atomic structure for two phases of SnSe. **a)** $Pnma$ (low-temperature) phase. **b)** $Cmcm$ (high-temperature) phase.

the usual Euclidean vectors. The atomic positions are for the $Pnma$ phase are:

$$\begin{pmatrix} \mathrm{Se}_1 \\ \mathrm{Se}_2 \\ \mathrm{Se}_3 \\ \mathrm{Se}_4 \\ \mathrm{Sn}_1 \\ \mathrm{Sn}_2 \\ \mathrm{Sn}_3 \\ \mathrm{Sn}_4 \end{pmatrix} = \begin{pmatrix} 0.14 & 3/4 & 0.52 \\ 0.36 & 1/4 & 0.02 \\ 0.64 & 3/4 & 0.98 \\ 0.86 & 1/4 & 0.48 \\ 0.12 & 1/4 & 0.09 \\ 0.38 & 3/4 & 0.59 \\ 0.62 & 1/4 & 0.41 \\ 0.88 & 3/4 & 0.91 \end{pmatrix} \begin{pmatrix} \mathbf{a} \\ \mathbf{b} \\ \mathbf{c} \end{pmatrix} \tag{4.5}$$

In monolayer form, SnSe is ferroelectric.[38,51]

The lattice vectors for the *conventional cell* of high-temperature phase $Cmcm$ are given by $\mathbf{a} = a\,\mathbf{e}_1$, $\mathbf{b} = b\,\mathbf{e}_2$, and $\mathbf{c} = b\,\mathbf{e}_3$ where $a = 11.71\,\text{Å}$ and $b = 4.31\,\text{Å}$. The atomic positions in

fractional coordinates are:

$$\begin{pmatrix} \mathrm{Se}_1 \\ \mathrm{Se}_2 \\ \mathrm{Se}_3 \\ \mathrm{Se}_4 \\ \mathrm{Sn}_1 \\ \mathrm{Sn}_2 \\ \mathrm{Sn}_3 \\ \mathrm{Sn}_4 \end{pmatrix} = \begin{pmatrix} 0.14 & 1/2 & 3/4 \\ 0.36 & 0 & 1/4 \\ 0.64 & 0 & 3/4 \\ 0.86 & 1/2 & 1/4 \\ 0.12 & 0 & 1/4 \\ 0.88 & 0 & 3/4 \\ 0.38 & 1/2 & 3/4 \\ 0.62 & 1/2 & 1/4 \end{pmatrix} \begin{pmatrix} \mathbf{a} \\ \mathbf{b} \\ \mathbf{c} \end{pmatrix} \tag{4.6}$$

The primitive cell for the $Pnma$ phase is twice the size of the primitive cell for the $Cmcm$ phase. For convenience, the conventional cells are used throughout this chapter. The atomic structures are shown in Figure 4.5.

4.3. Experimental methods

4.3.1. Bulk crystal growth

Sample preparation involves two steps. Bulk crystals of SnSe were first synthesized, followed by processed by which ultrathin samples were produced.

Bulk SnSe crystals (20 g) were synthesized by mixing appropriate ratios of high purity starting materials (Sn chunk, 99.999%, American Elements, USA and Se shot, 99.999%, 5N Plus, Canada) in 13 mm diameter quartz tube. The tube was flame-sealed at a residual pressure of 1×10^{-4} mmHg, then slowly heated to 1223 K over 10 h, soaked at this temperature for 6 h and subsequently furnace cooled to room temperature. The obtained ingot was crushed into powder and flame-sealed in a quartz tube, which was placed into another, bigger, flame-sealed quartz tube. A crystal with dimensions of $\sim$13 mm (diameter) $\times$ 20 mm (length) was obtained.

4.3.2. Preparation of electron-transparent samples

In order to obtain ultrathin samples suitable for ultrafast electron scattering experiments, two methods were tried. Ultramicrotomy yielded suitable samples, but the author wanted to rule out

the effect of strain induced by the sample preparation. To this end, a sample was also prepared via mechanical exfoliation.

4.3.2.1. Ultramicrotomy

Six samples were prepared via ultramicrotomy, a sample preparation technique which involves the cutting of samples using a diamond blade. While this technique has mostly been used to prepare organic samples for cryo-electron microscopy, it has been successfully used in the past decade to prepare samples of two-dimensional materials such as 4H-$TaSe_2$[52] and 1T-TaS_2.[53] The author initially tried ultramicrotomy to prepare samples of 1T-$TiSe_2$.[4]

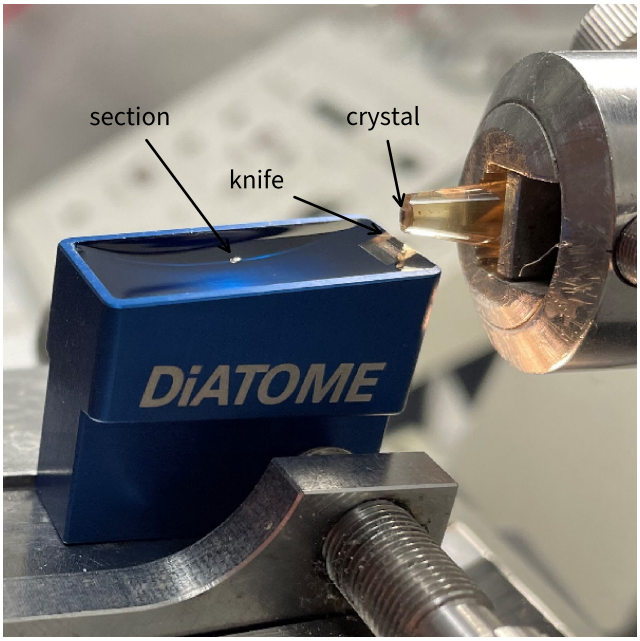

Figure 4.6.: Ultramicrotome setup used to prepare SnSe samples. Crystals embedded in epoxy are mounted, and a diamond knife is used to shave a section. Sections slide down into a boat filled with water, where they are lated fished out. This image was provided by S. K. Sears from McGill University's Facility for Electron Microscopy Research.

First, a bulk crystal of SnSe is embedded in epoxy, with the cutting plane parallel to the material layers. The surface of the bulk crystal is trimmed with a 45° diamond blade to reveal fresh cutting surface. Sections are then cut with a sharper, 35° diamond blade which then fall in a small water container. Floating sections are then fished out with a carbon-coated TEM grid. The assembly is shown in Figure 4.6. The effect of cutting on the embedded crystals is shown in Figure 4.7.

In the end, six samples were produced: three with a thickness of 70 nm and three with a thickness

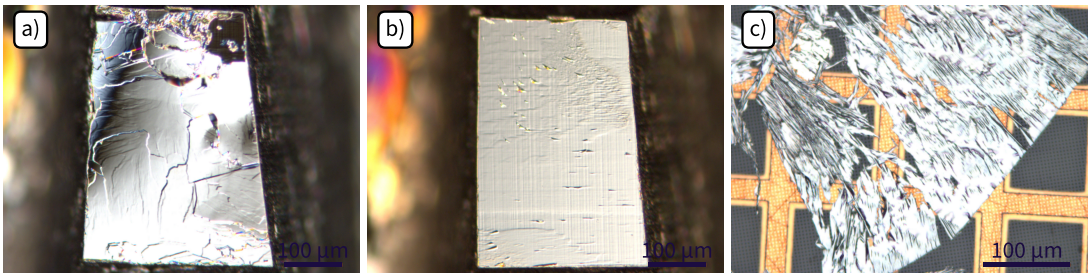

Figure 4.7.: Stages of sample preparation via ultramicrotome. **a)** Prism of SnSe embedded in epoxy showing large crystalline plateaus. **b)** Surface of embedded SnSe prism after trimming with a 45° diamond knife. **c)** 60 nm section of SnSe cut with a 35° diamond knife. The images were provided by H. Gnaegi from Diatome, Ltd.

of 90 nm, each with an area of approximately 200 µm $\times$ 200 µm.

4.3.2.2. Mechanical exfoliation

An ultrathin flake of SnSe was prepared via mechanical exfoliation, a procedure that is analogous to the work by Novoselov *et al.*[54] A small chunk of SnSe was embedded in CrystalBond glue, on a standard 3 mm copper TEM grid with a line spacing of 200 lines per inch. The embedded chunk was then exfoliated repeatedly using ordinary adhesive tape, until the embedded flake was translucent when observed with an optical microscope. The glue was washed away with acetone. This procedure resulted in a sample with an area of approximately 50 µm $\times$ 50 µm.

The sample thickness was determined by taking the ratio of various reflections at thicknesses of 70 nm and 90 nm as prepared via ultramicrotomy– correcting for sample volume and electron flux – and extrapolating to the intensity of the reflections in the exfoliated sample. Using this procedure, the thickness of the exfoliated sample was estimated to be 45 $\pm$ 5 nm, where the uncertainty comes from the variation in expected diffracted intensity across the two samples with known thicknesses.

4.3.3. Experimental parameters

The experiments presented in this chapter used the same experimental geometry that is presented in Section 1.4. Ultrashort laser pulses of 1.55 eV light were shone on the sample surface, with an incident angle of 10°, at $t = t_0$, on SnSe samples oriented in the $[100]$ direction. To ensure that the samples had enough time to cool down after every laser shot, the repetition rate

of experiments were varied from 50 Hz to 1000 Hz, but no changes were measured beyond the degradation of signal-to-noise. Therefore, a 1000 Hz repetition rate was used.

Compressed electron bunches of 10^6 electrons per bunch were transmitted through the sample at $t = t_0 + \tau$, where the time-delay τ was scanned from −10 ps to 30 ps. The total range of time-delay τ was limited compared to experiments presented in Chapter 3 (−40 ps to 680 ps) because the diffuse signals are much weaker in SnSe; limiting the total range of time-delay allowed for more averaging. The longest measurement presented in this chapter was taken over 72 h. This was only possible thanks to the advancements in laser-RF synchronization brought by work by the author in Otto *et al.*,[55] which completely eliminated the drift in t_0 over the experiment duration.

The samples were photoexcited with a pump spot with a full-width at half-maximum that was at least twice the width of the sample, ensuring nearly-uniform illumination of the sample. The samples were photoexcited with photoexcitation densities ranging from 6.6 mJ cm^{-2} to 13.2 mJ cm^{-2}. The absorbed energy will be discussed further in this chapter. The scattering patterns were collected with a Gatan Ultrascan 895 camera, consisting of a 2.54 × 2.54 cm^2 scintillator fiber-coupled to a 2048 px × 2048 px charge-coupled detector (CCD) placed 29.39 cm away from the sample. Example static diffraction patterns are shown in Figure 4.8.

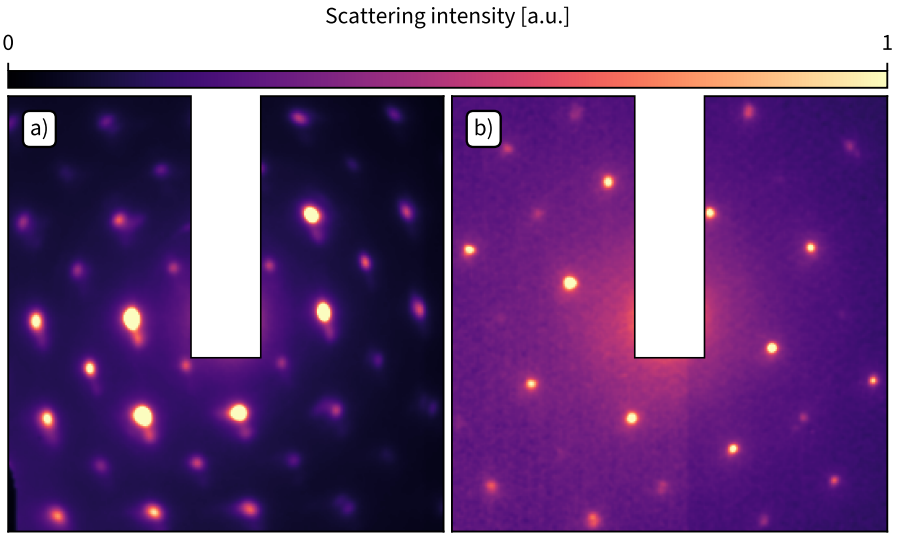

Figure 4.8.: Comparison of static diffraction patterns from samples prepared via two techniques. **a)** 90 nm-thick sample prepared via ultramicrotome. **b)** 45 nm-thick samples prepared via mechanical exfoliation.

Contrary to the symmetrization procedure described in Section 3.2.2 and shown in Figure 3.7,

SnSe only has a two-fold symmetry in-plane. Therefore, the data presented in this chapter was *not* symmetrized.

4.4. Ultrafast electron scattering measurements

The experimental results are presented in this section. The description will start with a presentation of the diffraction results, followed by the diffuse intensity dynamics.

4.4.1. Bragg peak profile analysis

An important point which will anchor the discussion below is that the lattice dimensions are not affected by photoexcitation in the range of time-delay explored herein ($<$30 ps). All Bragg peaks were fit with a Voigt profile[56] at each time-delay, and the changes to their positions and profile, were tracked. The results are presented in Figure 4.9 for a few representative reflections. It is clear that no lattice expansion occurred in the measurements, which would have manifested itself as a change in Bragg peak position. Moreover, no lattice strain was measured, which would appear as a change in Bragg peak width.[57] These checks are important given the strong dependence of SnSe's electronic bands on lattice dimensions[35] and strain.[46]

4.4.2. Debye-Waller dynamics

The Bragg peaks were modified in one important way: a photoinduced amplitude change was measured, attributable to the transient Debye-Waller effect (Section 2.4). In-plane reflections can be separated into two categories: the reflections which are nearly parallel to the $\mathbf{c}^\star$ axis, and the reflections which are not. For the reflections which are within $\sim$ 45° degrees of the $\mathbf{c}^\star$ axis, the amplitude of the Bragg peak follows a Debye-Waller suppression with two time-constants 400 ± 100 fs and 4 ± 1 ps. For reflections which are not nearly parallel to $\mathbf{c}^\star$, only the slower time-constant is present. Figure 4.10 shows the comparison between the amplitude suppression for reflections which are exactly parallel to $\mathbf{b}^\star$ ($\{ (020), (040), ... \}$) and reflections which are exactly parallel to $\mathbf{c}^\star$ ($\{ (002), (004), ... \}$).

Recall from Equation (2.59) that the Debye-Waller factor reports on the average mean-square-displacement of atoms $\langle |\mathbf{u}|^2 \rangle$ along the direction of the scattering vector $\mathbf{q}$. The fact that there is a fast component of the transient Debye-Waller dynamics in Bragg peaks nearly parallel to

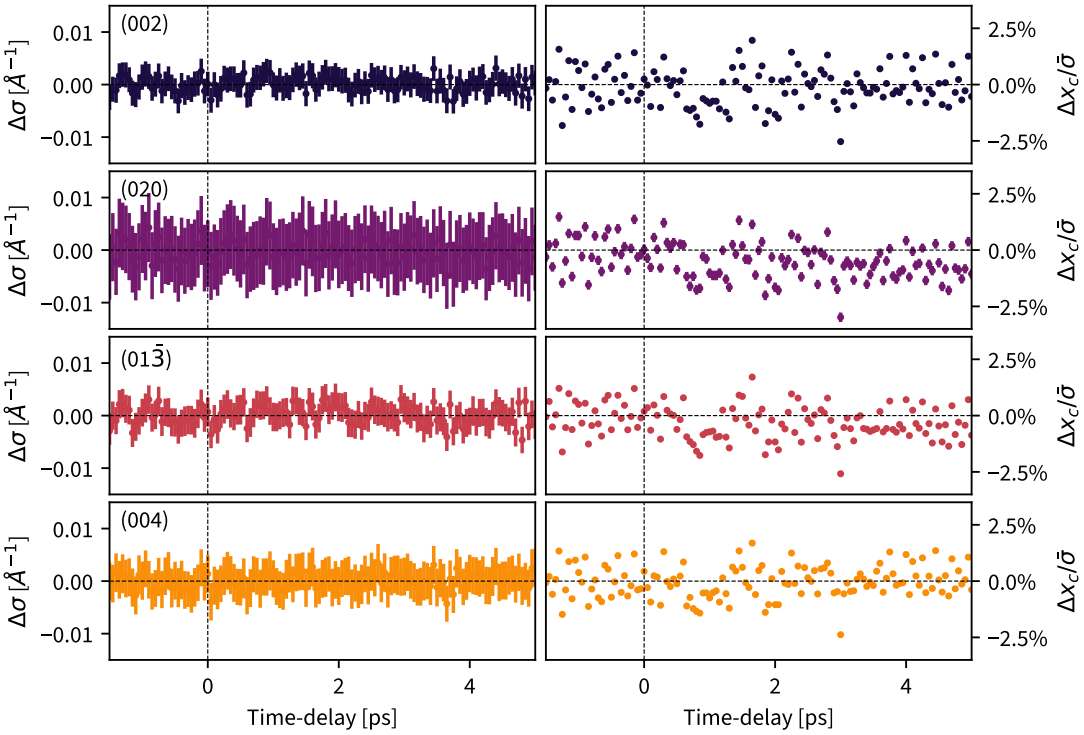

Figure 4.9.: Dynamics of the width and position of various Bragg peaks following photoexcitation. For every time-delay, Bragg peaks were fit with a Gaussian function. In the left column, the change in full-width at half-maximum $\Delta\sigma$ is shown over time. In the right column, the absolute shift in the center position of the peak Δx_c is shown, as a percentage of the average full-width at half-maximum $\bar{\sigma}$. For all plots, the error bars represent the covariance of fit parameter.

$\mathbf{c}^\star$ indicates that the mean-square-displacement of atoms along the $\mathbf{c}$ axis – i.e. the $Pnma$ lattice distortion – is particularly affected by photoexcitation. The increase in mean-square-displacement should be reflected in the diffuse intensity across the Brillouin zone, which is presented further below.

4.4.3. Large-wavevector phonons

The slow dynamics (4 ± 1 ps) in the Debye-Waller dynamics are correlated with the uniform rise of diffuse intensity away from zone-center. Figure 4.11 shows the differential intensity changes at three high-symmetry points in the Brillouin zone: $\mathbf{Y}$, $\mathbf{Z}$, and $\mathbf{T}$. See Figure 4.3 for the geometry of the in-plane section of the Brillouin zone. The diffuse intensity from the Brillouin zone near multiple reflection was averaged to increase signal-to-noise. The three in-plane points show the exact same dependence: a single exponential rise with time-constant 3.6 ± 0.6 ps. For reference,

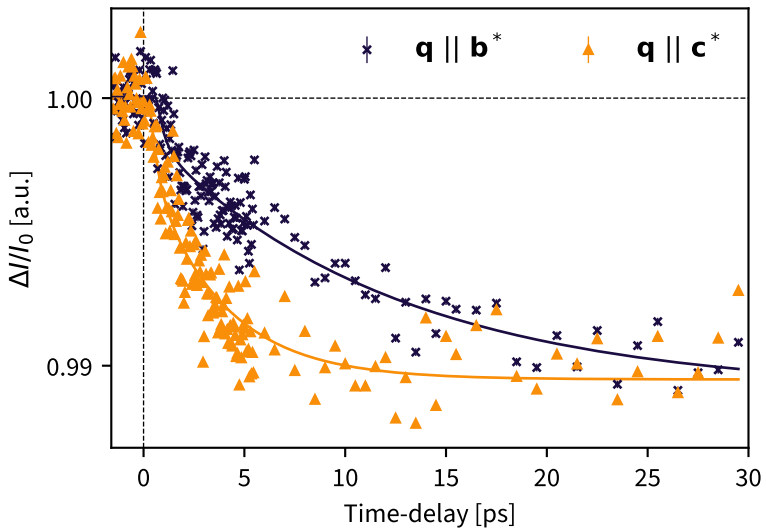

Figure 4.10.: Differential intensity dynamics on Bragg peaks for reflections either parallel to $\mathbf{b}^\star$ or $\mathbf{c}^\star$. Reflections parallel to $\mathbf{b}^\star$ are well-described by a single exponential with time-constant 4 ± 1 ps. However, reflections parallel to $\mathbf{c}^\star$ have a biexponential character with time-constants 400 ± 100 fs and 4 ± 1 ps. Error bars represent the fluctuations before photoexcitation ($\tau < 0$) but are too small to see.

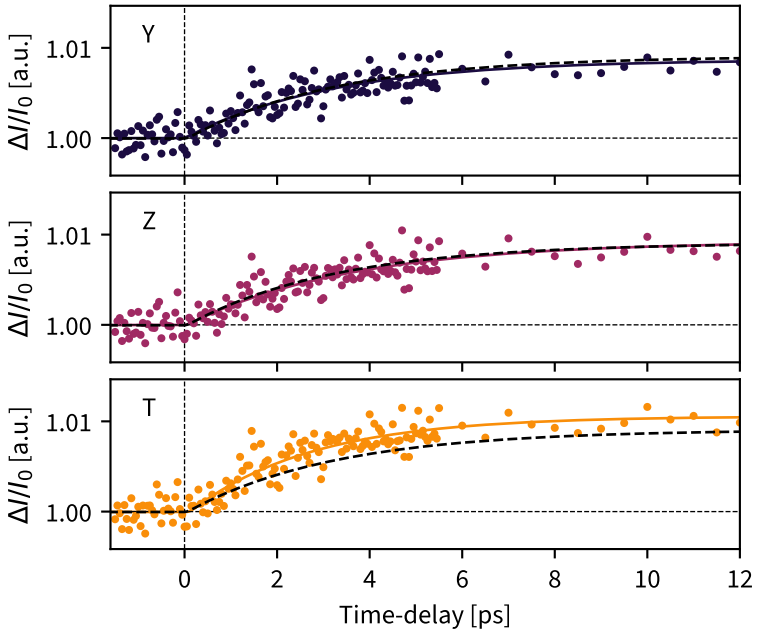

Figure 4.11.: Comparison of the diffuse intensity dynamics at various in-plane high-symmetry points. The fit to the average across the entire Brillouin zone where $|\mathbf{k}| > 0.285\,\text{Å}^{-1}$ is shown as a dashed black trace for reference.

the average across the Brillouin zone away from the zone-center ($|\mathbf{k}| > 0.285\,\text{Å}^{-1}$) is shown.

4.4.4. Small wavevectors phonons

The rapid increase in mean-square-displacement following excitation inferred from the Debye-Waller effect is not due to large wavevector phonons, as this rapid increase is not seen in the diffuse intensity away from zone-center. Recall that the $Pnma \rightarrow Cmcm$ phase transition involves the renormalization of many zone-center transverse optical modes polarized in the direction of the lattice distortion ($\mathbf{c}$ axis).

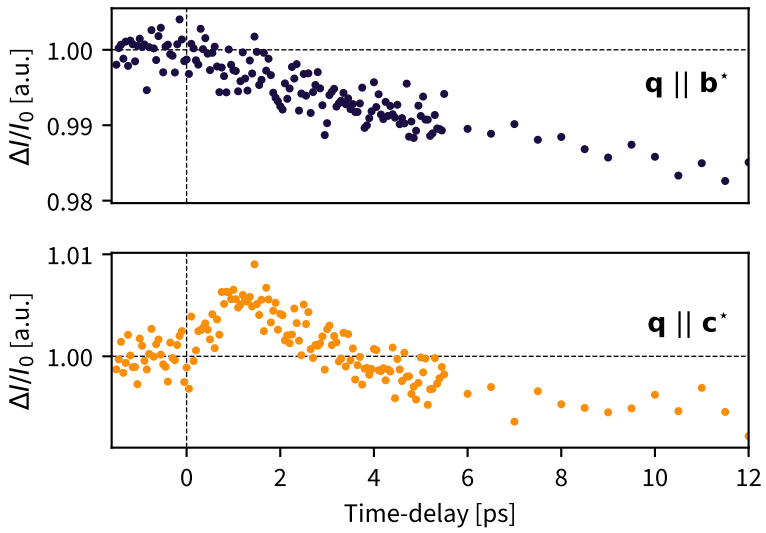

Figure 4.12.: Comparison of the differential intensity dynamics near reflections that are either almost parallel to $\mathbf{b}^\star$ or $\mathbf{c}^\star$. Near reflections almost parallel to $\mathbf{c}^\star$ (e.g. (004), $(01\bar{7})$, etc.), a fast initial rise in intensity is observed which is not measured close to reflections almost parallel to $\mathbf{b}^\star$ (e.g. (040), (051), etc.)

Diffuse intensity dynamics correlated with the fast part of the Debye-Waller dynamics are indeed observed near zone-center, for reflections which are nearly parallel to $\mathbf{c}^\star$. The one-phonon structure factors are expected to be large for the transverse modes polarized in the $\mathbf{c}$ direction near reflections that are almost parallel to the $\mathbf{c}^\star$ axis. Figure 4.12 shows the integration of the total scattering intensity around reflections that are either nearly parallel to $\mathbf{b}^\star$ or $\mathbf{c}^\star$.

These signals will be isolated appropriately and discussed in the next section.

4.5. Dynamics of c-polarized transverse modes

In this section, the initial findings presented in Section 4.4.4 will be developed further. There are two tasks at hand: confirm that the dynamics near zone-center are due to diffuse scattering, and separate isolate this trace from the nearby Bragg peak dynamics.

4.5.1. Confirmation of diffuse dynamics via multiple scattering

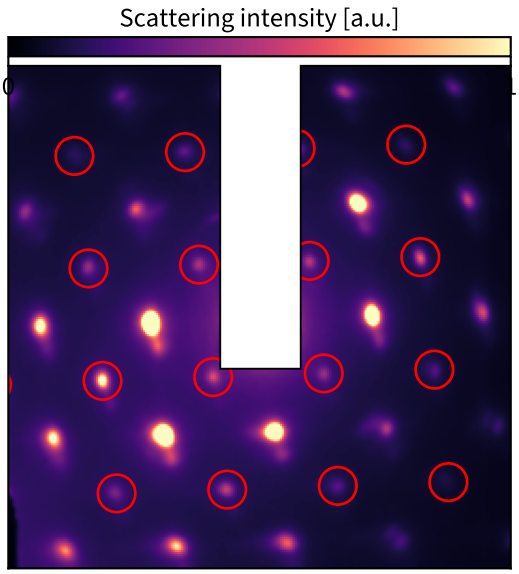

Figure 4.13.: Location of reflections which are forbidden in the $Pnma$ phase. These reflections are visible due to double diffraction.

The intensity dynamics shown in Figure 4.12 can be confirmed to be due to dynamics in the diffuse intensity by performing experiments on a thick sample. Note that the thicker SnSe sample prepared by ultramicrotome show some degree of double diffraction, in the form of *forbidden reflections*.[58] The $Pnma$ space group has a non-zero structure factor (Equation (2.28)) for following in-plane reflections:

$$\{\,(0kl) \mid k + l \in 2\mathbb{Z}\,\} \tag{4.7}$$

where $2\mathbb{Z}$ is understood to be the set of even integers. Forbidden reflections present in the thicker SnSe samples are indicated in Figure 4.13. While double diffraction is visible, the cross-section of a scattering event composed of a diffraction and diffuse scattering event is much less likely (see

Section 2.3). A comparison of the differential intensity dynamics near allowed and forbidden reflections is shown in Figure 4.14. For both allowed and forbidden reflections, only those which are nearly parallel to the $\mathbf{c}^*$ axis were used. It is clear that the fast intensity increase is not present near the zone-center of reflections which result from double diffraction, which confirms that the ultrafast rise in intensity initially shown in Section 4.4.4 is diffuse in nature.

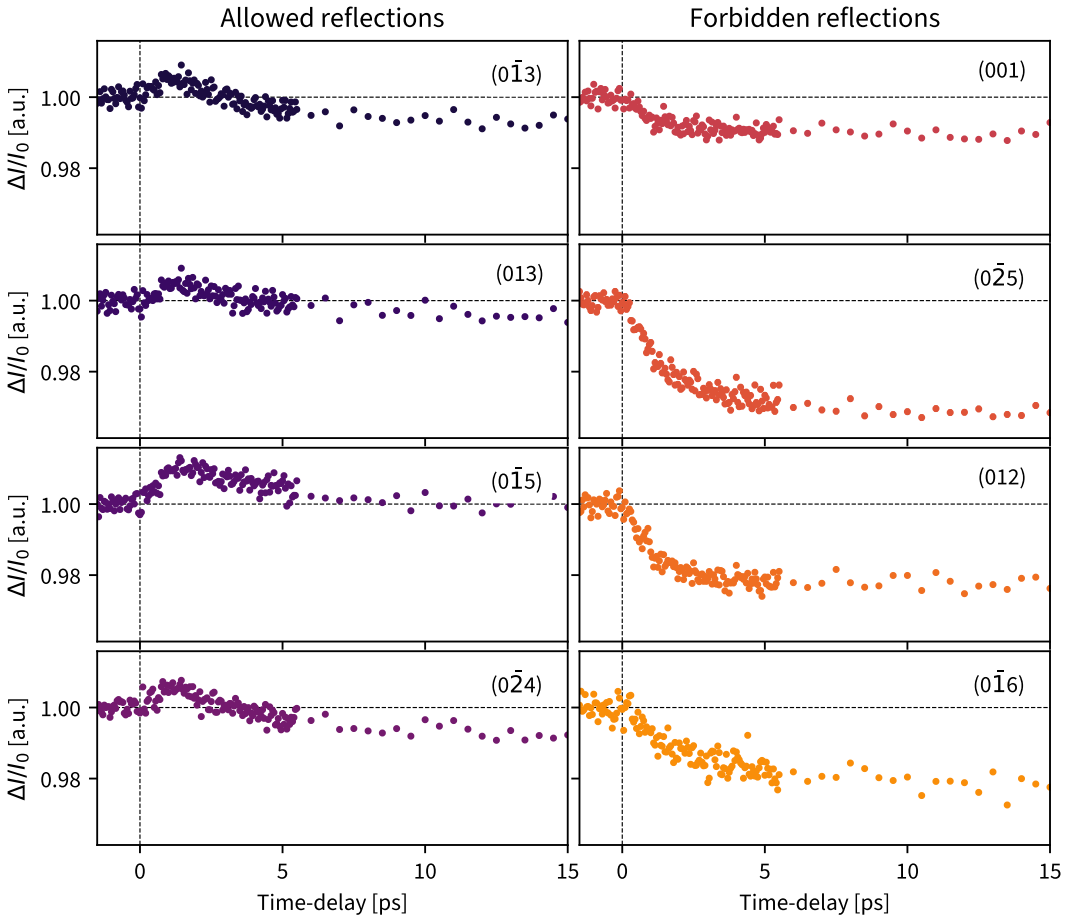

Figure 4.14.: Differential intensity dynamics in a ring near the Bragg peak of allowed and forbidden reflections. See Section 4.5.2 for a discussion on the geometry of the integration region.

4.5.2. Partitioning of the Brillouin zone

In order to be more quantitative about the diffuse intensity dynamics at zone center, the intensity dynamics of the Bragg peaks need to be removed. Directly on the Bragg peaks, the absolute intensity change observed in Figure 4.10 is 10^5 times larger than the diffuse rise observed in Figure 4.12. The transient Debye-Waller effect suppresses diffracted intensity, but does not change the peak profile. Therefore, there must be a region in reciprocal space – far enough

away from the peak location – where the absolute change in peak intensity due to the transient Debye-Waller effect is on the same order as the diffuse rise.

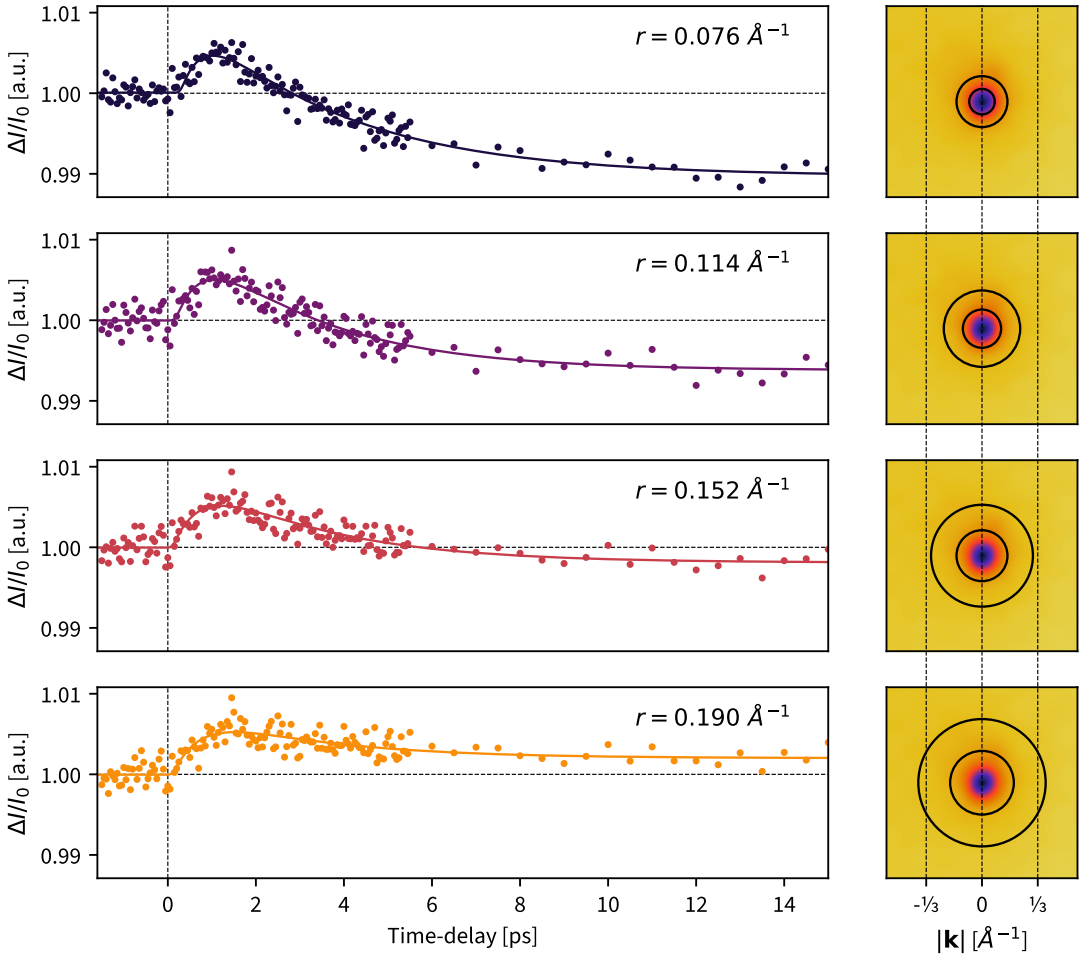

Figure 4.15.: Comparison of intensity dynamics integrated in a region defined by Equation (4.9) for multiple values of r. For each value of r, the associated integration region is shown on the right. The dynamics are all well-described by a biexponential trace with a fast rise and slow decay. The fitting results are summarized in Table 4.2.

By looking in a *ring* around Bragg peaks, the intensity dynamics can be separated between Debye-Waller (inner disk) and diffuse intensity near zone-center (outer torus) parametrized by:

$$\Omega_{\text{region 1}} = \{\mathbf{k} \mid |\mathbf{k}| < r\} \tag{4.8}$$

$$\Omega_{\text{region 2}} = \{\mathbf{k} \mid r \leq |\mathbf{k}| \leq 2r\} \tag{4.9}$$

$$\Omega_{\text{region 3}} = \{\mathbf{k} \mid 2r < |\mathbf{k}|\} \tag{4.10}$$

The amplitude of the diffuse rise near zone-center is affected by the parameter r, but the time-

constants are not. Figure 4.15 shows the intensity dynamics when integrating in region 2, for various parameters of r. In all cases, the differential intensity dynamics are well-described by a biexponential function. The relative amplitudes of the two exponentials determines the overall shape of the curves, as all the time-constants are comparable. The fitting results are summarized in Table 4.2. The sizes of the inner and outer radii which maximize the amplitude of the diffuse rise are $r = 0.114\,\text{Å}^{-1}$ and $r = 0.228\,\text{Å}^{-1}$; this geometry is shown in Figure 4.16. Region 1 and 2 are fairly small, considering that the in-plane Brillouin zone is $1.49\,\text{Å}^{-1} \times 1.41\,\text{Å}^{-1}$ in size.

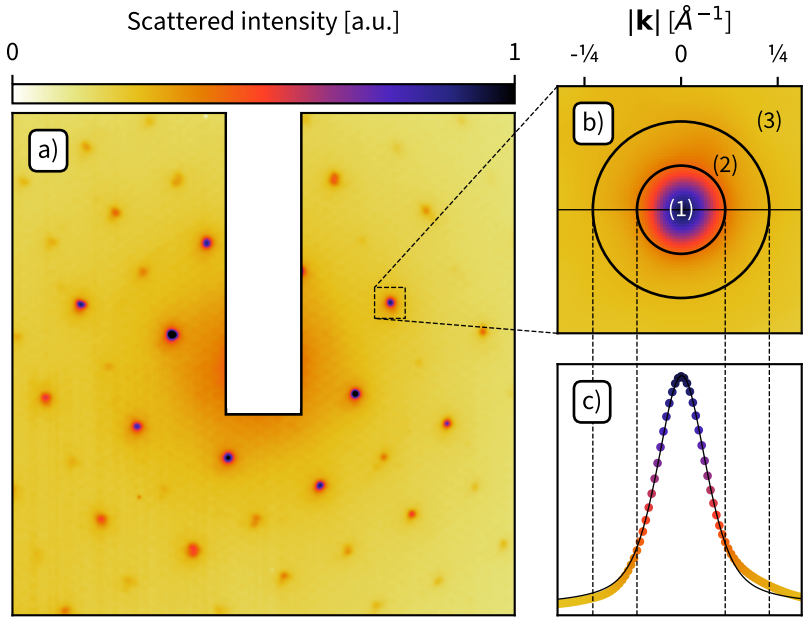

Figure 4.16.: Intensity integration geometry which allows to distinguish between physical processes. **a)** Static diffraction patterh of SnSe. **b)** Zoom on the (020) reflection showing three integration regions: the Debye-Waller dynamics (region 1), the small-wavevector diffuse dynamics (region 2), and the large wavevector diffuse dynamics (region 3). **c)** Linecut of the static intensity along the solid horizontal line in panel b), showing the diffraction peak profile. The Bragg peak is fit with a Voigt profile (solid black line) with a full-width at half-max of $0.158\,\text{Å}^{-1}$.

With the appropriate partitioning of the Brillouin zone (Figure 4.16), it is possible to separate the dynamics of the Bragg peak from the diffuse intensity for low wavevectors ($0.114\,\text{Å}^{-1} \leq |\mathbf{k}| \leq 0.228\,\text{Å}^{-1}$). The diffuse dynamics near zone-center presented in the previous section are definitely affected to some degree by the dynamics of the nearby Bragg peak. However, because it has been shown that the Bragg peak profiles are constant, the Debye-Waller dynamics from region 1 can be subtracted. The results are presented in Figure 4.17. Most importantly, this

Table 4.2.: Comparison of the time-constants determined from the diffuse intensity dynamics for various dimensions of region 2 in Figure 4.15. The parameter r defines the integration region with Equation 4.9.

r [Å^{-1}]	τ_1 [fs]	τ_2 [ps]
0.076	475 ± 120	3.5 ± 0.4
0.114	300 ± 100	2.9 ± 0.5
0.152	600 ± 220	2.9 ± 0.8
0.190	600 ± 270	2.9 ± 1.3

reveals that the slow diffuse intensity decrease near the zone-center is *not due* to the nearby Bragg peak, but is rather intrinsic to the diffuse dynamics.

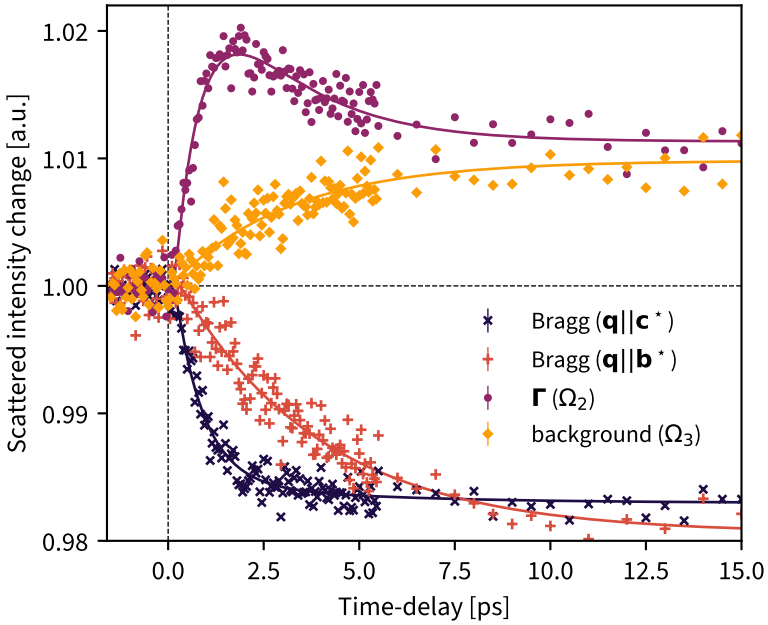

Figure 4.17.: Transient ultrafast electron scattering intensity at various points in the Brillouin zone. The integration geometry is shown in Figure 4.16 and defined by Equation (4.10) with $r = 0.114$ Å^{-1}. The decrease of intensity directly on the Bragg peak where $\mathbf{q}||\mathbf{c}^\star$ shows the expected transient Debye-Waller effect with fast and slow components, while the Debye-Waller suppression on Bragg peaks where $\mathbf{q}||\mathbf{b}^\star$ only displays slow exponential behavior. Average transient diffuse intensity across region Ω_3 is shown for context. Error bars represent the standard error in the mean of intensity before time-zero, but are generally smaller than the markers.

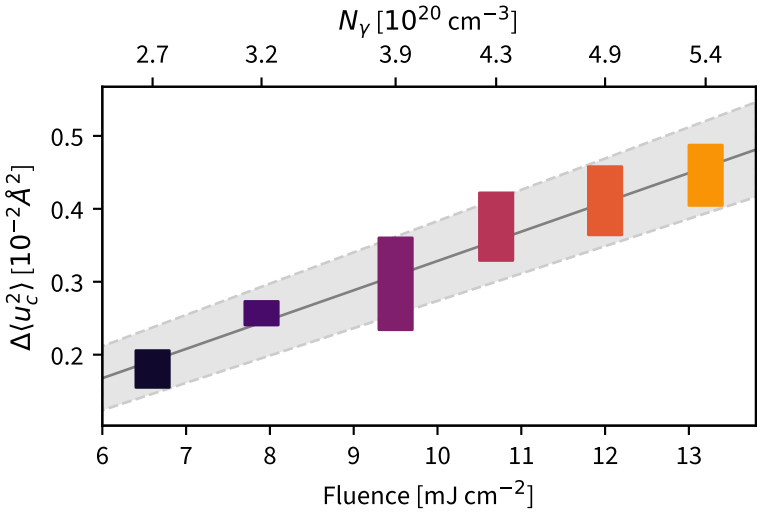

Figure 4.18.: Increase in mean-square-displacement of all atoms $\Delta\langle u^2\rangle$, due to the change in vibrational amplitude of the strongly-coupled small-wavevector $\mathbf{c}$-polarized modes exclusively. Boxes are used to represent error bars along both axes. Color bar shows associated photocarrier density N_γ.

4.5.3. Transient mean-square-displacement due to strongly-coupled modes

The fast component of the transient Debye-Waller dynamics (Figure 4.10) can be used to infer the change in vibrational amplitudes due exclusively to the strongly-coupled small-wavevector modes. The time-resolved suppression of Bragg intensity due to atomic vibrations is given by the following expression (Equation (2.75)):

$$\begin{aligned}\frac{I_0(\mathbf{q},\tau)-I_0(\mathbf{q},0)}{I_0(\mathbf{q},0)} &\equiv \Delta I_0(\mathbf{q},\tau)\\ &= \frac{e^{-2M(\mathbf{q},\tau)}-e^{-2M(\mathbf{q},0)}}{e^{-2M(\mathbf{q},0)}}\\ &= e^{-2[M(\mathbf{q},\tau)-M(\mathbf{q},0)]}-1\end{aligned} \tag{4.11}$$

Rearranging terms:

$$-\frac{1}{2}\ln\left[1+\Delta I_0(\mathbf{q},t)\right] = M(\mathbf{q},\tau)-M(\mathbf{q},0) \tag{4.12}$$

In this formulation, M is the appropriate average of all atom-specific W_s suppression factors from Equation (2.59), for which there is no general expression for diatomic crystals such as SnSe.[59] The fast component of the transient Debye-Waller dynamics are only visible for reflections nearly parallel to $\mathbf{c}^\star$, which informs on the atomic displacement in the $\mathbf{c}$ direction. Since the Debye-

Waller suppression is small ($\sim 1\%$, Figure 4.10), the harmonic approximation can be used. This approximation states that if atoms are vibrating very close to their equilibrium position, the potential is harmonic,[60] and the Debye-Waller factor M is given by:

$$M(\mathbf{q},\tau) = \frac{1}{2}|\mathbf{q}|^2\langle|\bar{\mathbf{u}}\cdot\mathbf{e}_3|^2\rangle \tag{4.13}$$

where the symbol $\bar{\mathbf{u}}$ signifies the atomic displacement averaged over the atoms in the unit cell, and $\mathbf{e}_3$ is the unit vector in the $\mathbf{c}$ direction. Then, the transient mean-square-displacement in the $\mathbf{c}$ direction, $\Delta\langle|\bar{\mathbf{u}}\cdot\mathbf{c}|^2\rangle \equiv \Delta\langle u_c^2\rangle$, is related to the Bragg intensity at zone center as:

$$\Delta\langle u_c^2\rangle = -\frac{\ln\left[1+\Delta I_0(\mathbf{q},t)\right]}{|\mathbf{q}|^2} \tag{4.14}$$

for $\mathbf{q}$ nearly parallel to $\mathbf{c}^\star$. The associated error σ_u as a function of the pre-photoexcitation transient intensity error σ_I is given by:[61]

$$\sigma_u = \left|\frac{\partial\Delta\langle u_c^2\rangle}{\partial I}\right|\sigma_I = \frac{-\sigma_I}{|\mathbf{q}|^2\left[1+\Delta I_0(\mathbf{q},t)\right]} \tag{4.15}$$

The extracted change in atomic displacement along the $\mathbf{c}$ axis due to small-wavevector $\mathbf{c}$-polarized transverse modes as a function of fluence is shown in Figure 4.18.

4.6. Discussion

In this section, the interpretation of the observations presented previously are discussed.

Consider first the ultrafast diffuse increase near zone-center. Recall the definition for the diffuse intensity (Equation (2.77)):

$$I_1(\mathbf{q}) \propto \sum_\lambda \frac{n_\lambda(\mathbf{k})+1/2}{\omega_\lambda(\mathbf{k})}|F_{1\lambda}(\mathbf{q})|^2 \tag{4.16}$$

This equation implies an increase of diffuse intensity is due to an increase in $(n_\lambda+1/2)/\omega_\lambda$ for one or more modes. Two potential causes of a rise are identified:

1. Selective mode-heating ($\uparrow\ n_\lambda$). Phonon modes may be populated selectively as the electronic system thermalizes. This is similar to the physics that was described in Chapter 3.
2. Frequency renormalization ($\downarrow\ \omega_\lambda$). There are multiple zone-center phonon modes polarized in the $\mathbf{c}$ direction which are known to soften towards the phase transition. The

opposite has been observed by the author in $TiSe_2$ in Otto *et al.*,[4] where the photodoping of carriers selectively stiffened a soft zone-boundary phonon.

Due to the energy-integrative nature of ultrafast electron diffuse scattering measurements, it is not possible to distinguish between these two types of dynamics. In analogy to Equation (2.54), terms of the form $(n_\lambda + 1/2)/\omega_\lambda$ are directly proportional to vibrational amplitude. In this formulation, the fast diffuse intensity rise at $\mathbf{\Gamma}$ is due to an increase in vibrational amplitude of one or more small-wavevector phonon modes polarized in the direction of the $Pnma$ lattice distortion.

4.6.1. Electron-phonon coupling

Given that the energy contained in pump pulses are absorbed by electrons, and that ultrafast electron scattering measures the subsequent lattice response, it is natural to ask how electron-phonon coupling can explain the experiments. The electron-phonon scattering rate $1/\tau_{\lambda\mathbf{k}_p}$, or rate of energy transfer between electrons at all wavevectors and phonons at wavevector $\mathbf{k}_p$, is given by:[10]

$$1/\tau_{\lambda\mathbf{k}_p} = -\frac{2\pi}{\hbar}\text{Im}\left[\Pi_\lambda(\mathbf{k}_p)\right] \tag{4.17}$$

where a and b label electron bands, $\mathbf{k}_e$ ($\mathbf{k}_p$) is the electronic (phonon) wavevector, and $\Pi_\lambda(\mathbf{k}_p)$ is the self-energy for phonons with quantum numbers $(\lambda, \mathbf{k}_p)$. The phonon self-energy also defines how vibrational frequencies are renormalized from ω_λ^0 to ω_λ due to electron-phonon interactions:[62]

$$\frac{\omega_\lambda(\mathbf{k}_p)^2}{\omega_\lambda^0(\mathbf{k}_p)^2} - 1 = \frac{2}{\hbar\omega_\lambda^0(\mathbf{k}_p)}\text{Re}\left[\Pi_\lambda(\mathbf{k}_p)\right] \tag{4.18}$$

The renormalization of phonon vibrational frequencies due to strong electron-phonon coupling was encountered in Section 3.1.2 in the form of Kohn anomalies.[63]

Both a large electron-phonon scattering rate (i.e. selective mode-heating) and phonon frequency renormalization can lead to an increase in the phonon vibrational amplitude measured in SnSe (Equation (2.54)). Regardless of the physical cause of the increased vibrational amplitude (mode-heating or phonon renormalization), the consequences boil down to an ultrafast modification of the phonon self-energy. Computing the phonon self-energy for particular situations is arduous,[64,65] but in the Migdal approximation:[66,67]

$$\Pi_\lambda(\mathbf{k}_p) = \sum_{a,b}\int \frac{d\mathbf{k}_e}{(2\pi)^3}\left|g_{ab}^\lambda(\mathbf{k}_p,\mathbf{k}_e)\right|^2 \frac{f\left[\epsilon_a(\mathbf{k}_e)\right] - f\left[\epsilon_b(\mathbf{k}_e+\mathbf{k}_p)\right]}{\epsilon_a(\mathbf{k}_e) - \epsilon_b(\mathbf{k}_e+\mathbf{k}_p) - \hbar\omega_\lambda(\mathbf{k}_p) + i\eta} \tag{4.19}$$

where a and b label electron bands, $\mathbf{k}_e$ ($\mathbf{k}_p$) is the electronic (phonon) wavevector, $f(\epsilon)$ is the electronic energy distribution, and η is an infinitesimally-small number. The electronic energy distribution $f(\epsilon)$ might be non-thermal in general, and indeed is non-thermal on the timescale of the experiments presented herein. The electron-phonon coupling tensor, $g^{\lambda}_{ab}(\mathbf{k}_e, \mathbf{k}_p)$, describes the rate of inelastic single electron scattering between bands a and b through the creation or annihilation of a phonon with quantum numbers $(\lambda, \mathbf{k}_p)$. The electron-phonon coupling tensor g was encountered in Section 1.1.4 and Section 3.6.4.

The electron-phonon scattering rate (Equation (4.17)) and phonon renormalization (Equation (4.18)) are therefore proportional to the $\mathbf{k}_e$-integrated electron-phonon coupling tensor via Equation (4.19). Photoexcitation perturbs the electronic energy distribution (f), and this non-thermal energy distribution will scatter to phonons $(\lambda, \mathbf{k}_p)$ based on the strength of g. Therefore, whether the diffuse intensity rise near zone-center is due to selective mode heating, phonon renormalization, or both, is not an important distinction. The diffuse intensity rise at small wavevectors can be associated with strong electron-phonon coupling to small wavevector modes polarized in the $\mathbf{c}$ direction and at least an order-of-magnitude lower coupling everywhere else in the plane.

This is not entirely unexpected. Calculations by Ma *et al.*[47] have revealed that the mobility of electrons and holes is strongly-modified at zone-center due to polar optical modes. Calculations by Caruso *et al.*[68] have reported strong electron-phonon coupling to zone-center optical modes polarized in the $\mathbf{c}$ direction, most importantly the B_u (8 meV) and the B_g (20 meV) modes. The results presented in this chapter corroborate these findings, at least qualitatively.

4.6.1.1. The Mott-Ioffe-Regel limit

Can strong and anisotropic electron-phonon coupling explain SnSe's low lattice thermal conductivity? The reduction of lattice thermal conductivity due to strong electron-phonon interactions at zone-center have been studied theoretically in silicon by Liao *et al.*[69] It was found that at high carrier concentrations ($> 10^{19}$ cm^{-3}), the overall lattice thermal conductivity was reduced by as much as 45%. Moreover, the scattering rate of phonons was dominated by electron-phonon interactions for low-energy phonon modes, and not (anharmonic) phonon-phonon interactions. Something similar was calculated in silicon germanium by Fan *et al.*[10] These ideas were tested experimentally in crystalline silicon membranes by Zhou *et al.*[70] using transient thermal grating diffraction which showed that at room temperature, the thermal transport was indeed strongly

affected by electron-phonon interactions when carrier concentration was increased via ultrafast photoexcitation above 10^{19} cm^{-3}.

The behavior of the thermal conductivity κ with increasing temperature in SnSe exhibits an asymptotic behavior above 600 K (Figure 4.2) which is reminiscent of the Mott-Ioffe-Regel limit on the resistivity in so-called *bad metals*.[71,72,73] The Mott-Ioffe-Regel limit expresses that the transport properties of quasiparticles saturate once their mean-free-path has fallen below the lattice dimensions.[74] Our measurements suggest that the phonon mean-free-path in SnSe might be close to the Mott-Ioffe-Regel limit above 600 K due to strong electron-phonon coupling. This happens at equilibrium due to the thermal enhancement of the electron-phonon scattering rate (Equation (4.17)), and ultrafast electron diffuse scattering reveals a similar behavior via impulsive photodoping.

4.6.2. Incompatibility of results with simple relaxation mechanisms

The experimental results show a relaxation of the intensity near zone-center after the initial fast rise described in the previous section, which is correlated to the rise of diffuse intensity across the Brillouin zone (4 ps). The energy stored in the small-wavevector strongly-coupled modes can relax in many ways. The two simplest potential explanations are anharmonic decay of phonons, and phonon-mediated valley scattering of charge-carriers. However, it is expected that those two energy relaxation pathways imprint the structure of the phononic and/or electronic dispersions, which is not observed in the ultrafast electron scattering measurements.

4.6.2.1. Anharmonic decay of phonons

The anharmonic decay relaxation mechanism sees one small-wavevector phonon generate two lower energy phonons in a process that conserves energy and momentum. There are several reports on the strong bonding anharmonicity in SnSe.[30,32,42,48,75] However, the phonon lifetimes are estimated to be longer (15 ps to 30 ps)[48,75,76] than what has been observed via ultrafast electron scattering (4 ps). The results presented here are *not compatible* with an anharmonic decay picture for a different reason: the lack of structure in the diffuse intensity dynamics. The measurements in graphite (Chapter 3) have shown that the anharmonic decay of phonons measured in the time-domain is highly representative of the phonon dispersion due to energy- and momentum-conservation rules. However, the diffuse rise in intensity away from zone-center is

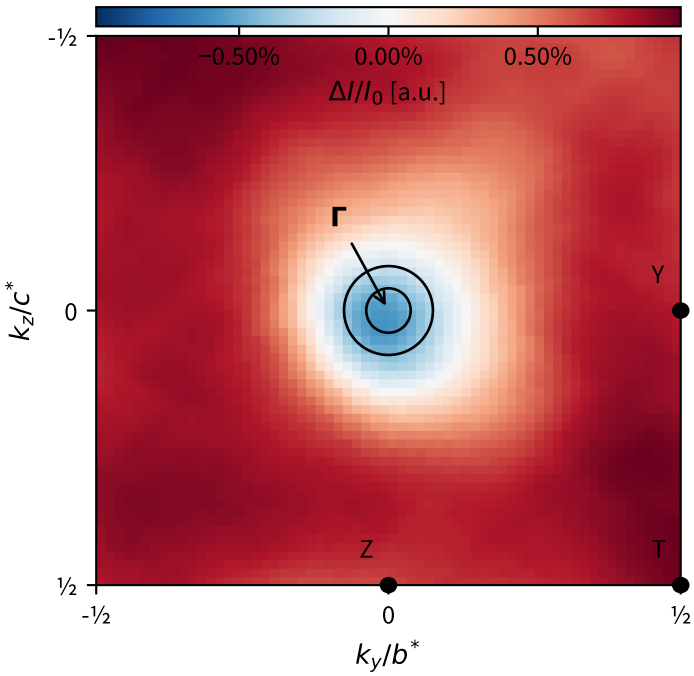

Figure 4.19.: Relative diffuse intensity change at 5 ps shows no structure representative of anharmonic decay of small-wavevector modes.

completely uniform. This is shown in Figure 4.19, where the average relative diffuse intensity increase at 5 ps shows no structure beyond the partitioning of the Brillouin zone described in Section 4.5.2. Most importantly, the diffuse rise everywhere is found to happen with the same characteristic time-scale (Figure 4.11).

4.6.2.2. Phonon-mediated valley-scattering

Another potential relaxation mechanism is phonon-mediated intra- and inter-valley charge-carrier scattering.[77] Electrons undergo vertical transitions when absorbing 1.55 eV photons, creating holes. Given that the direct, optical band gap of SnSe is less than the photon energy at 1.3 eV,[78] the electrons/holes have some excess energy above the local conduction/valence band extremum. The charge-carriers can relax in two (possibly simultaneous) steps.[77] The first step is the relaxation of charge-carriers to the local band extremum by interacting with small-wavevector phonons. The second step is the relaxation of charge-carriers to the global band extremum by interacting with small and large-wavevector phonons. This process is shown

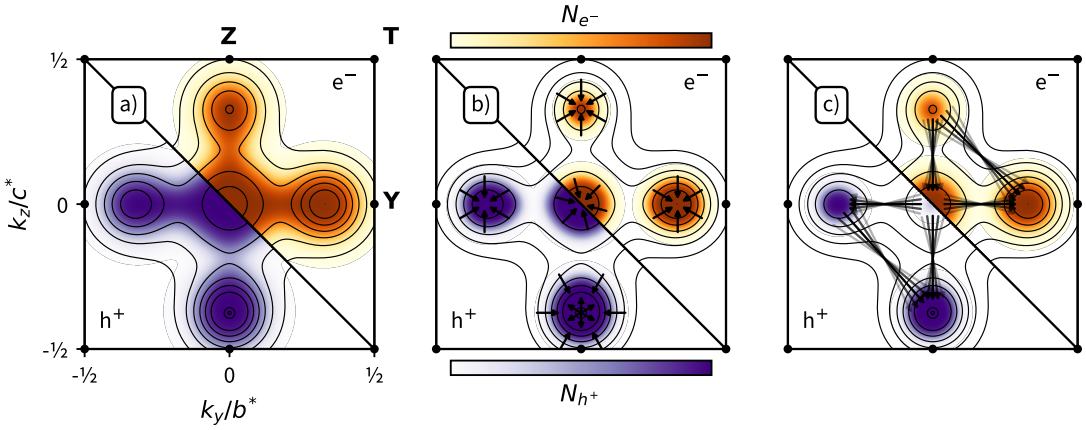

Figure 4.20.: Diagram showing the in-plane carrier relaxation process as phonon-mediated valley scattering, which does not match the experimental results (see text). Color intensity represents the photoelectron and photohole densities N_{e^-} and N_{h^+} respectively, where white is zero. The contours represent the dispersion of Figure 4.4. **a)** Carrier densities just after photoexcitation. **b)** Carrier densities after $\sim$ 1 ps showing that carriers have undergone intravalley scattering mediated by small wavevector phonons (arrows) to the local extrema of the conduction and valence bands. **c)** Carrier densities after $\sim$ 5 ps showing that carriers have undergone intervalley scattering mediated by large wavevector phonons (arrows) to the global extrema of the electronic dispersion.

schematically in Figure 4.20.

Intra- and inter-valley scattering are expected to imprint the structure of the electronic dispersion onto the created phonons. To understand why, the allowed intervalley relaxation pathways were simulated for electrons and holes; the following explanation focuses on electrons for simplicity. Consider $E(\mathbf{k})$ to be the in-plane electronic dispersion in reciprocal space. An initial electron density-of-states $g^i_{e^-}(\epsilon)$ around local band minima is assumed as shown in Figure 4.20 b). Electrons with energy ϵ can only relax to locations in reciprocal space where the dispersion is lower in energy. This constraint can be expressed using the Heaviside step function Θ, where $\Theta\left\{-g^i_{e^-}(\epsilon)\right\}$ is unity for $0 < g^i_{e^-}(\epsilon)$ and zero otherwise. The number of allowed relaxation pathways $P_{e^-}(\mathbf{k})$ in reciprocal space are therefore given by the cross-correlation between the initial electron density $g^i_{e^-}(\epsilon)E(\mathbf{k})$ and the allowed relaxation pathways $\Theta\left\{-g^i_{e^-}(\epsilon)\right\}E(\mathbf{k})$:

$$P_{e^-}(\mathbf{k}) \propto \int_0^\infty d\epsilon \left[g^i_{e^-}(\epsilon)E(\mathbf{k})\right] \star \left[\Theta\left\{-g^i_{e^-}(\epsilon)\right\}E(\mathbf{k})\right] \tag{4.20}$$

where $\star$ is the cross-correlation operation with symmetric boundary conditions, which accounts for Umklapp scattering processes.[79] The proportionality constant is chosen so that $P_{e^-}(\mathbf{k}) \leq 1$.

Similarly, holes scatter up in energy so that:

$$P_{h^+}(\mathbf{k}) \propto \int_0^\infty d\epsilon \left[g^i_{h^+}(\epsilon) E(\mathbf{k}) \right] \star \left[\Theta \left\{ g^i_{h^+}(\epsilon) \right\} E(\mathbf{k}) \right] \tag{4.21}$$

where $g^i_{h^+}(\epsilon)$ is the initial holes density-of-states as shown in Figure 4.20 b). The results of these calculations are shown in Figure 4.21. While these calculations are sensitive to the initial density-of-states, note that there are still many regions in reciprocal space where relaxation is forbidden regardless of the initial conditions (i.e. $P_{e^-}(\mathbf{k})$ and $P_{h^+}(\mathbf{k})$ are zero). The structures shown are *not compatible* – even qualitatively – with the measurements shown in Figure 4.19, which is azimuthally-symmetric.

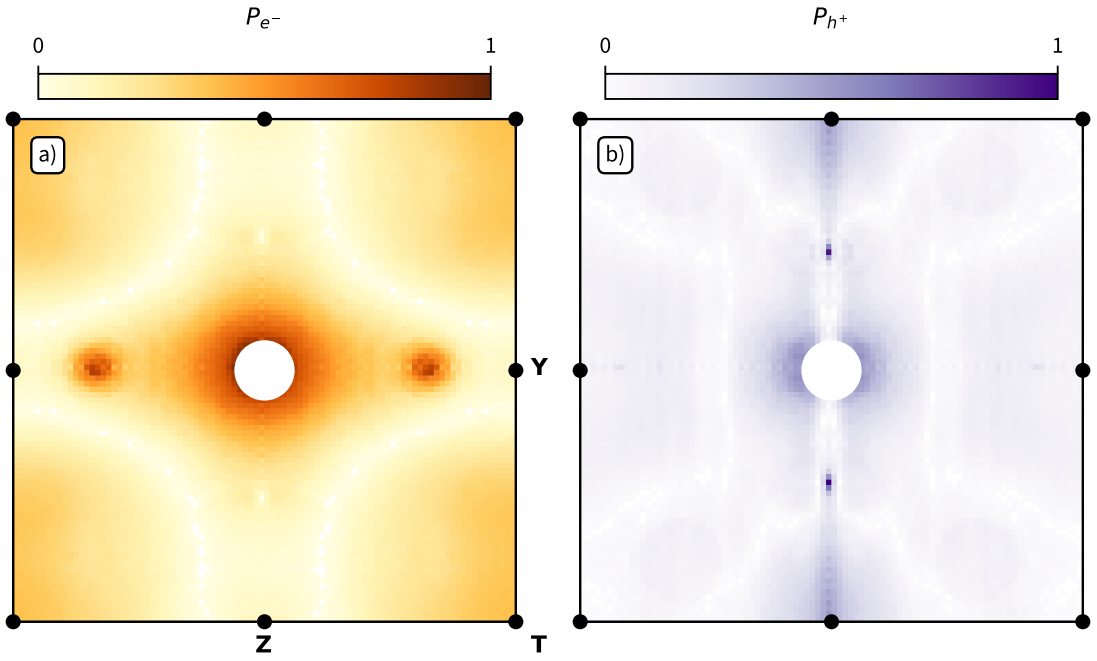

Figure 4.21.: Relative number of allowed relaxation pathways after initial intravalley scattering of charge-carriers. Regions in white represent relaxation pathways that are forbidden, no matter the initial distribution of hot charge carriers. **a)** Relative number of relaxation pathways for electrons. **b)** Relative number of relaxation pathways for holes.

4.6.3. Polaron formation

As described in the previous section, the relaxation of photogenerated carriers or the anharmonic decay of phonons is expected to imprint the structure of the electronic or phonon dispersion on the diffuse intensity, respectively, due to energy- and momentum-conservation.[4,80,81] However, measured changes in the diffuse intensity are broad and radially-symmetric in reciprocal space.

This is indicative of lattice distortions that are local in real-space. Given that SnSe is a polar lattice, and that strong electron-phonon coupling to polar phonon modes has been calculated,[68] our results can be understood as the formation of polarons.

Polarons are quasiparticles that combine a free charge carrier with the effect the charge carrier has on the polarizable lattice, creating a local lattice distortion.[82,83,84,85] The free charge is said to be *dressed* by polar phonons as the charge and lattice distortion propagate together. The configuration coordinate picture of this process is shown in Figure 4.22, where delocalized electrons are dressed by phonons which lowers the total free energy of the system. Polarons play a large role in many material properties, including charge transport and multiferroism; interested readers are encouraged to read Franchini *et al.*[86]

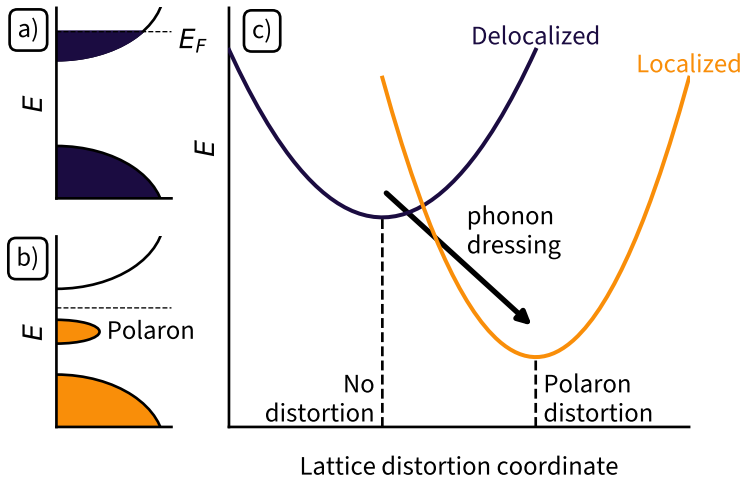

Figure 4.22.: Configuration coordinate diagram of the process of polaron formation as the dressing of charge carriers. **a)** Schematic band structure diagram following photoexcitation, depicting nonthermal delocalized conduction electrons (equivalent picture for holes not shown). **b)** Schematic band structure diagram after carrier localization indicating a polaron peak below the Fermi energy E_F. **c)** Configuration coordinate showing the free energy of the system as non-thermal delocalized carriers self-localize via phonon-dfressing, which generate local lattice distortions known as polarons.

A polaron, like any point-defect-like deformation of the lattice, involves many phonon modes, as local lattice distortions in real-space cannot be described with a finite number of lattice normal modes. Calculations by Sio *et al.*[87] have demonstrated that in other polar lattices, electron and hole polarons have widely different characteristic lengths. Electron polarons tend to be larger and hence are composed of low-wavevector modes, while hole polarons tend to be smaller due to the relative flatness of the valence band and thus involve phonons modes across a wider range

of wavevectors. This difference in size impacts the precise combination of lattice waves which make up a polaron, and is expected to be visible in ultrafast electron scattering measurements.

4.6.3.1. Point-defect model

In this section, the effect of a polaronic lattice distortion on the scattering intensity will be calculated. Recall the scattered wavefunction (Equation (2.29)):

$$\langle \mathbf{x}|\Psi\rangle_0 \equiv F(\mathbf{q}) \propto \sum_i f_{e,i}(\mathbf{q})\, e^{-i\mathbf{q}\cdot\mathbf{r}_i} \tag{4.22}$$

where $F(\mathbf{q})$ is the static structure factor, and $\{\, f_{e,i} \,\}$ and $\{\, \mathbf{r}_i \,\}$ are the atomic form factors and positions, respectively. The subscript 0 indicates that no polarons are present. A polaron induces a lattice distortion just like a point defect[88] based on the electrostatic interaction, which is expressed as the displacement field $\mathbf{u}(\mathbf{r})$. This displacement field will be given an explicit expression further below. For simplicity, assume that the polaron is located at the origin of the coordinate system. The effect of the polaron is given by the substitution $\mathbf{r}_i \to \mathbf{r}_i + \mathbf{u}(\mathbf{r}_i)$:[89]

$$\begin{aligned}\langle \mathbf{x}|\Psi\rangle &= \sum_i f_{e,i}(\mathbf{q})\, e^{-i\mathbf{q}\cdot[\mathbf{r}_i+\mathbf{u}(\mathbf{r}_i)]} \\ &= \sum_i f_{e,i}(\mathbf{q})\, e^{-i\mathbf{q}\cdot\mathbf{r}_i}\, e^{-i\mathbf{q}\cdot\mathbf{u}(\mathbf{r}_i)}\end{aligned} \tag{4.23}$$

Note that $e^{-i\mathbf{q}\cdot\mathbf{r}_i}$ is directly proportional to $e^{-i\mathbf{k}\cdot\mathbf{r}_i}$ by definition of the reciprocal vectors. For small displacement fields, $e^{-i\mathbf{q}\cdot\mathbf{u}(\mathbf{r}_i)}$ can truncated to first order in $|\mathbf{u}|$:

$$\langle \mathbf{x}|\Psi\rangle \approx \sum_i f_{e,i}(\mathbf{q})\, e^{-i\mathbf{k}\cdot\mathbf{r}_i}\, [1 - i\mathbf{H}\cdot\mathbf{u}(\mathbf{r}_i)] \tag{4.24}$$

where $\mathbf{q} = \mathbf{H} + \mathbf{k}$ as shown in Figure 2.4.

The displacement field can be modelled using the following phenomenological deformation:

$$\mathbf{u}(\mathbf{r}) = Ae^{-\frac{|\mathbf{r}|^2}{r_p^2}}\hat{\mathbf{r}} \tag{4.25}$$

where A is an arbitrary constant and r_p is a characteristic dimension of the polaron, with an associated full-width at half-maximum of $2\sqrt{2\ln 2}\, r_p$. As will be made clear shortly, the direction vector $\hat{\mathbf{r}}$ is arbitrary, and $\mathbf{u}(\mathbf{r})$ is not assumed to be spherically-symmetric. Substituting this

displacement field in Equation (4.24):

$$\langle \mathbf{x}|\Psi\rangle \approx \sum_i f_{e,i}(\mathbf{q})\, e^{-i\mathbf{k}\cdot\mathbf{r}_i} \left[1 - i\mathbf{H}\cdot\hat{\mathbf{r}} A e^{-\frac{|\mathbf{r}_i|^2}{r_p^2}}\right] \tag{4.26}$$

The evaluation of this expression is most easily done using continuous integration, rather than summation. Let $\mathbf{r}_i \to \mathbf{r}$, $\sum_i \to \int d\mathbf{r}$, and $f_{e,i} \to f_e$ be the appropriate average atomic form factor for all atomic species. Equation (4.26) becomes:

$$\begin{aligned}\langle \mathbf{x}|\Psi\rangle &\approx f_e(\mathbf{q}) \int d\mathbf{r}\, e^{-i\mathbf{k}\cdot\mathbf{r}} \left[1 - i\mathbf{H}\cdot\hat{\mathbf{r}} A e^{-\frac{|\mathbf{r}|^2}{r_p^2}}\right] \\ &\approx 4\pi f_e(\mathbf{q}) \left[\delta(\mathbf{k}) - i\mathbf{H}\cdot\hat{\mathbf{r}} A\sqrt{\pi} r_p e^{-\frac{|\mathbf{k}|^2 r_p^2}{4}}\right]\end{aligned} \tag{4.27}$$

The scattering intensity is proportional to $|\langle \mathbf{x}|\Psi\rangle|^2$:

$$\begin{aligned} I(\mathbf{q}) &= |\langle \mathbf{x}|\Psi\rangle|^2 \\ &= |4\pi f_e(\mathbf{q})|^2 \left|\delta(\mathbf{k}) - i\mathbf{H}\cdot\hat{\mathbf{r}} A\sqrt{\pi} r_p e^{-\frac{|\mathbf{k}|^2 r_p^2}{4}}\right|^2 \\ &= |4\pi f_e(\mathbf{q})|^2 \left[\delta(\mathbf{k}) - i\mathbf{H}\cdot\hat{\mathbf{r}} A\sqrt{\pi} r_p e^{-\frac{|\mathbf{k}|^2 r_p^2}{4}}\right]\left[\delta(\mathbf{k}) + i\mathbf{H}\cdot\hat{\mathbf{r}} A\sqrt{\pi} r_p e^{-\frac{|\mathbf{k}|^2 r_p^2}{4}}\right] \\ &= |4\pi f_e(\mathbf{q})|^2 \left[\delta(\mathbf{k})^2 + A^2\pi(\mathbf{H}\cdot\hat{\mathbf{r}})^2 r_p^2 e^{-\frac{|\mathbf{k}|^2 r_p^2}{2}}\right] \\ &= I_0(\mathbf{q}) + |4\pi f_e(\mathbf{q})|^2\, \pi r_p^2 e^{-\frac{|\mathbf{k}|^2 r_p^2}{2}} (\mathbf{H}\cdot\hat{\mathbf{r}})^2 \end{aligned} \tag{4.28}$$

where I_0 is the scattering intensity without lattice distortion. It follows that the fractional change in scattering intensity is given by:

$$\begin{aligned}\frac{I(\mathbf{q}) - I_0(\mathbf{q})}{I_0(\mathbf{q})} &\equiv \Delta I / I_0 \\ &\propto \frac{r_p^2 e^{-\frac{|\mathbf{k}|^2 r_p^2}{2}}}{I_0}\, \hat{\mathbf{H}}\cdot\hat{\mathbf{r}}\end{aligned} \tag{4.29}$$

where $\hat{\mathbf{H}}$ is used to denote the unit vector along the $\mathbf{H}$ reflection. Assuming that the scattering intensity without polaronic lattice distortion ($I_0 \sim \delta^2(\mathbf{k})$) falls off like $1/\mathbf{k}$:[88]

$$\Delta I / I_0 \propto |\mathbf{k}| r_p^2 e^{-\frac{|\mathbf{k}|^2 r_p^2}{2}}\, \hat{\mathbf{H}}\cdot\hat{\mathbf{r}} \tag{4.30}$$

Importantly, whether $\mathbf{u}(\mathbf{r})$ is three-dimensional or uniaxial only changes at which reflections are relative intensity changes visible ($\hat{\mathbf{H}}\cdot\hat{\mathbf{r}}$). Figure 4.23 shows the contribution of a polaron to

the total scattering intensity profile. Other radially-symmetric displacement fields have been modelled in Guzelturk *et al.*,[88] which only changes the definition of the polaron characteristic length r_p.

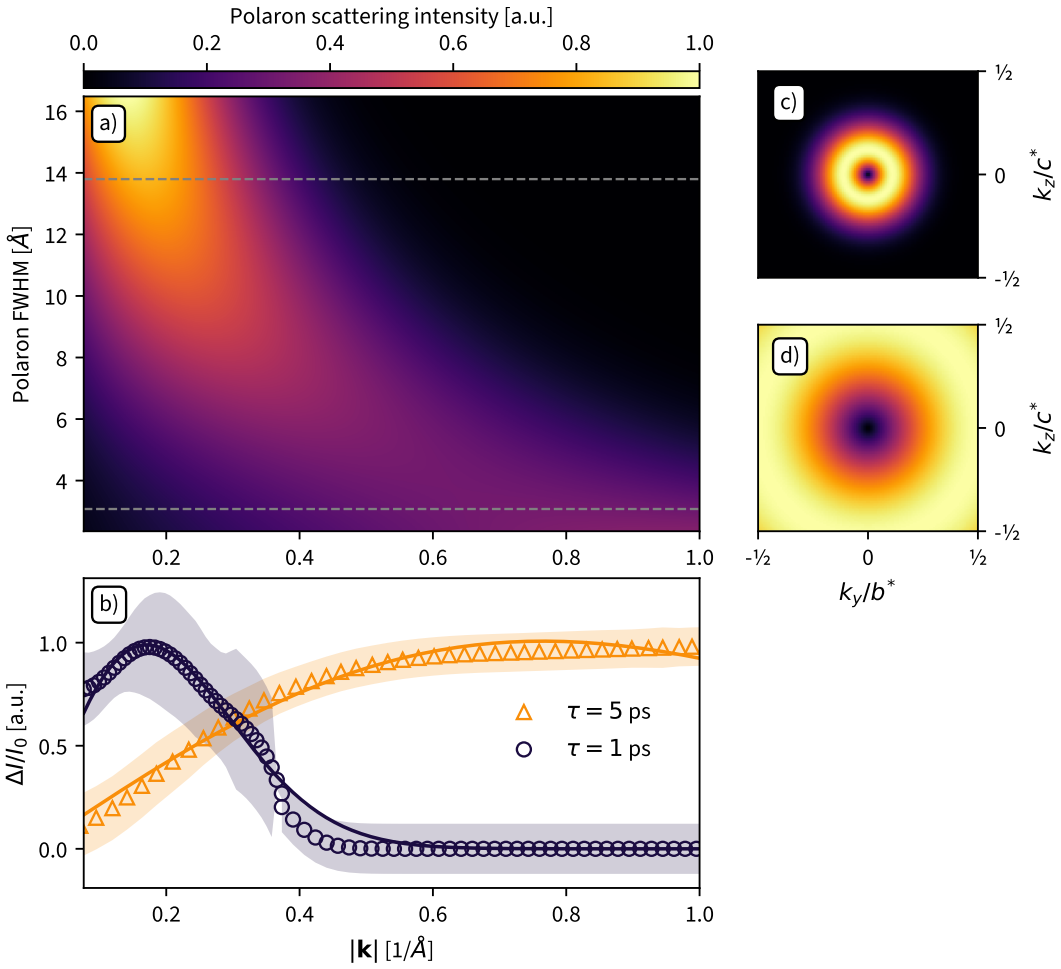

Figure 4.23.: Modeling and fit of scattering intensity due to polarons as a function of polaron size. **a)** Simulated radial intensity profile due to a polaron with a Gaussian displacement field (Equation (4.25)). The color scaling also applies to c) and d) subfigures. **b)** Change in the experimental radial scattering intensity profile for two time-delays after photoexcitation, for reflections nearly parallel to the $\mathbf{c}^*$ axis. The colored areas represents the standard error in the intensity change. Solid curves are best fits to Equation (4.30). The radial profile of the intensity change at 1 ps is consistent with a one-dimensional polaron with a full-width at half-maximum of 13.8 $\pm$ 0.1 Å along the $\mathbf{c}$-axis. The radial profile of the intensity change at 5 ps is consistent with a three-dimensional polaron with a full-width at half-maximum of 3.08 $\pm$ 0.05 Å in the $\mathbf{b}-\mathbf{c}$ plane. **c)** Scattering intensity across the Brillouin zone due to the large polaron fit in b). **d)** Scattering intensity across the Brillouin zone due to the small polaron fit in b).

4.6.3.2. Dynamic polaron formation

The change in the diffuse intensity profile at two characteristic timescales – 1 ps and 5 ps – can be fit using the modelling of Equation (4.30). Only reflections which are nearly parallel to $\mathbf{c}^\star$ were used in the following analysis.

For the fast time-scale, the radial diffuse intensity change is much easier to extract using a biexponential fitting over time, much like what is shown in Figure 4.15. This is because directly extracting the diffuse intensity profile at 1 ps includes the nearby Bragg peak contribution. The diffuse intensity change was integrated in a ring of radius $|\mathbf{k}|$, and fit with a biexponential. The diffuse intensity change at 1 ps – the maximum of the curve – is proportional to the amplitude of the fast exponential, and so the exponential amplitude is used as a proxy value. The error in the amplitude is taken to be the uncertainty in the fitting parameter. The fast time-scale is only visible on reflections which are parallel to $\mathbf{c}^\star$ (informing on atomic motion aong the $\mathbf{c}$-axis), and so it is fit with a one-dimensional polaronic strain field of the form $Ae^{-|\mathbf{r}|^2/r_p^2}\hat{\mathbf{c}}$

For the slow time-scale, the Bragg peak dynamics are mostly flat, and so the radial diffuse intensity profile can be extracted directly. This is effectively the azimuthal average of Figure 4.19. The error in the diffuse intensity change at 5 ps is taken to be the standard error in the diffuse intensity at equivalent radii. In this case, the slow diffuse intensity increase is found at all reflections, and so this data is fit to a three-dimensional, spherically-symmetric polaronic strain field of the form $Ae^{-|\mathbf{r}|^2/r_p^2}\hat{\mathbf{r}}$. It is important to recall that the experiments presented herein are insensitive to the atomic motion along the stacking axis $\mathbf{a}$, and so the fits are compatible with a polaronic strain field which is cylindrically-symmetric about the $\mathbf{a}$-axis.

The radial profile changes were fit with the modelling of Equation (4.30) using a nonlinear least-squares routine. The change in radial intensity profile at 1 ps is consistent with a polaron with a full-width at half-maximum of 13.8 $\pm$ 0.1 Å along the $\mathbf{c}$-axis, while the change in radial intensity profile at 5 ps is consistent with a much smaller polaron with a FWHM of 3.08 $\pm$ 0.05 Å in the $\mathbf{b}$–$\mathbf{c}$ plane. The fits are shown in Figure 4.23. In analogy with the work by Sio *et al.*,[87] the large, fast-forming polaron is assigned to be an electron polaron, while the small and slow-forming polaron is assigned to be a hole polaron. It must be emphasized that this assignment is tentative. However, with this assignment in mind, a visualization of the polaronic strain in real-space is shown in Figure 4.24, where the displacement of atoms is calculated based on Born effective charges from Caruso *et al.*[68]

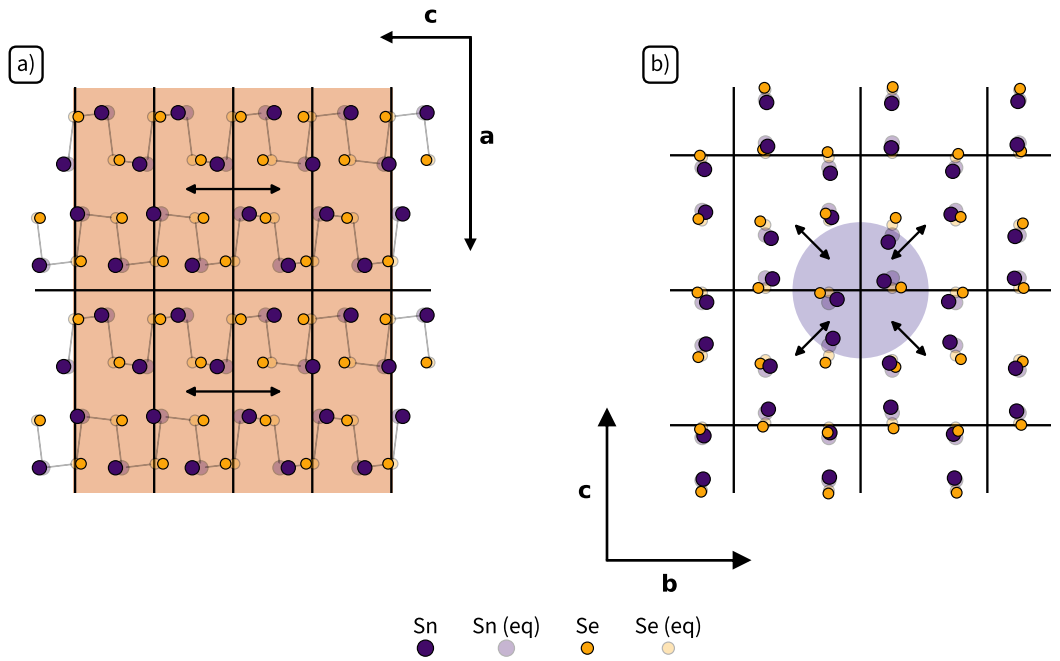

Figure 4.24.: Real-space visualization of the atomic displacement due to the large and small polarons. The magnitude of the atomic displacements is exaggerated for visual clarity. The unperturbed dimensions of the unit cell are marked by solid black lines. In both subpanels, the background color is used to show the full-width at half-maximum of the displacement associated with the polaron. **a)** Large one-dimensional electron polaron along the c-axis. **b)** Small symmetrical hole polaron in the b – c plane.

4.6.4. Polarons and thermoelectric properties

Assuming that the full-width at half-maximum of the polaronic strain field defines the polaron size, the density of overlapping polarons is 3.2 $\times$ 10^{19} cm^{-3} for the larger (electron) polarons and 3.2 $\times$ 10^{21} cm^{-3} for the smaller (hole) polarons. These densities can be compared to the carrier densities generated by the pump pulses. The photocarrier density N_γ is given by $E(f)/V/1.55$ eV, where V is the sample volume, and $E(f)$ is total energy deposited in the sample for a particular fluence f:

$$E(f) = (1-R)\eta f\left(1-e^{-\frac{t}{\delta}}\right) \tag{4.31}$$

Here $R = 0.54$ is the reflectivity at 1.55 eV,[90] $\eta = 0.27$ is the internal quantum efficiency[§], t is the sample thickness, and $\delta = 100$ nm is the penetration depth at 1.55 eV.[90,92] The relationship

[§]The quantum efficiency was determined by B. Dringoli and D. Cooke via time-resolved Terahertz spectroscopy, which is unpublished at this time.[91]

between fluence and N_γ is shown in Figure 4.25 for a 50 µm × 50 µm × 0.045 µm sample.

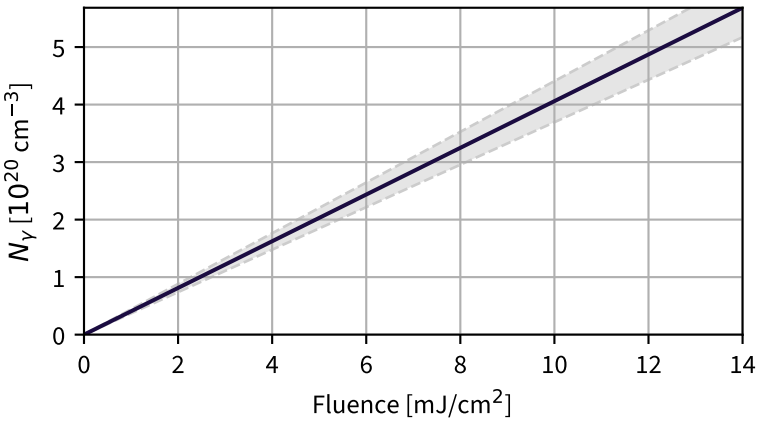

Figure 4.25.: Photocarrier density generated in SnSe for 800 nm pump fluences on a 50 µm × 50 µm × 0.045 µm sample. The lower and upper limits are shown as grey dashed lines, based on the uncertainty of ±5 nm in the thickness of the sample.

The similarity between photocarrier densities and maximal polaron densities imply that if most photocarriers are dressed by phonons, SnSe finds itself in a *polaron liquid* state in which polarons are overlapping, even at the lowest fluence investigated. This polaron density is also in line with the optimal carrier doping in SnSe required for the operation of efficient thermoelectric devices.[7,10,32]

The polaronic nature of the charge-carriers likely explains the phonon-glass, electron-crsytal nature of SnSe.[13] The dressed charges are better isolated from scattering mechanisms because of higher screening. The scattering of undressed charges might otherwise limit the carrier mobility at high temperatures and carrier doping.

4.7. Conclusion

In this chapter, combined ultrafast electron diffraction and diffuse scattering measurements on photodoped SnSe were presented. The measurements showed strong electron-phonon coupling to small-wavevector phonon modes polarized along the lattice distortion of the low-temperature $Pnma$ phase, and uniformly-weaker electron-phonon coupling everywhere else. Bimodal polaron formation was found to be the simplest self-consistent explanation of the data. These results reveal that strong, anisotropic electron-phonon coupling and emerging polaron formation may play a large role in SnSe's ultralow thermal conductivity and carrier

mobility. These findings bring insights into the physics behind one of the best bulk thermoelectric materials, and may pave the way for the design of better thermoelectric devices in the future.

4.7.1. Outlook

There are multiple natural extensions of the research presented in this chapter. Do the phonon dynamics change near 600 K, where the conduction band minimum changes? Can photoexcitation drive the material into a metastable $Cmcm$-like phase with impulsive photodoping? Performing similar ultrafast electron diffuse scattering experiments at higher temperatures would answer these questions. Another important avenue to explore is study high-quality, fully-dense crystals. The crystals used here are the exact same used in Zhao *et al.*,[30] which have been criticized for not being fully-dense[34] (5.43 g cm^{-3} vs. 6.13 g cm^{-3}). This discrepancy in densities brings a drop in DC electrical conductivity by a factor of 10.[30,35] Using high-quality, low-defect samples will enable the simultaneous application of ultrafast electron diffuse scattering and time-resolved terahertz spectroscopy to fully-characterize the determinants of thermoelectricity following impulsive photodoping.

Monolayer SnSe has been suggested as a possible platform for ultrathin ferroelectrics.[51] The measurements presented herein are not sensitive to the dynamics along the $\mathbf{a}$-axis (interlayer direction), but it is possible that interlayer coupling contributes to the results presented in this chapter. More experiments with a view of dynamics along the stacking axis are needed to determine the potential ferroelectric nature of polarons in SnSe as has been investigated in lead halide perovskites.[93,94,95]

Theoretical work from Sio *et al*[87] has demonstrated how density functional perturbation theory frameworks (which were used in Chapter 3) can be extended to the study of polaron formation in materials. With the modelling of polaronic strain on ultrafast electron diffuse scattering presented in Section 4.6.3, no doubt that experimental and computational approaches will be combined in the near future to further understand the effects of impulsive carrier doping in complex materials.

References

[1] X. Shi, W. You, Y. Zhang, Z. Tao, P. M. Oppeneer, X. Wu, R. Thomale, K. Rossnagel, M. Bauer, H. Kapteyn, and M. Murnane. *Ultrafast electron calorimetry uncovers a new long-lived metastable*

state in 1T-$TaSe_2$ mediated by mode-selective electron-phonon coupling. *Science Advances* **5** no. 3 (2019). DOI: 10.1126/sciadv.aav4449.

[2] S. Ji, O. Grånäs, K. Rossnagel, and J. Weissenrieder. *Transient three-dimensional structural dynamics in 1T-$TaSe_2$*. *Physical Review B* **101** no. 9 (2020), pp. 094303–094313. DOI: 10.1103/physrevb.101.094303.

[3] A. Kogar, M. S. Rak, S. Vig, A. A. Husain, F. Flicker, Y. I. Joe, L. Venema, G. J. MacDougall, T. C. Chiang, E. Fradkin, J. van Wezel, and P. Abbamonte. *Signatures of exciton condensation in a transition metal dichalcogenide*. *Science* **358** no. 6368 (2017), pp. 1314–1317. DOI: 10.1126/science.aam6432.

[4] M. R. Otto, J.-H. Pöhls, L. P. René de Cotret, M. J. Stern, M. Sutton, and B. J. Siwick. *Mechanisms of electron-phonon coupling unraveled in momentum and time: the case of soft phonons in $TiSe_2$*. *Science Advances* **7** no. 20 (2021). DOI: 10.1126/sciadv.abf2810.

[5] G. D. Mahan and J. O. Sofo. *The best thermoelectric*. *Proceedings of the National Academy of Sciences* **93** no. 15 (1996), pp. 7436–7439. DOI: 10.1073/pnas.93.15.7436.

[6] G. J. Snyder and E. S. Toberer. *Complex thermoelectric materials*. *Nature Materials* (2008), pp. 105–114. DOI: 10.1038/nmat2090.

[7] J. R. Sootsman, D. Y. Chung, and M. G. Kanatzidis. *New and old concepts in thermoelectric materials*. *Angewandte Chemie International Edition* **48** no. 46 (2009), pp. 8616–8639. DOI: 10.1002/chin.200952221.

[8] M. Zebarjadi, K. Esfarjani, M. S. Dresselhaus, Z. F. Ren, and G. Chen. *Perspectives on thermoelectrics: from fundamentals to device applications*. *Energy & Environmental Science* **5** no. 1 (2012), pp. 5147–5162. DOI: 10.1039/c1ee02497c.

[9] *Mars 2020 mission Perseverance rover technical specifications*. https://mars.nasa.gov/mars2020/spacecraft/rover/electrical-power/. Accessed: 2021-03-03. 2021.

[10] D. D. Fan, H. J. Liu, L. Cheng, J. H. Liang, and P. H. Jiang. *A first-principles study of the effects of electron-phonon coupling on the thermoelectric properties: a case study of the SiGe compound*. *Journal of Materials Chemistry A* **6** no. 25 (2018), pp. 12125–12131. DOI: 10.1039/c8ta01806e.

[11] M. Telkes. *The efficiency of thermoelectric generators I*. *Journal of Applied Physics* **18** no. 12 (1947), pp. 1116–1127. DOI: 10.1063/1.1697593.

[12] H. Zhang and D. V. Talapin. *Thermoelectric tin selenide: the beauty of simplicity*. *Angewandte Chemie International Edition* **53** no. 35 (2014), pp. 9126–9127. DOI: 10.1002/anie.201405683.

[13] D. M. Rowe. *CRC handbook of thermoelectrics*. Chemical Rubber Company Press, 1995.

[14] E. S. Rittner. *On the theory of the Peltier heat pump*. *Journal of Applied Physics* **30** no. 5 (1959), pp. 702–707. DOI: 10.1063/1.1735218.

[15] L. D. Hicks and M. S. Dresselhaus. *Effect of quantum-well structures on the thermoelectric figure of merit*. *Physical Review B* **47** no. 19 (1993), p. 12727. DOI: 10.1103/physrevb.47.12727.

[16] N. S. Bennett. *Thermoelectric performance in n-type bulk silicon: the influence of dopant concentration and dopant species*. *Physica Status Solidi A* **214** no. 7 (2017), p. 1700307. DOI: 10.1002/pssa.201700307.

[17] H. Ikeda and F. Salleh. *Influence of heavy doping on Seebeck coefficient in silicon-on-insulator*. *Applied Physics Letters* **96** no. 1 (2010), p. 012106. DOI: 10.1063/1.3282783.

[18] M. Fiorentini and N. Bonini. *Thermoelectric coefficients of n-doped silicon from first principles via the solution of the Boltzmann transport equation*. *Physical Review B* **94** no. 8 (2016), pp. 085204–085215. DOI: 10.1103/physrevb.94.085204.

[19] R. Franz and G. Wiedemann. *Ueber die Wärme-Leitungsfähigkeit der Metalle*. *Annalen der Physik* **165** no. 8 (1853), pp. 497–531. DOI: 10.1002/andp.18531650802.

[20] L. D. Hicks and M. S. Dresselhaus. *Thermoelectric figure of merit of a one-dimensional conductor*. *Physical Review B* **47** no. 24 (1993), p. 16631. DOI: 10.1103/physrevb.47.16631.

[21] J. P. Heremans, M. S. Dresselhaus, L. E. Bell, and D. T. Morelli. *When thermoelectrics reached the nanoscale*. *Nature Nanotechnology* **8** no. 7 (2013), pp. 471–473. DOI: 10.1038/nnano.2013.129.

[22] L. D. Hicks, T. C. Harman, X. Sun, and M. S. Dresselhaus. *Experimental study of the effect of quantum-well structures on the thermoelectric figure of merit*. *Physical Review B* **53** no. 16 (1996), R10493. DOI: 10.1109/ict.1996.553525.

[23] P. L. Kapitza. *The study of heat transfer in helium II*. In: *Helium 4*. Elsevier, 1971, pp. 114–153. DOI: 10.1016/b978-0-08-015816-7.50014-6.

[24] D. M. Rowe. *Theoretical optimization of the thermoelectric figure of merit of heavily doped hot-pressed germanium-silicon alloys*. *Journal of Physics D: Applied Physics* **7** no. 13 (1974), p. 1843. DOI: 10.1088/0022-3727/7/13/310.

[25] G. Joshi, H. Lee, Y. Lan, X. Wang, G. Zhu, D. Wang, R. W. Gould, D. C. Cuff, M. Y. Tang, M. S. Dresselhaus, G. Chen, and Z. Ren. *Enhanced thermoelectric figure-of-merit in nanostructured p-type silicon germanium bulk alloys*. *Nano Letters* **8** no. 12 (2008), pp. 4670–4674. DOI: 10.1021/nl8026795.

[26] A. J. Minnich, M. S. Dresselhaus, Z. F. Ren, and G. Chen. *Bulk nanostructured thermoelectric materials: current research and future prospects*. *Energy & Environmental Science* **2** no. 5 (2009), pp. 466–479. DOI: 10.1039/b822664b.

[27] H. Wang, A. D. LaLonde, Y. Pei, and G. J. Snyder. *The criteria for beneficial disorder in thermoelectric solid solutions*. *Advanced Functional Materials* **23** no. 12 (2013), pp. 1586–1596. DOI: 10.1002/adfm.201201576.

[28] G. A. Slack. In: *CRC handbook of thermoelectrics*. Ed. by D. M. Rowe. Chemical Rubber Company Press, 1995. Chap. 34, pp. 407–447.

[29] T. C. Harman, D. L. Spears, and M. J. Manfra. *High thermoelectric figures of merit in PbTe quantum wells*. *Journal of Electronic Materials* **25** no. 7 (1996), pp. 1121–1127. DOI: 10.1007/bf02659913.

[30] L.-D. Zhao, S.-H. Lo, Y. Zhang, H. Sun, G. Tan, C. Uher, C. Wolverton, V. P. Dravid, and M. G. Kanatzidis. *Ultralow thermal conductivity and high thermoelectric figure of merit in SnSe crystals*. *Nature* **508** no. 7496 (2014), pp. 373–377. DOI: 10.1038/nature13184.

[31] K. Miyata, T. L. Atallah, and X.-Y. Zhu. *Lead halide perovskites: crystal-liquid duality, phonon glass electron crystals, and large polaron formation*. *Science Advances* **3** no. 10 (2017). DOI: 10.1126/sciadv.1701469.

[32] L.-D. Zhao, G. Tan, S. Hao, J. He, Y. Pei, H. Chi, H. Wang, S. Gong, H. Xu, V. P. Dravid, C. Uher, G. J. Snyder, C. Wolverton, and M. G. Kanatzidis. *Ultrahigh power factor and thermoelectric performance in hole-doped single-crystal SnSe*. *Science* **351** no. 6269 (2016), pp. 141–144. DOI: 10.1126/science.aad3749.

[33] L.-D. Zhao, C. Chang, G. Tan, and M. G. Kanatzidis. *SnSe: a remarkable new thermoelectric material*. *Energy & Environmental Science* **9** no. 10 (2016), pp. 3044–3060. DOI: 10.1039/c6ee01755j.

[34] P.-C. Wei, S. Bhattacharya, J. He, S. Neeleshwar, R. Podila, Y. Y. Chen, and A. M. Rao. *The intrinsic thermal conductivity of SnSe*. *Nature* **539** no. 7627 (2016), E1–E2. DOI: 10.1038/nature19832.

[35] P.-C. Wei, S. Bhattacharya, Y.-F. Liu, F. Liu, J. He, Y.-H. Tung, C.-C. Yang, C.-R. Hsing, D.-L. Nguyen, C.-M Wei, M.-Y. Chou, Y.-C. Lai, T.-L. Hung, S.-Y. Guan, C.-S. Chang, H.-J. Wu, C.-H. Lee, W.-H. Li, R. P. Hermann, Y.-Y. Chen, and A. M. Rao. *Thermoelectric figure-of-merit of fully dense single-crystalline SnSe*. *ACS Omega* **4** no. 3 (2019), pp. 5442–5450. DOI: 10.1021/acsomega.8b03323.

[36] L. Li, Y. Yu, G. J. Ye, Q. Ge, X. Ou, H. Wu, D. Feng, X. H. Chen, and Y. Zhang. *Black phosphorus field-effect transistors*. *Nature Nanotechnology* **9** no. 5 (2014), pp. 372–377. DOI: 10.1038/nnano.2014.35.

[37] x. Ling, h. Wang, s. Huang, f. Xia, and M. S. Dresselhaus. *The renaissance of black phosphorus*. *Proceedings of the National Academy of Sciences* **112** no. 15 (2015), pp. 4523–4530. DOI: 10.1073/pnas.1416581112.

[38] M. Wu and X. C. Zeng. *Intrinsic ferroelasticity and/or multiferroicity in two-dimensional phosphorene and phosphorene analogues*. *Nano Letters* **16** no. 5 (2016), pp. 3236–3241. DOI: 10.1021/acs.nanolett.6b00726.

[39] H. Seiler, D. Zahn, M. Zacharias, P.-N. Hildebrandt, T. Vasileiadis, Y. W. Windsor, Y. Qi, C. Carbogno, C. Draxl, R. Ernstorfer, and F. Caruso. *Accessing the anisotropic nonthermal phonon populations in black phosphorus*. *Nano Letters* (2021). DOI: 10.1021/acs.nanolett.1c01786.

[40] T. Chattopadhyay, J. Pannetier, and H. G. Von Schnering. *Neutron diffraction study of the structural phase transition in SnS and SnSe*. *Journal of Physics and Chemistry of Solids* **47** no. 9 (1986), pp. 879–885. DOI: 10.1016/0022-3697(86)90059-4.

[41] J. M. Skelton, L. A. Burton, S. C. Parker, A. Walsh, C.-E. Kim, A. Soon, J. Buckeridge, A. A. Sokol, C. R. A. Catlow, A. Togo, and I. Tanaka. *Anharmonicity in the high-temperature $Cmcm$ phase of SnSe: soft modes and three-phonon interactions*. *Physical Review Letters* **117** no. 7 (2016), p. 075502. DOI: 10.1103/physrevlett.117.075502.

[42] J. Hong and O. Delaire. *Phase transition and anharmonicity in SnSe*. *Materials Today Physics* **10** (2019), p. 100093. DOI: 10.1016/j.mtphys.2019.100093.

[43] M. T. Dove. *Theory of displacive phase transitions in minerals*. *American Mineralogist* **82** no. 3-4 (1997), pp. 213–244. DOI: 10.2138/am-1997-3-401.

[44] X. Gong, H. Wu, D. Yang, B. Zhang, K. Peng, H. Zou, L. Guo, X. Lu, Y. Chai, G. Wang, and X. Zhou. *Temperature dependence of Raman scattering in single crystal SnSe*. *Vibrational Spectroscopy* **107** (2020), p. 103034. DOI: 10.1016/j.vibspec.2020.103034.

[45] F. Liu, P. Parajuli, R. Rao, P. C. Wei, A. Karunarathne, S. Bhattacharya, R. Podila, J. He, B. Maruyama, G. Priyadarshan, J. R. Gladden, Y. Y Chen, and A. M. Rao. *Phonon anharmonicity in single-crystalline SnSe*. *Physical Review B* **98** no. 22 (2018), p. 224309. DOI: 10.1103/physrevb.98.224309.

[46] D. D. Cuong, S. H. Rhim, J.-H. Lee, and S. C. Hong. *Strain effect on electronic structure and thermoelectric properties of orthorhombic SnSe: a first principles study*. *AIP Advances* **5** no. 11 (2015), p. 117147. DOI: 10.1063/1.4936636.

[47] J. Ma, Y. Chen, and W. Li. *Intrinsic phonon-limited charge carrier mobilities in thermoelectric SnSe*. *Physical Review B* **97** no. 20 (2018), pp. 205207–205215. DOI: 10.1103/physrevb.97.205207.

[48] C. W. Li, J. Hong, A. F. May, D. Bansal, S. Chi, T. Hong, G. Ehlers, and O. Delaire. *Orbitally driven giant phonon anharmonicity in SnSe*. *Nature Physics* **11** no. 12 (2015), pp. 1063–1069. DOI: 10.1038/nphys3492.

[49] K. Kutorasinski, B. Wiendlocha, S. Kaprzyk, and J. Tobola. *Electronic structure and thermoelectric properties of n- and p-type SnSe from first-principles calculations*. *Physical Review B* **91** no. 20 (2015), p. 205201. DOI: 10.1103/physrevb.91.205201.

[50] K. Kuroki and R. Arita. *"Pudding mold" band drives large thermopower in Na_xCoO_2*. *Journal of the Physical Society of Japan* **76** no. 8 (2007), pp. 083707–083707. DOI: 10.1143/jpsj.76.083707.

[51] R. Fei, W. Kang, and L. Yang. *Ferroelectricity and phase transitions in monolayer group-IV monochalcogenides*. *Physical Review Letters* **117** no. 9 (2016), pp. 097601–097607. DOI: 10.1103/physrevlett.117.097601.

[52] N. Erasmus, M. Eichberger, K. Haupt, I. Boshoff, G. Kassier, R. Birmurske, H. Berger, J. Demsar, and H. Schwoerer. *Ultrafast dynamics of charge density waves in $4H_b$ – $TaSe_2$ probed by femtosecond electron diffraction*. *Physical Review Letters* **109** no. 16 (2012), p. 167402. DOI: 10.1103/physrevlett.109.167402.

[53] M. Eichberger, M. Krumova, H. Berger, and J. Demsar. *Sample preparation methods for femtosecond electron diffraction experiments*. *Ultramicroscopy* **127** (2013), pp. 9–13. DOI: 10.1016/j.ultramic.2012.07.005.

[54] K. S. Novoselov, A. K. Geim, S. V. Morozov, D. Jiang, Y. Zhang, S. V. Dubonos, I. V. Grigorieva, and A. A. Firsov. *Electric field effect in atomically thin carbon films*. *Science* **306** no. 5696 (2004), pp. 666–669. DOI: 10.1126/science.1102896.

[55] M. R. Otto, L. P. René de Cotret, M. J. Stern, and B. J. Siwick. *Solving the jitter problem in microwave compressed ultrafast electron diffraction instruments: robust sub-50 fs cavity-laser phase stabilization*. *Structural Dynamics* **4** no. 5 (2017), p. 051101. DOI: 10.1063/1.4989960.

[56] T. Ida, M. Ando, and H. Toraya. *Extended pseudo-Voigt function for approximating the Voigt profile*. *Journal of Applied Crystallography* **33** no. 6 (2000), pp. 1311–1316. DOI: 10.1107/s0021889800010219.

[57] B. Fultz and J. Howe. In: *Transmission electron microscopy and diffractometry of materials*. Springer, 2013. Chap. 9.

[58] B. Fultz and J. Howe. In: *Transmission electron microscopy and diffractometry of materials*. Section 7.4. Springer, 2013.

[59] B. E. Warren. In: *X-ray diffraction*. Dover Publications, 1990. Chap. 11, pp. 191–193.

[60] B. E. Warren. In: *X-ray diffraction*. Dover Publications, 1990. Chap. 3, pp. 36–37.

[61] P. R. Bevington and D. K. Robinson. *Error analysis*. In: *Data reduction and error analysis*. McGraw-Hill, New York, 2003. Chap. 3.

[62] T. Ando. *Anomaly of optical phonon in monolayer graphene*. *Journal of the Physical Society of Japan* **75** no. 12 (2006), p. 124701. DOI: 10.1143/jpsj.75.124701.

[63] W. Kohn. *Image of the Fermi surface in the vibration spectrum of a metal*. *Physical Review Letters* **2** no. 9 (1959), p. 393. DOI: 10.1103/physrevlett.2.393.

[64] G. D. Mahan. In: *Many-particle physics*. Equation 2.73. Springer, 2000. Chap. 2.

[65] F. Giustino. *Electron-phonon interactions from first principles*. *Reviews of Modern Physics* **89** no. 1 (2017), p. 015003. DOI: 10.1103/revmodphys.89.015003.

[66] A. B. Migdal. *Interaction between electrons and lattice vibrations in a normal metal*. *Soviet Physics JETP* **7** no. 6 (1958), pp. 996–1001.

[67] J. Noffsinger, F. Giustino, B. D. Malone, C.-H. Park, S. G. Louie, and M. L. Cohen. EPW*: a program for calculating the electron–phonon coupling using maximally localized Wannier functions*. *Computer Physics Communications* **181** no. 12 (2010), pp. 2140–2148. DOI: 10.1016/j.cpc.2010.08.027.

[68] F. Caruso, M. Troppenz, S. Rigamonti, and C. Draxl. *Thermally enhanced Fröhlich coupling in SnSe*. *Physical Review B* **99** no. 8 (2019), p. 081104. DOI: 10.1103/physrevb.99.081104.

[69] B. Liao, B. Qiu, J. Zhou, S. Huberman, K. Esfarjani, and G. Chen. *Significant reduction of lattice thermal conductivity by the electron-phonon interaction in silicon with high carrier concentrations: a first-principles study*. *Physical Review Letters* **114** no. 11 (2015), p. 115901. DOI: 10.1103/physrevlett.114.115901.

[70] J. Zhou, H. D. Shin, K. Chen, B. Song, R. A. Duncan, Q. Xu, A. A. Maznev, K. A. Nelson, and G. Chen. *Direct observation of large electron-phonon interaction effect on phonon heat transport*. *Nature Communications* **11** no. 6040 (2020). DOI: 10.1038/s41467-020-19938-9.

[71] A. F. Ioffe and A. R. Regel. *Non-crystalline, amorphous and liquid electronic semiconductors*. *Progress in Semiconductors* **4** no. 89 (1960), pp. 237–291.

[72] N. F. Mott. *Metal-insulator transitions*. Taylor and Francis, 1974.

[73] M. Gurvitch. *Ioffe-Regel criterion and resistivity of metals*. *Physical Review B* **24** no. 12 (1981), p. 7404. DOI: 10.1103/physrevb.24.7404.

[74] J. Zhang, E. D. Kountz, E. M. Levenson-Falk, D. Song, R. L. Greene, and A. Kapitulnik. *Thermal diffusivity above the Mott-Ioffe-Regel limit*. *Physical Review B* **100** no. 24 (2019), p. 241114. DOI: 10.1103/physrevb.100.241114.

[75] T. Lanigan-Atkins, S. Yang, J. L. Niedziela, D. Bansal, A. F. May, A. A. Puretzky, J. Y. Y. Lin, D. M. Pajerowski, T. Hong, S. Chi, G. Ehlers, and O. Delaire. *Extended anharmonic collapse of phonon dispersions in SnS and SnSe*. *Nature Communications* **11** no. 1 (2020), pp. 1–9. DOI: 10.1038/s41467-020-18121-4.

[76] H. R. Chandrasekhar, R. G. Humphreys, U. Zwick, and M. Cardona. *Infrared and Raman spectra of the IV-VI compounds SnS and SnSe*. *Physical Review B* **15** no. 4 (1977), p. 2177. DOI: 10.1103/physrevb.15.2177.

[77] J. Sjakste, K. Tanimura, G. Barbarino, L. Perfetti, and N. Vast. *Hot electron relaxation dynamics in semiconductors: assessing the strength of the electron–phonon coupling from the theoretical and experimental viewpoints*. *Journal of Physics: Condensed Matter* **30** no. 35 (2018), p. 353001. DOI: 10.1088/1361-648x/aad487.

[78] W. Shi, M. Gao, J. Wei, J. Gao, C. Fan, E. Ashalley, H. Li, and Z. Wang. *Tin selenide (SnSe): growth, properties, and applications*. *Advanced Science* **5** no. 4 (2018), p. 1700602. DOI: 10.1002/advs.201700602.

[79] R. Peierls. *Zur kinetischen Theorie der Wärmeleitung in Kristallen*. *Annalen der Physik* **395** no. 8 (1929), pp. 1055–1101. DOI: 10.1002/andp.19293950803.

[80] M. J Stern, L. P. René de Cotret, M. R. Otto, R. P. Chatelain, J.-P. Boisvert, M. Sutton, and B. J. Siwick. *Mapping momentum-dependent electron-phonon coupling and nonequilibrium phonon dynamics with ultrafast electron diffuse scattering*. *Physical Review B* **97** no. 16 (2018), p. 165416. DOI: 10.1103/physrevb.97.165416.

[81] L. P. René de Cotret, J.-H. Pöhls, M. J. Stern, M. R. Otto, M. Sutton, and B. J. Siwick. *Time-and momentum-resolved phonon population dynamics with ultrafast electron diffuse scattering*. *Physical Review B* **100** no. 21 (2019), p. 214115. DOI: 10.1103/physrevb.100.214115.

[82] L. D. Landau. *On the motion of electrons in a crystal lattice*. *Physikalische Zeitschrift der Sowjetunion* **3** (1933), p. 664.

[83] H. Fröhlich, H. Pelzer, and S. Zienau. *Properties of slow electrons in polar materials*. *The London, Edinburgh, and Dublin Philosophical Magazine and Journal of Science* **41** no. 314 (1950), pp. 221–242. DOI: 10.1080/14786445008521794.

[84] R. P. Feynman. *Slow electrons in a polar crystal*. *Physical Review* **97** no. 3 (1955), pp. 660–665. DOI: 10.1103/physrev.97.660.

[85] T. Holstein. *Studies of polaron motion*. *Annals of Physics* **8** no. 3 (1959), pp. 325–342. DOI: 10.1016/0003-4916(59)90002-8.

[86] C. Franchini, M. Reticcioli, M. Setvin, and U. Diebold. *Polarons in materials*. *Nature Reviews Materials* (2021). DOI: 10.1038/s41578-021-00289-w.

[87] W. H. Sio, C. Verdi, S. Poncé, and F. Giustino. *Ab initio theory of polarons: formalism and applications*. *Physical Review B* **99** no. 23 (2019), pp. 235139–235160. DOI: 10.1103/physrevb.99.235139.

[88] B. Guzelturk, T. Winkler, T. W. J. Van de Goor, M. D. Smith, S. A. Bourelle, S. Feldmann, M. Trigo, S. W. Teitelbaum, H.-G. Steinrück, G. A. de la Pena, R. Alonso-Mori, D. Zhu, T. Sato, H. I. Karunadasa, M. F. Toney, F. Deschler, and A. M. Lindenberg. *Visualization of dynamic polaronic strain fields in hybrid lead halide perovskites*. *Nature Materials* **20** no. 5 (2021), pp. 618–623. DOI: 10.1038/s41563-020-00865-5.

[89] B. Fultz and J. M. Howe. In: *Transmission electron microscopy and diffractometry of materials*. Section 8.2. Springer, 2013, pp. 351–354.

[90] L. Makinistian and E. A. Albanesi. *On the band gap location and core spectra of orthorhombic IV–VI compounds SnS and SnSe*. *Physica Status Solidi B* **246** no. 1 (2009), pp. 183–191. DOI: 10.1002/pssb.200844235.

[91] B. J. Dringoli and D. G. Cooke. *Quantum efficiency of SnSe at 800nm*. Measured via time-resolved Terahertz spectroscopy following photoexcitation at 1.55 eV. 2021.

[92] E. Barrios-Salgado, M. T. S. Nair, and P. K. Nair. *Chemically deposited SnSe thin films: thermal stability and solar cell application*. *ECS Journal of Solid State Science and Technology* **3** no. 8 (2014), Q169. DOI: 10.1149/2.0131408jss.

[93] J. M. Frost, L. D. Whalley, and A. Walsh. *Slow cooling of hot polarons in halide perovskite solar cells*. *ACS Energy Letters* **2** no. 12 (2017), pp. 2647–2652.

[94] P. P. Joshi, S. F. Maehrlein, and X.-Y. Zhu. *Dynamic screening and slow cooling of hot carriers in lead halide perovskites*. *Advanced Materials* **31** no. 47 (2019), p. 1803054. DOI: 10.1002/adma.201803054.

[95] F. Wang, Y. Fu, M. E. Ziffer, Y. Dai, S. F. Maehrlein, and X.-Y. Zhu. *Solvated electrons in solids—ferroelectric large polarons in lead halide perovskites*. *Journal of the American Chemical Society* **143** no. 1 (2020), pp. 5–16. DOI: 10.1021/jacs.0c10943. URL: https://doi.org/10.1021%2Fjacs.0c10943.

5. Conclusion

Ultrafast electron diffuse scattering was the star of this dissertation. It was motivated in Chapter 1 as a way to get at a nearly-inaccessible facet of the impulse response of quantum systems. The theory of ultrafast diffuse scattering was developed in Chapter 2. It showed that the transient Debye-Waller effect – often measured in ultrafast electron diffraction – is intricately linked with diffuse scattering. In Chapter 3, the perfect benchmark system was studied with an eye for the particular strengths and limitations of diffuse scattering measurements. Those measurements were used to sidestep the ideas of the two-temperature model. Finally, in Chapter 4, ultrafast electron diffraction and diffuse scattering were used in conjunction to elucidate the mystery of thermoelectric performance in one of the best intrinsic thermoelectrics, SnSe. Strong electron-phonon coupling at zone-center suggested that strong carrier-lattice interactions are viable tuning parameters in the optimization of intrinsic thermoelectric performance.

The last chapter on SnSe is a taste of things to come; the future is bright for ultrafast electron scattering. Following fantastic improvements in electron compression stability, 50 fs time-resolution is not far. As new laboratories are built with more stable laser oscillators, further improvements in performance are to be expected, to the point where the observation of direct phonon emission might be realistic.

The author hopes that in the next 5-10 years, ultrafast electron scattering hardware will be commoditized, at which point it will become a standard tool in the study of low-dimensional materials. Given the unique ability to resolve lattice dynamics across the Brillouin zone, ultrafast electron diffuse scattering is poised to democratize the experimental access to strongly-coupled systems and revolutionize our understanding of strong interactions in functional materials.

5.1. Outlook

Beyond the application of ultrafast electron scattering to more functional materials, the advances in experimental capabilities and sample preparation techniques will allow for the reliable observation of lattice dynamics in monolayers. The inversion-symmetry-breaking in many monolayers suggest an important future directions of research regarding the momentum-resolved measurement of lattice dynamics with ultrafast electron scattering: chiral phonons.

The control of electron flow in semiconductor logic gates is approaching a fundamental limit.[1] However, inversion-symmetry breaking in many monolayers have given rise to *valleytronics*, in which electrons in separate conduction valleys have different transport properties.[2,3] In particular, transition metal dichalcogenides such as MoS_2 and WSe_2 couple spin and valley properties via spin-orbit coupling, which makes them a rich playground for the light-based control of valley physics.[4,5,6,7] Chiral phonons – that is, phonons with pseudoangular momentum – are modes which mediate the intravalley scattering of valley-polarized electrons in valleytronic materials.[8] The momentum-resolution of ultrafast electron diffuse scattering would be key in the study of chiral phonons, as in hexagonal lattices they are located at the K/K' points[9,10]

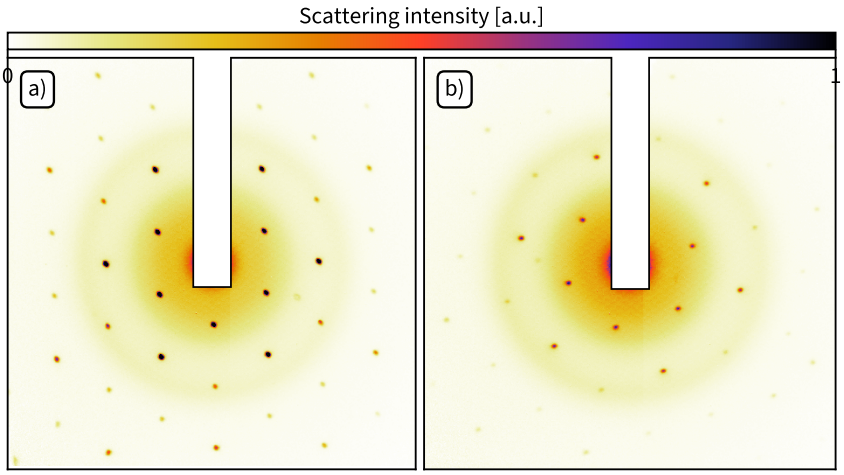

Figure 5.1.: Diffraction patterns of ultrawide (250 µm × 250 µm) monolayers on 10 nm-thick silicon nitride windows. **a)** Monolayer WSe_2. **b)** Monolayer MoS_2.

Although ultrafast electron scattering interacts very strongly with matter, it was not clear whether diffraction and diffuse scattering measurements were possible on such thin samples. In this regard, the future is looking bright. Figure 5.1 shows two diffraction patterns of monolayers

(WSe_2 and MoS_2). These ultrawide monolayers – (250 µm $\times$ 250 µm) – were extracted from a bulk crystal via gold-mediated exfoliation[11,12,13] and deposited on a 10 nm-thick silicon nitride windows. The large area of these monolayers results in a number of diffracting cells that is comparable to typical multilayer samples of smaller area. In fact, the exposition conditions of the diffraction patterns in Figure 5.1 (15 000 shots with a bunch charge of 0.16 pC) are equivalent to those used in Figure 3.7 and Figure 4.8, which shows that ultrafast electron scattaering experiments on monolayers are now possible. There is little doubt that future ultrafast electron scattering measurements will have a large impact on the understanding of lattice dynamics in valleytronics and other exotic phenomena that emerge from symmetry-breaking.

Moiré materials are another key areas where ultrafast electron scattering can make a significant contribution. Strong electron-electron correlations in moiré materials like magic-angle bilayer graphene can give rise to superconductivity[14,15,16] and Mott insulating phases,[17] among other phenomena.[18,19] As was shown in this work, ultrafast momentum-resolved measurements can disentangle interactions in the time- and momentum domains, and elucidate the mysteries behind macroscopic, equilibrium phenomena of interest.

References

1 I. L. Markov. *Limits on fundamental limits to computation*. *Nature* **512** no. 7513 (2014), pp. 147–154. DOI: 10.1038/nature13570.

2 D. Xiao, W. Yao, and Q. Niu. *Valley-contrasting physics in graphene: magnetic moment and topological transport*. *Physcal Review Letters* **99** no. 23 (2007), pp. 236809–236813. DOI: 10.1103/physrevlett.99.236809.

3 J. R. Schaibley, H. Yu, G. Clark, P. Rivera, J. S. Ross, K. L. Seyler, W. Yao, and X. Xu. *Valleytronics in 2D materials*. *Nature Reviews Materials* **1** no. 11 (2016). DOI: 10.1038/natrevmats.2016.55.

4 K. F. Mak, C. Lee, J. Hone, J. Shan, and T. F. Heinz. *Atomically thin MoS_2: a new direct-gap semiconductor*. *Physical Review Letters* **105** no. 13 (2010), pp. 136805–136809. DOI: 10.1103/physrevlett.105.136805.

5 D. Xiao, G.-B. Liu, W. Feng, X. Xu, and W. Yao. *Coupled spin and valley physics in monolayers of MoS_2 and other group-VI dichalcogenides*. *Physical Review Letters* **108** no. 19 (2012), pp. 196802–196807. DOI: 10.1103/physrevlett.108.196802.

[6] T. Cao, G. Wang, W. Han, H. Ye, C. Zhu, J. Shi, Q. Niu, P. Tan, W. Wang, B. Liu, and J. Feng. *Valley-selective circular dichroism of monolayer MoS_2*. *Nature Communications* **3** no. 1 (2012). DOI: 10.1038/ncomms1882.

[7] A. M. Jones, H. Yu, N. J. Ghimire, S. Wu, G. Aivazian, J. S. Ross, B. Zhao, J. Yan, D. G. Mandrus, D. Xiao, W. Yao, and X. Xu. *Optical generation of excitonic valley coherence in monolayer WSe_2*. *Nature Nanotechnology* **8** no. 9 (2013), pp. 634–638. DOI: 10.1038/nnano.2013.151.

[8] S.-Y. Chen, C. Zheng, M. S. Fuhrer, and J. Yan. *Helicity-resolved Raman scattering of MoS_2, $MoSe_2$, WS_2, and WSe_2 atomic layers*. *Nano Letters* **15** no. 4 (2015), pp. 2526–2532. DOI: 10.1021/acs.nanolett.5b00092.

[9] L. Zhang and Q. Niu. *Chiral phonons at high-symmetry points in monolayer hexagonal lattices*. *Physical Review Letters* **115** no. 11 (2015), pp. 115502–115507. DOI: 10.1103/physrevlett.115.115502.

[10] H. Zhu, J. Yi, M.-Y. Li, J. Xiao, L. Zhang, C.-W. Yang, R. A. Kaindl, L.-J. Li, Y. Wang, and X. Zhang. *Observation of chiral phonons*. *Science* **359** no. 6375 (2018), pp. 579–582. DOI: 10.1126/science.aar2711.

[11] S. B. Desai, S. R. Madhvapathy, M. Amani, D. Kiriya, M. Hettick, M. Tosun, Y. Zhou, M. Dubey, J. W. Ager III, D. Chrzan, and A. Javey. *Gold-mediated exfoliation of ultralarge optoelectronically-perfect monolayers*. *Advanced Materials* **28** no. 21 (2016), pp. 4053–4058. DOI: https://doi.org/10.1002/adma.201506171.

[12] F. Liu, M. E. Ziffer, K. R. Hansen, J. Wang, and X.-Y. Zhu. *Direct determination of band-gap renormalization in the photoexcited monolayer MoS_2*. *Physical Review Letters* **122** no. 24 (2019), pp. 246803–246809. DOI: 10.1103/physrevlett.122.246803.

[13] F. Liu, W. Wu, Y. Bai, S. H. Chae, Q. Li, J. Wang, J. Hone, and X.-Y. Zhu. *Disassembling 2D van der Waals crystals into macroscopic monolayers and reassembling into artificial lattices*. *Science* **367** no. 6480 (2020), pp. 903–906. DOI: 10.1126/science.aba1416.

[14] R. Bistritzer and A. H. MacDonald. *Moiré bands in twisted double-layer graphene*. *Proceedings of the National Academy of Sciences* **108** no. 30 (2011), pp. 12233–12237. DOI: 10.1073/pnas.1108174108.

[15] Y. Cao, V. Fatemi, S. Fang, K. Watanabe, T. Taniguchi, W. Kaxiras, and P. Jarillo-Herrero. *Unconventional superconductivity in magic-angle graphene superlattices*. *Nature* **556** no. 7699 (2018), pp. 43–50. DOI: 10.1038/nature26160.

[16] M. Yankowitz, S. Chen, H. Polshyn, Y. Zhang, K. Watanabe, T. Taniguchi, D. Graf, A. F. Young, and C. R. Dean. *Tuning superconductivity in twisted bilayer graphene*. *Science* **363** no. 6431 (2019), pp. 1059–1064. DOI: 10.1126/science.aav1910.

[17] L. Wang, E.-M. Shih, A. Ghiotto, L. Xian, D. A. Rhodes, C. Tan, M. Claassen, D. M. Kennes, Y. Bai, B. Kim, K. Watanabe, T. Taniguchi, X.-Y. Zhu, J. Hone, A. Rubio, A. N. Pasupathy, and C. R. Dean. *Correlated electronic phases in twisted bilayer transition metal dichalcogenides*. *Nature Materials* **19** no. 8 (2020), pp. 861–866. DOI: 10.1038/s41563-020-0708-6.

[18] B. Hunt, J. D. Sanchez-Yamagishi, A. F. Young, M. Yankowitz, B. J. LeRoy, K. Watanabe, T. Taniguchi, P. Moon, M. Koshino, P. Jarillo-Herrero, and R. C. Ashoori. *Massive Dirac fermions and Hofstadter butterfly in a van der Waals heterostructure*. *Science* **340** no. 6139 (2013), pp. 1427–1430. DOI: 10.1126/science.1237240.

[19] K. Tran, G. Moody, F. Wu, X. Lu, J. Choi, K. Kim, A. Rai, D. A. Sanchez, J. Quan, A. Singh, J. Embley, A. Zepeda, M. Campbell, T. Autry, T. Taniguchi, K. Watanabe, N. Lu, S. K. Banerjee, K. L. Silverman, S. Kim, E. Tutuc, L. Yang, A. H. MacDonald, and X. Li. *Evidence for moiré excitons in van der Waals heterostructures*. *Nature* **567** no. 7746 (2019), pp. 71–75. DOI: 10.1038/s41586-019-0975-z.

A. Appendix: Interactive ultrafast electron scattering data exploration

The pursuit of science is accompanied by serious software development in most fields, often in the forms of instrument control, data acquisition, data analysis, and data presentation. One project spearheaded by the author, a graphical program for the interactive exploration of ultrafast electron scattering data,[1] has had such a profound impact on the research within the Siwick research group that it deserves its own brief section.

A.1. Data processing and graphical user interface

Ultrafast electron scattering datasets contain a lot of information, even compared to other time-resolved techniques like optical spectroscopies. The research presented in this dissertation, as well as other research projects within the Siwick group,[2,3] have benefitted from the ability to interactively explore the data. A program was designed and implemented by the author for this very purpose. This program, named `iris`, solves three problems:

1. Data processing: the reduction of raw data, which is often very redundant, into a processed dataset;
2. The interactive exploration of the reduced, processed dataset in real-time in a graphical-user interface;
3. The ability to access the processed data in other computing environments.

A.1.1. Flexible data reduction

Ultrafast electron scattering experiments within the Siwick research group have always had a similar structure. The experiment is divided into subexperiments called *scans*. One scan involves

the acquisition of scattering patterns for all desired time-delays. The scan is then repeated until either some desired number of scans, or until some time has passed. For example, the longest experiments on tin selenide presented in Chapter 4 is composed of 66 scans, each of which is a one hour subexperiment.

Over the years, the specific data-acquisition scheme has changed. For example, time-delays started being acquired in random order (to minimize the effect of drifts in the laser power); a diagnostic of the instrument started being performed every 10 minutes. These new additions changed the way the raw data was acquired, but not what the processed data looked like. To abstract the specifics of the data acquisition scheme, `iris` includes a plug-in system. The specifics of the raw data are described in a Python plug-in, which `iris` reads and determines how to reduce the raw data appropriately. This allows the data acquisition scheme to change within the Siwick research group. Another consequence of the plug-in architecture is that other research groups can write plug-ins for `iris`, and use it in combination with their data acquisition scheme.

A.1.2. Open-source data format

`iris` is designed to store the processed data in an open data format called Hierarchical Data Format version 5 (HDF5). This standardized format possesses three clear advantages when it comes to ultrafast electron scattering datasets. First, data in the form of multi-dimensional arrays can be natively stored in HDF5 files, with control over memory alignment. This means that sections of the data – most importantly time-traces – can be read from file at a high rate. Second, metadata of any type can also be stored in the same HDF5 file as the binary data. Third, there are interfaces between the HDF5 format and many programming languages and computing environments: official bindings[4] include C, C++, Fortran, and Java, while third-party bindings are available for Python,[5] MATLAB,[6] R,[7] and many others.

A.1.3. Interactive exploration

The alignment of HDF5 datasets in memory allows to extract time-series from time-resolved scattering datasets in real-time. This allows datasets reduced by `iris` to be explored interactively. Interactive exploration of time-resolved scattering datasets has profoundly impacted the way research is done in the Siwick research group because the observation of diffuse scattering

signals is not limited to Bragg peaks. With time-resolved diffraction experiments, the dynamics – however complex[8] – can reduced to a set of time-traces, one for each reflection. With diffuse scattering, the space of possibilities is so large that measurements cannot be neatly reduced *a-priori*. Interactive exploration of datasets has been central to the understanding of time-resolved studies on graphite,[2,9] $TiSe_2$,[3] and SnSe (Chapter 4).

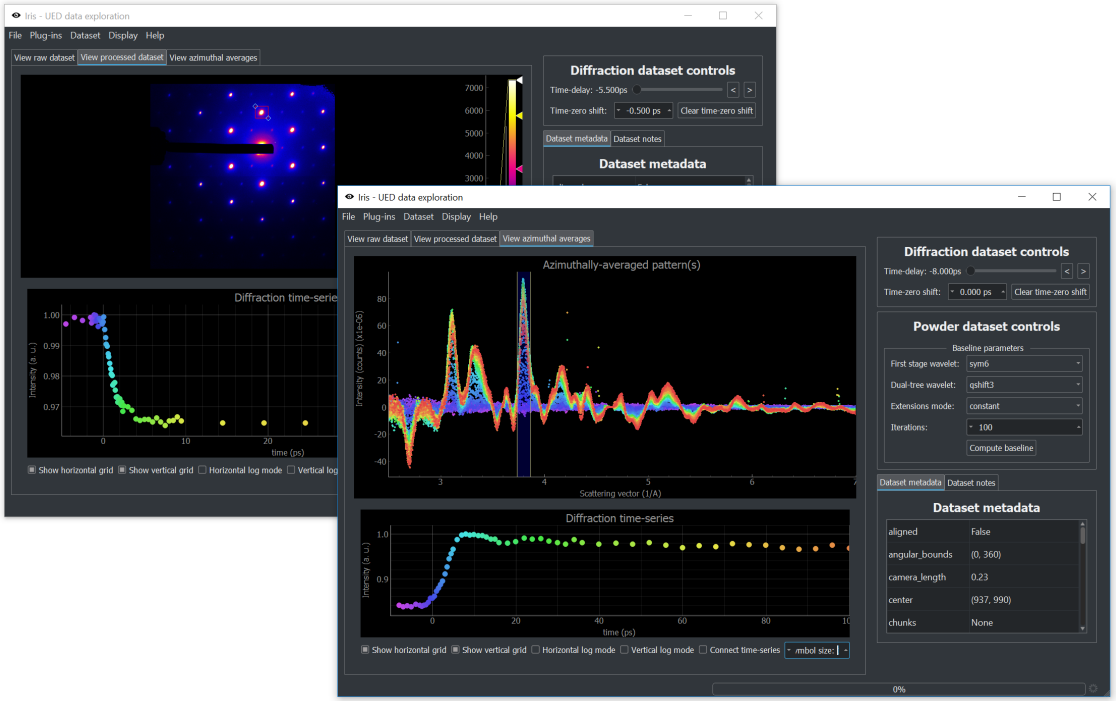

Figure A.1.: Graphical user interface of `iris`. **Background** Interactive exploration of a dataset of photoexcited $TiSe_2$. **Foreground** Interactive exploration of a dataset of photoexcited polycrystalline VO_2

Time-series extraction in the graphical user-interface is shown in Figure A.1 for two types of samples: single-crystal $TiSe_2$ and polycrystalline VO_2. Further data transformations are also possible, some of which are described in Appendix A.3.

A.2. Streaming data reduction

Raw ultrafast electron scattering datasets can reach sizes hundreds of gigabytes. The data reduction operations such as averaging of equivalent scattering patterns is a slow process. Before the author joined the Siwick research group, it used to take multiple hours to finally look at scattering patterns following the end of an experiment.

To effectively reduce the data, a streaming data reduction engine called `npstreams` was developed. `npstreams` extends the de-facto standard array processing library `numpy`[10,11] to work on streams of arrays, that is, sequences of arrays that are not all available in memory at once. Such streams can be created, for example, by loading images one by one from disk; while thousands of images may need to be processed, only 10 or 20 of them might be loaded into memory at any moment. The advantage of streaming lies in the memory savings, which in turns results in much better performance. There are also many streaming algorithms are more performant than the algorithms used by `numpy`.[12]

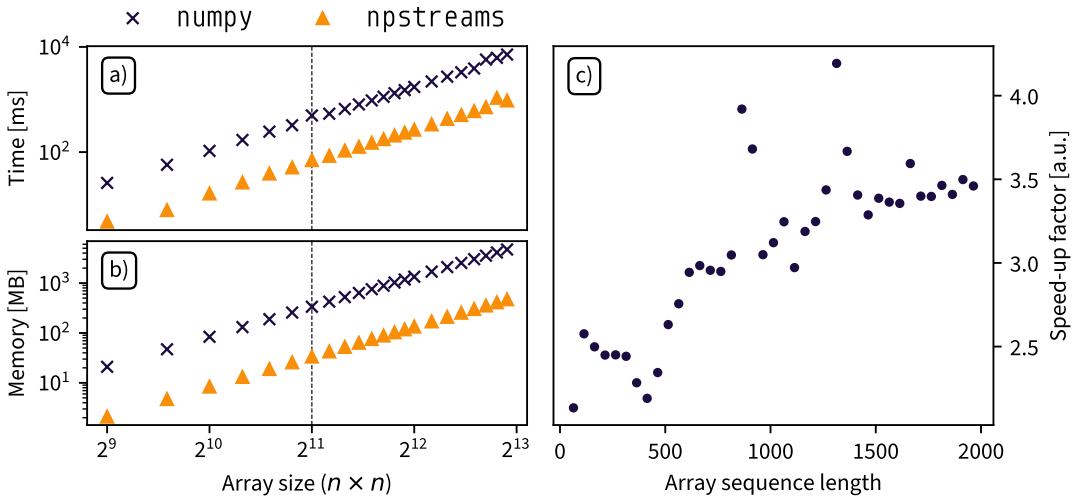

Figure A.2.: Performance comparison between the `npstreams` computational engine and the *de-facto* standard `numpy` at averaging sequences of two-dimensional arrays (representing scattering patterns). **a)** Wall time when averaging a sequence of 10 arrays of size $n \times n$. **b)** Maximum memory usage when averaging a sequence of 10 arrays of size $n \times n$. The vertical line marks the scattering pattern size of the electron camera used in this work (2048×2048). **c)** Speed-up factor of using `npstreams` vs. `numpy` to average a sequence of arrays of size 512×512.

The performance comparison between `npstreams` and `numpy` at averaging sequences of images is presented in Figure A.2. In Figure A.2 a), fixed-length sequences of arrays of size $n \times n$ are averaged. This benchmark shows that the time-saving of using `npstreams` is correlated to the memory savings, as expected. Figure A.2 b), on the other hand, shows how much faster is `npstreams` at averaging variable-length streams of images with a fixed size. For reference, sequences of 100 – 200 arrays of size 2048×2048 had to be averaged for the experiments shown in Chapter 3 and Chapter 4. As a final note, the low memory usage of `npstreams` also allows to parallelize the averaging of images at different time-delays, which increases data reduction

performance by a factor equal to the number of computer cores. Effectively, the data reduction step in the Siwick research group was improved from multiple hours down to less than five minutes.

A.3. Functions and data structure for ultrafast electron scattering

The scientific Python community has access to multiple research-oriented packages called *scikits*,[13] which are extensions of the general-purpose SciPy package.[14]

`scikit-ued` is a package which specializes in routines and data structures relevant to ultrafast electron diffraction and related techniques. `scikit-ued` powers most of the functionality of the graphical program `iris`; it is therefore easy for researchers to incorporate the same analysis techniques in their own workflow. The functionality of `scikit-ued` covers a large area of subjects, including but not limited to:

- Baseline-determination;
- Time-series analysis;
- Image processing;
- Diffraction simulation;
- Visualization and plotting;
- Interface to specialized file formats;
- Electron beam properties.

Some important examples are presented below.

A.3.1. Baseline-determination

Baseline-determination of polycrystalline and single-crystal diffraction patterns is included in `scikit-ued`. For polycrystalline diffraction patterns, an iterative baseline-removal routine[15] based on the dual-tree complex transform.[16] This routine allows for the removal of a baseline without any *a-priori* knowledge. Most importantly, the baseline-removal is stable; small changes in the time-resolved data do not result in large spontaneous changes in the baseline. An example of baseline-removal from a static polycrystalline diffraction pattern of rutile VO_2 is shown in Figure A.3. This approach has also been extended to optical spectroscopy with great success.[17]

For single-crystal diffraction patterns, a two-dimensional iterative baseline-removal based on the discrete wavelet transform is provided.[18]

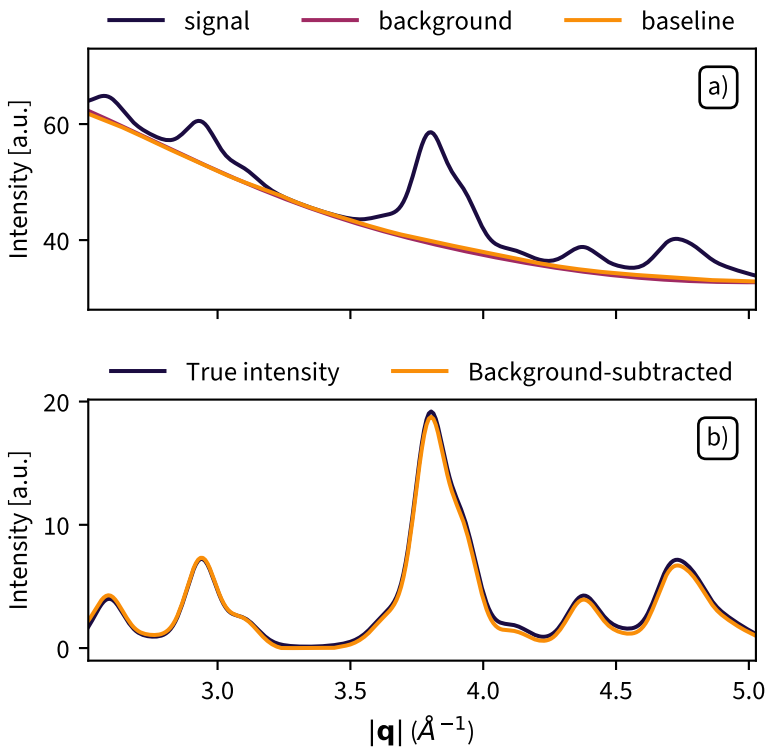

Figure A.3.: Example of baseline-determination using the dual-tree complex wavelet transform. **a)** Polycrystalline diffraction of rutile VO_2 with an added known background, compared to the calculated baseline. **b)** Comparison of the true intensity (signal without background) and the background-subtracted intensity shows excellent agreement, without any prior knowledge about the background.

A.3.2. Parsing

`scikit-ued` includes a parser for multiple obscure file formats in which diffraction patterns are regularly found. Supported file formats include Merlin Image Binary (`.mib`), a proprietary image format for Quantum Detectors' MerlinEM direct electron imaging systems,[19] and Digital Micrograph 3 and 4 (`.dm3`, `.dm4`), proprietary image formats for Gatan Digital Micrograph software suite. In addition, all formats supported by `scikit-image`[13] are also transitively supported, including the Tagged Image File Format (`.tiff`).

A.3.3. Simulation

Simple kinematic simulations of diffraction patterns and associated quantities are available within `scikit-ued`. These simulations are based on the parametrization of atomic electrostatic potential by Kirkland.[20] The simulation modes include polycrystalline diffraction, single-crystal diffraction, electrostatic potential in real space, and projected electrostatic potential in real space. Some examples are presented in Figure A.4.

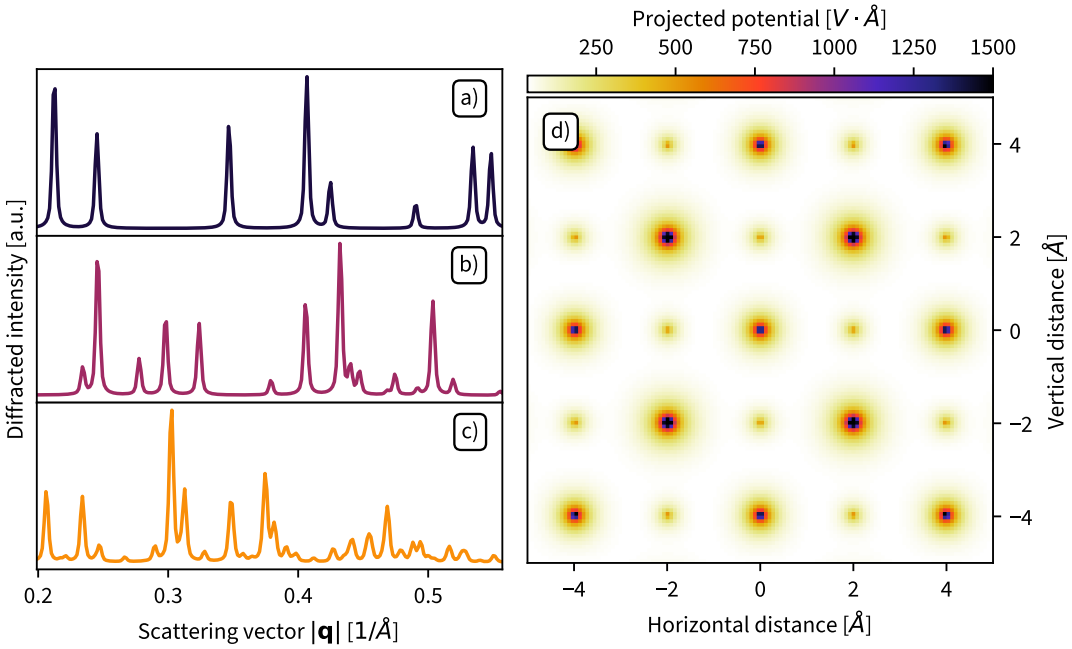

Figure A.4.: Examples of the simulation capabilities. **a)** Polycrystalline diffraction pattern of gold. **b)** Polycrystalline diffraction of graphite. **c)** Polycrystalline diffraction of M_1 vanadium dioxide. **d)** Electrostatic potential of a unit cell of cubic barium titanate, projected down the c axis.

A.3.4. Image processing

The processing of diffraction patterns largely overlaps with photography and image processing. Many routines pertaining to image processing are available in `scikit-image`.[13] `scikit-ued` includes a few routines specific to ultrafast electron scattering which are presented below.

A.3.4.1. Image alignment

During data acquisition, the pointing of the electron beam may shift slightly, which appears as a shift in diffraction patterns. This misalignment prevents the reduction of images which should be equivalent (e.g. same time-delay). This problem is hard to solve because some parts of images – the beam-block, or dead pixels – don't shift with the electron beam, as they are static with respect to the electron detector. To circumvent this problem, `scikit-ued` includes an alignment procedure based on the masked normalized cross-correlation algorithm.[21] This algorithm extends the cross-correlation in the Fourier domain, which is highly optimized, to images with masked segments. An example of this procedure is shown in Figure A.5.

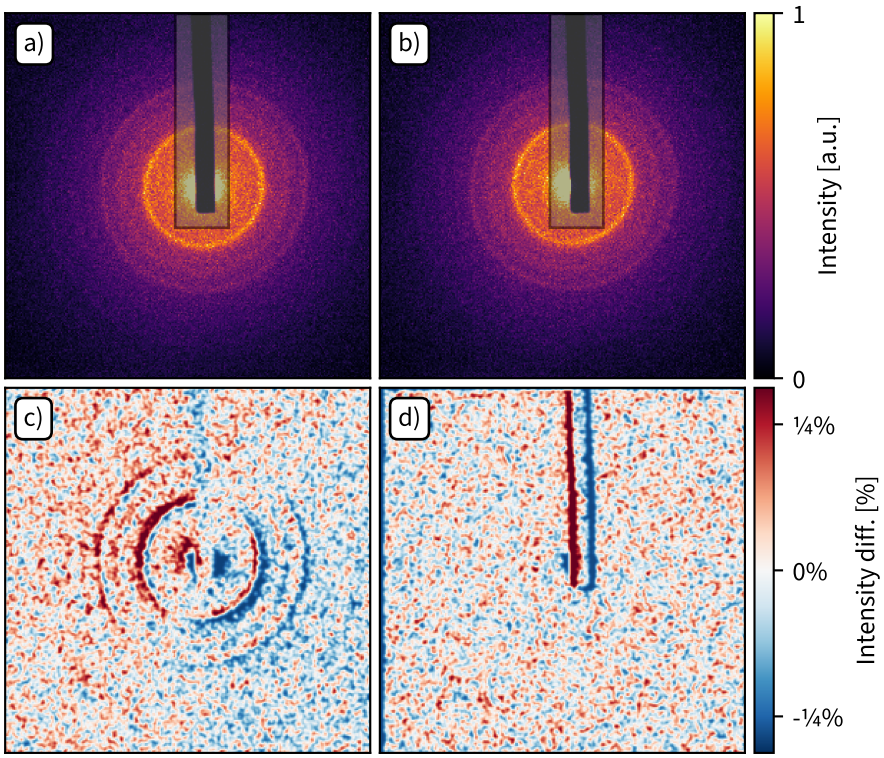

Figure A.5.: Scattering pattern alignment based on the masked normalized cross-correlation algorithm. **a)** Reference diffraction pattern of polycrystalline chromium. The static area to be ignored is shown as a light gray overlay. **b)** Shifted diffraction pattern. **c)** Difference between the reference and shifted pattern. **d)** Difference between the reference and shifted pattern after translation.

A.3.4.2. Automatic center-finding

Many data processing steps require the knowledge of the center of the diffraction patterns, such as Bragg peak-finding and symmetrization. `scikit-ued` includes a routine to automatically find the center of diffraction patterns. The routine measures the shift between an image and the centro-inverted image, based on initial guesses of the center. This shift is then used to infer the center of the image in a procedure similar to the previous section. This procedure is a generalization of the approach presented in Liu,[22] extended to work on any centrosymmetric image. An example of automatic center-finding for both polycrystalline and single-crystal diffraction patterns is shown in Figure A.6.

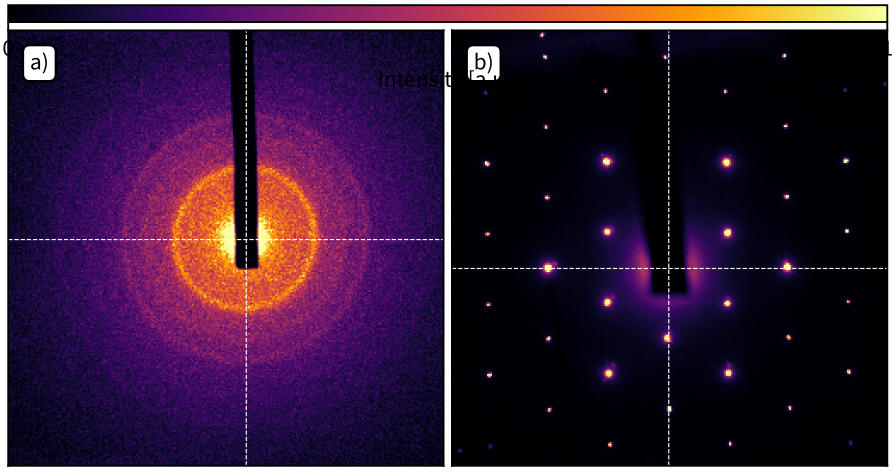

Figure A.6.: Automatic determination of the center of diffraction patterns for **a)** polycrystalline chromium and **b)** single-crystal graphite.

A.3.4.3. Symmetrization

The symmetrization of diffraction pattern, first used in Section 3.2.2, is an image processing technique which point-group applies symmetry rules to images to enhance the signal-to-noise ratio. Supported symmetry operations are mirror planes and discrete rotational symmetry. An example of symmetrization based on the $D6h$ point group is shown in Figure A.7.

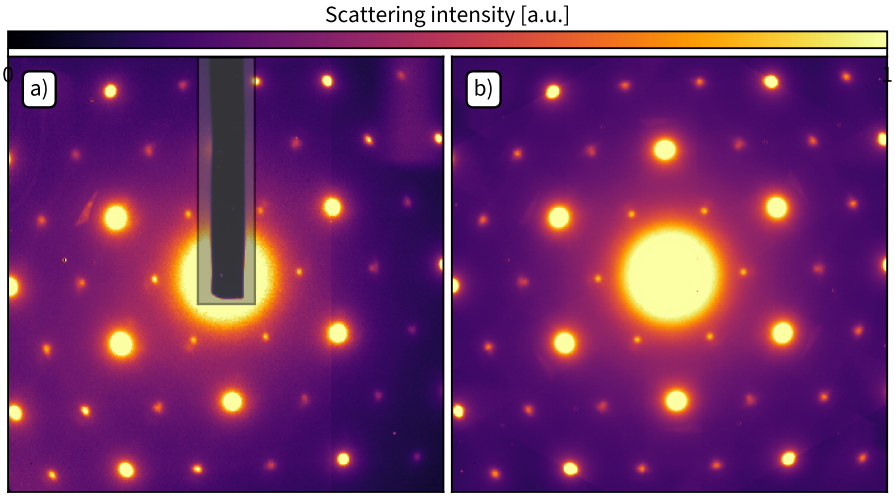

Figure A.7.: Symmetrization of a $TiSe_2$ diffraction pattern according to the $D6h$ point group (6-fold rotational symmetry). **a)** Diffraction pattern. The area that bounds the beam-block, which is ignored during symmetrization, is shown as a light-gray overlay. **b)** Symmetrized diffraction pattern.

A.4. Functions and data structures for crystallography

Accessing and manipulating crystal structures is an important component of many analysis workflows in electron microscopy, and ultrafast electron scattering is no different. `crystals` is a Python package designed and implemented by the author which facilitates the handling of crystallographic data. Some features of `crystals` are presented below.

A.4.1. Parsing of crystal structure

`crystals` includes parsers for many standard crystallographic information files. Crystal structures can be parsed from the *de-facto* standard Crystallography Information File (CIF) format (`.cif`).[23,24] Crystal structures can also be downloaded from the Crystallography Open Database,[25,26] which are stored in the CIF format. `crystals` also includes an internal database of simple crystal structures, stored in the CIF format. `crystal` also support downloading and parsing crystal structures from the Protein DataBank.[27,28]

`crystals` also supports the parsing of crystal structures determined by calculations. The conversion to and from the Atomic Simulation Environment[29] is supported. Additionally, the crystal structures resulting from plane-wave self-consistent field calculations from Quantum Espresso[30]

are parseable by `crystals`. Finally, `crystals` can download and parse structures calculated by the Materials Project.[31,32,33]

A.4.2. Representation of crystallographic information

The results of the parsing described in the previous section is stored a fundamental data structure called `Crystal`. A `Crystal` is a container of atomic positions and lattice information from which everything else can be derived. Most of the information in a `Crystal` is calculated on-the-fly, when requested by the user, so that the presented information is always up to date. Below is an example of the information that can be derived from the crystal structure of graphite:

```
> python -m crystals info graphite.cif
Crystal object with following unit cell:
    Atom C  @ (0.00, 0.00, 0.25)
    Atom C  @ (0.00, 0.00, 0.75)
    Atom C  @ (0.33, 0.67, 0.25)
    Atom C  @ (0.67, 0.33, 0.75)
Lattice parameters:
    a=2.464Å, b=2.464Å, c=6.711Å
    α=90.000°, β=90.000°, γ=120.000°
Chemical composition:
    C: 100.000%
Symmetry information:
    International symbol
                (short) ..... P6_3/mmc
                (full) ...... P 6_3/m 2/m 2/c
    International number .... 194
    Hermann-Mauguin symbol .. P63/mmc
    Pointgroup .............. 6/mmm
    Hall Number ............. 488
    Centering ............... CenteringType.primitive
```

A.4.3. Symmetry-determination

The determination of crystal symmetries from atomic positions is included in `crystals`, based on the space-group library `spglib`.[34,35] This allows to either check if a known structure possesses the expected symmetries, or to determine the point-group and space-group of a new structure.

References

1 L. P. René de Cotret, M. R. Otto, M. J. Stern, and B. J. Siwick. *An open-source software ecosystem for the interactive exploration of ultrafast electron scattering data*. *Advanced Structural and Chemical Imaging* **4** no. 1 (2018), p. 11. DOI: 10.1186/s40679-018-0060-y.

2 M. J Stern, L. P. René de Cotret, M. R. Otto, R. P. Chatelain, J.-P. Boisvert, M. Sutton, and B. J. Siwick. *Mapping momentum-dependent electron-phonon coupling and nonequilibrium phonon dynamics with ultrafast electron diffuse scattering*. *Physical Review B* **97** no. 16 (2018), p. 165416. DOI: 10.1103/physrevb.97.165416.

3 M. R. Otto, J.-H. Pöhls, L. P. René de Cotret, M. J. Stern, M. Sutton, and B. J. Siwick. *Mechanisms of electron-phonon coupling unraveled in momentum and time: the case of soft phonons in $TiSe_2$*. *Science Advances* **7** no. 20 (2021). DOI: 10.1126/sciadv.abf2810.

4 *HDF5 Language Bindings*. https://portal.hdfgroup.org/display/HDF5/HDF5+Language+Bindings. Accessed: 2021-04-05.

5 A. Collette. *Python and HDF5*. O'Reilly, 2013.

6 *MATLAB Help: HDF5 Files*. https://www.mathworks.com/help/matlab/hdf5-files.html. Accessed: 2021-04-05.

7 B. Fischer, M. Smith, and G. Pau. *rhdf5: R Interface to HDF5*. https://github.com/grimbough/rhdf5. Accessed: 2021-04-05.

8 M. Gao, C. Lu, H. Jean-Ruel, L. C. Liu, A. Marx, K. Onda, S. Koshihara, Y. Nakano, X. Shao, T. Hiramatsu, G. Saito, H. Yamochi, R. R. Cooney, G. Moriena, G. Sciaini, and R. J. D. Miller. *Mapping molecular motions leading to charge delocalization with ultrabright electrons*. *Nature* **496** no. 7445 (2013), pp. 343–346. DOI: 10.1038/nature12044.

9 L. P. René de Cotret, J.-H. Pöhls, M. J. Stern, M. R. Otto, M. Sutton, and B. J. Siwick. *Time-and momentum-resolved phonon population dynamics with ultrafast electron diffuse scattering*. *Physical Review B* **100** no. 21 (2019), p. 214115. DOI: 10.1103/physrevb.100.214115.

[10] S. Van Der Walt, S. C. Colbert, and G. Varoquaux. *The NumPy array: a structure for efficient numerical computation*. *Computing in Science & Engineering* **13** no. 2 (2011), pp. 22–30. DOI: 10.1109/mcse.2011.37.

[11] C. R. Harris, K. J. Millman, S. J. van der Walt, R. Gommers, P. Virtanen, D. Cournapeau, E. Wieser, J. Taylor, S. Berg, N. J. Smith, R. Kern, M. Picus, S. Hoyer, M. H. van Kerkwijk, M. Brett, A. Haldane, J. F. del Río, M. Wiebe, P. Peterson, P. Gérard-Marchant, K. Sheppard, T. Reddy, W. Weckesser, H. Abbasi, C. Gohlke, and T. E. Oliphant. *Array programming with NumPy*. *Nature* **585** no. 7825 (2020), pp. 357–362. DOI: 10.1038/s41586-020-2649-2.

[12] D. H. D. West. *Updating mean and variance estimates: an improved method*. *Communications of the ACM* **22** no. 9 (1979), pp. 532–535. DOI: 10.1145/359146.359153.

[13] S. Van der Walt, J. L. Schönberger, J. Nunez-Iglesias, F. Boulogne, J. D. Warner, N. Yager, E. Gouillart, and T. Yu. *Scikit-image: image processing in Python*. *PeerJ* **2** (2014), e453. DOI: 10.7717/peerj.453.

[14] P. Virtanen, R. Gommers, T. E. Oliphant, M. Haberland, T. Reddy, D. Cournapeau, E. Burovski, P. Peterson, W. Weckesser, J. Bright, S. J. van der Walt, M. Brett, J. Wilson, K. J. Millman, N. Mayorov, A. R. J. Nelson, E. Jones, R. Kern, E. Larson, C. J. Carey, İ. Polat, Y. Feng, E. W. Moore, J. VanderPlas, D. Laxalde, J. Perktold, R. Cimrman, I. Henriksen, E. A. Quintero, C. R. Harris, A. M. Archibald, A. H. Ribeiro, F. Pedregosa, and P. van Mulbregt. *SciPy 1.0: fundamental algorithms for scientific computing in Python*. *Nature Methods* **17** no. 3 (2020), pp. 261–272. DOI: 10.1038/s41592-019-0686-2.

[15] L. P. René de Cotret and B. J. Siwick. *A general method for baseline-removal in ultrafast electron powder diffraction data using the dual-tree complex wavelet transform*. *Structural Dynamics* **4** no. 4 (2017), p. 044004. DOI: 10.1063/1.4972518.

[16] I. W. Selesnick, R. G. Baraniuk, and N. C. Kingsbury. *The dual-tree complex wavelet transform*. *IEEE Signal Processing Magazine* **22** no. 6 (2005), pp. 123–151. DOI: 10.1109/msp.2005.1550194.

[17] R. B. Chevalier and J. R. Dwyer. *An open source, iterative dual-tree wavelet background subtraction method extended from automated diffraction pattern analysis to optical spectroscopy*. *Applied Spectroscopy* **73** no. 12 (2019), pp. 1370–1379. DOI: 10.1177/0003702819871330.

[18] C. M. Galloway, E. C. Le Ru, and P. G. Etchegoin. *An iterative algorithm for background removal in spectroscopy by wavelet transforms*. *Applied Spectroscopy* **63** no. 12 (2009), pp. 1370–1376. DOI: 10.1366/000370209790108905.

[19] I. MacLaren, T. A. Macgregor, C. S. Allen, and A. I. Kirkland. *Detectors—the ongoing revolution in scanning transmission electron microscopy and why this important to material characterization*. *APL Materials* **8** no. 11 (2020), p. 110901. DOI: 10.1063/5.0026992.

[20] E. J. Kirkland. In: *Advanced computing in electron microscopy*. Appendix C. Springer Science & Business Media, 2010. DOI: 10.1007/978-1-4419-6533-2.

[21] D. Padfield. *Masked object registration in the Fourier domain*. *IEEE Transactions on Image Processing* **21** no. 5 (2011), pp. 2706–2718. DOI: 10.1109/tip.2011.2181402.

[22] F. Liu, W. Wu, Y. Bai, S. H. Chae, Q. Li, J. Wang, J. Hone, and X.-Y. Zhu. *Disassembling 2D van der Waals crystals into macroscopic monolayers and reassembling into artificial lattices*. *Science* **367** no. 6480 (2020), pp. 903–906. DOI: 10.1126/science.aba1416.

[23] J. R. Hester. *A validating CIF parser: PyCIFRW*. *Journal of Applied Crystallography* **39** no. 4 (2006), pp. 621–625. DOI: 10.1107/s0021889806015627.

[24] T. Björkman. *CIF2Cell: Generating geometries for electronic structure programs*. *Computer Physics Communications* **182** no. 5 (2011), pp. 1183–1186. DOI: 10.1016/j.cpc.2011.01.013.

[25] S. Gražulis, D. Chateigner, R. T. Downs, A. F. T. Yokochi, M. Quirós, L. Lutterotti, E. Manakova, J. Butkus, P. Moeck, and A. Le Bail. *Crystallography Open Database–an open-access collection of crystal structures*. *Journal of Applied Crystallography* **42** no. 4 (2009), pp. 726–729. DOI: 10.1107/s0021889809016690.

[26] S. Gražulis, A. Daškevič, A. Merkys, D. Chateigner, L. Lutterotti, M. Quiros, N. R. Serebryanaya, P. Moeck, R. T. Downs, and A. Le Bail. *Crystallography Open Database (COD): an open-access collection of crystal structures and platform for world-wide collaboration*. *Nucleic Acids Research* **40** no. D1 (2012), pp. D420–D427. DOI: 10.1093/nar/gkr900.

[27] H. M. Berman. *The Protein Data Bank*. *Nucleic Acids Research* **28** no. 1 (2000), pp. 235–242. DOI: 10.1093/nar/28.1.235.

[28] T. Hamelryck and B. Manderick. *PDB file parser and structure class implemented in Python*. *Bioinformatics* **19** no. 17 (2003), pp. 2308–2310. DOI: 10.1093/bioinformatics/btg299.

[29] A. H. Larsen, J. J. Mortensen, J. Blomqvist, I. E. Castelli, R. Christensen, M. Dułak, J. Friis, M. N. Groves, B. Hammer, C. Hargus, E. D. Hermes, P. C. Jennings, P. D. Jensen, J. Kermode, J. R. Kitchin, E. L. Kolsbjerg, J. Kubal, K. Kaasbjerg, S. Lysgaard, J. Bergmann Maronsson, T. Maxson, T. Olsen, L. Pastewka, A. Peterson, C. Rostgaard, J. Schiøtz, O. Schütt, M. Strange, K. S. Thygesen, T. Vegge, L. Vilhelmsen, M. Walter, Z. Zeng, and K. W. Jacobsen. *The atomic simula-*

tion environment —- a Python library for working with atoms. *Journal of Physics: Condensed Matter* **29** no. 27 (2017), p. 273002. DOI: 10.1088/1361-648x/aa680e.

[30] P. Giannozzi, O. Andreussi, T. Brumme, O. Bunau, M. B. Nardelli, M. Calandra, R. Car, C. Cavazzoni, D. Ceresoli, M. Cococcioni, N. Colonna, I. Carnimeo, A. Dal Corso, S. de Gironcoli, P. Delugas, R. A. DiStasio, A. Ferretti, A. Floris, G. Fratesi, G. Fugallo, R. Gebauer, U. Gerstmann, F. Giustino, T. Gorni, J. Jia, M. Kawamura, H.-Y. Ko, A. Kokalj, E. Küçükbenli, M. Lazzeri, M. Marsili, N. Marzari, F. Mauri, N. L. Nguyen, H.-V. Nguyen, A. Otero-de-la-Roza, L. Paulatto, S. Poncé, D. Rocca, R. Sabatini, B. Santra, M. Schlipf, A. P. Seitsonen, A. Smogunov, I. Timrov, T. Thonhauser, P. Umari, N. Vast, X. Wu, and S. Baroni. *Advanced capabilities for materials modelling with Quantum ESPRESSO*. *Journal of Physics: Condensed Matter* **29** no. 46 (2017), p. 465901. DOI: 10.1088/1361-648x/aa8f79.

[31] G. Hautier, C. Fischer, V. Ehrlacher, A. Jain, and G. Ceder. *Data mined ionic substitutions for the discovery of new compounds. Inorganic Chemistry* no. 17 (2010), pp. 656–663. DOI: 10.1021/ic102031h.

[32] A. Jain, S. P. Ong, G. Hautier, W. Chen, W. D. Richards, S. Dacek, S. Cholia, D. Gunter, D. Skinner, G. Ceder, and K. A. Persson. *The Materials Project: a materials genome approach to accelerating materials innovation*. *APL Materials* **1** no. 1 (2013), p. 011002. DOI: 10.1063/1.4812323.

[33] S. P. Ong, S. Cholia, A. Jain, M. Brafman, D. Gunter, G. Ceder, and K. A. Persson. *The Materials Application Programming Interface (API): a simple, flexible and efficient API for materials data based on REpresentational State Transfer (REST) principles*. *Computational Materials Science* **97** (2015), pp. 209–215. DOI: 10.1016/j.commatsci.2014.10.037.

[34] R. W. Grosse-Kunstleve. *Algorithms for deriving crystallographic space-group information*. *Acta Crystallographica A* **55** no. 2 (1999), pp. 383–395. DOI: 10.1107/s0108767301016658.

[35] A. Togo and I. Tanaka. `spglib`*: a software library for crystal symmetry search*. *arXiv preprint arXiv:1808.01590* (2018).